The Pennsylvania State University

The J. Jeffrey and Ann Marie Fox Graduate School

FERROELECTRIC PROPERTIES AND SWITCHING KINETICS IN ZINC MAGNESIUM OXIDE THIN FILMS

A Dissertation in

Engineering Science and Mechanics

by

Leonard Jacques

Submitted in Partial Fulfillment
of the Requirements
for the Degree of

Doctor of Philosophy

August 2025

The dissertation of Leonard Jacques was reviewed and approved by the following:

Susan E. Trolier-McKinstry
Steward S. Flaschen Professor of Ceramic Science and Engineering
Evan Pugh University Professor
Director, Center for Dielectrics and Piezoelectrics
Director, Center for Three-Dimensional Ferroelectric Microelectronics
Co-Dissertation Advisor
Co- Chair of Committee

Michael Lanagan
Professor of Engineering Science and Mechanics
Co-Dissertation Advisor
Co- Chair of Committee

Osama Awadelkarim
Professor of Engineering Science and Mechanics
UNESCO Chair Professor
Director, Center for Nanotechnology Education and Utilization

Adri van Duin
Distinguished Professor, Mechanical Engineering
Professor of Engineering Science and Mechanics

Christopher Rahn
J. Lee Everett Professor of Mechanical Engineering

Laura Cabrera
Associate Professor of Engineering Science and Mechanics
Associate Professor of Philosophy
Dorothy Foehr Huck and J. Lloyd Huck Chair in Neuroethics
Associate Head for Graduate Programs

ABSTRACT

Zinc magnesium oxide (ZMO) thin films are being studied for their robust ferroelectric properties and as a candidate for ferroelectric memory. Unlike most ferroelectrics, ZMO can be deposited in a ferroelectric state at room temperature via RF-magnetron sputtering, making it compatible with back-end-of-the-line CMOS processes. ZMO has a remanent polarization of approximately ± 80 μC cm^{-2} and a coercive field ranging from 2.7 to 5 MV cm^{-1}; these can be varied by changing the Mg content and deposition processes.

The coercive field of ZMO is strongly temperature dependent between -40 and 300°C, and a pseudo-activation energy of the coercive field of ~ 30 meV was determined. The coercive field was also found to undergo fluid imprint. The fluid imprint is also thermally activated, having an activation energy of ~ 70 meV. The polarization retention properties in ZMO are exceptional, with virtually no degradation in the same state and opposite state retention beyond 1,000 hours at 200°C. However, fatigue lifetimes are on the order of 10^3 cycles before dielectric breakdown.

Switching kinetics of wurtzite $Zn_{1-x}Mg_xO$ (ZMO) thin films were studied. RF-magnetron reactively sputtered ~200 nm thick ZMO thin films with x=0.41 and x=0.27 were prepared on $Pt/Ti/SiO_2/Si$ substrates. Switching kinetics were measured at applied fields near the coercive fields, ranging from 3.4 to 5.1 MV cm^{-1}, and at temperatures ranging from room temperature to 100°C. Polarization reversal in ZMO was found to obey the Kolmogorov-Avrami-Ishibashi (KAI) kinetics model for nucleation and growth at applied fields near the coercive field, and to obey a nucleation-controlled model at higher applied fields required to switch the whole spontaneous polarization. Switching in the high-applied field regime can be described using either the Gaussian or inverse gamma distribution functions depending on the mole fraction of magnesium in the film. The switching current transients of the high-Mg content ZMO film (x=0.41) are

always bi-modal, whereas the low Mg composition film (x=0.27) obeys the Gaussian distribution initially following wake-up, and becomes bimodal with continued cycling. Rayleigh-like behavior of the dielectric constant revealed a simultaneous increase of the irreversible and decrease of the reversible contributions to the dielectric constant, which was ascribed to an increase in the density of domain walls with cycling. This also resulted in faster switching.

A process was developed to allow ferroelectric measurements to be made using a via access on thin ZMO films. Using this process, robust ferroelectricity was observed at a film thickness as low as 43 nm. Switching in ZMO depends strongly on pre-treatment conditions. For example, sub-coercive field switching of up to ¼ of the spontaneous polarization can be engendered at 3 MV cm^{-1} and 1 kHz. This occurs after films are cycled at fields high enough to switch the whole spontaneous polarization (i.e. 5 MV cm^{-1}), followed by a pre-treatment step at intermediate fields (i.e. 3 MV cm^{-1}), presumably to generate nuclei. Switching at lower fields is then possible, but results in switching less of the spontaneous polarization. Without introducing the intermediate step of switching at 3 MV cm^{-1} and 100 Hz, there is no switching at 1 kHz, showing the importance of preconditioning the material.

TABLE OF CONTENTS

LIST OF FIGURES

LIST OF TABLES

ACKNOWLEDGEMENTS

First and foremost, I give thanks to God Elohim, my Father Christ Ahnsahnghong and my Mother Heavenly Jerusalem. They have given me the ability, wisdom, strength, and courage to sustain me throughout graduate school. The amount of encouragement and support I received and continue to receive from Them transcends dimensions and is beyond what words can describe, or what modern science can ever hope to quantify.

I am thankful for my advisor, Prof. Susan Trolier-McKinstry, who over the past 7 ½ years has strived for me to do my best and always to put forth good and honest work. Surely, the values I learned from Prof. Trolier-McKinstry extend beyond applications in scientific fields. Her passion, dedication, loyalty, and servitude to science and to her students are of an extraordinary magnitude. I could not have asked for a better advisor and experience in graduate school, and because of her, I give even more thanks to God.

Next, I thank my parents Lionel and Clunie Jacques who supported me through my whole life and only encourage me. My mother has contributed significantly to who I am. She never tolerated excuses from me, always quickly correcting my mindset with her sharp wit. My dad always set an example of modesty, which has become a subtle anchor for me and to this day guides me to focus my time and attention on what is important.

I express thanks to all my co-authors who are mentioned in chapters 4 and 5. I also would like to thank the staff at the Materials Research Institute who have been nothing but helpful over the past 7 ½ years. Namely, Jeff Long, Fan He, Andy Fitzgerald, Michael LaBella, and Kathleen Gehoski provided much support for the work in this thesis. Prof. Keisuke Yazawa at the National Renewable Energy Laboratory helped tremendously by assisting with troubleshooting the switching kinetics set-up and providing a transimpedance amplifier for us to use. Prof. Jon-Paul

Maria at Penn State and his postdoc and students Ryu Gyunghyun, Devin Goodling, and Jackson Spurling were generous in depositing high quality ZMO samples for me to test.

I would like to thank my committee, Professors Michael Lanagan, Osama Awadelkarim, Adri van Duin, and Chris Rahn for taking time out of their busy schedules to provide guidance for my thesis.

This work is supported as part of the Center for 3D Ferroelectric Microelectronics (3DFeM), an Energy Frontier Research Center funded by the U.S. Department of Energy (DOE), Office of Science, Basic Energy Sciences under Award DE-SC0021118.

The findings and conclusions do not necessarily reflect the view of the funding agency.

Chapter 1

Introduction

Ferroelectricity has fascinated scientists and ceramists since its discovery in 1920.[1,2,3] Ferroelectrics such as Rochelle salt and potassium dihydrogen phosphate (KDP) were tested extensively to unveil their ferroelectric properties.[4] In the 1950s, lead zirconate titanate, or PZT was discovered.[5] To date, PZT transducers have been used in technologies from ultrasonic imaging and physical therapy[6] to massive transducers in submarines (i.e. sonar);[7] as an actuator, it has been employed in military applications[8], space telescopes[9], ultrasonic fingerprint scanners[10], and low-density memory in microcontroller chips, among others.[11]

However, the desire for dense, fast, non-volatile memory has increased significantly, at the time of this dissertation,[12] due in part to the rapid progression of artificial intelligence and training operations at data centers.[13,14] In fact, data centers are projected to consume 6 to 12% of all U.S. electricity by the year 2028, and over 50% of this increase is due to AI specialized data centers (see Figures 1-1 and 1-2).[14] Although the energy efficiency of AI chips has increased exponentially since 2008 (Figure 1-3),[15] 90% of the energy costs are due to memory retrieval.[16] Therefore, reducing the distance between memory and compute can produce large energy savings in AI processes.[16]

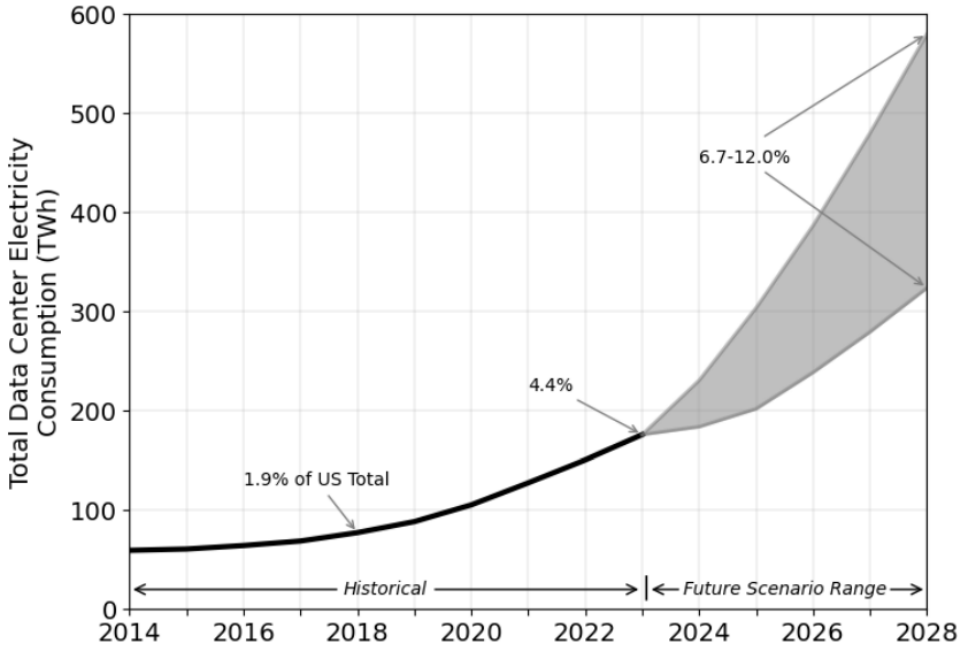

Figure **1-1**: Trends and projected increase in energy usage from data centers up to the year 2028.[14]

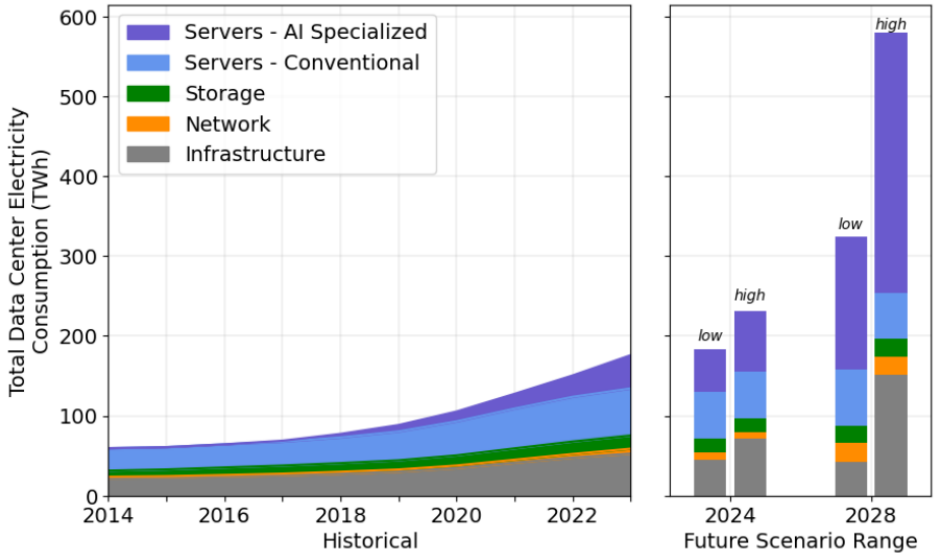

Figure **1-2**: Trends in specified data center energy usage and predictions on usage up to the year 2028.[14]

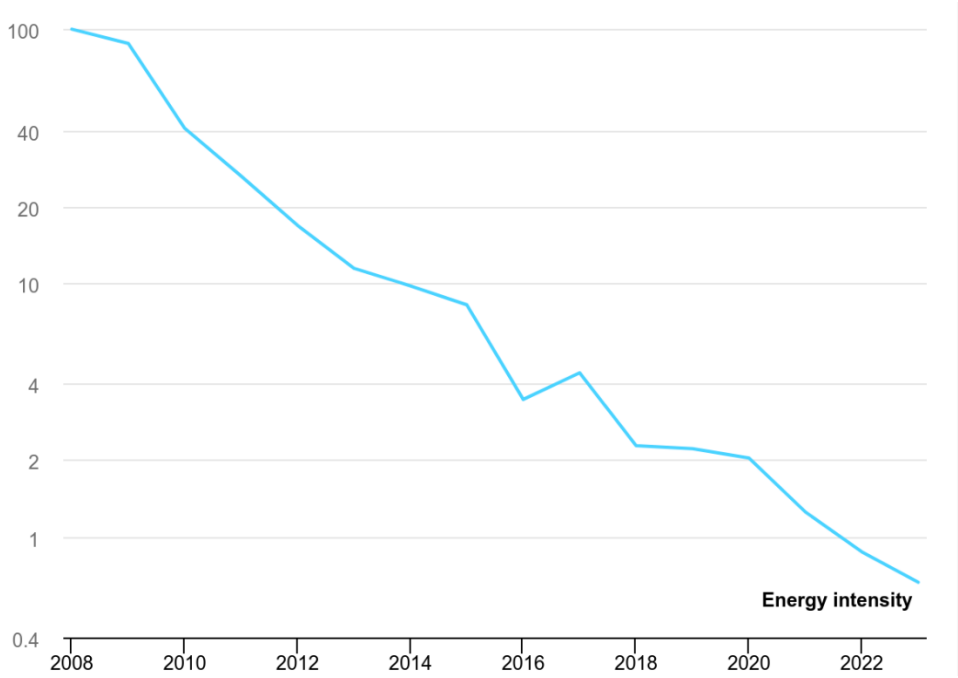

Figure **1-3**: The efficiency of AI chips has increased exponentially between 2008 and 2023.[15]

To counter energy expenditures due to computer memory, non-von Neumann architectures are sought (see Figure 1-4). “von-Neumann” indicates that the memory (RAM) and control processing unit (CPU) are separated in the computer architecture. This separation causes energy loss and delays in computation due to data latency. These energy losses can be mitigated by co-locating the RAM and the CPU in a non-von Neumann architecture. This means the RAM should be processed directly on top of the CPU, which imposes strict process limitations, including that the processing temperatures cannot exceed 400°C, or 450°C for a short period of time.[17]

One challenge of collocating current DRAM technology with the CPU is that charge must continually be pumped into the memory cells to refresh them, which would cause the CPU to get too hot.[18] An alternative is ferroelectric RAM (FeRAM) where in the place of a dielectric, a ferroelectric is used. Ferroelectrics retain their polarization states for long periods of time, such that they do not need to be refreshed so long as the memory cells are not being read or written.

Therefore, non-von Neumann architectures can be fulfilled with FeRAM technology. This would provide a two-fold cut-back on energy consumption in computing: (1) the energy latency between the CPU and the RAM is decreased due to their colocation, and (2) removing the constant refresh from the memory.

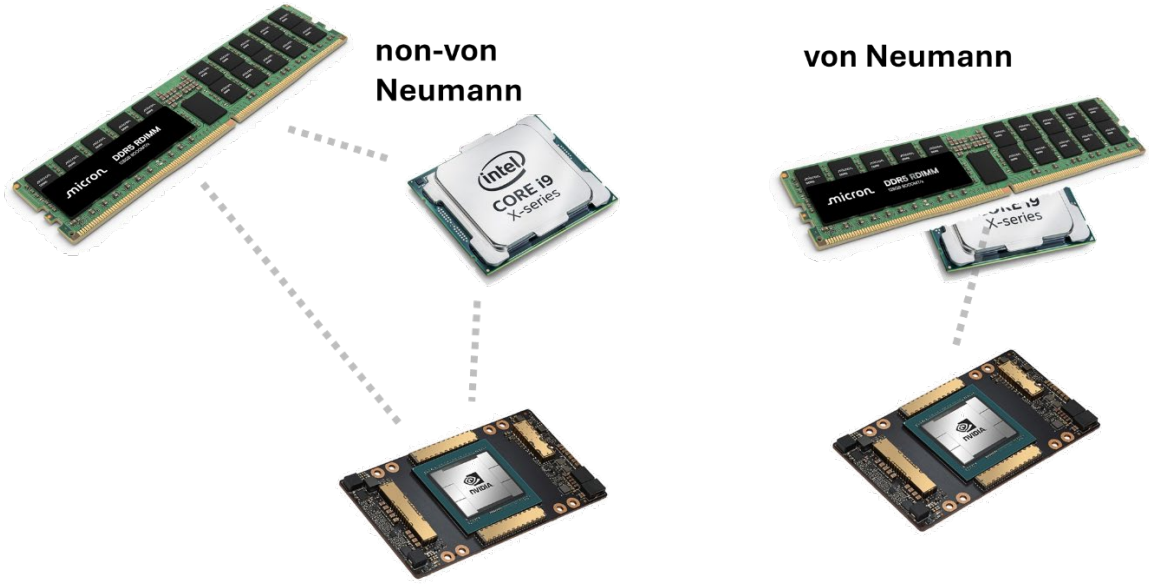

Figure **1-4**: A schematic showing the difference between von Neumann and non-von Neumann architectures.

Due to scaling limits of lead zirconate titanate films, commercial ferroelectric memory is currently low-density and is not suitable for most computation applications.[11] Conventional dynamic random access memory (DRAM) requires pumping charge 16 to 32 times per second, and each device can contain billions of capacitors.[19] Energy expenditures associated with computation are further aggravated by the need to reach deeper into the memory stack for many data-intensive applications. Transfer of data and instructions thus adds to both the energy cost and the latency of many compute systems. This, in turn, results in emission of egregious amounts of CO_2 into the atmosphere, especially as the infrastructure for AI learning and datacenters

increases. For example, last year Microsoft reported a 30% increase in their CO_2 emissions because of their expanding AI infrastructure.[20]

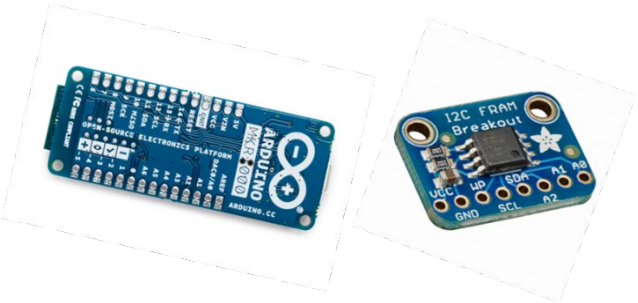

Figure **1-5**: To the left is an Arduino MKR1000 Wifi microcontroller, and to the right is a Adafruit MCCI FRAM 12C 256 kbit memory card applicable with microcontrollers.

The FeRAM technology commercially available today (see Figure 1-5) is relatively low density, < 16 Mb capacity,[21] primarily due to thickness limitations of the ferroelectric PZT layer.[22] Processing temperatures for PZT also exceed 400°C,[23] making it incompatible with back end of the line (BEOL) processes. Therefore, the driving force for development of new ferroelectrics which are (1) scalable and (2) can be processed at low temperatures (< 400 °C) promotes this investigation.

The first of the potentially BEOL compatible materials to emerge was ferroelectric Hafnia (HfO_2), first reported publicly in 2011,[24] and later its solid solutions, the most studied being $(Hf,Zr)O_2$.[25] Ferroelectricity exists in HfO_2 down to thicknesses as low as 2 nm.[26] Most reports on ferroelectric hafnia and its derivatives show ferroelectricity depends on the existence of a strain-induced[27] polar orthorhombic phase, and that other phases such as a monoclinic and an antipolar orthorhombic coexist in the film which do not contribute to the ferroelectric response. Tensile strain is often induced by the top electrode,[28] and most reports emphasize the dependence of the ferroelectric properties on the electrode stack. Ferroelectric $(Hf,Zr)O_2$ can be deposited at

400°C which is BEOL compatible for CMOS processes, as shown in Figure 1-6.[29] The cubic hafnia structure is shown in Figure 1-7.

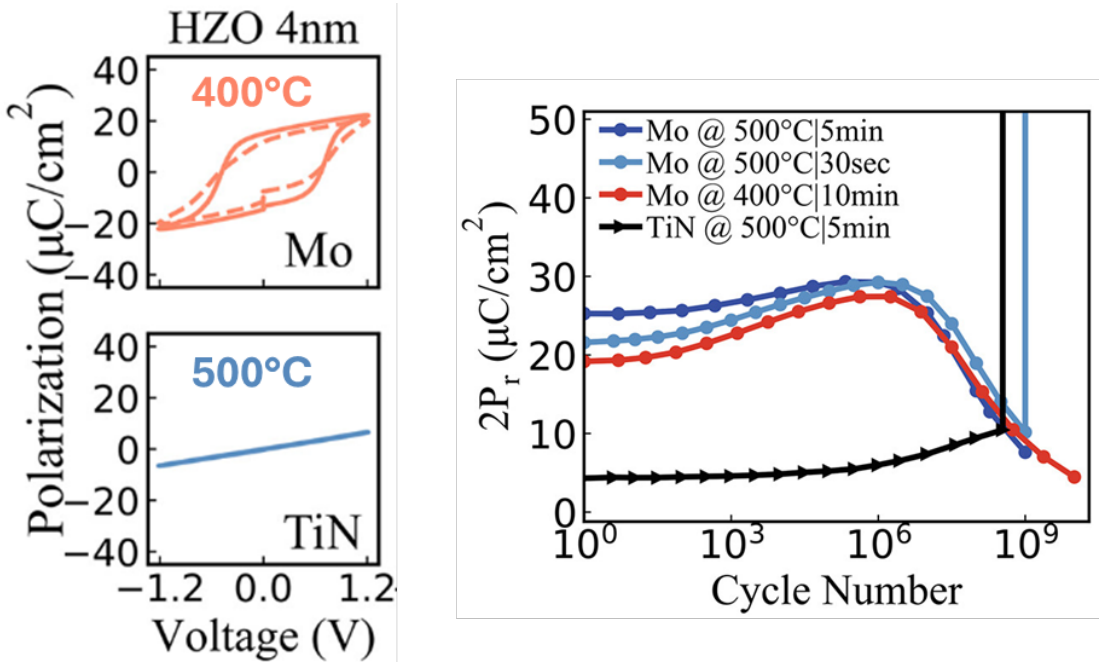

Figure **1-6**: Ferroelectric (Hf,Zr)O_2 can be deposited at 400°C with Mo electrodes, and scaled to < 5 nm with an operating voltage of ± 1.2 V.[29]

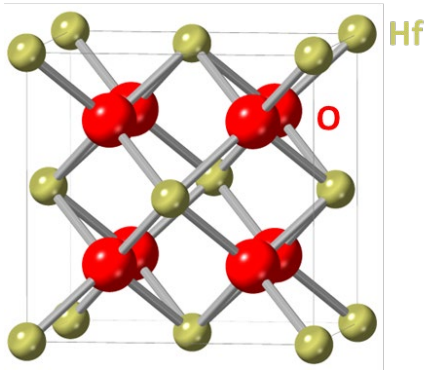

Figure **1-7**: The structure of cubic hafnia.

FeRAM with large density memory arrays (32 Gb) have been demonstrated for hafnia technology by Micron Technologies with reasonable fatigue properties extending past 10^{10} cycles and retention > 10 years.[12] To summarize the desired specifications for FeRAM in a non-von Neumann architecture vs. standalone FeRAM, some processing and device requirements are listed in Table 1-1.

Table **1-1**: Design constraints and device property comparisons between conventional FeRAM and non von Neumann FeRAM incorporated into a BEOL process. Parameter values are taken from Khan et al.[30] and from Micron Technology.[12]

Parameter	Non von Neumann FeRAM	Conventional FeRAM
Processing temperature limit	≤ 400°C	> 700°C
Operating voltage	~ 1 V	≤ 4 V
Cycling endurance	> 10^{12} cycles	> 10^{12} –10^{14} cycles
Retention	10 years	10 years

In 2019, a new class of ferroelectric materials was discovered based on the wurtzite structure; the first exemplar was $Al_{1-x}Sc_xN$.[31] One promising aspect of the discovery is that processing temperatures for rf magnetron sputtering are < 400°C and hence are compatible with BEOL processes. This discovery commenced a race to discover new ferroelectrics, and within two years, ferroelectricity was discovered in two more systems at the Pennsylvania State University: (Al,B)N[32] and (Zn,Mg)O[33], both of which can be deposited in a ferroelectric state at <400°C. Polarization-Electric field hysteresis loops for (Al,B)N and (Zn,Mg)O are presented in Figure 1-8.

The (Al,B)N has a larger coercive field and remanent polarization than (Zn,Mg)O. However, the coercive field for ZMO is still two orders of magnitude larger than that for PZT, which presents challenges for memory applications. The first of these is that scaling to < 10 nm

ferroelectric layer thickness is required to achieve low voltage operation (~ 1 V). The second is that such a large coercive field and remanent polarization can pose reliability including limited fatigue lifetimes.

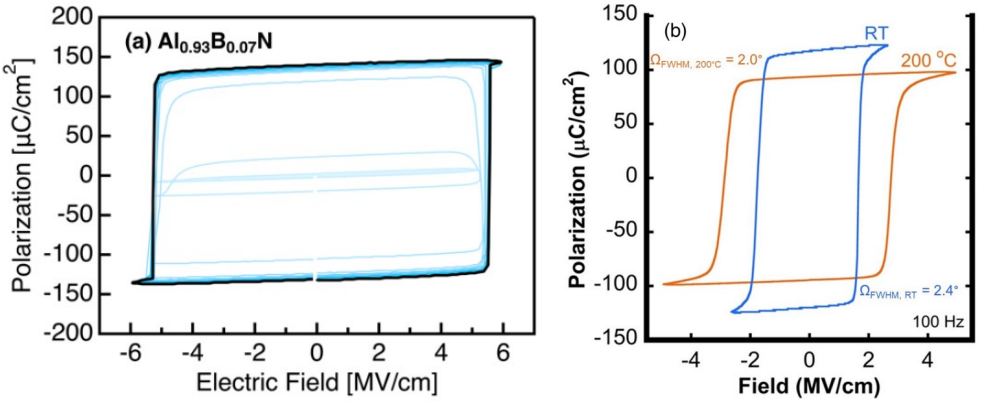

Figure **1-8**: Polarization-Electric field hysteresis loops of ferroelectric (a) $Al_{0.93}B_{0.07}N$ (left) and (b) $Zn_{0.66}Mg_{0.34}O$ (ZMO). ZMO can deposited ferroelectric at room temperature.[32,33]

There have been many studies on ferroelectric (Al,Sc)N and (Al,B)N for their properties including retention, wake-up, and fatigue lifetimes. However, The (Zn,Mg)O system is much less well studied after the initial report on ferroelectricity in 2020.[33] This dissertation undertakes to experimentally explore the ferroelectric behavior of ZMO with an emphasis on switching and retention, alongside computational methods employed by colleagues in the field.

1.1 Thesis Organization

A literature review with some preliminary data is presented in Chapter 2 for the reader to gain sufficient background knowledge to understand the relevant properties of ZnO and ZMO in ferroelectric applications. Various deposition methods are summarized, the presence and role of defects is discussed, and applications which can be influenced by ferroelectric properties are

presented. Chapter 3 presents a detailed list of experimental methods used in this work and supplements the abbreviated experimental methods sections in Chapters 4 and 5. Chapter 4 reports experimental results on properties of ZMO films which are relevant to memory applications, including wake up, retention, fatigue, fluid imprint, and identifying the conduction mechanism in ZMO. Chapter 5 discusses the switching behavior in ZMO and introduces a kinetics model to describe a newly discovered polarization reversal mechanism in wurtzite structure ferroelectrics: Individual-Column Switching (ICS). Chapter 6 presents a detailed non-aqueous 3-step process for depositing remote probe contact devices on ZMO. Using this approach, ferroelectric switching was demonstrated in ZMO films scaled to 43 nm in thickness. The major conclusions from the thesis along with potential future work is discussed in Chapter 7. The future work considers alternative deposition methods such as sol-gel and a reduced graphene oxide intercalation method for depositing thin ZMO (< 30 nm). A domain engineering method to switch part of the spontaneous polarization at sub-coercive fields (≤ 3 MV cm^{-1}) is also presented. Appendix A presents an attempt at reducing the coercive field of ZMO by seeding the top electrode interface with SiO_2 nanodots. This was found to have no benefit on the switching kinetics – later-on ICS was discovered in ZMO. The non-aqueous process for patterning top electrodes in ZMO is presented in Appendix B. Calculations and MATLAB codes which were used in this work are presented in Appendix C.

References

[1] Valasek, J. (1921). Piezo-electric and allied phenomena in Rochelle salt. *Physical Review*, *17*(4), 475.

[2] Trolier-McKinstry, S. (2020). Impact of ferroelectricity. *American Ceramic Society Bulletin*, *99*, 22-30.

[3] Cross, L. E., & Newnham, R. E. (1987). History of ferroelectrics. *Ceramics and Civilization*, *3*, 289-305.

[4] Jaffe, H. (1958). Piezoelectric ceramics. *Journal of the American Ceramic Society, 41*(11), 494-498.

[5] Shirane, G., Suzuki, K., & Takeda, A. (1952). Phase transitions in solid solutions of $PbZrO_3$ and $PbTiO_3$ (II) X-ray study. *Journal of the Physical Society of Japan*, *7*(1), 12-18.

[6] Chilibon, I. (2008). Ultrasound transducer for medical therapy. *Sensors and Actuators A: Physical*, *142*(1), 124-129.

[7] Rodrigo, G. C. (1970). *Analysis and Design of Piezoelectric Sonar Transducers* (Doctoral Dissertation, Queen Mary University of London).

[8] American Piezo, Inc. (2020, March 12). What is the purpose of a piezo motor? American Piezo. Retrieved October 21, 2024, from https://www.americanpiezo.com/blog/what-is-the-purpose-of-a-piezo-motor/

[9] Wallace, M. L., Ramirez, J. I., Allured, R., Prieskorn, Z., Marquez, V., Burrows, D. N., Reid, P., Jackson, T. N., & Trolier-McKinstry, S. (2018). Integrated electronics for control of large-area piezoelectric arrays for adjustable optics. *Sensors and Actuators A: Physical*, *276*, 304-311.

[10] Cheng, C. Y., Dangi, A., Ren, L., Tiwari, S., Benoit, R. R., Qiu, Y., Lay, H. S., Agrawal, S., Pratap, R., Kothapalli, S. R., Mallouk, T. E., Cochran, S., & Trolier-McKinstry, S. (2019). Thin film PZT-based PMUT arrays for deterministic particle manipulation. *IEEE Transactions on Ultrasonics, Ferroelectrics, and Frequency Control*, *66*(10), 1606-1615.

[11] Fujitsu Semiconductor Limited. Reasons to Choose FeRAM. Fujitsu Semiconductor. Retrieved October 21, 2024, from https://www.fujitsu.com/jp/group/fsm/en/products/feram/overview/

[12] Ettisserry, D., Visconti, A., Bonanomi, M., Pazzocco, R., Locatelli, A., Sebastiani, A., Chavan, A., Hollander, M., Servalli, G., Calderoni, A., & Ramaswamy, N. (2024, April). Comprehensive Reliability

Assessment of 32Gb (Hf,Zr)O_2-Based Ferroelectric NVDRAM. In *2024 IEEE International Reliability Physics Symposium (IRPS)* (pp. 1-8). IEEE.

[13] Zhang, J., & Tao, D. (2020). Empowering things with intelligence: a survey of the progress, challenges, and opportunities in artificial intelligence of things. *IEEE Internet of Things Journal*, *8*(10), 7789-7817.

[14] Shehabi, A., Smith, S. J., Hubbard, A., Newkirk, A., Lei, N., Siddik, M. A. B., Holecek, B., Koomey, J., Masanet, E., & Sartor, D. (2024). *2024 United States data center energy usage report* (LBNL-2001637). Lawrence Berkeley National Laboratory. https://eta-publications.lbl.gov/sites/default/files/2024-12/lbnl-2024-united-states-data-center-energy-usage-report.pdf

[15] IEA. (2024). *What the data centre and AI boom could mean for the energy sector*. International Energy Agency. Retrieved from https://www.iea.org/commentaries/what-the-data-centre-and-ai-boom-could-mean-for-the-energy-sector

[16] Bourzac, K. (2024). Fixing AI's energy crisis. *Nature*.

[17] Beals, M., Michel, J., Liu, J. F., Ahn, D. H., Sparacin, D., Sun, R., Hong, C. Y., Kimerling, L. C., Pomerene, A., Carothers, D., Beattie, J., Kope, A., Apsel, A., Rasras, M. S., Gill, D. M., Patel, S. S., Tu, K. Y., Chen, Y. K., & White, A. E. (2008, February). Process flow innovations for photonic device integration in CMOS. In Silicon Photonics III (Vol. 6898, pp. 31-44). SPIE.

[18] Heyman, K. (2022, June 9). DRAM thermal issues reach crisis point. *Semiconductor Engineering*. https://semiengineering.com/dram-thermal-issues-reach-crisis-point/

[19] Bhati, I., Chang, M. T., Chishti, Z., Lu, S. L., & Jacob, B. (2015). DRAM refresh mechanisms, penalties, and trade-offs. *IEEE Transactions on Computers*, *65*(1), 108-121.

[20] Robinson, D. (2024, May 16). *Microsoft's carbon emissions up nearly 30% thanks to AI*. The Register. Retrieved October 21, 2024, from https://www.theregister.com/2024/05/16/microsoft_co2_emissions/

21 Infineon Technologies. (n.d.). *F-RAM (Ferroelectric RAM)*. Infineon Technologies. Retrieved October 30, 2023, from https://www.infineon.com/cms/en/product/memories/f-ram-ferroelectric-ram/

[22] Ihlefeld, J. F., Harris, D. T., Keech, R., Jones, J. L., Maria, J-P., & Trolier-McKinstry, S. (2016). Scaling effects in perovskite ferroelectrics: fundamental limits and process-structure-property relations. *Journal of the American Ceramic Society*, *99*(8), 2537-2557.

[23] Kwok, C. K., Desu, S. B., & Kammerdiner, L. (1990). Effect of thermal processing conditions on ferroelectric PZT thin films. *MRS Online Proceedings Library (OPL)*, *200*, 83.

[24] Böscke, T. S., Müller, J., Bräuhaus, D., Schröder, U., & Böttger, U. J. A. P. L. (2011). Ferroelectricity in hafnium oxide thin films. *Applied Physics Letters*, *99*(10), 102903.

[25] Lee, M. H., Wei, Y. T., Liu, C., Huang, J. J., Tang, M., Chueh, Y. L., Chu, K. Y., Chen, M. J., Lee, H. Y., Chen, Y. S., Lee, L. H., & Tsai, M. J. (2015). Ferroelectricity of $HfZrO_2$ in energy landscape with surface potential gain for low-power steep-slope transistors. *IEEE Journal of the Electron Devices Society*, *3*(4), 377-381.

[26] Shen, Y., Ooe, K., Yuan, X., Yamada, T., Kobayashi, S., Haruta, M., Kan, D., & Shimakawa, Y. (2024). Ferroelectric freestanding hafnia membranes with metastable rhombohedral structure down to 1-nm-thick. *Nature Communications*, *15*(1), 4789.

[27] Shiraishi, T., Katayama, K., Yokouchi, T., Shimizu, T., Oikawa, T., Sakata, O., Uchida, H., Imai, Y., Kiguchi, T., Konno, T. J., & Funakubo, H. (2016). Impact of mechanical stress on ferroelectricity in $(Hf_{0.5}Zr_{0.5})O_2$ thin films. *Applied Physics Letters*, *108*(26), 262904.

[28] Athle, R., Persson, A. E., Irish, A., Menon, H., Timm, R., & Borg, M. (2021). Effects of tin top electrode texturing on ferroelectricity in $Hf_{1-x}Zr_xO_2$. *ACS Applied Materials & Interfaces*, *13*(9), 11089-11095.

[29] Huang, F., Saini, B., Wan, L., Lu, H., He, X., Qin, S., Tsai, W., Gruverman, A., Meng, A. C., Wong, H. -S. P., McIntyre, P. C., & Wong, S. (2024). Dimensional scaling of ferroelectric properties of hafnia-zirconia thin films: Electrode interface effects. *ACS Nano*, *18*(27), 17600-17610.

[30] Khan, A. I., Keshavarzi, A., & Datta, S. (2020). The future of ferroelectric field-effect transistor technology. *Nature Electronics*, *3*(10), 588-597.

[31] Fichtner, S., Wolff, N., Lofink, F., Kienle, L., & Wagner, B. (2019). AlScN: A III-V semiconductor based ferroelectric. *Journal of Applied Physics*, *125*(11).

[32] Hayden, J., Hossain, M. D., Xiong, Y., Ferri, K., Zhu, W., Imperatore, M. V., Giebink, N., Trolier-McKinstry, S., Dabo, I., & Maria, J-P. (2021). Ferroelectricity in boron-substituted aluminum nitride thin films. *Physical Review Materials*, *5*(4), 044412.

[33] Ferri, K., Bachu, S., Zhu, W., Imperatore, M., Hayden, J., Alem, N., Giebink, N., Trolier-McKinstry, S., & Maria, J-P. (2021). Ferroelectrics everywhere: Ferroelectricity in magnesium substituted zinc oxide thin films. *Journal of Applied Physics*, *130*(4), 044101.

Chapter 2

Literature Review with Preliminary Data

2.1 Introduction

The study of wurtzite structure ferroelectrics is relatively new[1] and more work is necessary to obtain a well-rounded understanding of the mechanisms responsible for their ferroelectric properties. This literature review summarizes the structural origin of ferroelectricity, various deposition methods for (Zn,Mg)O (from here on, called "ZMO"), important defects in ZMO, doping, secondary phases, electrical properties, optical properties, some applications of ZMO, and special considerations for the switching kinetics in wurtzite ferroelectrics.

2.2 Origin of Ferroelectricity

Ferroelectric materials are a subset of piezoelectric materials.[2] The term "ferroelectric" describes a class of materials with a spontaneous polarization that can be reoriented by an applied electric field between two or more crystallographically-defined directions. This reorientation produces hysteresis in the polarization response. The polarization remaining at zero field is the remanent polarization (P_r). In order to achieve polarization reversal, the applied electric field should be greater than the coercive field (E_c). The applied field can be driven beyond the coercive field to further increase the polarization, and achieve the maximum polarization (P_{max}). Figure 2-1 shows the ferroelectric hysteresis loop, which relates the polarization response to an applied field, for potassium sodium niobate ($K_{0.5}Na_{0.5}NbO_3$), a perovskite ferroelectric.

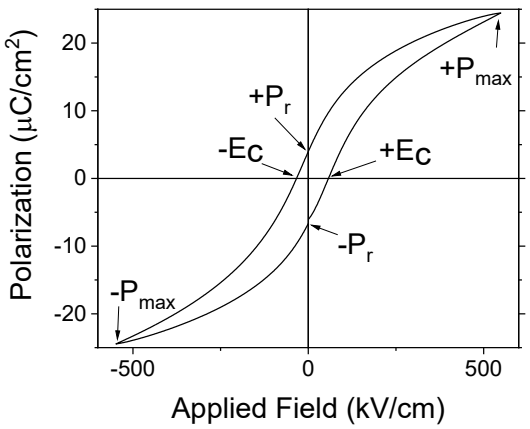

Figure **2-1**: A polarization-electric field (P-E) hysteresis loop of manganese doped potassium sodium niobate. The coercive field, E_c, remanant polarization, P_r, and maximum polarization, P_{max}, are labelled.

The reversible spontaneous dipole which enables ferroelectricity requires the absence of a center of symmetry in the crystal structure. In the well-known perovskite ferroelectrics, there is a displacement of a central cation along one of the polar axes for the crystal lattices as defined in Figure 2-2.[3] The applied fields required to switch the polarization in this class of ferroelectrics is relatively low, typically on the order of 30 kV/cm – 100 kV/cm in thin films.

There are two types of ferroelectrics: extender and rotator.[3] In extender ferroelectrics such as $PbTiO_3$, the spontaneous polarization can only be oriented along a crystallographically defined direction. In rotator ferroelectrics such as $K_{0.5}Na_{0.5}NbO_3$, the polarization vector can rotate in the direction of the applied field if it is not along the polar axis. When the field is removed, the polarization rotates back to the crystallographically-defined orientation.

To achieve the strongest dielectric and piezoelectric responses, ferroelectric materials are often designed so their composition lies at or near their morphotropic phase boundary (MPB). This describes the composition at which two or more phases of a material coexist, and the material is poised on the brink of structural instability. The benefit of this is easy polarization

reversal (i.e. at low coercive fields) and large response. Compositions situated at the MPB often show anomalies in their piezoelectric and dielectric properties such as high piezoelectric coefficients and high dielectric constants.[4, 5]

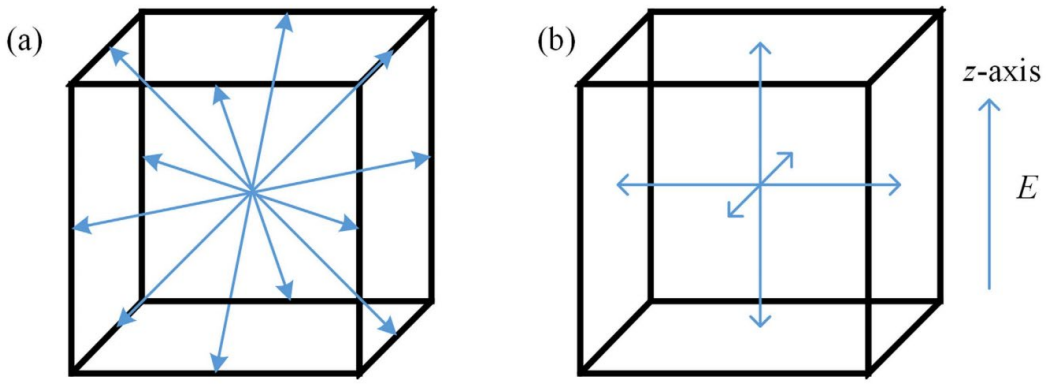

Figure **2-2**: Spontaneous polarization directions in the orthorhombic (left) lattice along the <110> axes, and the tetragonal (right) perovskite lattice along the <001> axes.[3]

2.3 The Zinc Magnesium Oxide System

2.3.1 The Ferroelectric Wurtzite Structure

There are both similarities and differences in the newly discovered wurtzite ferroelectrics when compared with ferroelectrics based on the perovskites structure. AlN, GaN, and ZnO are mid- to high- band gap materials which also have relatively high breakdown fields (> 4 MV cm^{-1}), compared to typical ferroelectrics.[6,7] The wurtzites are "extender" ferroelectrics, and have only one reversible polarization direction, along the crystallographic *c*-axis, as shown in Figure 2-3. Therefore, films strongly oriented along the crystallographic {0001} plane are useful for the ferroelectric wurtzites. In addition, polarization reversal involves the breaking of bonds (i.e. a

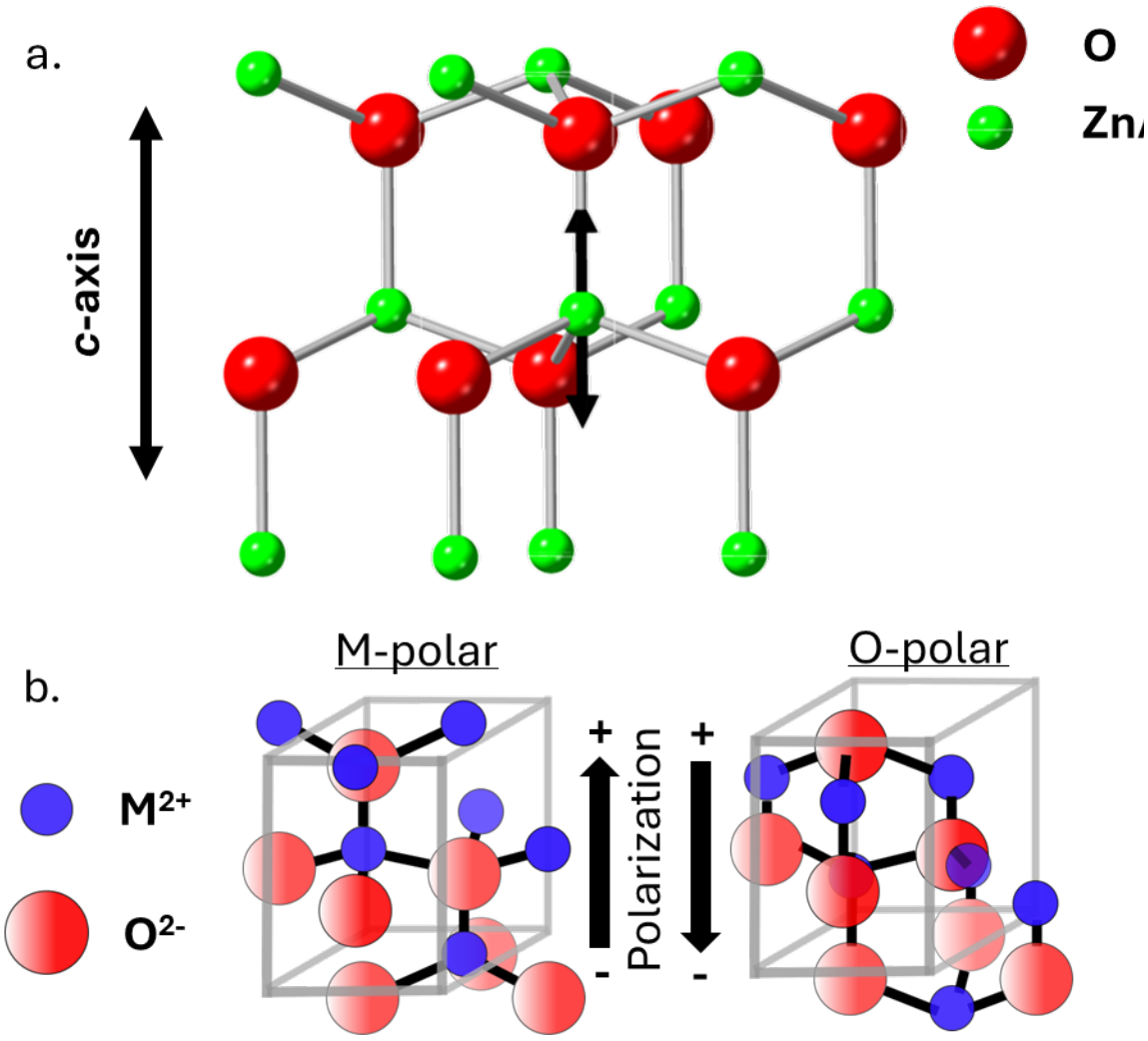

Figure **2-3**: The hexagonal wurtzite structure ZnO has only one polarization axis in the *c*-direction, indicated by the black arrows in (a). (b) The cation must traverse the basal plane in order for polarization reversal to occur, as for all wurtzite ferroelectrics. This action involves the breaking of bonds, which is the reason for the large coercive field. In this work, the ferroelectric wurtzite films are grown "O-polar", that is, terminated by the anion at the top electrode surface, and by the cation at the bottom electrode surface.

reconstructive transition), making the coercive fields (E_c) two or three orders of magnitude larger than perovskite ferroelectrics where polarization reversal involves displacive transitions, as shown in Figure 2-4. The larger coercive fields and larger remanent polarizations compared to other ferroelectrics also indicate the larger amount of energy it requires to switch the films.

Polarization reversal has been observed to occur by domain nucleation and growth in the wurtzite-structure ferroelectrics.[8] Domains are typically defined as regions with a uniform polarization in a ferroelectric crystal, similar to magnetic domains in magnetic materials.[9] Domains of a particular orientation expand or shrink under a sufficiently large applied field, and this behavior is nearly always governed by the motion of domain walls. Unlike conventional ferroelectrics, like PZT, which already have a population of reorientable or reversible domains in their as-grown state, ferroelectric wurtzites are typically grown unipolar; for the films utilized in this thesis, the dipole is oriented towards the substrate.[10, 11]

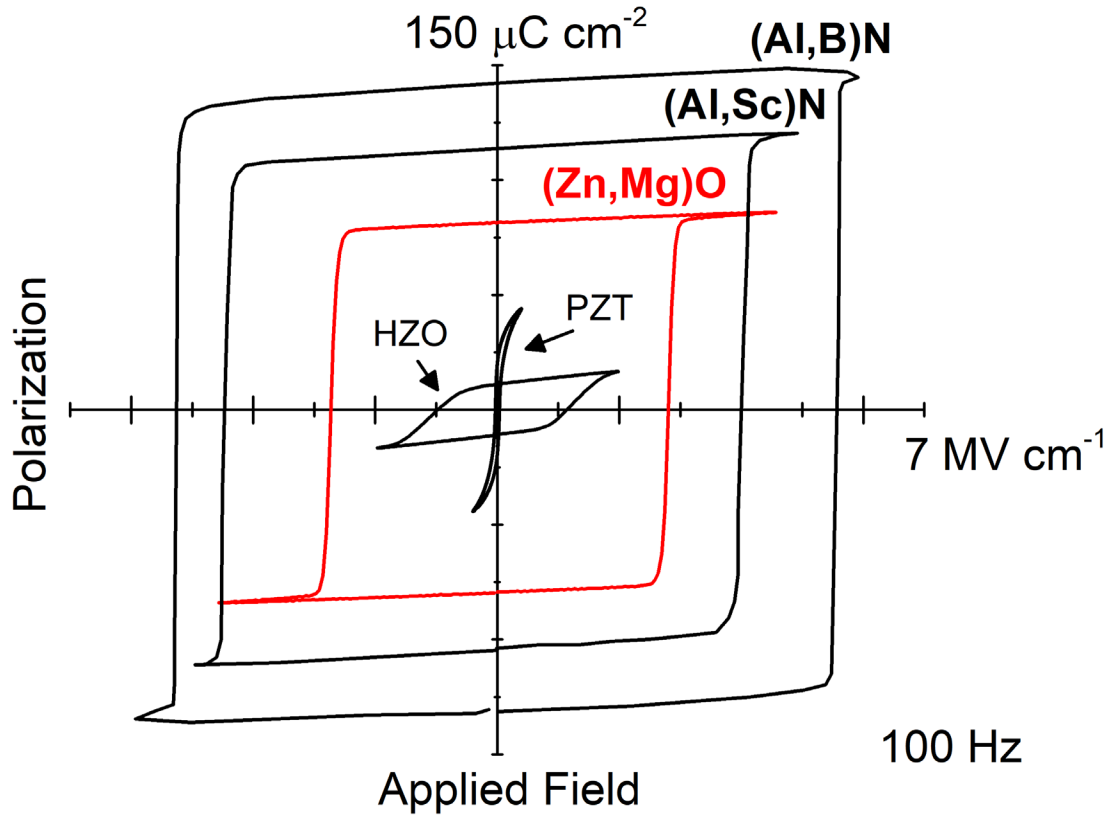

Figure **2-4**: ZMO has a coercive field two orders of magnitude greater than PZT, and 3 times the magnitude of ferroelectric $(Hf,Zr)O_2$. The PZT film was deposited by Kae Nakamura.

A finite population of reverse domains must develop before robust ferroelectricity can be observed in wurtzite structure films, because they typically do not have a large population of oppositely oriented domains in the as-grown state. In order to generate a population of ferroelectric domains, the films must be subjected to field cycling at magnitudes greater than the typical coercive field. This is due to domain nucleation being more energetically expensive than growth due to the motion of domain walls.[12] Therefore, for the ferroelectric wurtzites an energetically expensive "wake-up" process is required in order to generate a large enough population of domains for robust ferroelectricity to be observed.[10] The wake-up process under

various applied fields is shown in Figure 2-5 for ZMO. Wake-up has been similarly observed in the ferroelectric hafnia system,[13] among others.

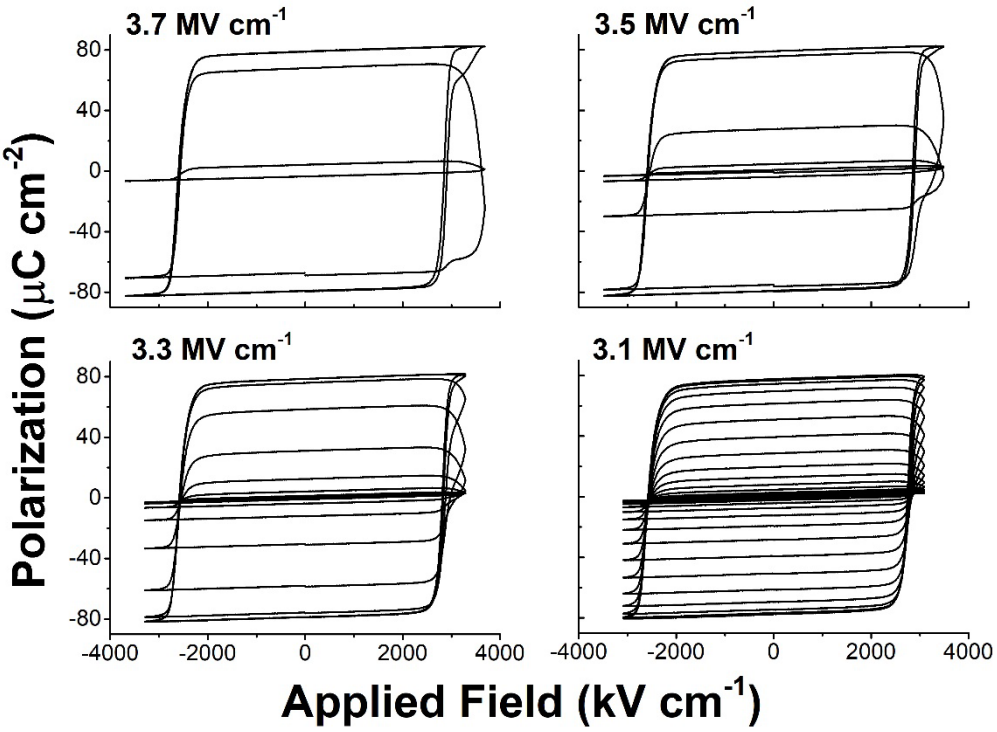

Figure **2-5**: Examples of wake-up in ZMO films. The initial hysteresis loops are those with the smallest magnitude of the switchable polarization. Progressive cycling at the same electric field increases the magnitude of the switchable polarization until the entire volume of the film can be switched. More wakeup cycles are required for lower electric fields. This ZMO film was 493 nm thick and grown on a platinum-coated *c*-Al_2O_3 substrate. All loops are centered on the polarization axis.

2.3.2 Methods for Depositing ZMO

ZMO films can be grown by various methods including sputtering, pulsed laser deposition, chemical vapor deposition, and molecular beam epitaxy. ZMO films grown by each of these methods will be summarized in this section.

2.3.2.1 Sputtering

Sputtering is a technique commonly used in BEOL processes in chip fabrication and is a scalable process, which makes it an attractive fabrication method for ZMO. Sputtering also offers versatile control of the composition of ZMO since two targets can be sputtered simultaneously in dual RF-magnetron sputtering.[14, 15] Using this technique, the power applied to the Mg target can be varied to change the mol% of Mg in the films. This allows the power on the Mg target to control the band gap of the film. Incorporation of Mg into the ZnO film was reported to increase by increasing the substrate temperature during deposition.[16]

Crystallization can be achieved at room temperature in cases where adequate adatom mobility is provided by close working distances ~6 cm and low process pressures ~1 mTorr.[15] These conditions promote the energetic bombardment of the substrate, as the mean free path for sputtering in Ar/O at 1 mTorr is approximately 6 cm, as will be seen in Figure 3-1.[17, 18]

It should be noted that the Mg target is susceptible to react with the oxygen, one of the process gasses. At a process gas Ar:O_2 ratio of 18:2 for the deposition system utilized in this work, the Mg target is poised on the boundary of poisoning, meaning, the target forms a thin layer of oxide on its surface. Despite sputtering from a purely poisoned surface at higher Ar:O_2 ratios, process drift with hysteresis is still encountered.[15] In addition, unexplained composition variations occur in ZMO films where ToF SIMS depth profiling revealed a small increase in Mg

composition and decrease in Zn and O near the bottom electrode interface of a $Zn_{0.68}Mg_{0.32}O$ film (as will be described in Figure 7-5).[19]

2.3.2.2 Pulsed Laser Deposition

Pulsed laser deposition can also be used to deposit ZMO thin films. For this technique, incorporation of Mg on Zn sites is often promoted by higher substrate temperatures during deposition ($\geq 400°C$).[20, 21, 22] Typically, the film composition is controlled by the target composition. Deposition parameters such as the substrate temperature, process pressure, and partial pressure of oxygen are varied to alter the ZMO electrical properties.[22] Increasing the oxygen partial pressure during the deposition step reduces the crystallinity of ZMO. Likewise, annealing in air or oxygen results in oxygen interstitials and growth of secondary orientations.[23] In contrast, it has been reported that annealing in vacuum improves the crystallinity, and suppresses the growth of secondary orientations. However, vacuum annealing can result in Zn interstitials.[23]

2.3.2.3 Chemical Vapor Deposition

Various forms of chemical vapor deposition (CVD) have been used to grow ZMO including ultrasonic spray deposition (Mist CVD) and metal-organic chemical vapor deposition (MOCVD). Ultrasonic spray depositions consist of spraying Zn and Mg ion suspended in a solvent through a nozzle to form microdroplets onto a heated substrate. The precursors, Zn acetate dihydrate and Mg acetate tetrahydrate, were added to acetic acid and water to form the spray solution. Though this method is fast and relatively simple, it does not produce high quality films of ZMO and often results in the formation of nanorod-like structures unless the films are

subjected to high temperatures, beyond those compatible with BEOL processes (> 450°C). Incorporation of Mg into ZnO was successful via MIST CVD when the substrate was heated to 750°C, as shown by the shift in the cathodoluminescence energy with Mg content in Figure 2-6.[24] It should be noted however, that some rocksalt MgO had precipitated out of the films.

MOCVD was also used to grow ZMO thin films at temperatures compatible with BEOL processing, ranging from 250 to 450°C.[25,26,27] Common precursors for Zn and Mg are diethylzinc and bis(cyclopentadienyl)magnesium(II), respectively. Mg concentrations are relatively low in MOCVD grown ZMO (< 6 mol% Mg) because the adatom energetics cannot be manipulated to force the existence of metastable ZMO with higher Mg contents, as in sputtering processes. This makes the effects of ZMO nearing and exceeding the solubility limit (e.g. precipitation of secondary phases) observable.[28] In a report on MOCVD grown ZMO, at concentrations well in excess of 4 mol% Mg, two or more PL peaks appear at or above the band gap energy for ZnO, suggesting that ZMO grown by MOCVD does not remain single phase above the solubility limit, as shown in Figure 2-7.[29,30]

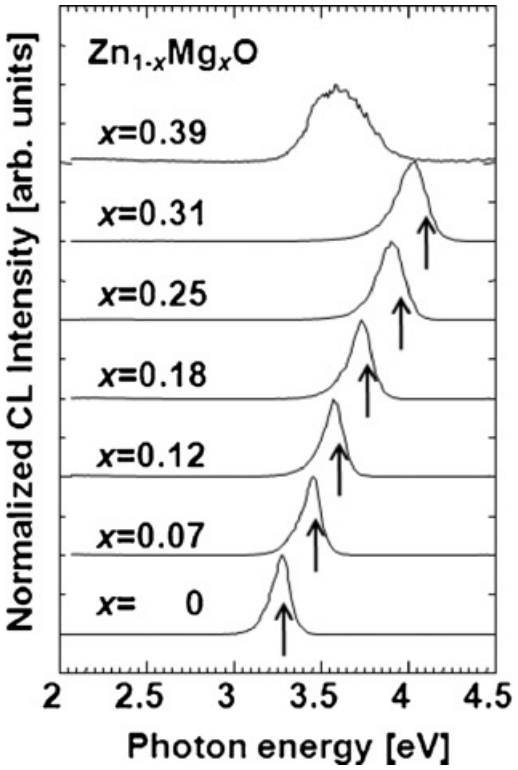

Figure **2-6**: Shifts in the cathodoluminescence (CL) spectra with the incorporation of Mg in ZnO via Mist CVD, indicate shifting of the optical band gap.[24]

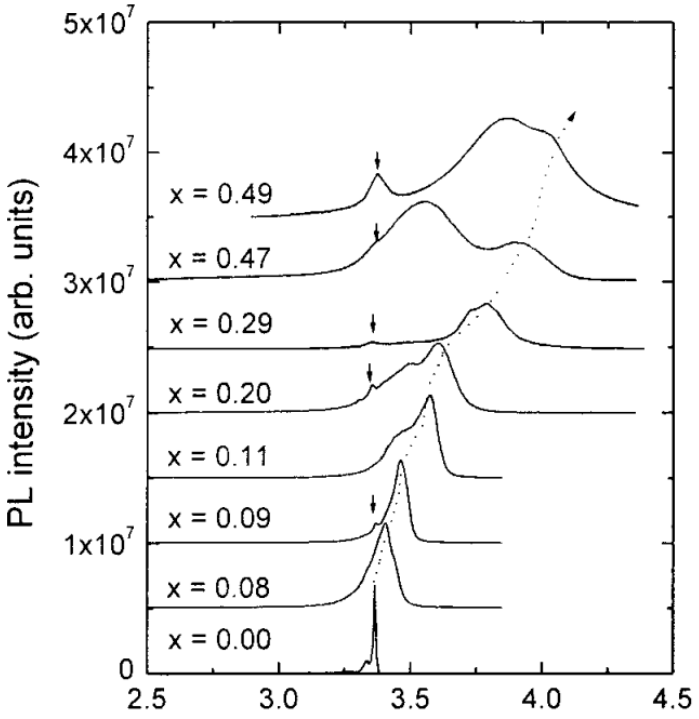

Figure **2-7**: PL spectra of MOCVD-grown $Zn_{1-x}Mg_xO$ with various concentrations. Films were grown at 500-650°C.[29]

2.3.2.4 Molecular Beam Epitaxy

Molecular Beam Epitaxy (MBE) is employed for producing high quality films with relatively low concentrations of extended defects, compared to the three former deposition methods.[31] For this reason, MBE can be useful in determining intrinsic defects in ZnO, which will be elaborated in the next section.[32] MBE has been used to grown ZMO films with a low roughness of 0.7 nm, which are necessary in quantum well structures.[31] High quality ZnO/ZMO heterostructures with electron mobilities of up to 250 $cm^2 \cdot V^{-1} s^{-1}$ (for compositions ≥ 20 mol% Mg) have been grown by MBE.[33] The unusually high mobility (for ZnO) is due to a highly

conductive 2-D electron gas (2DEG) at the interface between ZnO and ZMO , which will be expounded on later in this chapter. Such a high mobility was the result of growing the ZMO layer at 650°C. At a lower growth temperature of 350°C, compatible with BEOL processing, the mobility of the 2DEG is expected to decrease.[34] Solubility limits of approximately 45 – 50 mol% Mg are reported for MBE grown ZMO at temperatures between 350 and 650°C.[33,34,35]

2.3.3 Defects and Doping in ZMO

Modifying ZnO with Mg increases the band gap nearly linearly with the substitution of Mg on Zn sites, as shown in Figure 2-8.[35,24] ZMO is transparent in the visible range, and absorbs in the UV range; the UV absorption edge can be modified by the Mg mol fraction. Transparent ZMO can also be exploited for photovoltaic applications, since it can be degenerately doped with Al^{3+}, Ga^{3+}, B^{3+}, or In^{3+} to make a non-toxic transparent conducting oxide layer.[36,37,38,39,40,41] Doping with In^{3+} up to 1 mol% increased the conductivity of ZnO, but significantly decreased the absorbance in the UV range compared to other group III dopants. Doping with B^{3+} increased the conductivity, while maintaining high optical transmittance > 90%.[40] Al and Ga also increased the conductivity while maintaining transparency, and deposition at higher temperatures between 300 and 500°C further improved the transmittance in the visible range.[36,38]

By degenerately doping ZMO, low resistivities (i.e. high conductivities) can be achieved due to the increased carrier concentration, as shown below. First the intrinsic carrier concentration is described by:

$$n_i{}^2 = n \times p$$

where n_i is the intrinsic carrier concentration, n is the concentration of electrons in the conduction band, and p is the concentration of holes in the valence band. In doped semiconductors, n and p are governed by the concentration of dopants (N_A for acceptors and N_D for donors, when both

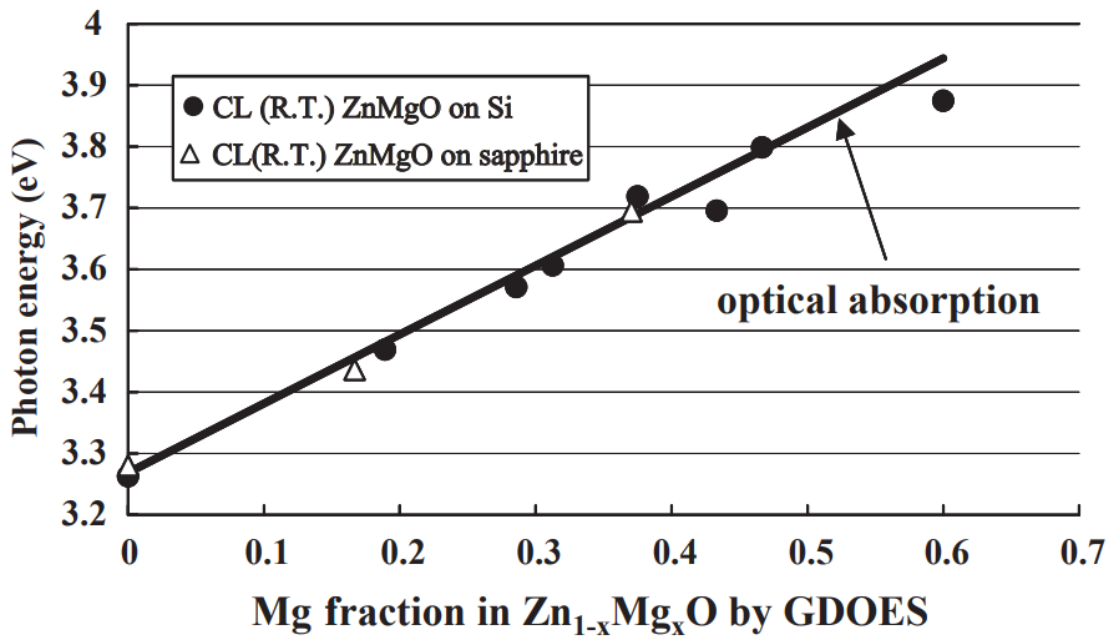

Figure **2-8**: The optical band gap (photon energy) of ZMO grown by MBE increases linearly with increasing Mg mol fraction. The data were measured by glow discharge optical emission spectroscopy (GDOES). The figure is reproduced from reference.[35]

carrier types can be activated), their carrier energies relative to the Fermi level (E_A - E_F or E_D - E_F), and the temperature T. The equations which describe their relationships are shown below:

$$n = \frac{N_D}{\exp\left(\frac{E_D - E_F}{k_b T}\right) + 1}$$

$$p = \frac{N_A}{\exp\left(\frac{E_A - E_F}{k_b T}\right) + 1}$$

In this case, the carrier concentration for doped semiconductors can be assumed to be much greater than the intrinsic carrier concentration, and the carrier concentration for n-type and p-type semiconductors can be assumed to be n and p, respectively. However, the conductivity is also affected by their respective mobilities, called the carrier mobilities.

$$\sigma = q \cdot (n\mu_e + p\mu_h)$$

where σ is the conductivity, q is the charge of an electron or hole (1.6×10^{-19} C), and μ_e and μ_h are the electron and hole mobilities in the semiconductor, respectively. The mobilities are described by the equation below:

$$\mu = \frac{v_D}{E} = \frac{q \cdot \tau_s}{m_{eff}}$$

where v_D is the drift velocity, E is the applied electric field, τ_s is the scattering time, and m_{eff} is the effective mass of the carrier. The effective mass is a measure of the ease with which an electron or hole can move through the semiconductor.

According to the equation for mobility, the scattering time τ_s must be increased to increase the conductivity of ZMO. The scattering time is the average lifetime of a carrier before it collides. This can be improved by reducing the concentration of defects such as interstitial Zn or Mg atoms, or oxygen vacancies which disrupt the crystal structure and thus the motion of carriers. Therefore, although degenerate doping in ZMO increases the carrier concentration substantially to make it conductive, the carrier mobilities are low, on the order of 1 – 10 $cm^2 \cdot V^{-1} s^{-1}$.[36] Increasing the grain size and removing impurity scatterers such as interstitial atoms or vacancies by annealing increases the scattering time, leading to increased conductivity in ZMO.[38] Likewise, depositing ZMO at higher temperatures can reduce defect concentration and improve carrier mobility, as described below.

The most common intrinsic defects in ZnO are oxygen vacancies and zinc interstitials, as shown in MBE-grown ZnO films.[32] The concentration of oxygen vacancies increases after annealing in nitrogen at temperatures ≥ 600°C, and decreases on annealing in oxygen at similar temperatures. Separately, the concentration of zinc interstitials could be decreased by either decreasing the Zn flux during growth, or by annealing at temperatures ≥ 700°C. Zn interstitials were found to act as photoluminescence centers for emitted photons with an energy of ~ 2.3 eV,

below the band gap energy. In MOCVD grown ZMO, doping with 5% Mg intensified the PL emission at ~ 2.3 eV, suggesting an increase in the concentration of interstitial cation defects.[25] In a separate study in MOCVD-grown ZMO with 6 mol% Mg, annealing in oxygen was not found to affect Mg incorporation, but annealing in nitrogen improved Mg incorporation.[27] This finding is consistent with annealing effects on transparent ZMO for photovoltaic applications where annealing in vacuum was also suggested.[42] In summary, it is hypothesized that the presence of cation (Zn,Mg) interstitials will be important, especially in the fatigue cycling endurance of ZMO, since the open cage structure of the wurtzite structure may allow facile migration of interstitial species at the high electric fields required for polarization reversal.

2.3.4 Secondary Phases in ZMO

According to available ternary phase diagrams, Mg is soluble in bulk $Zn_{1-x}Mg_xO$ by up to 4%.[30] However, several reports have incorporated Mg into ZMO at concentrations greater than x=0.4 (10 times the solubility limit) before forming secondary phases. This has been possible via RF magnetron sputtering, PLD and MBE grown ZMO films. Thus, Mg can be considered metastable in ZMO at the concentrations which favor ferroelectricity in ZMO ($x > 0.04$).

In this work, even at concentrations above x=0.3, Mg has been found to be stable in ZMO, for heating up to 200°C as was required in the lithographic patterning process to deposit top electrodes. However, there were some cases where second phase peaks were observed in x-ray diffraction (XRD) patterns at 44.3° 2θ, as shown in Figure 2-9. The cause for the precipitation of this phase as opposed to the typical 111 MgO rocksalt at ~ 36° 2θ is unknown. However, the literature suggests the presence of hydroxide (see Figure 7-5) is responsible for the secondary phase peak at 44.3°.[19] It was reported that the 400 reflection of a $MgO/Mg(OH)_2$ compound with a spinel structure occurs at 44.3° in rf-magnetron sputtered MgO films (see Figure 2-10).[43] This

peak is associated with sputtering from an MgO target, rather than a pure Mg target. Sputtering from a pure Mg target yielded a peak at 42.9°, which was associated with the cubic 200 reflection of MgO (see Figure 2-10).

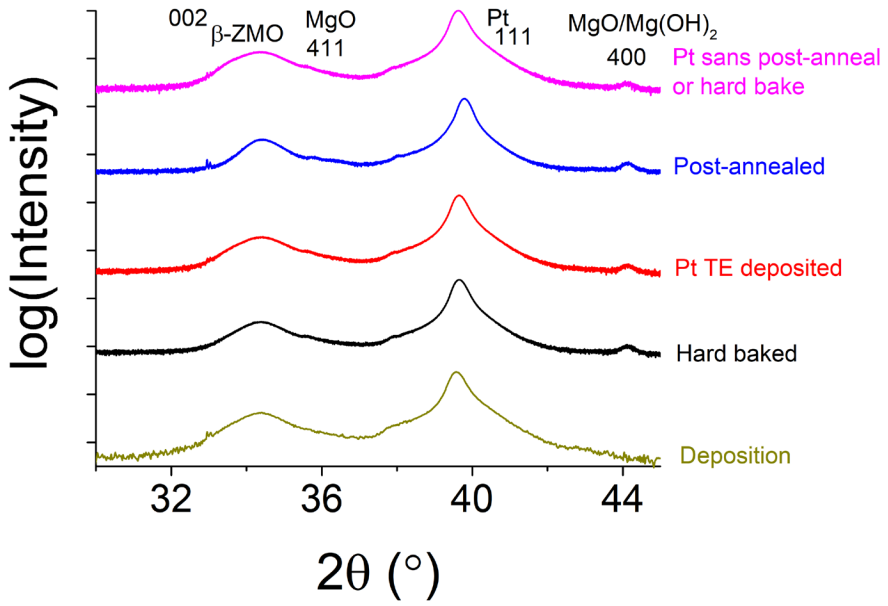

Figure **2-9**: A second phase peak at 44.3° 2θ reportedly corresponds to a compound of MgO and $Mg(OH)_2$.[43]

It had been noted by the growers that poisoning of the Mg target (that is – oxidizing the surface of the pure Mg target to MgO) occurs at O:Ar ratios ≥ 2:16, and that sputtering from a purely poisoned target was preferred in order to increase the process repeatability.[15] Therefore, the appearance of a peak at 44.3° 2θ is likely due to a compound of $MgO/Mg(OH)_2$. This is as opposed to an equivalent peak at 42.9° 2θ for MgO deposited from a pure Mg target.[43] Again, these second phase peaks appeared in only a handful of films; data from those films is not presented later in this work.

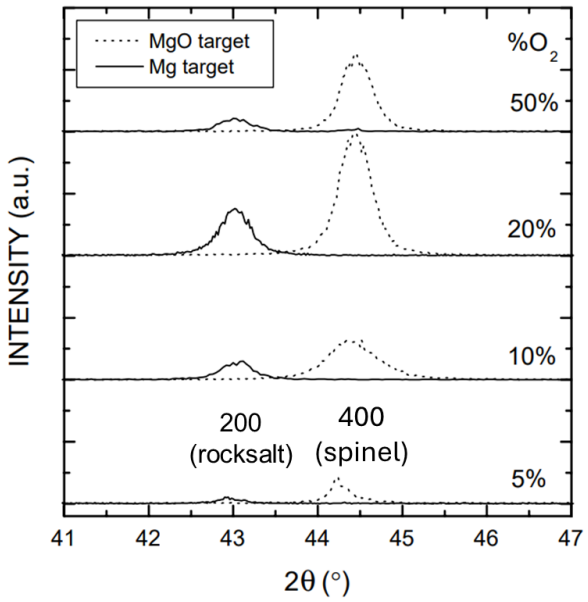

Figure **2-10**: MgO deposited from a pure Mg target, and from a MgO target via rf-magnetron sputtering. The peak at 42.9° for MgO sputtered from a pure Mg target corresponds to the 200 diffraction of rocksalt MgO. The peak at 44.3° for MgO sputtered from an MgO target reportedly corresponds to the 400 diffraction of a compound of $MgO/Mg(OH)_2$ in the spinel structure. This figure was adapted from Cáceres et al.[43]

2.3.5 Selected Properties of ZMO

2.3.5.1 Optical Properties

ZMO has a band gap (E_g) which can be modified by doping or by introducing defects.[44] In particular, ZMO has a direct band gap that is tunable by the incorporation of Mg.[45] ZMO is also useful as a light emitter from the UV range to red light, depending on how it is doped.[44] For compositions with an E_g of ~ 3.5 eV, ZMO is useful as a UV detector with high UV selectivity.[46]

Some basic properties of the direct optical band gap are:

$$\alpha hv = C\sqrt{hv - E_g}$$

$$\alpha = \frac{4\pi k}{\lambda}$$

where hv is the photon energy, α is the absorption coefficient, C is a constant, k is the extinction coefficient, and λ is the wavelength of incident light. Figure 2-11 shows the optical response of ZMO thin films prepared via PLD from a $Zn_{0.9}Mg_{0.1}O$ target, with the substrate held at various temperatures during deposition. The shift of $(\alpha hv)^2$ curve to higher energies with deposition temperature suggests that Mg incorporation into the wurtzite structure increased with deposition temperature up to 600°C. A sharp increase in absorption is observed above 3.5 eV, making ZMO an excellent candidate for UV absorber/detector that is mostly transparent to visible light.

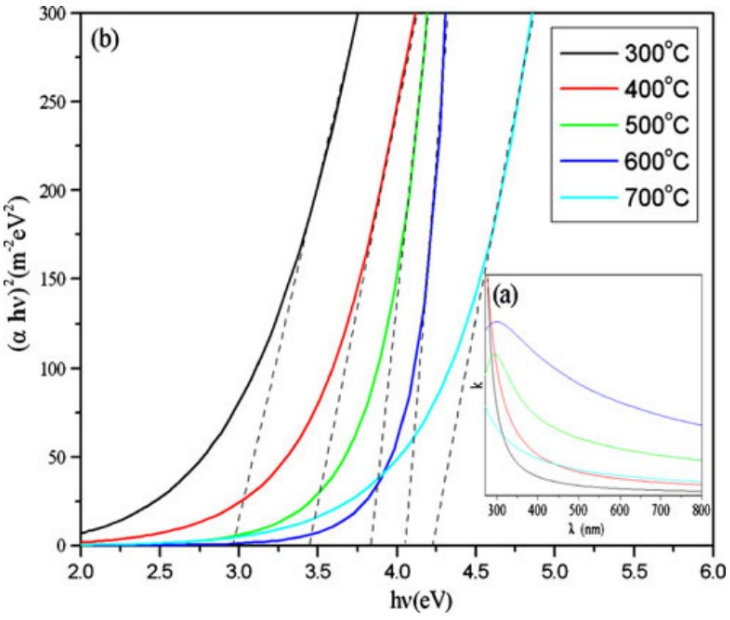

Figure **2-11**: (a) (inset) A plot of the extinction coefficient k vs. wavelength λ of incident photons of $Zn_{0.9}Mg_{0.1}O$ films deposited via PLD, at various substrates temperatures. (b) A measure of $(\alpha hv)^2$ vs. energy of incident photons.[45]

For this reason, in addition to its large exciton binding energy,[47] ZMO finds use in solar cells as a transparent window layer.[42] High efficiency CdTe solar cells with a ZMO window layers were fabricated, and after rapid thermal annealing the ZMO window layer at 600°C the overall efficiency of the solar cell was improved by 4 %, to 15.6 % efficiency. This was due to the increased carrier mobility of the ZMO, likely due to the doubled grain size and the removal of oxygen interstitials during the anneal, which minimized impurity and grain boundary scattering.

Transparent ZnO is also an excellent candidate for wearable electronics. Enhancement mode transparent field-effect transistors (TFETs) were demonstrated using a composite layer structure $InGaO_3(ZnO)_5$ (IGZO) as the channel material.[48] The $InGaO_3$ served to manage and maintain the stoichiometry of the ZnO layers, as In_2O_3 acts as a barrier layer for oxygen diffusion between ZnO layers, as shown in Figure 2-12. Successful demonstration of transistor action was reported, with > 80% transparency through the whole device.

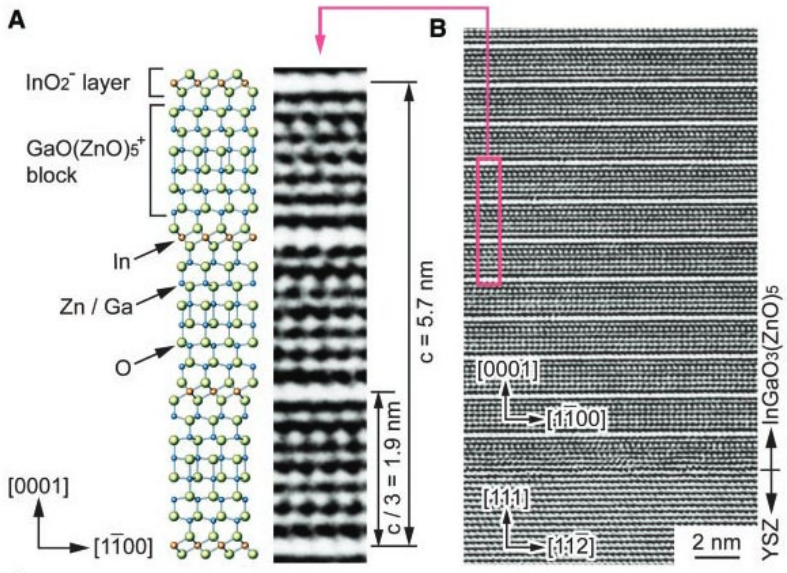

Figure **2-12**: $InGaO_3(ZnO)_5$ (GIZO) grown by reactive solid-phase epitaxy on yttrium-stabilized zirconia (YSZ) substrate. InO_2^- layers separate $GaO(ZnO)_5^+$ layers to control the stoichiometry of the channel.[48]

2.3.5.2 2-D Electron Gas Heterostructures

An emerging property of ZnO/ZMO heterostructures is the 2-Dimensional Electron Gas (2DEG) effect. A 2DEG describes a scenario where mobile electrons are confined in a 2-D sheet of material.[49] One example of 2DEGs are conductive graphene, where electrons conduct in the plane of the hexagonal structure.[50] Another example of the application of 2DEGs are 2-D MOSFETS with channel materials such as $MoSe_2$ and WSe_2, where the 2-D channel is turned into a 2DEG via electrostatic gate control.[51,52] Perhaps a more common example of a 2DEG occurs in Si MOSFETs, where the Si channel under sufficient gate and drain bias (V_{GS} and V_{DS}, respectively), becomes conductive. A depiction of a ferroelectric field effect transistor with a Si channel is shown in Figure 2-13.

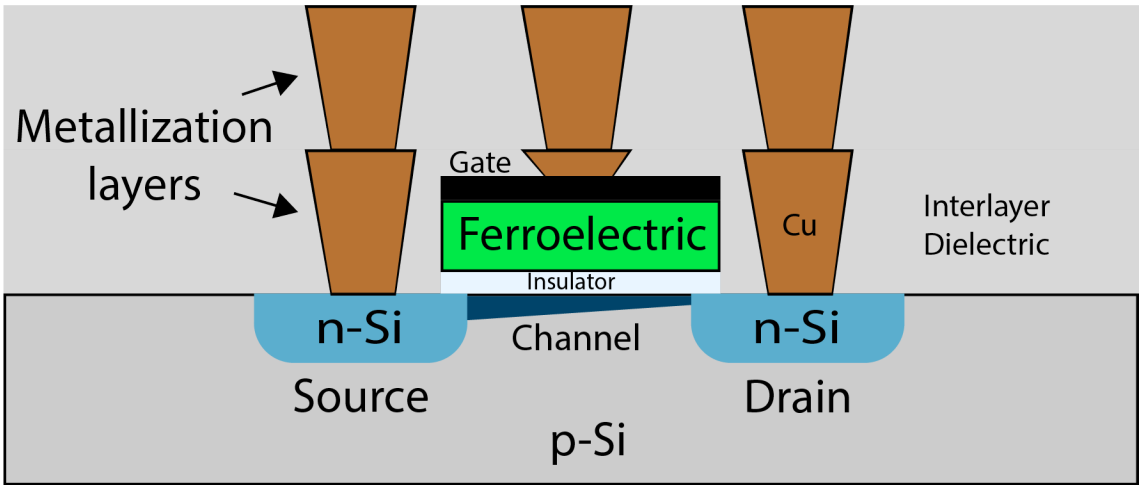

Figure **2-13**: A schematic of an enhancement mode ferroelectric field effect transistor (FeFET) with a p-Si channel. The conducting channel behaves as a 2DEG as the area underneath the gate dielectric becomes saturated with carriers. This image is modified from [53].

The 2DEG in ZnO/ZMO heterostructures originates from the difference in spontaneous polarization between the two layers, which forms a charged layer at the junction between the two

layers. An equation to determine whether a 2DEG forms at the heterostructure is provided below[54]:

$$\sigma = P_{SP\,ZnO} + P_{PE\,ZnO} - P_{SP\,ZMO}$$

where $P_{SP\,ZnO}$ and $P_{SP\,ZMO}$ are the spontaneous polarizations of ZnO and ZMO, respectively, and $P_{PE\,ZnO}$ is a strain factor which can be described by[55]:

$$P_{PE\,ZnO} = 2\varepsilon_{12}\left(e_{31} - e_{33}\frac{C_{13}}{C_{33}}\right)$$

where *e* is the piezoelectric strain coefficient in C m^{-2}, ε_{12} is the in-plane strain, and C are elastic coefficients in units of Pa. ε_{12} for ZnO on $Zn_{1-x}Mg_xO$ can be quantified by[55,56]:

$$\varepsilon_{12} = 0.027x^2 + 0.0083x$$

When $\sigma > 0$, a 2DEG forms at the interface between the two materials – in this case, ZnO and ZMO.

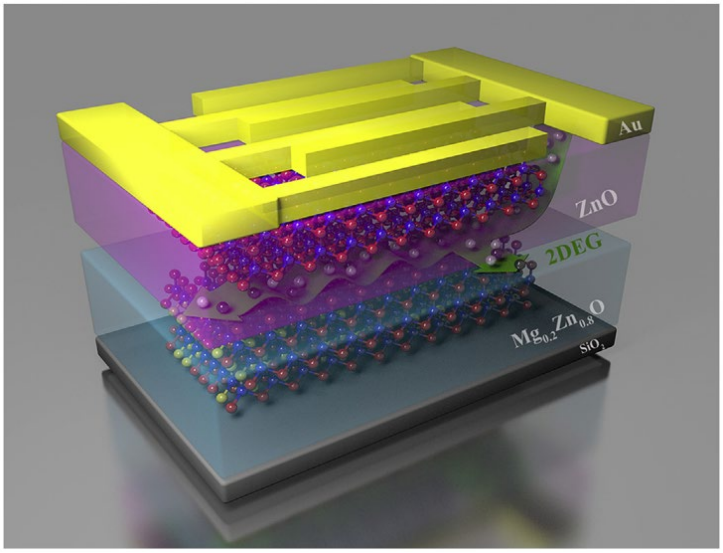

Figure **2-14**: A ZnO/ZMO heterostructure, illustrating the location of the 2DEG at the junction. Au IDTs with applied bias at the surface collect excited carriers when incident UV photons of an appropriate energy are absorbed by the ZMO or ZnO layer.[56]

Formation of a 2DEG in a ZnO/ZMO heterostructure significantly increased the gain of the UV photodetector, and consequently, the sensitivity of the device, as shown in Figures 2-14 and 2-15.[56] The sensitizing effect of the 2DEG at the heterojunction takes advantage of the greater mobility of electrons compared to holes. Therefore, the electrons travel more quickly to the interdigitated electrodes (IDTs) than the holes, which may cause an amplifying effect by attracting more electrons to the 2DEG. Thus, a gain of nearly 150x and 33x were observed at 10 V and at 5 V operating voltage, respectively.

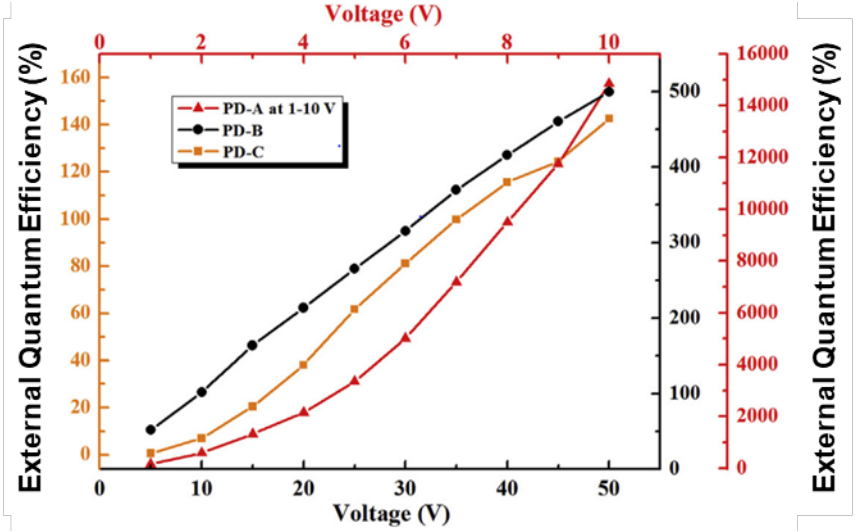

Figure **2-15**: 150x gain in the external quantum efficiency (EQE) is reported for a ZnO/ZMO heterojunction (PD-A, far right axis) due to the enhancing effects of a 2DEG. This is the same architecture as depicted in Figure 2-14. Heterojunction structure PD-B (right axis) is in the reverse order of PD-A, and PD-C (left axis) represents a device with only ZMO. Note that the top x-axis is the voltage axis for PD-A, and the bottom x-axis is for both PD-B and PD-C. This figure was adapted from [56].

2DEG devices may become advantageous in FeFET devices, where the channel currents can be modulated by electrostatic gate control. Since the polarization must be modulated enough

to satisfy $\sigma < 0$ for the 2DEG to be turned off, transistor action could potentially be enabled in ZnO/ZMO heterostructure devices.

2.4 Ferroelectric Properties of ZMO

There is little prior experimental work done on ferroelectric ZMO, with only three known experimental works (two of them being theses) from the Pennsylvania State University.[15,57] Ferroelectric ZMO is a fairly difficult material to grow successfully.[15] Other groups have attempted to grow ferroelectric ZMO,[58] but, at the time of the completion of this dissertation, only the Maria group at the Pennsylvania State University demonstrated completely switchable films. There is a recent report on ferroelectricity in (Ce,Mn) substituted ZnO films, with similar functional mechanisms as ZMO, whereby substituted cations flatten the cation tetrahedra, decrease the *c*/*a* ratio, and facilitate ferroelectric switching.[59]

2.4.1 Wurtzite Structure (Al,B)N and (Al,Sc)N

Therefore, to understand the ferroelectric properties of ZMO, work on other wurtzite ferroelectrics was referenced, especially (Al,B)N and (Al,Sc)N (see Figure 2-16). These films are much better studied for a few reasons: (1) there are more research groups working on them; (2) the ZMO system is more defective than (Al,B)N and (Al,Sc)N,[32] and (3) ZMO is more difficult to study for some techniques due to its high defect concentrations. For example, transmission electron microscopy (TEM) study of ZMO is limited because the electron beam causes significant damage to the sample within seconds of incidence.[11] In addition, charge-dependent measurements such as thermally stimulated depolarization current (TSDC) and deep-level transient spectroscopy (DLTS) which are used to characterize the defect energies cannot be performed on current ZMO

due to the preponderance of shorted channels encountered over the large electrode areas required for these measurements. Computational methods have benefitted the understanding of switching mechanisms in ZMO; findings from both DFT[60] and ReaxFF[61] simulations were in accordance with the experimental work in this thesis.

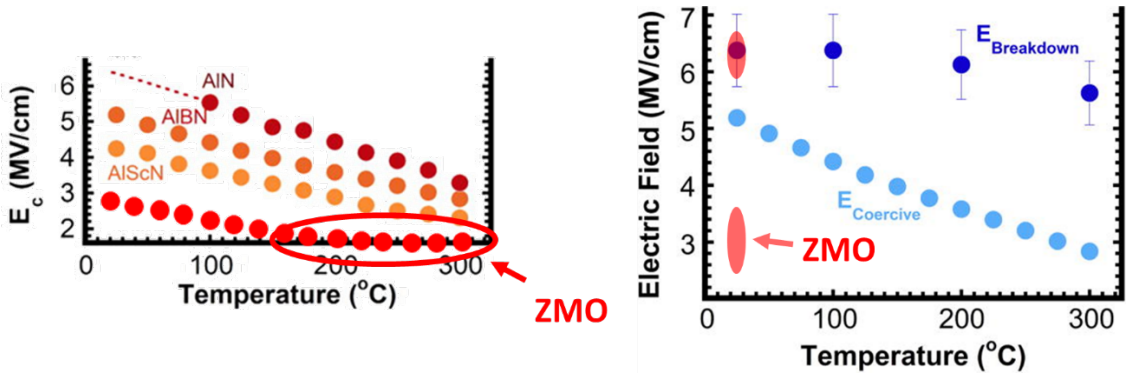

Figure **2-16**: (left) The temperature dependence of the coercive fields of AlN, (Al,B)N, and (Al,Sc)N are compared with ZMO. (right) The breakdown field of (Al,B)N is compared with ZMO.[8]

2.4.2 Computational Analysis of the Origin of Ferroelectricity in ZMO

Density functional theory (DFT) simulations were performed on ZMO. It was discovered that local strains introduced by the substitution of Mg on ZnO sites enable ferroelectricity in ZMO thin films.[60] The pathway for polarization reversal in pure ZnO is reported to follow a uniform switching behavior, where the film switches through an intermediate planar hexagonal phase (the h-BN phase) before reversing to the opposite polarization. Solid solution with Mg introduces alternative, lower energy switching pathways for polarization reversal by switching to other intermediate phases, which reduces the coercive field by up to 45%. The origin of this effect is due to strain fluctuations in the crystal lattice introduced by Mg substitution on Zn sites.

Uniaxial strains and biaxial strains were preferred on the Mg and Zn sites, respectively. When a large enough electric field is applied to the material, the most favorably distorted cation switches first, followed by neighboring cations. Figure 2-17 depicts the switching pathways and intermediate states in pure ZnO and in ZMO.

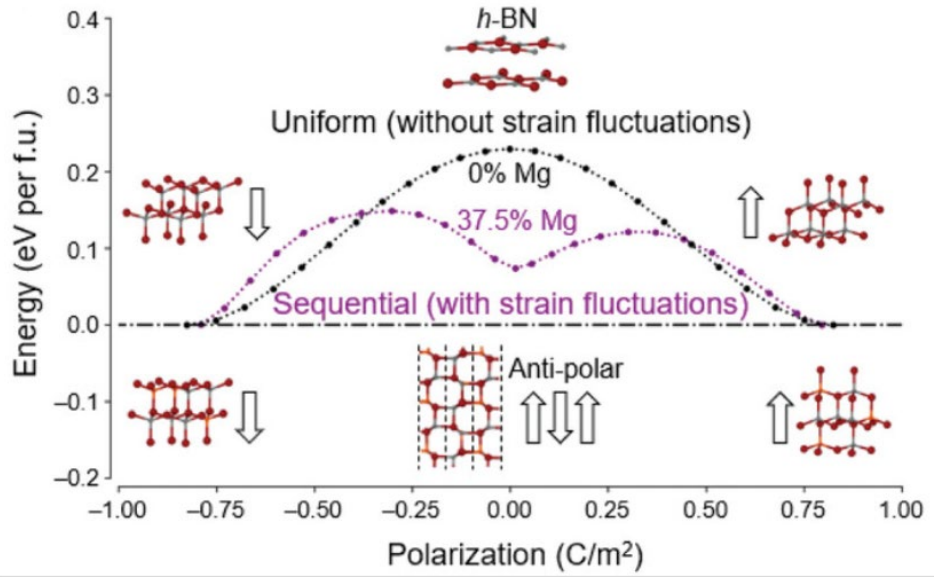

Figure **2-17**: Strain fluctuations reduce the energy barrier for polarization reversal in $Zn_{0.625}Mg_{0.375}O$ compared to pure ZnO.[60]

Reactive force field (ReaxFF) simulations calibrated using the DFT results revealed ferroelectric behavior of ZMO on a larger scale of several unit cells.[61] Key findings suggest that out-of-plane domain wall motion along the direction of the applied field dominates the switching response. The distribution of Mg atoms in the structure had a large effect on the coercive field, where randomly distributed Mg atoms resulted in the lowest coercive field, uniformly distributed Mg sites resulted in a moderately higher coercive field, and clustering of the Mg sites resulted in the highest coercive fields. These results are depicted in Figure 2-18. The Mg cluster regions switch first to an intermediate phase, followed by the complete reversal of the ZnO rich regions

surrounding them. Then, the MgO clusters retard the remainder of the switching process because they are the last to switch to the opposite polarity.

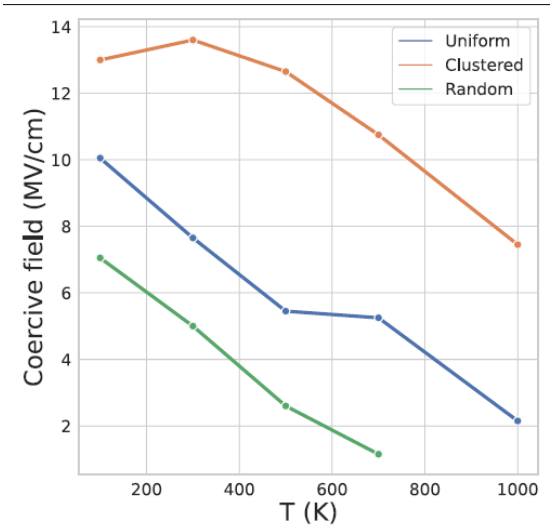

Figure **2-18**: ReaxFF simulations show the dependence of the coercive field on the distribution of Mg sites in the simulated 14 nm thick ZMO film.[61]

2.5 Ferroelectric Switching Kinetics

2.5.1 Kolmogorov-Avrami-Ishibashi (KAI) Model

The Kolmogorov-Avrami-Ishibashi model was developed over several decades by statisticians and mathematicians. Kolmogorov and Avrami presented their discussions in the 1930s and 40s. Then in the 1970s, Ishibashi presented a simple model to summarize the more involved equations of Avrami and Kolmogorov, called the KAI model[62,63,64]:

$$X_t = 1 - \exp\left(-\left(\frac{t}{t_0}\right)^n\right)$$

where t is the elapsed time, t_0 is the characteristic switching time, and n is the rate law. In thin films, it is expected that nuclei should propagate quickly through the thickness and grow outward radially. This process is described by a rate law of $n = 2$. Exponents greater than 2 describe a complicated nucleation and growth pathway, and the maximum theoretical rate law for processes in thin films is 3 according to the KAI model. The KAI model was reported in ferroelectric films of PZT, $BiFeO_3$, and $(Hf,Zr)O_2$ under certain conditions.[65,66,67] In PZT, there was an obvious change in the switching kinetics between the application of low electric fields and high electric

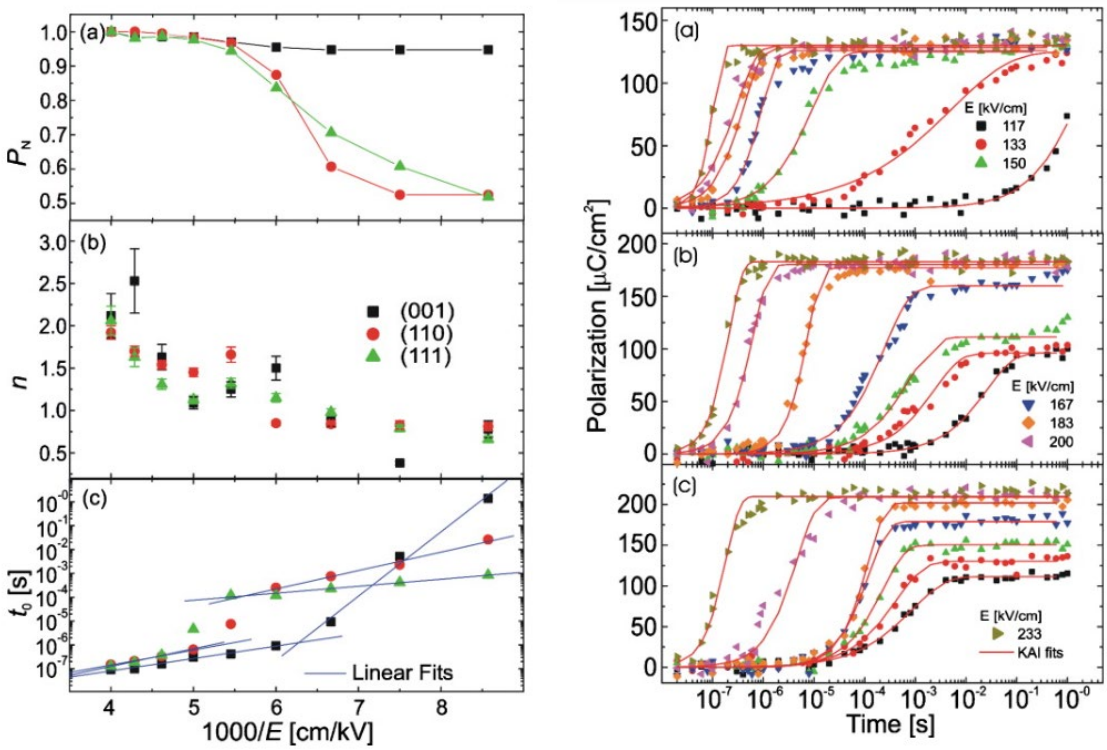

Figure 2-**19**: Left: (a) The normalized switching polarizations for 001, 110, and 111 oriented ferroelectric $BiFeO_3$ thin films. (b) The rate constant n and (c) the characteristic switching times t_0 are plotted with respect to the applied electric fields. Reproduced from reference [66].

Right: The corresponding switching transients for (a) 001, (b) 110, and (c) 111 oriented $BiFeO_3$ thin films.[66]

fields.[65] In $BiFeO_3$ the KAI model was only found to apply at high fields.[66] At low fields, switching was orientation-dependent, as shown in Figure 2-19. In $(Hf,Zr)O_2$ the KAI model was found to apply at temperatures < 170 K or in devices which consisted of single grains.[67] However, as will be discussed in Chapter 5, rate laws in ZMO, and other wurtzites, can exceed $n = 3$. Therefore, other statistical descriptions of polarization reversal were explored.

2.5.2 Nucleation-Limited Switching (NLS) Model

The NLS model was presented by Taganatsev et al.[68] to describe polarization reversal in defective ferroelectric films. The NLS model can be derived assuming:

i. The film is an ensemble of elementary regions (i.e. domains).

ii. There is only one nuclei per elementary region.

iii. The time to switch a domain is the same as the waiting time for it to switch (since the actual switching occurs at a much smaller time scale which cannot be measured).

iv. Switching times span several decades with modulation of the applied field.

An additional note about this model is that it applies where nuclei are relatively sparse compared to applications where the KAI model may be more appropriate. The NLS model was later modified by Jo et al.[69] to incorporate the Lorentzian distribution to describe polarization reversal in $PbZr_{0.3}Ti_{0.7}O_3$ with a substantial concentration of defect dipoles which acted as domain pinning sites. The NLS model is described by the following equation:

$$f = \int_{-\infty}^{+\infty} \left[1 - e^{-\left(\frac{t}{t_0}\right)^n}\right] \cdot F(\log t_0) d(\log t_0)$$

where t is the time, t_0 is the characteristic switching time, n is the dimensionality of growth, and $F(\log t_0)$ is a distribution function describing the polarization reversal. Jo et al. used the Lorentzian distribution described by:

$$F(\log t_0) = \frac{A}{\pi} \cdot \frac{w}{(\log t - \log t_1)^2 + w^2} \quad (3)$$

where A is an arbitrary fitting constant ($A \approx 1$), t is the elapsed switching time, t_1 is the position of the center of the distribution function, and w describes the half-width at half-maximum by the relationship $w \cdot \log(t_1)$. The NLS model has been found to apply to some ferroelectric films for memory applications.[67,68,69] In (Al,Sc)N, the NLS model switching converges with KAI mode switching at high applied fields, as shown in Figure 2-20.[70]

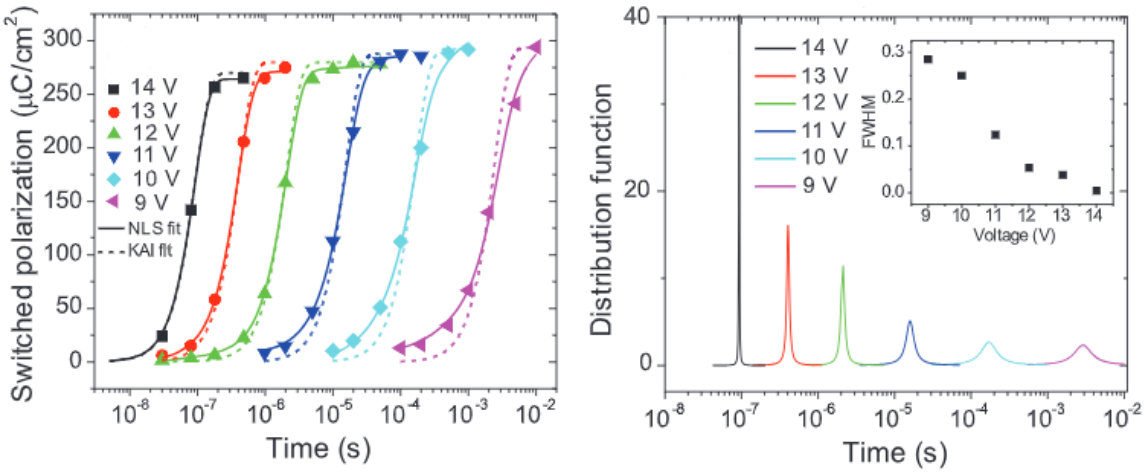

Figure **2-20**: The NLS and KAI models were applied to switching transients in $Al_{0.72}Sc_{0.28}N$ (left), and the corresponding Lorentzian distribution functions (right).[70]

2.5.3 Simultaneous Non-linear Nucleation and Growth (SNNG) Model

For some (Al,B)N and (Al,Sc)N films where conventional KAI or NLS kinetics do not apply, a modified KAI model was proposed by Yazawa et al., called the Simultaneous Non-linear Nucleation and Growth (SNNG) model.[71] The equation for this model is:

$$f = 1 - exp\left[-2\pi d v^2 N(\infty)\alpha m \int_0^t \tau^{m-1}(t-\tau)^2 \exp(-\alpha t^m)\, d\tau\right]$$

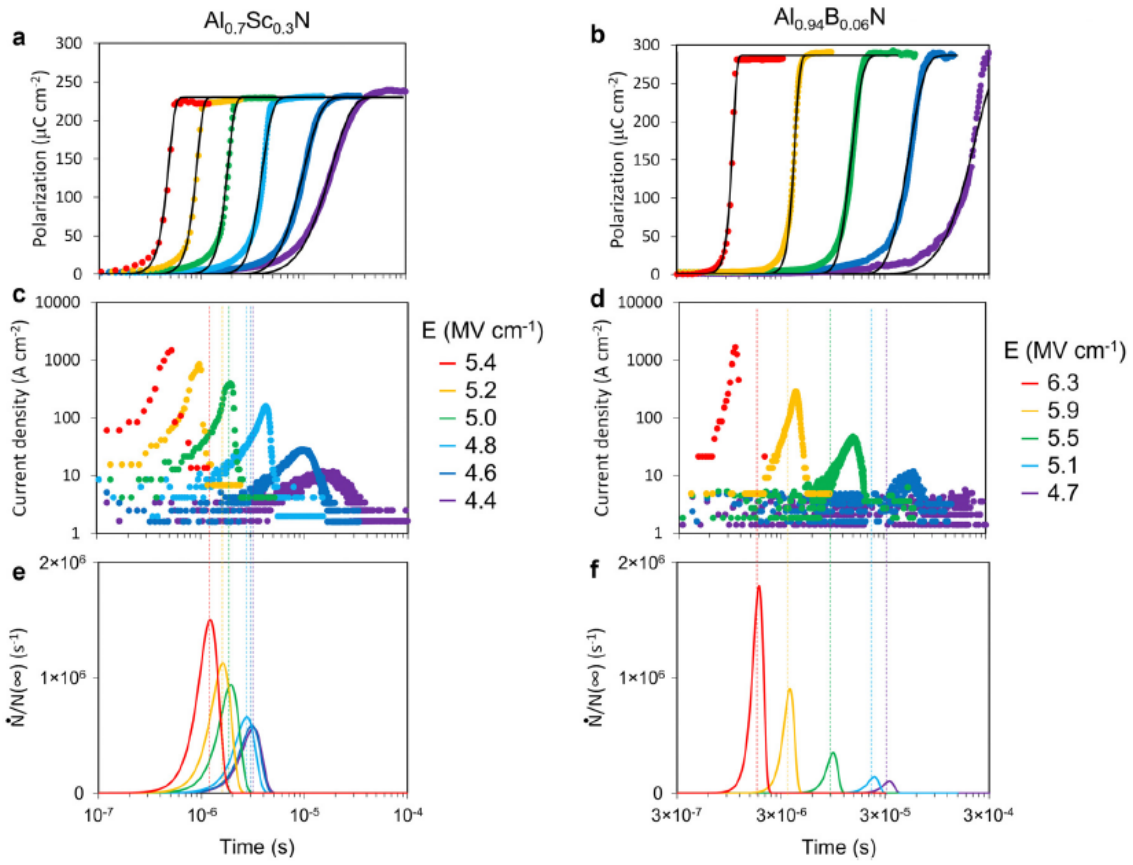

Figure **2-21**: Fitting of the SNNG model to polarization reversal in (left) $Al_{0.7}Sc_{0.3}N$ and in (right) $Al_{0.94}B_{0.06}N$ at various applied fields. (a-b) are the polarization transients, (c-d) are the current transients, and (e-f) are the relative nucleation rates, $\frac{\dot{N}(\tau)}{N(\infty)}$.[71]

where f is the fraction of switched polarization, d is the film thickness, v is the domain wall velocity, $N(\infty)$ is the saturated nucleation density, τ is the nucleation time, and α and m are fitting parameters for the nucleation curve position and slope, respectively. The nucleation curve is given by:

$$\frac{\dot{N}(\tau)}{N(\infty)} = \alpha m \tau^{m-1} \exp(-\alpha \tau^{m})$$

where $\frac{\dot{N}(\tau)}{N(\infty)}$ is the relative nucleation rate. This model attributes extra dimensionality in the KAI model, where $n > 2$, to a changing nucleation rate throughout the switching process, and is applicable for situations where significant domain growth occurs before the maximum nucleation rate is achieved. This model also extends the JMAK model, another extension of the KAI model, which cannot accommodate for a decreasing nucleation rate.[72,73] The excess dimensionality in the rate constant n, is captured by the term m in the equation for the SNNG model, where $m = n - 2$.

Application of the SNNG model in (Al,B)N and in (Al,Sc)N under various applied fields is shown in Figure 2-21. Since the SNNG model is an extension of the KAI or JMAK models, it still applies when the rate law $n < 2$. Several studies have applied the SNNG model to ferroelectric switching in wurtzites.[74]

References

[1] Fichtner, S., Wolff, N., Lofink, F., Kienle, L., & Wagner, B. (2019). AlScN: A III-V semiconductor based ferroelectric. *Journal of Applied Physics*, *125*(11), 114103.

[2] Davis, M., Budimir, M., Damjanovic, D. & Setter, N. (2007). Rotator and extender ferroelectrics: Importance of the shear coefficient to the piezoelectric properties of domain-engineered crystals and ceramics. *Journal of Applied Physics*, *101*(5), 054112.

[3] Tian, H., Meng, X., Hu, C., Tan, P., Cao, X., Shi, G., Zhou, Z., & Zhang, R. (2016). Origin of giant piezoelectric effect in lead-free $K_{1-x}Na_xTa_{1-y}Nb_yO_3$ single crystals. *Scientific Reports, 6*, 25637.

[4] Jaffe, B., Cook, W.R. & Jaffe, H. (1971). *Piezoelectric Ceramics*. Academic Press.

[5] Zhang, B. P., Li, J. F., Wang, K., & Zhang, H. (2006). Compositional dependence of piezoelectric properties in $Na_xK_{1-x}NbO_3$ lead-free ceramics prepared by spark plasma sintering. *Journal of the American Ceramic Society*, *89*(5), 1605-1609.

[6] Li, X., Xu, Z., He, Z., Cao, H., Su, W., Chen, Z., Zhou, F. & Wang, E. (1986). On the properties of AlN thin films grown by low temperature reactive rf sputtering. *Thin Solid Films*, *139*(3), 261-274.

[7] Gong, Y., & Jackson, T. N. (2017). Offset drain ZnO thin-film transistors for high-voltage operation. *IEEE Electron Device Letters*, *38*(8), 1047-1050.

[8] Zhu, W., Hayden, J., He, F., Yang, J. I., Tipsawat, P., Hossain, M. D., Maria, J-P., & Trolier-McKinstry, S. (2021). Strongly temperature dependent ferroelectric switching in AlN, $Al_{1-x}Sc_xN$, and $Al_{1-x}B_xN$ thin films. *Applied Physics Letters*, *119*(6).

[9] Scott, J. F., & Paz de Araujo, C. A. (1989). Ferroelectric memories. *Science*, *246*(4936), 1400-1405.

[10] Zhu, W., He, F., Hayden, J., Fan, Z., Yang, J. I., Maria, J-P., & Trolier-McKinstry, S. (2022). Wake-up in $Al_{1-x}B_xN$ ferroelectric films. *Advanced Electronic Materials*, *8*(6), 2100931.

[11] Jacques, L., Ryu, G., Goodling, D., Bachu, S., Taheri, R., Yousefian, P., Shetty, S., Akkopru-Akgun, B., Randall, C., Alem, N., Maria, J-P., & Trolier-McKinstry, S. (2023). Wake up and retention in zinc magnesium oxide ferroelectric films. *Journal of Applied Physics*, *133*(22), 224102.

[12] Lines, M. E., & Glass, A. M. (2001). *Principles and Applications of Ferroelectrics and Related Materials*. Oxford University Press.

[13] Lee, T. Y., Lee, K., Lim, H. H., Song, M. S., Yang, S. M., Yoo, H. K., Suh, D. I., Zhu, Z., Yoon, A., MacDonald, M. R., Lei, X., Jeong, H. Y., Lee, D., Park, K., Park, J., & Chae, S. C. (2018). Ferroelectric polarization-switching dynamics and wake-up effect in Si-doped HfO_2. *ACS Applied Materials & Interfaces*, *11*(3), 3142-3149.

[14] Tang, K., Wang, L. J., Huang, J., Xu, R., Zhang, J. J., Shi, W. M., & Xia, Y. B. (2012). Growth of high quality ZnMgO films on diamond substrates. *Physics Procedia*, *32*, 719-722.

[15] Goodling, D. (2023). *Compositional Dependence of Ferroelectric Properties in Thin Film $Zn_{1-x}Mg_xO$.* M.S. Thesis, The Pennsylvania State University.

[16] Kim, I. S., & Lee, B. T. (2009). Structural and optical properties of single-crystal ZnMgO thin films grown on sapphire and ZnO substrates by RF magnetron sputtering. *Journal of Crystal Growth*, *311*(14), 3618-3621.

[17] Li, J. M. & Talu, O. (1993). Effect of structural heterogeneity on multicomponent adsorption: Benzene and p-xylene mixture on silicalite. In *Studies in Surface Science and Catalysis* (Vol. 80, pp. 373-380). Elsevier.

[18] Ismail, A. F., Khulbe, K. C.,& Matsuura, T. (2015). Gas separation membranes. *Switz. Springer*, *10*, 973-978.

[19] Yang, J., Ievlev, A. V., Morozovska, A. N., Eliseev, E. A., Poplawsky, J. D., Goodling, D., Spurling, R. J., Maria, J-P., Kalinin, S. V., & Liu, Y. (2024). Coexistence and interplay of two ferroelectric mechanisms in $Zn_{1-x}Mg_xO$. *Advanced Materials*, *36*(39), 2404925.

[20] Wei, X. Q., Zhao, R. R., Wang, Y. J., Liu, L. Y., & Cao, B. Q. (2012). Annealing effects in non-polar ZnMgO thin films fabricated by PLD. *Surface Engineering*, *28*(9), 678-682.

[21] Wang, Y. J., Wei, X. Q., Zhao, R. R., Chen, C. S., Gao, S., & Lian, J. (2011). Effects of temperature on structural and optical properties of ZnMgO films fabricated by pulsed laser deposition. *Journal of Electroceramics*, *27*, 203-208.

[22] Fang, Q. Q., Wang, W. N., Li, J. G., Ding, Q. Q., Wang, C., Huang, W. J., Zhang, H. M., & Zhang, Q. P. (2012). The room-temperature ferromagnetism of defect-rich ZnMgO semiconductor thin films. *Applied Physics A*, *108*, 871-876.

[23] Luo, J., Liu, H., Deng, W., Zhang, R., & He, C. (2023). Effect of annealing atmosphere on structure and photoluminescence of ZnMgO thin films. *Journal of Materials Science: Materials in Electronics*, *34*(33), 2172.

[24] Nishinaka, H., Kamada, Y., Kameyama, N., & Fujita, S. (2010). Growth characteristics of single-crystalline ZnMgO layers by ultrasonic spray assisted mist CVD technique. *Physica Status Solidi (B)*, *247*(6), 1460-1463.

[25] Park, S. H., Kim, K. B., Seo, S. Y., Kim, S. H., & Han, S. W. (2006). Structural and optical properties of $Zn_{1-x}Mg_xO$ thin films synthesized with metal organic chemical vapor deposition. *Journal of Electronic Materials*, *35*, 1680-1684.

[26] Li, C., Meng, F. Y., Zhang, S., & Wang, J. Q. (2010). Effects of Mg content and B doping on structural, electrical and optical properties of $Zn_{1-x}Mg_xO$ thin films prepared by MOCVD. *Journal of Crystal Growth*, *312*(12-13), 1929-1934.

[27] Yang, A. L., Song, H. P., Liang, D. C., Wei, H. Y., Liu, X. L., Jin, P., Qin, X. B., Yang, S. Y., Zhu, Q. S., & Wang, Z. G. (2010). Photoluminescence spectroscopy and positron annihilation spectroscopy probe of alloying and annealing effects in nonpolar m-plane ZnMgO thin films. *Applied Physics Letters*, *96*(15), 151904.

[28] Shi, K., Yang, A. L., Wang, J., Song, H. P., Xu, X. Q., Sang, L., Wei, H. Y., Yang, S. Y., Liu, X. L., Zhu, Q. S., & Wang, Z. G. (2011). The effect of different oriented sapphire substrates on the growth of polar and non-polar ZnMgO by MOCVD. *Journal of Crystal Growth*, *314*(1), 39-42.

[29] Park, W. I., Yi, G. C., & Jang, H. M. (2001). Metalorganic vapor-phase epitaxial growth and photoluminescent properties of $Zn_{1-x}Mg_xO$ ($0 \leqslant x \leqslant 0.49$) thin films. *Applied Physics Letters*, *79*(13), 2022-2024.

[30] Segnit, E. R., & Holland, A. E. (1965). The System MgO-ZnO-SiO_2. *Journal of the American Ceramic Society*, *48*(8), 409-413.

[31] El-Shaer, A., Bakin, A., Al-Suleiman, M., Ivanov, S., Mofor, A. C., & Waag, A. (2007). Growth of wide band gap wurtzite ZnMgO layers on (0001) Al_2O_3 by radical-source molecular beam epitaxy. *Superlattices and Microstructures*, *42*(1-6), 129-133.

[32] Tatsumi, T., Fujita, M., Kawamoto, N., Sasajima, M., & Horikoshi, Y. (2004). Intrinsic defects in ZnO films grown by molecular beam epitaxy. *Japanese Journal of Applied Physics*, *43*(5R), 2602.

[33] Tampo, H., Matsubara, K., Yamada, A., Shibata, H., Fons, P., Yamagata, M., Kanie, H., & Niki, S. (2007). High electron mobility Zn polar ZnMgO/ZnO heterostructures grown by molecular beam epitaxy. *Journal of Crystal Growth*, *301*, 358-361.

[34] Koike, K., Hama, K., Nakashima, I., Sasa, S., Inoue, M., & Yano, M. (2005). Molecular beam epitaxial growth of Al-doped ZnMgO alloy films for modulation-doped ZnO/ZnMgO heterostructures. *Japanese Journal of Applied Physics*, *44*(6R), 3822.

[35] Fujita, M., Sasajima, M., Deesirapipat, Y., & Horikoshi, Y. (2005). Molecular beam epitaxial growth of hexagonal ZnMgO films on Si (1 1 1) substrates using thin MgO buffer layer. *Journal of Crystal Growth*, *278*(1-4), 293-298.

[36] Cohen, D. J., Ruthe, K. C., & Barnett, S. A. (2004). Transparent conducting $Zn_{1-x}Mg_xO$:(Al, In) thin films. *Journal of Applied Physics*, *96*(1), 459-467.

[37] Matsubara, K., Tampo, H., Shibata, H., Yamada, A., Fons, P., Iwata, K., & Niki, S. (2004). Band-gap modified Al-doped $Zn_{1-x}Mg_xO$ transparent conducting films deposited by pulsed laser deposition. *Applied Physics Letters*, *85*(8), 1374-1376.

[38] Chen, Z., Fang, G., Li, C., Sheng, S., Jie, G., & Zhao, X. Z. (2006). Fabrication and vacuum annealing of transparent conductive Ga-doped $Zn_{0.9}Mg_{0.1}O$ thin films prepared by pulsed laser deposition technique. *Applied Surface Science*, *252*(24), 8657-8661.

[39] Wenas, W. W., Yamada, A., Takahashi, K., Yoshino, M., & Konagai, M. (1991). Electrical and optical properties of boron-doped ZnO thin films for solar cells grown by metalorganic chemical vapor deposition. *Journal of Applied Physics*, *70*(11), 7119-7123.

[40] Li, C., Meng, F. Y., Zhang, S., & Wang, J. Q. (2010). Effects of Mg content and B doping on structural, electrical and optical properties of $Zn_{1-x}Mg_xO$ thin films prepared by MOCVD. *Journal of Crystal Growth*, *312*(12-13), 1929-1934.

[41] Kumar, P. R., Kartha, C. S., Vijayakumar, K. P., Abe, T., Kashiwaba, Y., Singh, F., & Avasthi, D. K. (2004). On the properties of indium doped ZnO thin films. *Semiconductor Science and Technology*, *20*(2), 120.

[42] Ren, S., Wang, H., Li, Y., Li, H., He, R., Wu, L., Li, W., Zhang, J., Wang, W., & Feng, L. (2018). Rapid thermal annealing on ZnMgO window layer for improved performance of CdTe solar cells. *Solar Energy Materials and Solar Cells*, *187*, 97-103.

[43] Cáceres, D., Colera, I., Vergara, I., Gonzalez, R., & Román, E. (2002). Characterization of MgO thin films grown by rf-sputtering. *Vacuum*, *67*(3-4), 577-581.

[44] Markevich, I., Stara, T., Khomenkova, L., Kushnirenko, V., & Borkovska, L. (2016). Photoluminescence engineering in polycrystalline ZnO and ZnO-based compounds. *AIMS Materials Science*, *3*(2), 508-524.

[45] Wang, Y. J., Wei, X. Q., Zhao, R. R., Chen, C. S., Gao, S., & Lian, J. (2011). Effects of temperature on structural and optical properties of ZnMgO films fabricated by pulsed laser deposition. *Journal of Electroceramics*, *27*, 203-208.

[46] Zhou, X., Jiang, D., Zhao, M., Wang, N., Duan, Y., Wang, W., Li, M., Li, Q., Shan, C., & Sun, J. (2020). Polarization induced two-dimensional electron gas in ZnO/ZnMgO heterointerface for high-performance enhanced UV photodetector. *Journal of Alloys and Compounds*, *820*, 153416.

[47] Jiao, S. J., Lu, Y. M., Shen, D. Z., Zhang, Z. Z., Li, B. H., Zhang, J. Y., Yao, B., Liu, Y. C., & Fan, X. W. (2006). Ultraviolet electroluminescence of ZnO based heterojunction light emitting diode. *Physica Status Solidi C*, *3*(4), 972-975.

[48] Nomura, K., Ohta, H., Ueda, K., Kamiya, T., Hirano, M., & Hosono, H. (2003). Thin-film transistor fabricated in single-crystalline transparent oxide semiconductor. *Science*, *300*(5623), 1269-1272.

[49] Sun, L. F., Dong, L. M., Wu, Z. F., & Fang, C. (2013). A comparison of the transport properties of bilayer graphene, monolayer graphene, and two-dimensional electron gas. *Chinese Physics B*, *22*(7), 077201.

[50] Das Sarma, S., Adam, S., Hwang, E. H., & Rossi, E. (2011). Electronic transport in two-dimensional graphene. *Reviews of Modern Physics, 83*(2), 407-470.

[51] Das, M., Sen, D., Sakib, N. U., Ravichandran, H., Sun, Y., Zhang, Z., Ghosh, S., Venkatraman, P., Radhakrishnan, S. S., Sredenschek, A., Yu, Z., Sarkar, K. J., Sadaf, M. U. K., Meganathan, K, Pannone, A., Han, Y., Sanchez, D. E., Somvanshi, D., Sofer, Z., Terrones, M., Yang, Y., & Das, S. (2024). High-performance p-type field-effect transistors using substitutional doping and thickness control of two-dimensional materials. *Nature Electronics*, *8*, 24-35.

[52] Jadczak, J., Kutrowska-Girzycka, J., Kapuściński, P., Huang, Y. S., Wójs, A., & Bryja, L. (2017). Probing of free and localized excitons and trions in atomically thin WSe_2, WS_2, $MoSe_2$ and MoS_2 in photoluminescence and reflectivity experiments. *Nanotechnology*, *28*(39), 395702.

[53] Cepheiden. (Dec. 9, 2006). *CMOS Chip Structure in 2000s [SVG image].* Wikimedia Commons. https://commons.wikimedia.org/wiki/File:Cmos-chip_structure_in_2000s_(en).svg

[54] Yano, M., Hashimoto, K., Fujimoto, K., Koike, K., Sasa, S., Inoue, M., Uetsuji, Y., Ohnishi, T., & Inaba, K. (2007). Polarization-induced two-dimensional electron gas at $Zn_{1-x}Mg_xO$/ZnO heterointerface. *Journal of Crystal Growth*, *301*, 353-357.

[55] Tsukazaki, A., Ohtomo, A., Kita, T., Ohno, Y., Ohno, H., & Kawasaki, M. (2007). Quantum Hall effect in polar oxide heterostructures. *Science*, *315*(5817), 1388-1391.

[56] Zhou, X., Jiang, D., Zhao, M., Wang, N., Duan, Y., Wang, W., Li, M., Li, Q., Shan, C., & Sun, J. (2020). Polarization induced two-dimensional electron gas in ZnO/ZnMgO heterointerface for high-performance enhanced UV photodetector. *Journal of Alloys and Compounds*, *820*, 153416.

[57] Ferri, K. M. (2021). *Ferroelectricity in Magnesium Substituted Zinc Oxide Thin Films*. The Pennsylvania State University.

[58] Dalba, D. A., Zhang, X., Xu, W., Bhattarai, B., Gamachchi, D. M., Karunarathne, I. M., Meng, W. J., & Meng, A. C. (2024). Effect of ZnO Interfacial Seed Layer in Sol–Gel Grown ZnMgO Ferroelectric. *ACS Applied Electronic Materials*.

[59] Ogawa, R., Tamai, A., Tanaka, K., Adachi, H., & Kanno, I. (2024). Ferroelectricity of Ce–Mn substituted ZnO thin films. *Japanese Journal of Applied Physics, 63* (1), 010902.

[60] Baksa, S. M., Gelin, S., Oturak, S., Spurling, R. J., Sepehrinezhad, A., Jacques, L., Trolier-McKinstry, S., van Duin, A. C. T., Maria, J-P., Rappe, A., & Dabo, I. (2024). Strain fluctuations unlock ferroelectricity in wurtzites. *Advanced Electronic Materials*, 2400567. Early view

[61] Sepehrinezhad, A., Baksa, S. M., Dabo, I., & van Duin, A. C. (2024). ReaxFF reactive force field for exploring electronically switchable polarization in $Zn_{1-x}Mg_xO$ ferroelectric semiconductors. *The Journal of Physical Chemistry C*, *128*(30), 12534-12543.

[62] Kolmogorov, A. N. (1937). On the statistical theory of crystallization. *Izvestiya Akademii Nauk SSSR, Seriya Matematicheskaya*, 1(2), 355-359.

[63] Avrami, M. (1939). Kinetics of phase change. I. General theory. *Journal of Chemical Physics*, 7(12), 1103-1112.

[64] Ishibashi, K. (1960). The kinetics of the crystallization process in solids. *Journal of the Society of Material Science, Japan*, 9(4), 148-157.

[65] So, Y. W., Kim, D. J., Noh, T. W., Yoon, J. G., & Song, T. K. (2005). Polarization switching kinetics of epitaxial $Pb(Zr_{0.4}Ti_{0.6})O_3$ thin films. *Applied Physics Letters*, *86*(9), 092905.

[66] Pantel, D., Chu, Y. H., Martin, L. W., Ramesh, R., Hesse, D., & Alexe, M. (2010). Switching kinetics in epitaxial $BiFeO_3$ thin films. *Journal of Applied Physics*, *107*(8), 084111.

[67] Wei, W., Zhang, W., Tai, L., Zhao, G., Sang, P., Wang, Q., Chen, F., Tang, M., Feng, Y., Zhan, X., Luo, Q., Li, Y., & Chen, J. (2021, December). In-depth understanding of polarization switching kinetics in

polycrystalline $Hf_{0.5}Zr_{0.5}O_2$ ferroelectric thin film: A transition from NLS to KAI. In *2021 IEEE International Electron Devices Meeting (IEDM)* (Vol. 19, No. 1-19.1, p. 4).

[68] Tagantsev, A. K., Stolichnov, I., Setter, N., Cross, J. S., & Tsukada, M. (2002). Non-Kolmogorov-Avrami switching kinetics in ferroelectric thin films. *Physical Review B*, *66*(21), 214109.

[69] Jo, J. Y., Han, H. S., Yoon, J. G., Song, T. K., Kim, S. H., & Noh, T. W. (2007). Domain switching kinetics in disordered ferroelectric thin films. *Physical Review Letters*, *99*(26), 267602.

[70] Lu, H., Schönweger, G., Petraru, A., Kohlstedt, H., Fichtner, S., & Gruverman, A. (2024). Domain dynamics and resistive switching in ferroelectric $Al_{1-x}Sc_xN$ thin film capacitors. *Advanced Functional Materials*, *34*(28), 2315169.

[71] Yazawa, K., Hayden, J., Maria, J-P., Zhu, W., Trolier-McKinstry, S., Zakutayev, A., & Brennecka, G. L. (2023). Anomalously abrupt switching of wurtzite-structured ferroelectrics: simultaneous non-linear nucleation and growth model. *Materials Horizons*, *10*(8), 2936-2944.

[72]Fanfoni, M., & Tomellini, M. (1998). The Johnson-Mehl-Avrami-Kolmogorov model: a brief review. *Il Nuovo Cimento D*, *20*, 1171-1182.

[73] Johnson, W. A., & Mehl, R. F. (1939) Reaction Kinetics in Processes of Nucleation and Growth. *Transaction Metallurgical Society AIME*, *135*, 416-442.

[74] Guido, R., Lu, H., Lomenzo, P. D., Mikolajick, T., Gruverman, A., & Schroeder, U. (2024). Kinetics of N-to M-polar switching in ferroelectric $Al_{1-x}Sc_xN$ capacitors. *Advanced Science, 11*(16), 2308797.

Chapter 3

Experimental Procedures

This chapter provides detailed descriptions of the experimental procedures used in this thesis. For procedures which require more detail pertaining to the specific application, the relevant details are provided in the respective chapter where the work is described.

3.1 Film Deposition

The work in this thesis is performed solely on films deposited via Dual RF Magnetron Sputtering from pure metal targets.

Dual RF Magnetron Sputtering

Sputtering describes the bombardment of a surface (target) with high energy ions in order to eject materials from the target and onto a substrate. One advantage of this method is that the energy of ejected (sputtered) material can be controlled by modifying parameters such as the sputter power, the process pressure and the distance between the target and the substrate.[1] The latter two parameters influence the mean free path of the process gasses. The mean free path describes the average distance a particle can travel before colliding, where each collision scatters the traveling particle, causing a net reduction in the bombardment energy on the substrate. The sputter mean free path (λ) can be described by:[2]

$$\lambda = \frac{k_b T}{\sqrt{2}\pi d^2 P}$$

where k_b is Boltzmann's constant (1.38×10^{-23} J/K), T is the absolute temperature in Kelvin, d is the average kinetic diameter (3.40 Å for Ar[3] and 3.46 Å for O[4]), and P is the pressure in Pascals. The average mean free path for a mixture of argon and oxygen is shown in Figure 3-1.

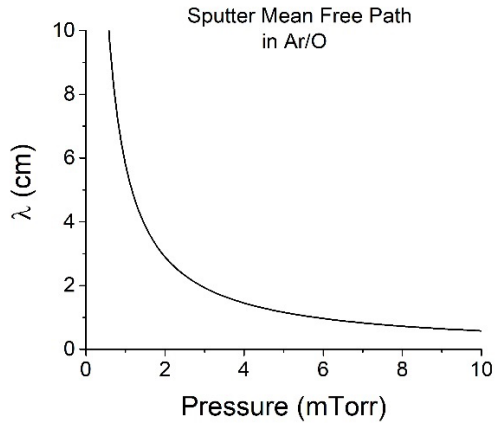

Figure 3-**1**: The mean free path (λ) for Ar/O gas mixture, assuming the average kinetic diameter is 3.43 Å.

Therefore, choice of process pressure can determine the bombardment energy on the substrate and affect the properties of the resulting film.

In this work, ZMO was sputtered from either 1" or 2" diameter pure Zn and Mg metallic targets at a process pressure of 1 mTorr and a working distance of 6 cm. The Zn/Mg composition ratio was determined by the sputter powers on each of the targets. The power applied to the Zn target was varied between 60 and 80 W, and to the Mg was varied between 40 and 60 W. Films were deposited in either Ar/O_2 or $Ar/(O_2/O_3)$. O_3 was generated in house with an ozone generator. $Ar:O_2$ and $Ar:O_3$ gas flow ratios were maintained at 3:1, and flow rates were 18 sccm and 6 sccm, respectively. All films in chapter 4 were deposited in Ar/O_2 and all films in chapter 5 were deposited in the $Ar/(O_2/O_3)$ mixture, unless otherwise specified. Films were grown by the Maria group at Penn State by R. Jackson Spurling, D. Goodling, or Gyunghyun Ryu. Sputter parameters are presented in Table 3-1.

Table 3-**1**: Deposition parameters for sputtered ZMO thin films.

Process Parameter	Deposition Conditions
Process Gasses	Ar/O_2 or $Ar/O_2/O_3$
Pressure	1 mTorr
Temperature	20 °C
Zn Power	60 – 80 W
Mg Power	40 – 60 W
Deposition rate	~ 20 nm/min

3.2 Structural and Morphological Characterization

3.2.1 X-ray Diffraction (XRD)

The crystallinity, orientation and phase purity in ZMO films was determined by X-ray diffraction (XRD). XRD patterns were obtained using a Malvern Panalytical Empyrean Diffractometer with a θ-2θ goniometer and equipped with multi-core optics (Incident beam path: 0.03 rad soller slit, 14 mm primary mask, 6 mm secondary mask, ¼° divergence slit; Diffracted beam path: ¼° anti-scatter slit, 0.04 rad soller slit). X-rays were generated in a Cu tube powered at 45 kV and 40 mA, with a Kα wavelength of 1.54059 Å. Diffracted x-ray photons were collected with a PIXcel 3D detector.

XRD patterns revealed 002 *c*-axis oriented ZMO, and rocksalt where compositions exceeded 41% Mg.

3.2.2 Field Emission Scanning Electron Microscopy (FESEM)

Field emission scanning electron microscopy (FESEM) (Zeiss Merlin) was used to obtain high resolution images of the microstructure of ZMO. Electrons were accelerated at a voltage of 5

kV and beam current of 216 pA, unless otherwise specified. FESEM was used to determine the grain sizes in ZMO, and to observe structures in devices with ZMO.

3.2.3 Energy Dispersive Spectroscopy (EDS)

Energy dispersive spectroscopy (EDS/EDX) was used to determine film compositions with an accuracy of ± 2 atomic % for Zn and Mg. The Zeiss Merlin FESEM equipped with a Ultim® Max EDS detector (Oxford Instruments) was used for EDS. Electrons were accelerated at 10 kV and at a beam current of 2 nA.

3.3 Preparation of Top Electrodes

All ZMO films were deposited on platinized-silicon substrates sourced from Applied Materials. In this dissertation only the top electrode material was varied. Various techniques can be used to deposit top electrodes – the simplest being shadow masking which is a quick one-step process to check the quality of ferroelectric ZMO. However, the definition of electrode boundaries with the shadow masking technique is poor and can lead to inflated values in area-dependent electrical properties, due to an inflation of the area. Shadow masking is acceptable when large electrode diameters are being used such that the error in the boundary does not cause significant errors. However, for small electrode areas, it is desirable to have well-defined electrode boundaries to preserve the accuracy of electrical and ferroelectric measurements. For this, a non-aqueous lithographic process for depositing top electrodes on ZnO was adapted from Prof. Tom Jackson's group at the Pennsylvania State University.[5]

3.3.1 Non-aqueous Lithographic Process for ZMO

The lithographic process is a process wherein photoresists are deposited, baked/cured, then exposed to high intensity UV light through a mask or with a high-definition laser in order to define a pattern for a subsequent deposition or etch. The top layer is the photosensitive layer that either hardens (negative photoresist) or delinks (positive photoresist) when exposed UV light. The lift-off resist beneath the photosensitive (photoresist) layer, is typically not photosensitive, and will dissolve at a controlled rate in a resist developer, to form an undercut. The undercut provides improved patterning of the electrode material during removal of the remaining resists and unwanted material after the deposition step.

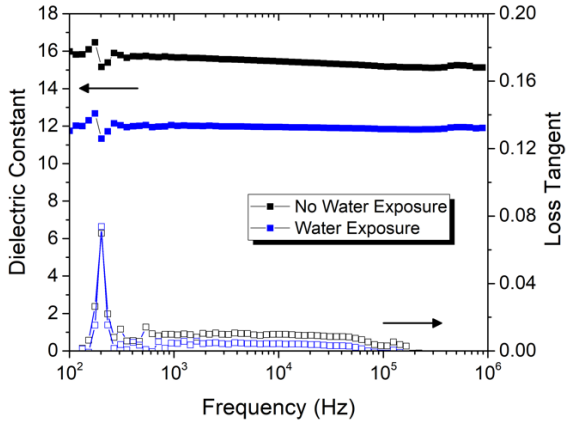

Figure **3-2**: The dielectric constant of ZMO with Pt top electrodes is measured before and after 110 seconds of exposure to water. The top electrode was deposited through a shadow mask, which artificially inflates the electrode area and the dielectric constant.

Typical lithographic processes such as those used for PZT and KNN expose the ferroelectric surface to water and resist developer.[6] For those films, it is not problematic so long as exposure is short, however, for ZMO even brief exposure to water can degrade the film (see Figure 3-2). To avoid this degradation, a non-aqueous lithographic process originally proposed by

the Jackson group for ZnO semiconductors was adapted here for ZMO. This was accomplished by depositing a 120 nm thick layer of polymethylmethacrylate (PMMA A3, Kayaku Advanced Materials) before a conventional lithography process. The detailed non-aqueous process is provided in the appendix (Appendix section A-1).

In brief, the PMMA acts as a barrier layer to protect ZMO from water and developer during the lithographic process. After the develop step, the sample is exposed to high intensity UV light at $\lambda = 248$ nm and intensity of 385 mW cm^{-2} for 2 minutes to delink the PMMA polymer while simultaneously making a hard mask of the top SPR 3012 photoresist layer. The sample is then exposed to gentle agitation in toluene for 2 minutes to dissolve the delinked PMMA which was exposed to UV light, revealing the patterned ZMO surface for electrode deposition. This is followed by an oxygen plasma ash in a Metroline M4L ICP tool at 300 W and 550 mTorr with

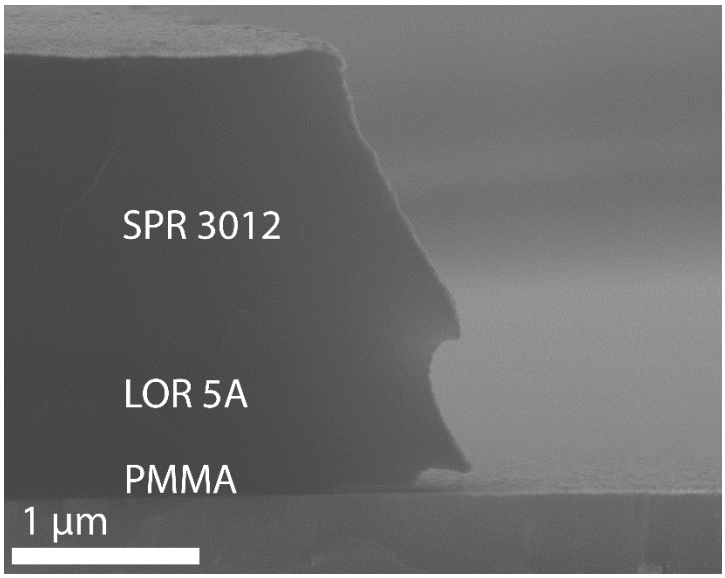

Figure **3-3**: A cross-sectional view of the SPR 3012 (1.2 µm), LOR 5A (0.5 µm) and PMMA (120 nm) stack, after electrode deposition of 50 nm thick Pt. FESEM accelerating voltage was set to 10 kV to obtain this micrograph.

150 sccm O_2 flow and 50 sccm He flow for at least 2 minutes. Longer ash times are typically necessary for large electrode diameters to completely remove residual PMMA from the ZMO surface.

The maximum electrode thicknesses for this process are approximately 100 nm, as shown in Figure 3-3. Due to the non-aqueous nature of this process, CD-26 developer or other aqueous developers cannot be used during the lift-off process. Instead, acetone was used in combination with a sonicating bath in order to remove the LOR 5A/PMMA layer. Both the top photoresist layer and the bottom PMMA layer dissolve in acetone, however the middle lift-off resist layer (LOR 5-A) will not. So, a sonicating bath is required to dissolve the underlying PMMA layer in order to remove the LOR 5A.

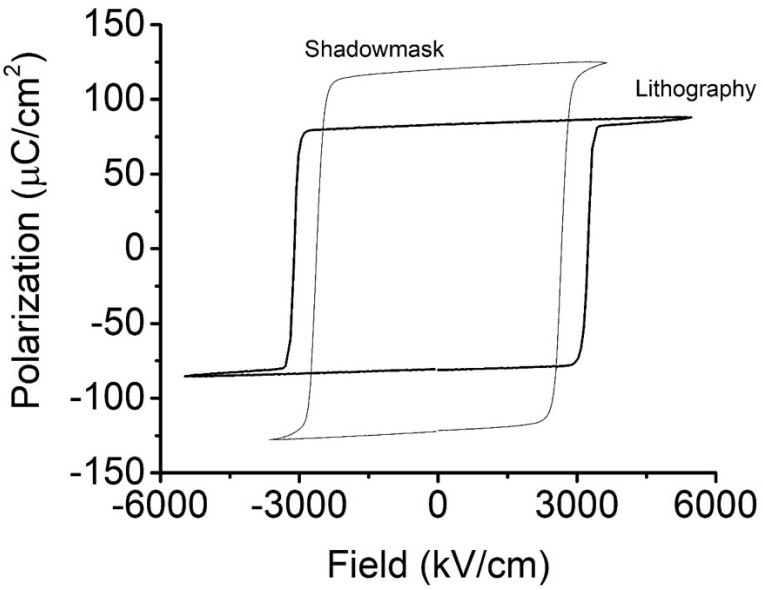

Figure **3-4**: Inflation of the remanent polarization of ZMO in samples with shadow masked electrodes, compared to lithographically defined electrodes. Note that the two films shown here were grown at different times, which may account for the different coercive fields. The films were both cycled at 100 Hz to measure the P-E hysteresis loops.

Ultimately, the lithographic process produces well-defined electrode areas, avoiding errors in the electrode areas associated with shadow masking. These errors become more significant as capacitor sizes decrease. An example of area inflation due to shadow masking on comparable samples of ZMO is shown in Figure 3-4. Use of the wrong electrode area results in incorrect polarizations, permittivities, and leakage currents, for example

3.3.2 Top Electrodes

Platinum top electrodes were used for many of the ZMO films in this work. Oxide top electrodes were also explored in an attempt to increase the fatigue cycling lifetime of ZMO, as is done for PZT films.[7] IrO_2 is a metallic conductor which can be deposited at room temperature[8] with a resistivity of approximately 25 μΩ·m for in house grown films. The resistivity was measured on IrO_2 film deposited on a p-type Si substrate using the van der Pauw method. A Cascade 1200 probe station and Keithley 4200A-SCS parameter analyzer were used to measure

Table **3-2**: Deposition parameters for sputtered Pt top electrodes.

Process Parameter	Deposition Conditions
Process Gasses	Argon
Pressure	2 mTorr
Temperature	20 °C
Power	200 W
Time	417 s

Table **3-3**: Deposition parameters for sputtered IrO_2 top electrodes.

Process Parameter	Deposition Conditions
Process Gasses	Ar/O_2
Pressure	5 mTorr
$Ar:O_2$ flow ratio	10:1 (16 sccm Ar flow)
Temperature	20 °C
Power	70 W
Working Distance	4 in.
Deposition Rate	10 nm/min

the sheet resistivity which was converted to resistivity by multiplying the film thickness, which was measured using a KLA Tencor P16+ profilometer. Deposition conditions are described in Tables 3-2 and 3-3. Top electrodes were sputtered using Kurt J. Lesker CMS-18 sputter systems. Typical platinum thicknesses were 100 nm and IrO_2 thicknesses were 70 nm.

Various top electrodes were deposited to assess the conduction mechanism in ZMO. In addition to Pt and IrO_2, these included W, Ti, Ir and $SrRuO_3$. W, Ti and Ir were deposited via magnetron sputtering, and $SrRuO_3$ was deposited via pulsed laser deposition (PLD). All films were deposited at room temperature, and the $SrRuO_3$ film was capped with a thin layer of Pt for better electrical contact. Deposition conditions for each of the top electrode materials are described in Tables 3-4 and 3-5.

Table 3-**4**: Deposition parameters for sputtered W, Pt and Ir top electrodes.

Process Parameter	Deposition Conditions		
Material	W	Ti	Ir
Process Gasses	Ar	Ar	Ar/O_2
Pressure	1 mTorr		5 mTorr
Temperature	20 °C	20 °C	20 °C
Power			500 W
Deposition time			60 s

Table 3-**5**: Deposition parameters for PLD $SrRuO_3$.

Process Parameter	Deposition Conditions
Process Gasses	Ar/O_2
Pressure	mTorr
Temperature	20 °C
Laser	KrF, 248 nm
Pulse Frequency	5 Hz
Time	10 minutes

3.3.4 Accessing the Bottom Electrode

The bottom platinum electrode was accessed by etching the ZMO layer with nitric acid. Microposit 1800 series photoresist was used protect most of the sample from exposure to acid, and baked at 120°C to harden the photoresist. A photoresist layer was applied by dip-coating the sample and heating it to 120°C for 2 minutes, leaving an unprotected area for etching to the bottom electrode. This process was repeated twice to minimize the possibility of pinholes in the protection layer. Next, the sample was either placed in a beaker containing nitric acid/H_2O 50/50 or a drop of concentrated nitric acid was placed on the surface to be exposed with a dropper. The sample was exposed to nitric acid/H_2O 50/50 for 1 to 2 minutes, or until the bottom electrode was revealed. Afterward, the sample was rinsed with DI water, followed by removal of the photoresist by spraying acetone as the sample was held vertically, and minimizing exposure of the ZMO to nitric acid retained in the photoresist.

When the eyedropper was used to deposit concentrated nitric acid, the whole thickness of ZMO etched almost immediately, and the photoresist began to degrade. In this case, the application of nitric acid was followed by rinsing in DI water within 10 seconds. Afterwards, the sample was dried immediately by using a nitrogen gun, and the photoresist was removed by spraying the sample with acetone (with the etched corner of the sample facing downwards to avoid unnecessary nitric acid exposure to the surface of the ZMO). Samples were then rinsed in isopropanol and blow dried with nitrogen.

3.4 Electrical Characterization

In all cases, electrical contact was made to samples with tungsten probe tips attached to a micromanipulator. BNC cable lengths between the probe station and testing instruments varied

from 1 to 2 meters in length. The electrical characterization performed included capacitance and dielectric loss, Polarization-Electric field (P-E) hysteresis loops, Current-Voltage (I-V) measurements, modulus spectroscopy and switching speed measurements taken with a custom in house set-up.

3.4.1 Dielectric Studies

Low-field to moderate-field (20 V maximum) measurements were taken with a precision LCR meter 4264A (Hewlett-Packard, Palo Alto, CA). The capacitance and loss tangent of samples were recorded for frequency sweeps from 100 Hz to 1 MHz at an amplitude of 30 mV. The dielectric permittivity was related to the capacitance by:

$$\varepsilon_r = \frac{Cd}{\varepsilon_0 A}$$

where C is the capacitance, d is the film thickness, A is the area of the top electrode, and ε_r and ε_0 are the relative and the absolute permittivity, respectively.

The dielectric constant and loss of ZMO at 1 kHz was used to observe Rayleigh behavior in Chapter 5. The AC applied field (voltage) was increased from 10 mV to 20 volts to observe the field-dependance of the dielectric constant and loss tangent. Rayleigh behavior of the dielectric constant was described by:[9]

$$\varepsilon = \alpha E + \varepsilon_{init}$$

where α is the irreversible Rayleigh coefficient and ε_{init} is the reversible contribution to the dielectric constant.

3.4.2 Modulus Spectroscopy

Modulus spectroscopy was performed to characterize bulk conduction in thin films, and to assign activation energies to the conduction modes.[10] This technique was performed with a Modulab XM (Solartron Analytical). Samples were subjected to an applied field with an amplitude of 100 kV cm^{-1} and at frequencies ranging from 0.1 Hz to 100 kHz. Tests were performed at elevated temperatures on a probe station equipped with a hotplate to observe peaks in the modulus spectra whose frequencies were used to determine the activation energy according to:[11]

$$f_{max} = f_0 e^{-\frac{E_a}{k_b T}}$$

where f_{max} is the frequency of the maximum modulus at a given temperature, f_0 is a constant, E_a is the activation energy, k_b is Boltzmann's constant, and T is the absolute temperature.

3.4.3 Switching Kinetics Module

A system consisting of a function (or signal) generator, a voltage amplifier, and an oscilloscope, designed by Kei Yazawa, [12] was used to measure switching speeds and perform kinetics analysis on ferroelectric switching in ZMO thin films (see Figure 3-5). An Agilent 33220A 20 MHz function generator with ± 10 V range was used to generate pulse sequences. The output of the function generator was supplied to a Trek Model 2100HF amplifier with 50x voltage amplification, ± 150 V range, and with built-in voltage overshoot protection. The sample response was collected by a transimpedance amplifier (TIA) with a low-noise operational amplifier (OPA657UB, Texas Instruments) with a maximum current output of 70 mA. The voltage output from the TIA could be converted to current by multiplying the output voltage by 22 Ω. Other details about the TIA can be found elsewhere.[12]

The function generator output voltage, amplifier output voltage, and the TIA output voltage were received simultaneously by a 4-channel Tektronix TBS 2000B Series Oscilloscope with voltages collected at 1 ns intervals. Python was used to design PUND waveforms applied by the function generator (see Figure 3-6). MATLAB was used to analyze raw data files and apply various statistical models to the switching transients. The MATLAB codes are provided in the thesis appendix.

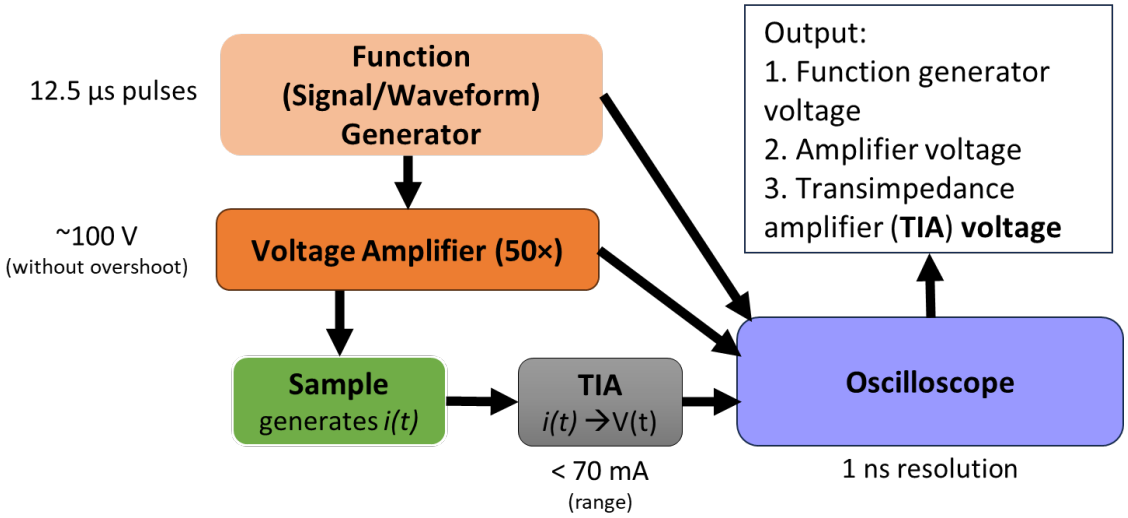

Figure **3-5**: The switching kinetics measurement set-up consisting of an Agilent 33220A 20 MHz function generator, Trek Model 2100HF voltage amplifier, TIA, and Tektronix TBS 2000B Series oscilloscope which collects the response from each component.

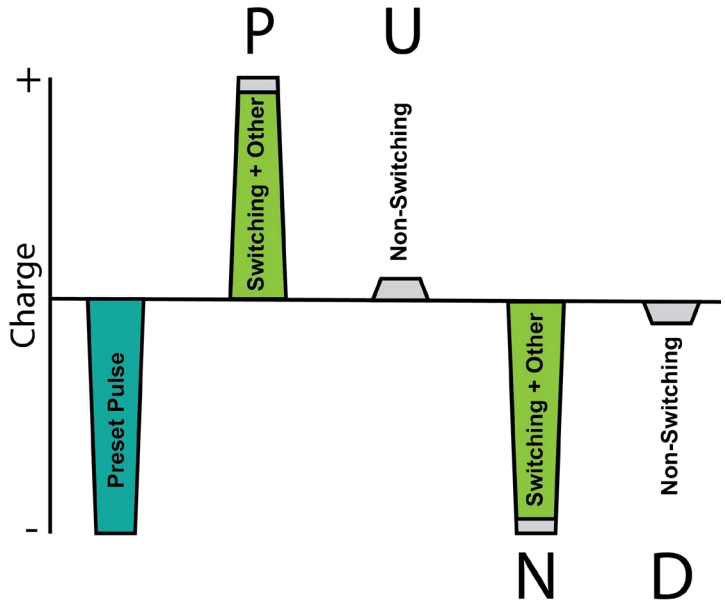

Figure **3-6**: The basic PUND waveform that is applied to samples. A double-PUND waveform is used in the switching kinetics set-up, and kinetics data are taken from the second PUND waveform to exclude imprint effects.

3.5 Si Nanodots Deposition

Deposition of SiO_2 nanodots on a ZMO film surface was attempted in order to reduce the coercive field of ZMO by promoting dense nucleation sites associated with local field concentrations. More details and the motivation for this work are described in Chapter 7. Nanodots were patterned with E-beam lithography (by Mike Labella, Materials Research Institute) via the procedure in Table 3-6.

SiO_2 was deposited via E-beam evaporation in a Temescal F-2000 at a pressure of 10^{-6} Torr. The deposition rate was 0.5 Å/s, and the film thickness was 20 nm. The morphology of the nanodots was analyzed with atomic force microscopy in tapping mode. Scan parameters are in Table 3-7.

Table **3-6**: The E-beam lithography patterning process.

Step	Process
1	Dehydration bake at 180°C for 3 minutes.
2	Spin coat ZEP520A (diluted 1:1 with Anisole)
3	Soft bake at 180°C for 3 minutes.
4	Exposure Beam: 5 nA, 200 μm diameter Dose: 180 μC cm^{-2} (Patterns were fractured with a 5 nm beam step size)
5	Develop N-Amyl Acetate, 3 minutes
6	Rinse in Isopropanol for 1 minute
7	SiO_2 deposition
8	Lift-off in PRS 3000 (photoresist stripper) at 80°C for 30 minutes.

Table **3-7**: Atomic force microscopy measurement settings.

Parameter	Setting
Probe (tip)	ScanAsyst – Air (Si_3N_4)
Scan size	2 μm
Scan rate	0.5 Hz
Tip velocity	2 μm/s
Samples per line	512
Number of lines	512
Peak Force setpoint	1.5 nN
Peak Force amplitude	150 nm
Peak Force frequency	2 kHz
Lift height	29.3 nm

References

[1] Ferri, K., Bachu, S., Zhu, W., Imperatore, M., Hayden, J., Alem, N., Giebink, N., Trolier-McKinstry, S., & Maria, J-P. (2021). Ferroelectrics everywhere: Ferroelectricity in magnesium substituted zinc oxide thin films. *Journal of Applied Physics*, *130*(4), 044101.

[2] Schmidt, M., Ruff, S., & O'Handley, R. (2007). *6.152J Micro/nano processing technology*. MIT OpenCourseWare. https://ocw.mit.edu/courses/electrical-engineering-and-computer-science/6-152j-micro-nano-processing-technology-spring-2007/

[3] Breck, D. W. (1974). *Zeolite molecular sieves: structure, chemistry, and use.* Wiley.

[4] Ismail, A. F., Khulbe, K. C., & Matsuura, T. (2015). Gas separation membranes. *Switz. Springer, 10*, 973-978.

[5] Gupta, A. (2021). *Zinc Oxide Thin Film Transistor (ZnO TFT)- Lipid Membrane Based Electronic Biosensor* (Doctoral Dissertation, The Pennsylvania State University).

[6] Marincel, D. M., Jesse, S., Belianinov, A., Okatan, M. B., Kalinin, S. V., Jackson, T. N., Randall, C. A., & Trolier-McKinstry, S. (2015). A-site stoichiometry and piezoelectric response in thin film $PbZr_{1-x}Ti_xO_3$. *Journal of Applied Physics*, *117*(20), 204104.

[7] Chen, M. S., Wu, T. B., & Wu, J. M. (1996). Effect of textured $LaNiO_3$ electrode on the fatigue improvement of Pb $(Zr_{0.53}Ti_{0.47})O_3$ thin films. *Applied Physics Letters*, *68*(10), 1430-1432.

[8] Zhang, L. M., Gong, Y. S., Wang, C. B., & Shen, Q. (2007). Microstructure and resistivity of iridium oxide thin films by pulsed laser deposition technique. *Key Engineering Materials*, *336*, 2215-2217.

[9] Keech, R., Shetty, S., Kuroda, M. A., Hu Liu, X., Martyna, G. J., Newns, D. M., & Trolier-McKinstry, S. (2014). Lateral scaling of $Pb(Mg_{1/3}Nb_{2/3})O_3$-$PbTiO_3$ thin films for piezoelectric logic applications. *Journal of Applied Physics*, *115*(23), 234106.

[10] Coşkun, M., Polat, Ö., Coşkun, F. M., Durmuş, Z., Çağlar, M., & Türüt, A. (2018). The electrical modulus and other dielectric properties by the impedance spectroscopy of $LaCrO_3$ and $LaCr_{0.90}Ir_{0.10}O_3$ perovskites. *RSC Advances*, *8*(9), 4634-4648.

[11] Coşkun, M., Polat, Ö., Coşkun, F. M., Durmuş, Z., Çağlar, M., & Türüt, A. (2018). The electrical modulus and other dielectric properties by the impedance spectroscopy of $LaCrO_3$ and $LaCr_{0.90}Ir_{0.10}O_3$ perovskites. *RSC Advances*, *8*(9), 4634-4648.

[12] Yazawa, K., Zakutayev, A., & Brennecka, G. L. (2022). High-speed and high-power ferroelectric switching current measurement instrument for materials with large coercive voltage and remanent polarization. *Sensors*, *22*(24), 9659.

Chapter 4

Ferroelectric Properties of (Zn,Mg)O Thin films: Wake-up, Retention and Fatigue

This chapter is reproduced from Jacques, L., Ryu, G., Goodling, D., Bachu, S., Taheri, R., Yousefian, P., Shetty, S., Akkopru-Akgun, B., Randall, C., Alem, N., Maria, J-P., & Trolier-McKinstry, S. (2023). Wake up and retention in zinc magnesium oxide ferroelectric films. Journal of Applied Physics, 133(22), 224102.

4.1 Introduction

Energy conservation to mitigate CO_2 emissions while green energy sources are developed is a critical global need. As such, it is interesting to consider which technologies are responsible for significant energy consumption. Computing, including data centers, is reported to account for ~5-15% of energy usage worldwide,[1] in which the "on" state of computational devices is a major contributor to loads on the electrical grid[2]. One approach to lowering the energy burden associated with computing is to recognize that information retrieval from memory requires energy, and the deeper in the memory stack, the more energetically expensive the data retrieval becomes[3,4]. This is increasingly problematic as the size of machine learning data models grows explosively[5]. Non-volatile memory technologies that are closely and densely connected to the compute engine would reduce this energy demand.

Ferroelectricity offers one approach to non-volatile memory. Ideally, the memory should be processed on top of the CMOS, in the Back End of the Line (BEOL) with a maximum processing temperature of 400°C. Conventional perovskite ferroelectrics typically require thermal

processing at temperatures well above 400°C, complicating integration. Moreover, despite excellent fatigue characteristics,[6] conventional perovskite ferroelectrics such as lead zirconate titanate ferroelectric random-access memories have not been commercially scaled to thicknesses below 70 nm. This makes high density memory impractical. Thus, new BEOL-compatible ferroelectric materials with good memory properties are needed. Desirable properties include long-term retention (~10 years), fatigue resistance (~10^{12} cycles), and the ability to operate at CMOS-typical voltages (≤1.5 Volts).

Among the newer ferroelectric materials, doped hafnia ferroelectrics scale to very low thicknesses, and have been successfully integrated into non-volatile memory devices, with interesting retention and fatigue characteristics; some reports record memory retention greater than 10 years and 10 billion cycles.[7,8,9] While some HfO_2-based systems are annealed at back-end-of-the-line compatible temperatures (<400°C), in many cases[10,11] higher temperatures are employed to optimize the properties.[12] It is of interest to develop more ferroelectrics which can be optimized at temperatures below 400°C, to facilitate BEOL processing.

The newly discovered class of hexagonal wurtzite structure ferroelectrics satisfies the temperature limits for processing on CMOS chips, with substrate temperatures of < 400°C for all parts of the deposition process. They are promising for many applications, including non-volatile memory.[13,14,15] The first of these discovered, Sc-doped AlN, shows large remanent polarizations ~80 – 120 μC/cm^2, but coupled with large coercive fields.[13] When Sc is replaced by boron at concentrations between 2% and 15%,[14,15] ferroelectricity is retained, and the films generally show lower leakage currents relative to the Sc-doped analogs.[14,15] Moreover, the polarization remains large up to 200°C.[13,15] However, the large coercive fields, ~ 2 - 6 MV cm^{-1} in Sc- and B-doped AlN[16] necessitate use of extremely thin layers to be compatible with available voltages in CMOS devices (≤ 1.5 volts). It is therefore interesting to consider alternatives with lower coercive fields.

$Zn_{1-x}Mg_xO$ (ZMO) thin films are an oxide analog of the AlN-based ferroelectrics, with large remanent polarizations (±80 μC cm^{-2}), coupled with lower coercive fields (~2 - 4 MV cm^{-1}) relative to (Al,B)N (~5-6 MV cm^{-1})[15], and square-shaped P-E hysteresis loops.[17] Additionally, their low deposition temperatures are compatible with back end of the line (BEOL) processes; therefore, ZMO films are of potential interest for embedded non-volatile memory. However, little is known about the memory capabilities of ZMO systems. Thus, this paper explores wake-up and retention in $Zn_{1-x}Mg_xO$ films.

4.2 Experimental Procedure

Films were deposited via dual RF magnetron sputtering at room temperature from pure Zn and Mg targets onto Pt coated *c*-sapphire substrates at a working distance of 4 cm. The Ar:O ratio and deposition pressure were maintained at 4:1 and 3.5 mTorr, respectively. Targets were subjected to DC/RF powers of 130/18 W and 133/57 W for Zn and Mg, respectively. The deposition rate was approximately 6 nm/minute. *c*-axis oriented wurtzite ZMO was confirmed via X-ray diffraction (XRD) by Bragg-Brentano and Omega (ω) scans with Cu Kα radiation.

Microstructure was observed with a field emission scanning electron microscope (FESEM) (Merlin) at accelerating voltages below 5 kV. The FESEM, with an attached energy dispersive spectroscopy (EDS) detector, was used to assess the composition and homogeneity of the films. Cross-sectional TEM samples were prepared by focused ion beam (FIB) milling. Bright-field TEM images were acquired using a Thermo Fisher Talos F200X microscope operated at 200 kV.

A non-aqueous lithographic patterning process, adapted from [18] was optimized to deposit elliptically shaped electrodes with 0.4 mm^2 areas. This is important since ZnO is susceptible to chemical interactions on exposure to water, as well as to some developers. First, polymethyl methacrylate (PMMA A5) was spun at 4,000 RPM for 60 s, and baked for 10 minutes at 200°C to

prevent outgassing in the following steps. Then, LOR 5a was spun at 4,000 RPM for 40 s and baked at 190°C for 2 minutes. Finally, a layer of SPR 3012 was spun at 4,000 RPM for 40 s and baked at 95°C for 1 minute. The layers were then exposed to UV light for a dose of 60 mJ cm^{-2} under a chromium plated mask for patterning, followed by developing in CD-26 for 60 seconds. After this step, the SPR and LOR layers act as a UV mask[32], while the PMMA layer completely covered the ZMO surface. The sample was then exposed to a high intensity UV flood at 385 mW cm^{-2} for two minutes to destroy cross-linking in the remaining PMMA in the patterned sections [19]. A 1 minute bath in toluene dissolved the PMMA to reveal the ferroelectric ZMO surface. The surface was gently cleaned in a He/O_2 plasma etch before DC magnetron sputtering of the 100 nm thick platinum top electrode. Final lift-off was achieved by a 30-minute sonicating bath in pure acetone. Electrodes were elliptically shaped with an area of 0.04 mm^2.

Polarization-Electric field (P-E) hysteresis loops, switching current densities, and retention data were generated using a Precision Multiferroic II tester manufactured by Radiant Technologies. The tester had a 500 V, 20 mA amplifier. P-E loops were measured using triangle voltage wave forms at 100 Hz and at room temperature, with the applied field sequence of ↑↓ relative to the ZMO as-grown poled-down state (↓), unless otherwise indicated. The bottom electrode was chosen for the drive, unless otherwise specified. Temperatures were varied between -40°C and 300°C using a FormFactor 11000B probe station. All capacitors used for retention measurements were woken with the single-loop wake up method at a maximum driving field of 4 MV cm^{-1} [6]. DC leakage current – electric field (J-E) data was measured with a Hewlett-Packard pA meter 4140B, using a staircase voltage increase with 1 volt increments and 60 second delay to measure the steady state leakage current. Modulus spectroscopy was performed with a Modulab XM (Solatron Analytical), testing at 100 kV cm^{-1} and frequencies from 0.1 Hz to 100 kHz. Retention measurements were performed using the Radiant tester, with 1 ms duration square wave pulses at 4 MV cm^{-1}. Cycling endurance was measured with the Radiant tester at parameters

ranging from 1-5 kHz cycling frequency, 50 μs – 1 ms pulse width, 40 μs – 50 μs rest, and at 4 – 4.5 MV cm^{-1} applied field.

4.3 Results and Discussion

4.3.1 Structural Characterization

Figures 4-1a and 4-1b show X-ray diffraction scans in 2θ and ω respectively. They indicate uniform single-phase 0002 oriented ZMO, with strong out of plane texture with a 1.7° wide rocking curve. These stacks feature an epitaxial Pt bottom electrode grown directly on *c*-plane sapphire at 350 °C. An average ZMO lateral grain size of 70 nm was determined via atomic force microscopy. Energy dispersive spectroscopy (EDS) confirmed the film composition to be ~ 36% Mg; no variation in composition was detected across the film surface. Additional films were grown on Pt/Ti/SiO_2/Si substrates, with comparable structural quality.

A bright-field transmission electron microscopy (TEM) image of the cross-section of the film reveal significant strain contrast throughout the film thickness (Figure 4-1c); the microstructure was found to be heterogeneous, wherein some regions of the film show fewer defects near the top surfaces, and other regions showed similar levels of contrast across the film thickness.

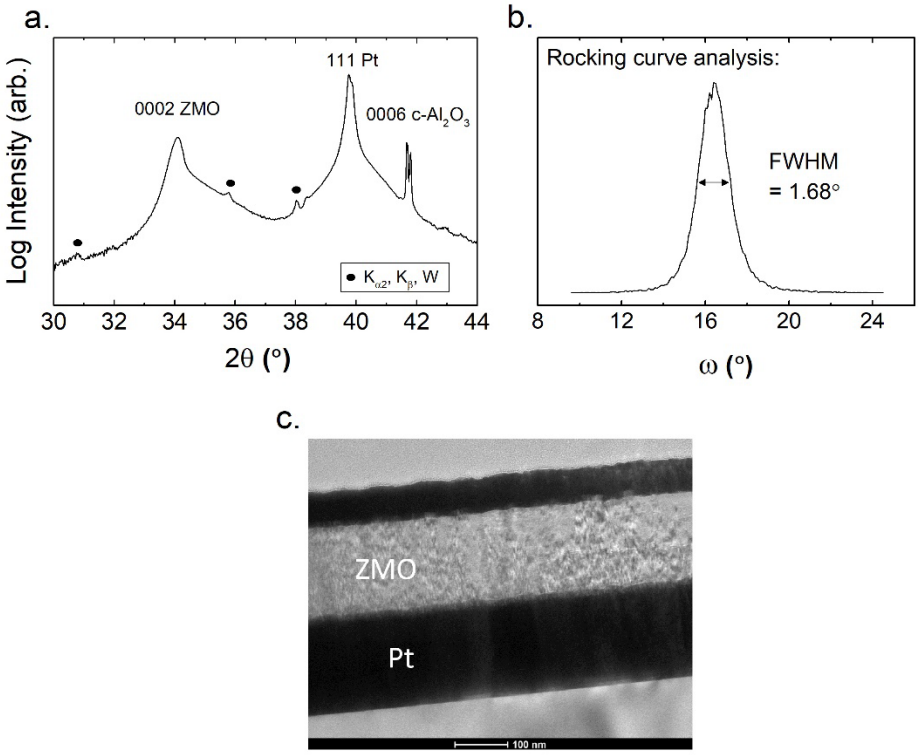

Figure **4 -1**: Structural and microstructural characterization of ZMO films (a) X-ray diffraction pattern confirming a *c*-axis oriented ZMO with the wurtzite structure on Pt/Al_2O_3 and (b) rocking curve of 1.7° for a 490 nm thick ZMO film on Pt/Al_2O_3. Peaks marked with a circle come from wavelengths other than Cu Ka. (c) Transmission electron microscopy image of Ir/ZMO/Pt/sapphire cross section, contrast in this image is attributed primarily to local strain with a non-uniform microstructure with a general trend of more contrast near to the bottom Pt electrode.

4.3.2 Ferroelectric Properties

Figure 4-2 shows the temperature dependence of the polarization hysteresis for a ZMO film on Pt/Al_2O_3. It is clear that the coercive field of ZMO films is strongly temperature dependent, where the films are much easier to switch at high temperatures. A plot of the coercive field as a function of inverse temperature is not linear. Therefore, there is not a single well-defined activation energy for domain switching; comparable behavior has been previously reported for undoped, B-doped, and Sc-doped AlN thin films. [20] The temperature dependence of the coercive field E_c has a pseudo-activation energy of 23 ± 0.3 meV at temperatures below 60°C, as shown in Figure 4-2b. The pseudo-activation energy increases to 41 ± 0.6 meV between 120°C and 200°C. This pseudo-activation energy is similar to that for the ferroelectric wurtzite $Al_{0.9}B_{0.1}N$ and is indicative of polarization reversal by domain nucleation and growth, rather than intrinsic switching, which would require a larger activation energy.[16]

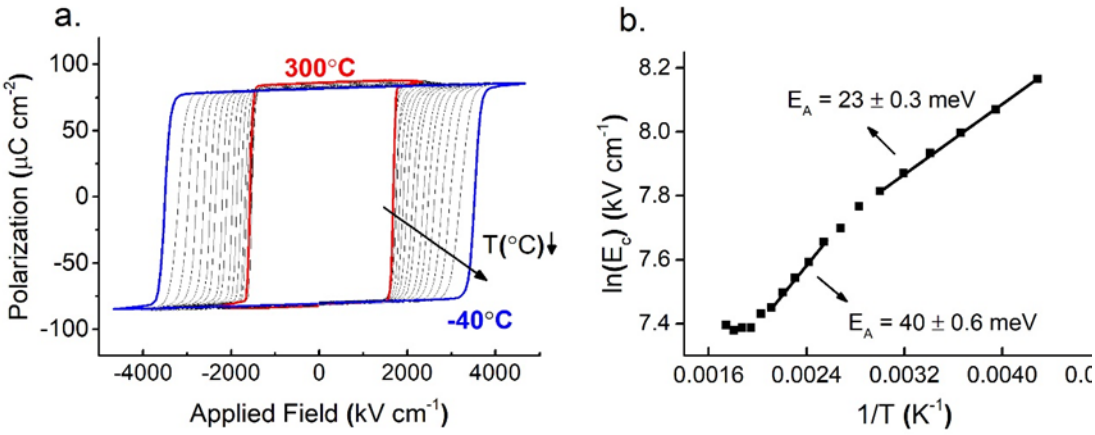

Figure **4-2**: (a) The temperature dependence of P-E hysteresis and the coercive field. Loops are shown in the order of decreasing temperature from 300°C to -40°C. Note: The driving field is reduced as the temperature increases to suppress spurious leakage currents. (b) The pseudo-activation energy E_A is plotted for the same temperature range on Pt/Al_2O_3.

4.3.3 Wake-up

As was previously observed for other wurtzite nitrides,[13,15] ZMO films must be *woken-up* to realize ferroelectric switching – that is to say, from the as-deposited state the polarization cannot be fully reversed by applying one electric field cycle where E_{max} is greater than E_c unless the duration is sufficiently long. Wake-up can be induced in three ways: **i.** applying E_{max} just greater than E_c in a single cycle for a "long" time, *i.e.*, a triangle wave hysteresis loop at 0.1 Hz; **ii.** applying E_{max} just greater than E_c with a higher frequency swing and many cycles, *i.e.*, a triangle wave hysteresis loop at 100 Hz for > 100 cycles; or **iii.** applying E_{max} substantially greater than E_c but with one fast cycle, *i.e.*, a single triangle wave hysteresis loop at 100 Hz with E_{max} = 1.25 E_c. It is observed that the number of polarization – electric field (P-E) loops necessary to wake-up the ZMO thin film is inversely correlated with the maximum driving field, as shown in

Figure 4-3. When woken at applied fields greater than the coercive field (E_c) from a major hysteresis loop, the E_c is 2.7 to 3.3 MV cm^{-1} at the end of the wake-up process and for subsequent loops. When woken up at fields slightly below the coercive field (*e.g.* a minor loop), the full switchable P_r is not realized. Thus, wake-up in ZMO is dependent on the ratio of the maximum applied field to the E_c.

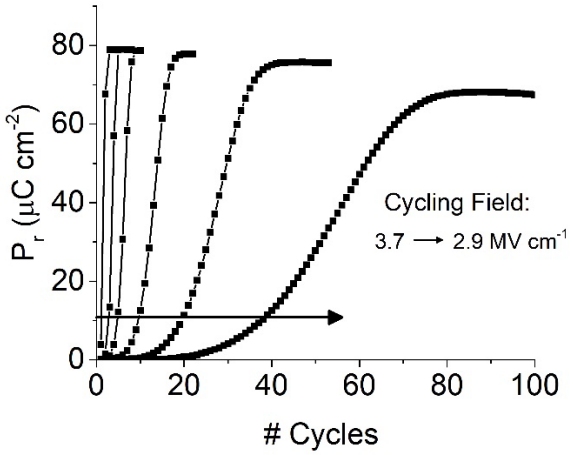

Figure **4-3**: Remanent polarization vs. number of field cycles for a ZMO thin film showing the wake-up process for different maximum applied electric fields. The cycling fields from left to right are 3.7, 3.5, 3.3, 3.1, 3.0, and 2.9 MV cm^{-1}. The full switchable polarization is not realized after wake-up at 2.9 MV cm^{-1}, which is slightly below the major loop coercive field. All loops were acquired at 100 Hz. While not shown, it is also noted that the number of field excursions required for wake-up increases with frequency.

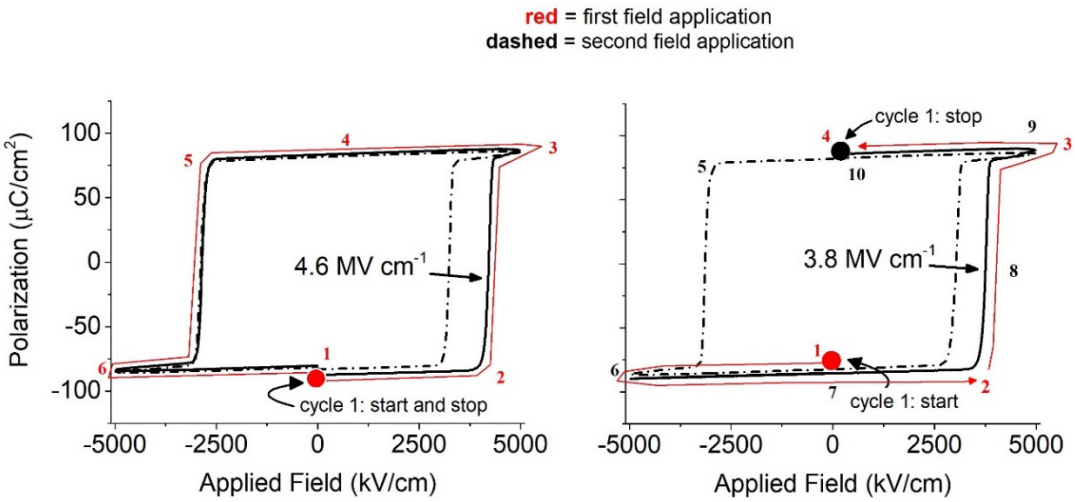

Figure **4-4**: ZMO on Pt/Al_2O_3 can be fully woken in a single P–E loop when driven at 5 MV cm^{-1}. Part (a) shows wake-up while driving first with a positive voltage on the bottom electrode, with the top electrode as the ground. Part (b) used a reversed P-E loop beginning with a negative bias on the bottom electrode. There is a lower wake-field in this case.

In addition to the electric field magnitude and time dependence of wake-up, an asymmetry associated with the direction of the first electric field was observed in single cycle wake-up. Figure 4-4 shows hysteresis behavior for two identical ZMO capacitors that are woken up with a single 5 MV/cm triangle wave and then subjected to a second identical cycle. In both cases the remanent polarization is ± 80 μC cm^{-2}. In Figure 4-4a the first electric field is parallel to the polarization while in Figure 4-4b, the first electric field is anti-parallel to the as-grown polarization. Both capacitors start at the red dot labeled 1 and follow the light red pathways as indicated by the thin red arrows and the numbering sequence, each completing a full bipolar field excursion. Both capacitors are subject to a second identical loop, this time shown as dashed lines, however, the left capacitor (4-4a) is polarization "down" while the right capacitor (4-4b) is polarization "up". There are important differences to note: **i.** for the initial cycle, the positive coercive field is 0.8 MV/cm lower when the first half-cycle field reinforces the initial polarization

state; **ii.** for the second cycle, the positive coercive fields for both capacitors fall to a nearly identical value of ~3.1 MV/cm; and **iii.** the negative coercive fields do not depend strongly on the initial field application direction.

Zhu *et al*. reported a model to explain wake-up in ferroelectric nitrides based on the need to generate a critical population of oppositely oriented nuclei if the original matrix is unipolar before full switching can occur at a given frequency.[20] Since the present ZMO films are unipolar with polarization oriented to the bottom electrode, it is conceivable that built-in asymmetry in the as-deposited structure, composition, or defects can alter the opposite nuclei generation process, particularly for those that can be altered by voltage application. Three possibilities for this asymmetry are considered below.

Due to the directional nature of growth, it is possible that acceptor-like or donor-like trap states exist and are concentrated close to the bottom electrode interface as illustrated in Figure 4-5(a). If this occurs, then carriers can be injected into trap levels during one hysteresis half-cycle, but remain trapped during the other half-cycle. In this case, given sufficient trap density, the dielectric experiences a moving cathode, as the trapped charge layer reduces the net insulator thickness thus lowering the switching voltage and the perceived electric field. Having initially vacant traps that fill during the first half cycle and are slow to empty would explain the present observation.

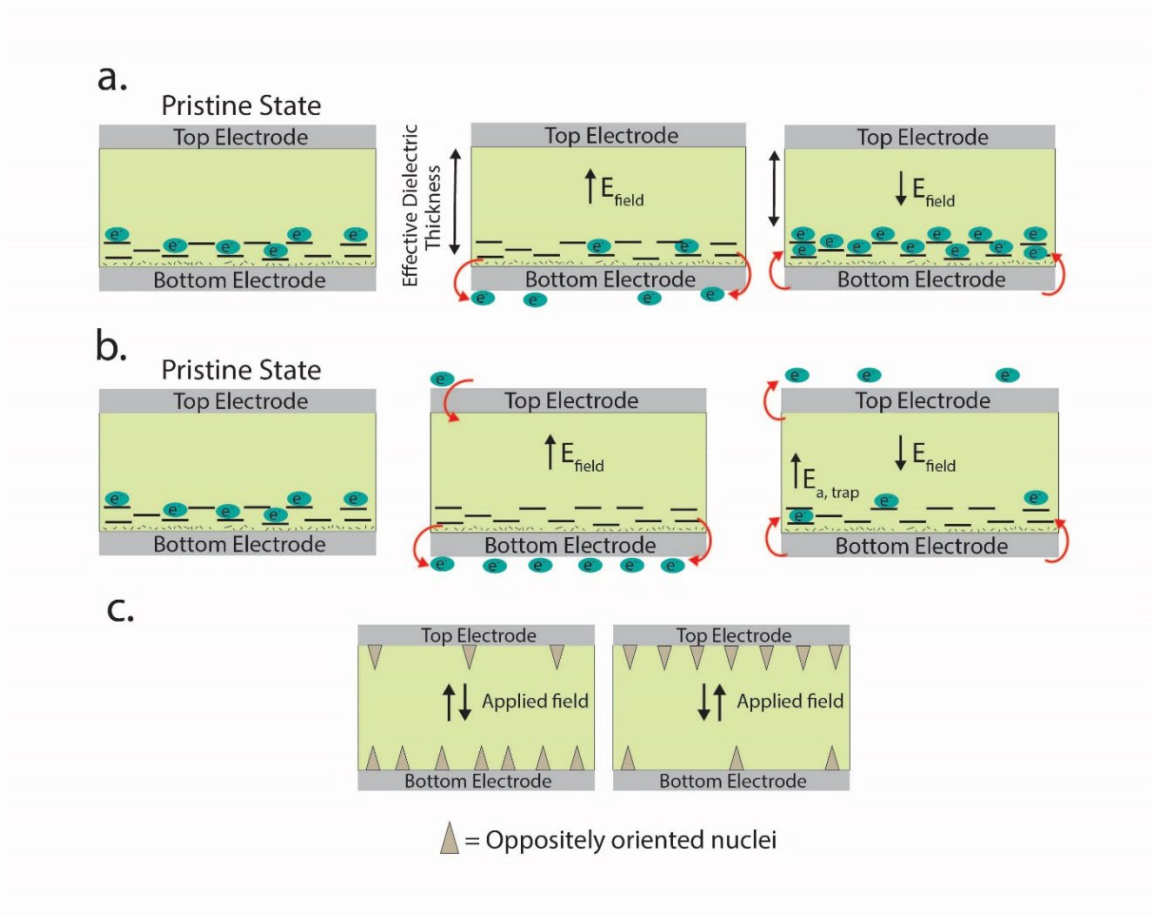

Figure **4-5**: (a) The moving cathode phenomenon where layers of trapped charges extend the effective electrode boundary into the thickness of the ferroelectric. (b) Lower structural quality of the bottom interface introduces locally trapped charges which can be de-trapped during the wake-up process. (c) The directions of the applied field may govern the location of oppositely oriented nuclei in the film. The black arrows indicate the field orientations that would be encountered in a P–E hysteresis loop.

A second possible mechanism can occur due to asymmetric charge injection as illustrated in Figure 4-5b. The TEM cross section in Figure 4-1c shows both the contrast adjacent to the top and bottom electrode interfaces differ, which indicates at minimum, a difference in their relative structural disorder. Asymmetric disorder can then facilitate preferential carrier trapping and

detrapping presumably at the bottom interface which appears more defective. This could in turn change the internal electric field, the imprint state, and the field necessary for nucleating oppositely oriented nuclei. If the bottom interface indeed contains more charge traps that interfere with domain nucleation, and if those traps fill after the initial field cycle, this could explain the initially higher coercive field and the more symmetric behavior on subsequent sweeps.

A third possibility is that the order in which the electric field is applied alters the location of the first oppositely oriented nuclei, as depicted in Figure 4-5c. That is, it is possible that the field order could change which interface was the one at which oppositely oriented nuclei form. Given that the structural quality of the two interfaces differs, this could also change the barrier for nucleation. This might be possible if the films contain a small number of oppositely oriented nuclei as grown. When the film is first excited parallel to the predominant built-in polarization direction, this could eliminate whatever fraction of opposite nuclei are present. Then, on sweeping in the opposite direction, the coercive field is larger, as nuclei first need to be generated.[21] In contrast, when the first sweep is in the opposite direction, there are additional naturally occurring nuclei, and the coercive voltage is slightly lower.

4.3.4 Fluid Imprint

Imprint is manifested as a lateral shift of the P-E hysteresis loop along the field axis. It can be due to the migration of defects to the interfaces, or the population of deep traps, which can create deep trap states that produce an internal field in the film,[23] this is a known possibility in films which experience Poole-Frenkel conduction. Buragohain et al. reported that the internal fields associated with charge injection can be altered on a comparatively short time scale in La-

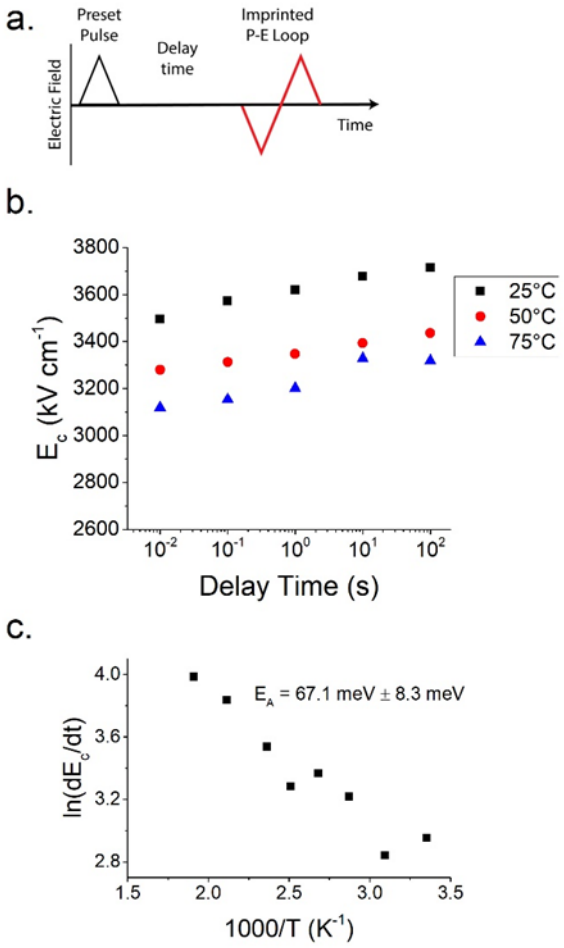

Figure **4-6**: (a) Field excitation conditions for observing fluid imprint for ZMO films on Pt/Al_2O_3 substrates. The cycling was driven from the bottom electrode. The first switch after a pulse is affected; the time delay for fluid imprint resets after each switch. (b) The positive coercive field has a logarithmic relationship with the delay time after a pulse. P-E loops were measured at 1 kHz, because the fluid imprint becomes more apparent at higher switching frequencies. (c.) The slopes in plot (b) are thermally activated with a pseudo-activation energy of 67 ± 8 meV for the fluid imprint.

doped HfO_2 films, inducing a fluid imprint.[22] Accordingly, the possibility of fluid imprint of the coercive field was assessed in ZMO thin films, as shown in Figure 4-6. Fluid imprint is characterized by the shift of the coercive field due to the switching prehistory, without any electric field being applied to the sample, which in the literature is reported to be due to charge injection and trapping at the electrode interfaces.[22]

Fluid imprint imparts a rapid change of the coercive field with time delay after a previous ferroelectric polarization switch. This effect can be observed by manipulating the delay time between a preset P-E hysteresis loop and the measured P-E hysteresis loop, as shown in Figure 4-6. Delay times were varied from 10 ms to 100 s to assess the rapidly progressing imprint in ZMO films. This process is thermally activated;[23] a pseudo-activation energy of 67 ± 8 meV was determined. This pseudo-activation energy differs from that of the coercive field temperature dependence, suggesting that the mechanisms are distinct.

4.3.5 Conduction Mechanism

To probe the nature of the Pt/ZMO interfaces and the state of traps in ZMO, the electrical conduction mechanisms were analyzed by measuring the leakage current density, J, as a function of applied electric field. J-E plots were generated for temperatures ranging from room temperature to 200°C to determine an activation energy for conduction. Leakage curves were virtually polarity independent. Conduction was Poole-Frenkel limited (Equation 1) with compensation[24,25] at temperatures above 100°C and was by a hopping mechanism from a shallower trap at room temperature. Since it is observed that the electrode interfaces are asymmetric, the predominance of Poole-Frenkel conduction and symmetric leakage behavior, suggests that the conduction is limited by the bulk of the film, rather than the interfaces (c.f. Figure 4-S5).

$$J_{PF} = cE \exp\left(-\frac{E_i}{2k_BT}\right) \exp\left[\frac{1}{2k_BT}\left(\frac{q^3E}{\pi\varepsilon_i}\right)^{\frac{1}{2}}\right] \quad (1)$$

$$\frac{d\left(\ln\left|\frac{J_{PF}}{E}\right|\right)}{d(\sqrt{E})} = \frac{1}{2k_BT}\sqrt{\frac{q^3}{\pi\varepsilon_0\varepsilon_r}} \quad (2)$$

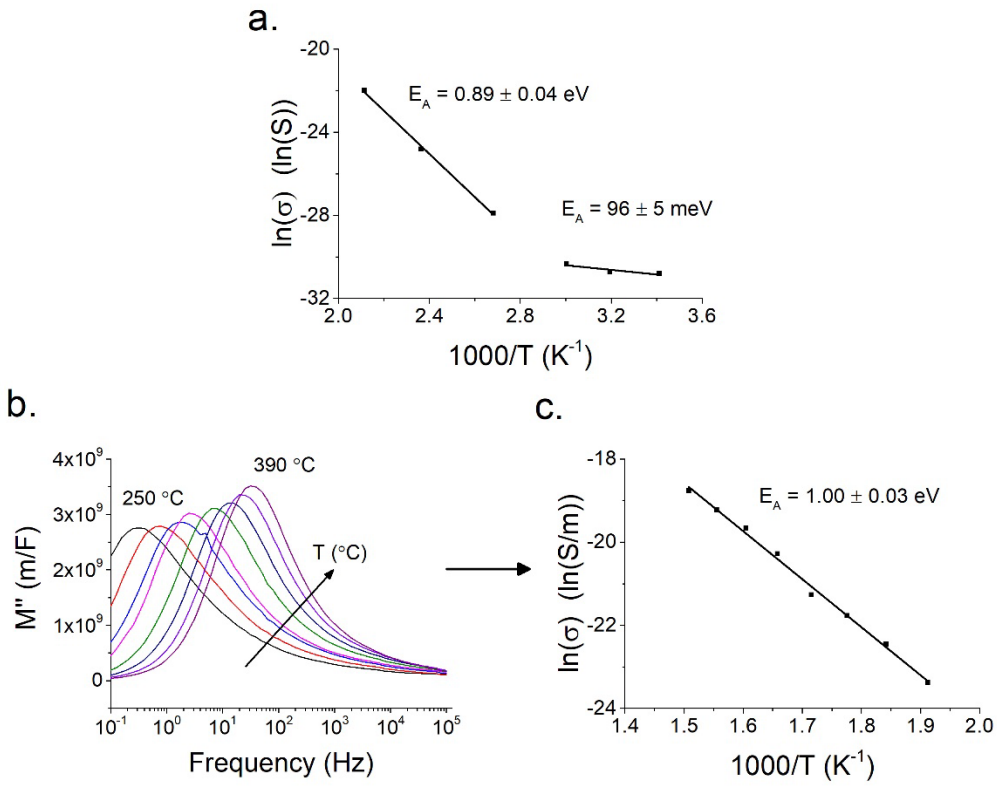

Figure **4-7**: (a) The activation energy for conduction in ZMO films on Pt/Al_2O_3 was measured from temperatures of 20°C to 200°C at an applied field of 1.28 MV cm^{-1}. An activation energy of 0.89 ± 0.04 eV for temperatures above 100°C and 96 ± 5 meV between 60°C and 20°C. (b, c) Modulus spectroscopy was performed to confirm that the activation energy for conduction corresponds to the bulk of the film, rather than the interfaces.

where J is the respective current density, ε is the permittivity, E is the electric field, and E_i is the hopping conduction barrier. The coefficient of 2 in front of the Boltzmann constants in equations

(1) and (2) is a compensation due to large trap densities in the film, which has been reported for ZnO thin films.[25] The high frequency dielectric constants extracted from Poole-Frenkel modeling are shown in Table 4-1; these values approach those reported for the optical frequency response on similar films above 100°C.[26]

Table **4-1**: Dielectric constants extracted from the compensated Poole-Frenkel model for conduction. The unphysical values for the relative permittivity below 100°C are consistent with a change in conduction mechanism.

Temperature (°C)	Relative permittivity
20	10.8 ± 0.0
60	10.5 ± 0.57
80	15.8 ± 0.4
100	5.14 ± 0.60
150	4.23 ± 0.03
200	4.45 ± 0.05

The activation energy for compensated Poole-Frenkel emission was extracted using data at a constant applied field of 1.28 MV cm^{-1}. Two distinct activation energies for conduction were observed from 100 to 200°C, and from 20 to 60°C, as shown in Figure 4-7a. The former was 0.89 ± 0.04 eV, which is in agreement with the literature for Mg-substituted ZnO-based films.[32] Kılınç et al. reported that 90% ZnO – 10% Mg has a trap level with an activation energy of 0.86 eV (in contrast to pure ZnO, for which the trap level is 0.39 eV).[32]

In contrast, the activation energy for conduction at room temperature is calculated to be 0.096 ± 0.005 eV, which suggests an electron hopping mechanism between shallow trap states.[27, 28] Ju et al. reported activation energies between 60 and 160 meV for Mg-doped ZnO nanorods between 180 K and 300 K.[28] It is noted that in general, the activation energies are higher for Mg substituted ZnO (0.1 ~ 1 eV)[28,32,33] than for pure ZnO (0.03 ~ 0.4 eV),[29] corresponding to deeper

trap levels[29, 30, 31, 32]. This is due to Mg-substitution raising the energy of the band edge, making shallow trap states deeper.[33, 34]

To confirm whether or not the conduction corresponded to a bulk mechanism in the films, modulus spectroscopy measurements were conducted.[35] In these columnar films, the impedance data at low frequencies are expected to correspond to the grain conductivity, since there are no grain boundaries parallel to the electrodes. As shown in Figures 4-7b and 4-7c, the modulus data show a comparable activation energy of 1 ± 0.03 eV from 250 – 390°C.

P-E loops were performed on samples after subjecting them to large DC fields during the J-E measurements. The capacitors were heavily imprinted in the direction which the field was applied for the first subsequent P-E loop after the J-E experiment, and the imprint diminished steadily with continued cycling (see the Supplementary Materials section). This observation supports the development of electron trapping and detrapping interactions which occur simultaneously with ferroelectric switching. The presence of deeper traps in Mg-doped ZnO was confirmed by the activation energies for conduction presented earlier.

As is true of most ferroelectrics,[9, 36] the coercive field of ZMO is a function of frequency, as shown in Figure 4-8. It is clear that the maximum switching current density shifts to higher fields as the cycling frequency increases. When measured using stepped DC voltages, where each 1 V increase was held for 60 s prior to current measurement, the minimum field for switching observed is 1.5 MV cm^{-1} at 200°C, and coercive field remains below 2 MV cm^{-1} at room temperature. In Figure 4-8 it is also evident that there is a strong anisotropy in the coercive field such that $|+E_c| > |-E_c|$. This behavior is due to fluid imprint since the preswitching conditions of the films were in the poled-down state, or the negative polarity.

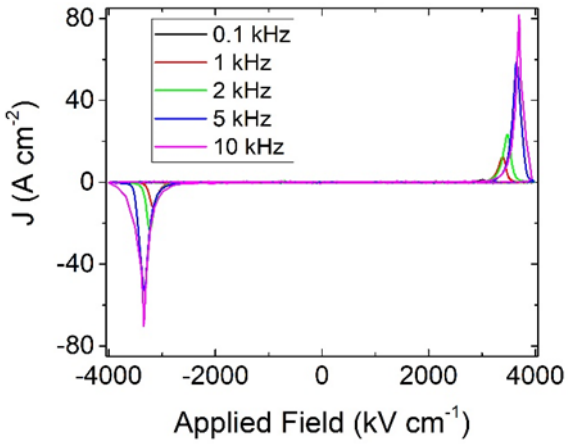

Figure **4-8**: Current density vs. applied field plots for ZMO at room temperature.

4.3.6 Reliability

Imprint in ZMO is a concern for memory applications because if the coercive field changes to a magnitude beyond the write voltage in a device, that device will fail[23]. To assess the importance of this factor, the same-state and opposite-state retention properties of ZMO were measured, as shown in Figure 4-9. The waveforms used may be found in the Supplementary Materials section of this chapter. A pulse of 4 MV cm^{-1} was used for the preset and switching operations, as these were not affected by fluid imprint over the chosen time and temperature ranges. For these measurement conditions, ZMO retained virtually all of the polarization margin for both the same and opposite retention states, even for bake temperatures up to 200°C. This performance is similar to that reported for (Al,Sc)N and (Al,B)N capacitors[13,14] and outperforms PZT capacitors,[6] making ZMO a strong candidate for high temperature memory applications.

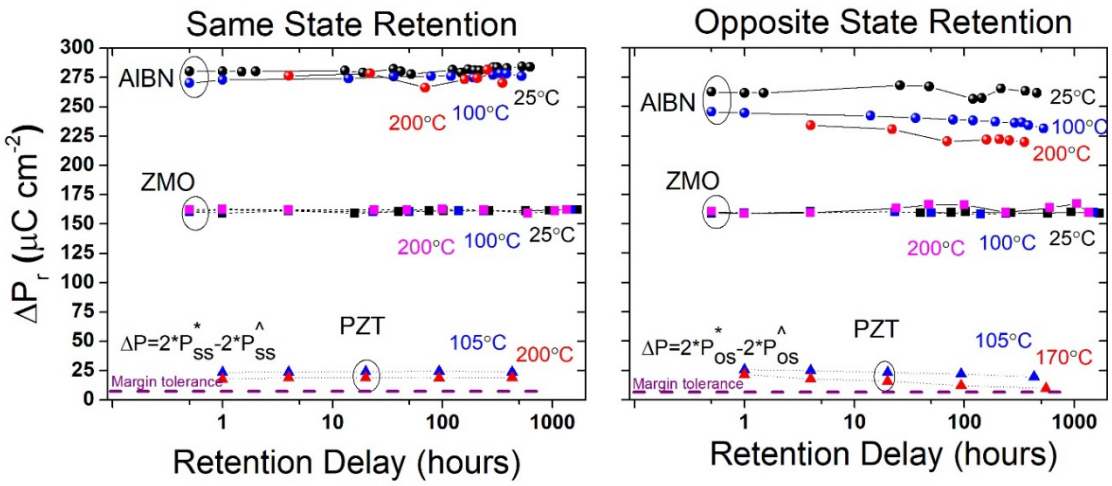

Figure **4-9**: Retention characteristics of ZMO films compared to doped AlN[14] films and commercial PZT capacitors.[6]

When measured using 100 Hz triangular waveforms, the cycling endurance in in this first generation of ZMO thin films with electrodes patterned as described above is on the order of 10^3 cycles, as shown in Figure 4-10. Cycling endurance is strongly dependent on the cycling field, where the number of loops required for breakdown is inversely proportional to the ratio of the driving field to the breakdown field of the ZMO. The film with applied field of 3.1 MV cm^{-1} showed a significant decrease in the remanent polarization with continued cycling which was associated with an increase in the coercive field with the number of cycles, shown in Figure 4-10a. The film fell asleep, i.e. the polarization decreased due to cycling near or below the coercive field, before it finally broke down. In this case, if a greater cycling field is applied to the film before it breaks down, it will re-wake up to its full P_r value. The coercive field is also observed to increase after "re-wake up", as shown in Figure 4-10b.

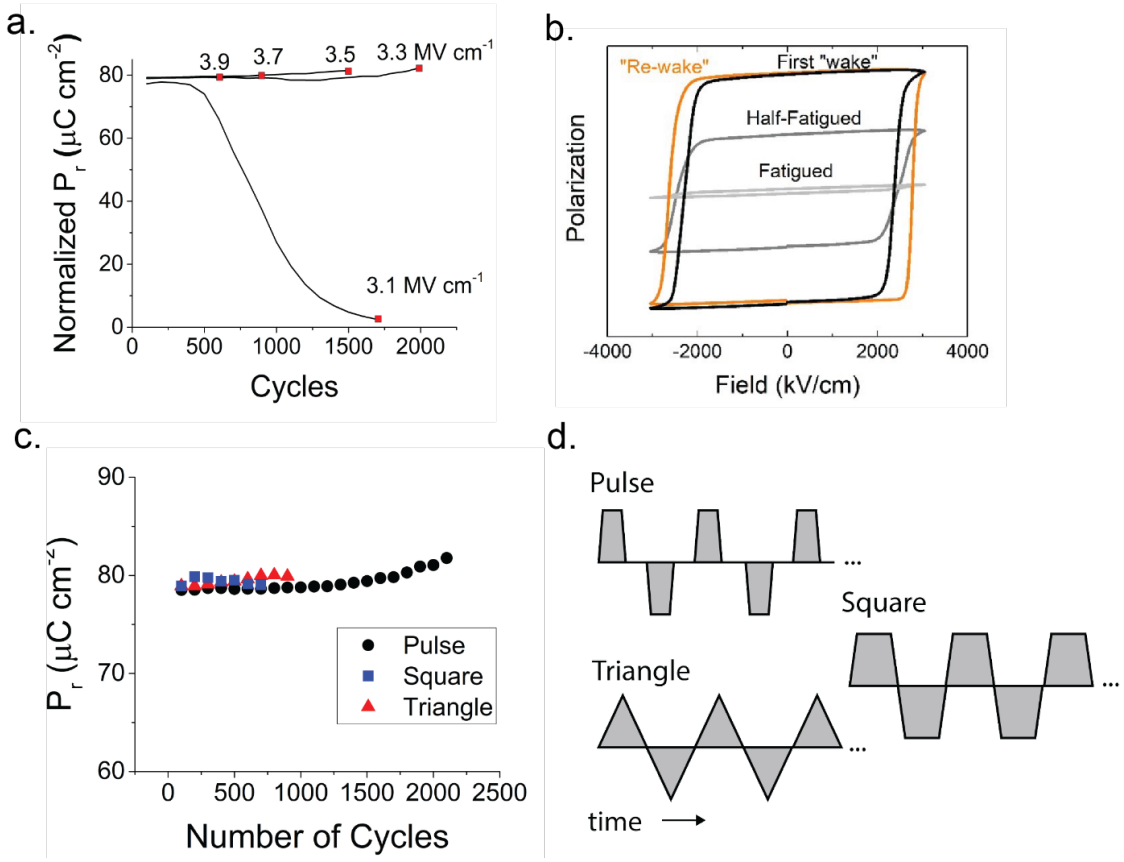

Figure **4-10**: (a) Cycling endurance with an applied triangular wave at various cycling fields indicated on the plot. (b) Films which fall asleep due to cycling at low field can be re-woken at a higher cycling field. (c) 300 nm thick ZMO capacitors on a platinum-coated Si substrate were subjected to fatigue at various waveforms, shown in (d). The maximum field was 4.5 MV cm^{-1} and the frequency was 100 Hz for each waveform. Pulses of 50 μs duration were used for the pulse waveform.

Using a pulse waveform instead of a triangular waveform improves the cycling endurance before breakdown. 50 μs pulses at 4.5 MV cm^{-1} field, and 100 Hz frequency were used to pulse the films. Data was collected on ZMO samples with Al_2O_3 and Si substrates. Breakdown occurs fastest for square wave pulses where there is no time between pulses for the sample to rest

between maximum field excursions. Further, more detailed, investigation into the fatigue properties is warranted.

4.4 Conclusions

The wake-up and retention performance of ferroelectric wurtzite structure ZMO films is reported. Strong field dependence of the wake-up is observed, where higher fields require fewer cycles for the film to fully awaken. High quality ZMO films with breakdown strengths in excess of 5 MV cm^{-1} can be fully woken in a single P-E loop. Fluid imprint was found to affect the coercive field and wake-up of aged samples. A strong imprint effect on the coercive field was also observed after DC I-V experiments at high temperatures. Ferroelectric switching is kinetically limited, whereby slower switching frequencies yield a lower coercive field for polarization reversal. Strong temperature dependence of the coercive field is observed, with a pseudo-activation energy of 23.2 ± 0.3 meV at room temperature and of 40.6 ± 0.6 meV between 120 and 240°C. Over this same temperature range, there was also a transition in the activation energy for electrical conduction. The minimum observed coercive field was 1.5 MV cm^{-1} at temperatures above 240°C. The same-state and opposite-state polarization retention was excellent, showing no reduction in the polarization margin, even for bakes at temperatures up to 200°C, making ZMO an interesting candidate for high temperature memory applications.

4.5 Supplementary Materials

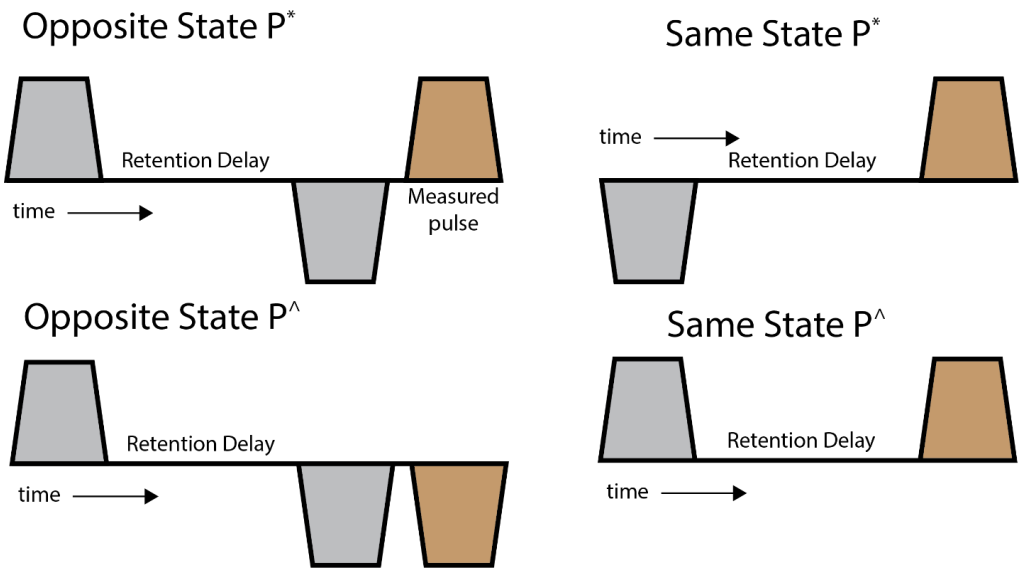

Figure **4-S1**: The waveforms for Same State (SS) and Opposite State (OS) retention measurements.

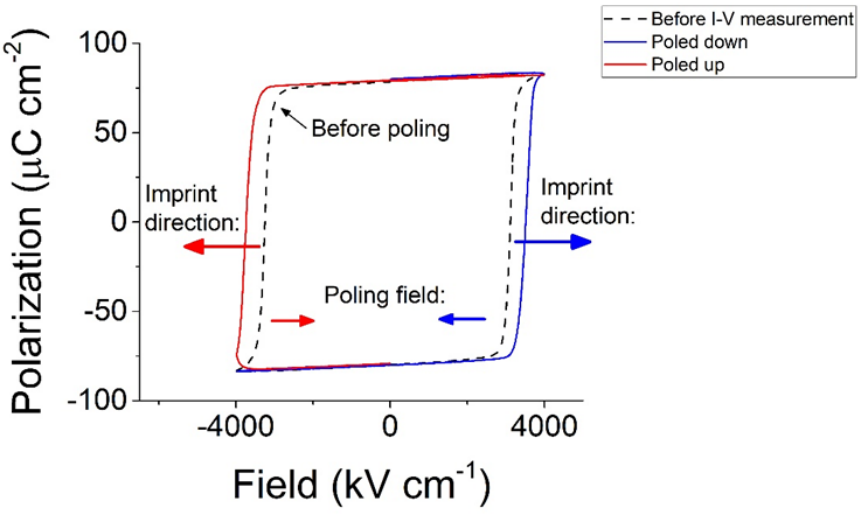

Figure **4-S2**: Imprint in ZMO after poling at fields up to 2 MV/cm in DC J-E measurements. The poling fields and respective imprint directions are labelled.

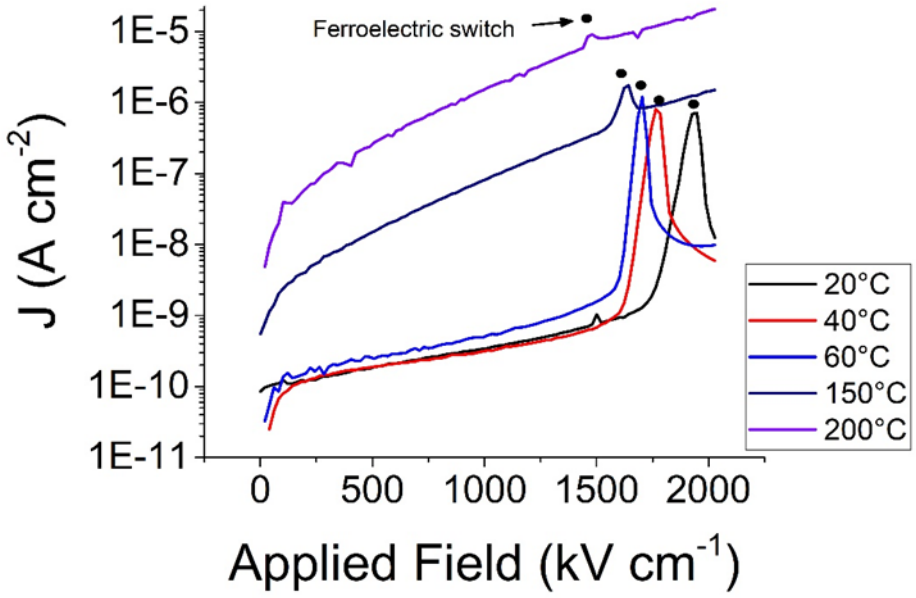

Figure **4-S3**: Ferroelectric switching under stepped DC applied fields during a J-E measurement. Ferroelectric switches are indicated by the black circles. Voltage steps of 1 V with a 60 second settling time were used for each measurement.

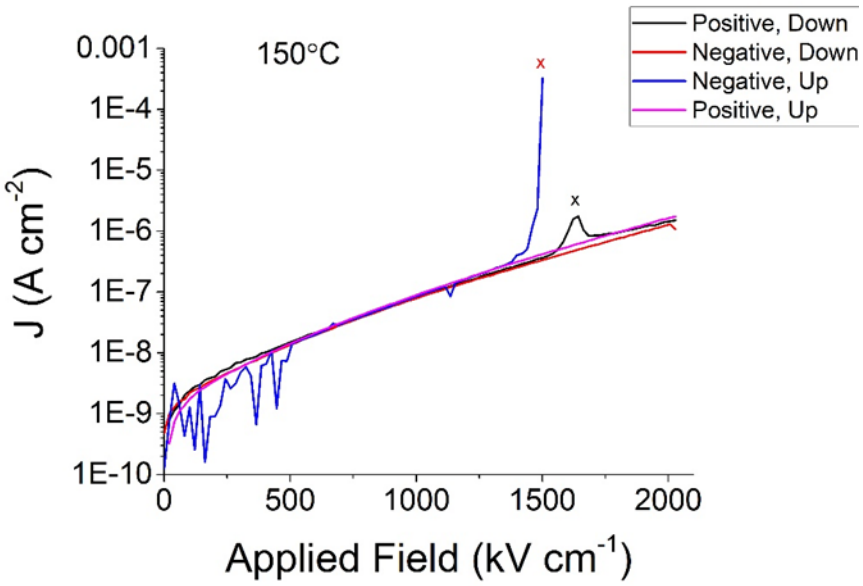

Figure **4-S4**: There is no polarity dependence of the leakage current density in DC measurements following the same method as for Figure 4-S3. The sample was heated to 150°C. The black x is a ferroelectric switch. The red "x" is a breakdown event. The breakdown event is not representative of all subjects tested at the same conditions. In the legend, "positive" and "negative" indicate the state of the polarity of the film at the beginning of the measurement. "Up" and "down" indicate the direction of the electric field that is applied to the sample during the J-V measurement.

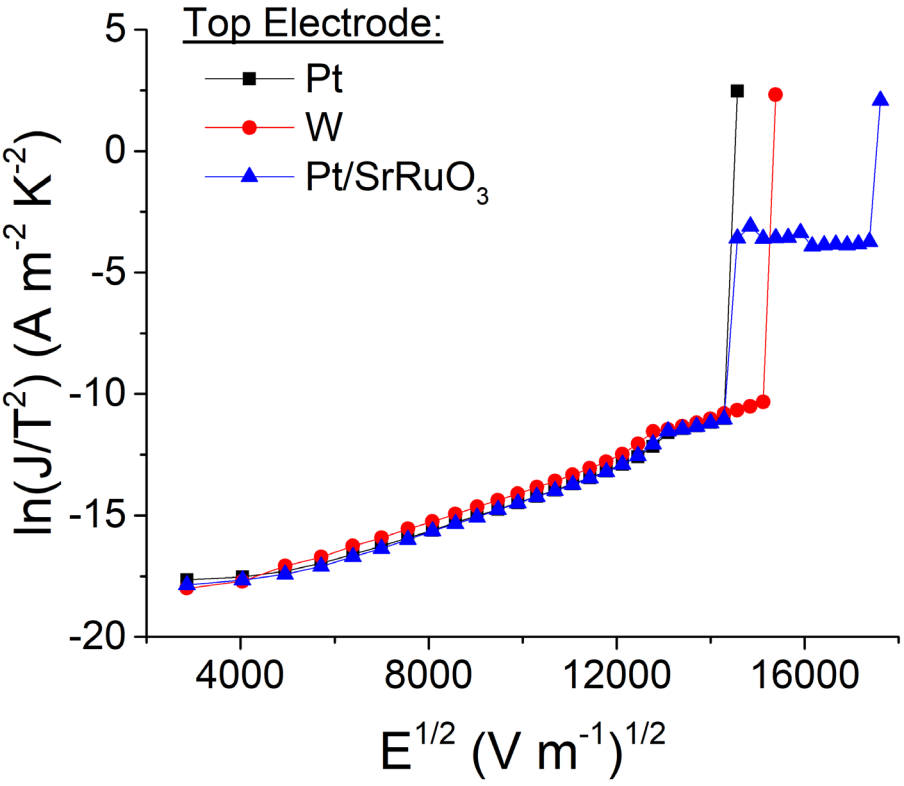

Figure **4-S5**: J-V measurements were performed with electron injection from Pt, W, and Pt/$SrRuO_3$ top electrodes. Tests for linearity in $\ln(J/T^2)$ vs. $E^{1/2}$ show that Poole Frenkel conduction applies. The respective work functions of Pt, W and $SrRuO_3$ are 5.65[37], 4.6[38], and 5.2[39] eV, and Schottky barrier heights ($\Phi_B = \Phi_M - \Phi_{ZMO}$) are 1.15, 0.1, and 0.7 eV. There are negligible differences between the leakage current values although the Φ_B differ greatly between the top electrodes, showing that conduction is not contact mediated, and therefore not Schottky limited.

References

[1] Andrae, A. S., & Edler, T. (2015). On global electricity usage of communication technology: trends to 2030. Challenges, 6(1), 117-157.

[2] Desroches, L. B., Fuchs, H., Greenblatt, J., Pratt, S., Willem, H., Claybaugh, E., Beraki, B, Nagaraju, M., Price, S., & Young, S. (2015). Computer usage and national energy consumption: Results from a field-metering study.

[3] Ramanathan, A. (2022). *Stacked-3D and Processing-in-memory Solutions for Data-intensive and Persistent Applications* (Doctoral Dissertation, The Pennsylvania State University).

[4] Liu, J., Zhao, H., Ogleari, M. A., Li, D., & Zhao, J. (2018, October). Processing-in-memory for energy-efficient neural network training: A heterogeneous approach. In *2018 51st Annual IEEE/ACM International Symposium on Microarchitecture (MICRO)* (pp. 655-668). IEEE.

[5] McLellan, P. (2022, April 27). *Linley: AI moving to the edge*. Breakfast Bytes - Cadence Blogs. Cadence. https://community.cadence.com/cadence_blogs_8/b/breakfast-bytes/posts/linleyspr22

[6] Rodriguez, J. A., Remack, K., Boku, K., Udayakumar, K. R., Aggarwal, S., Summerfelt, S. R., Celii, F. G., Martin, S., Hall, L., Taylor, K., Moise, T., McAdams, H., McPherson, J., Bailey, R., Fox, G., & Depner, M. (2004). Reliability properties of low-voltage ferroelectric capacitors and memory arrays. *IEEE Transactions on Device and Materials Reliability*, *4*(3), 436-449.

[7] Song, T., Bachelet, R., Saint-Girons, G., Solanas, R., Fina, I., & Sánchez, F. (2020). Epitaxial ferroelectric La-doped $Hf_{0.5}Zr_{0.5}O_2$ thin films. *ACS Applied Electronic Materials*, *2*(10), 3221-3232.

[8] Tan, A. J., Liao, Y. H., Wang, L. C., Shanker, N., Bae, J. H., Hu, C., & Salahuddin, S. (2021). Ferroelectric HfO_2 memory transistors with high-κ interfacial layer and write endurance exceeding 10^{10} cycles. *IEEE Electron Device Letters*, *42*(7), 994-997.

[9] Park, M. H., Lee, Y. H., Mikolajick, T., Schroeder, U., & Hwang, C. S. (2018). Review and perspective on ferroelectric HfO_2-based thin films for memory applications. *MRS Communications*, *8*(3), 795-808.

[10] Yu, Z., Saini, B., Liu, Y., Huang, F., Mehta, A., Baniecki, J. D., Philip Wong, H.-S., Tsai, W., & McIntyre, P. C. (2022). Nanocrystallite seeding of metastable ferroelectric phase formation in atomic layer-deposited Hafnia–Zirconia alloys. *ACS Applied Materials & Interfaces*, *14*(47), 53057-53064.

[11] Mohan, J., Jung, Y. C., Hernandez-Arriaga, H., Kim, J. H., Onaya, T., Sahota, A., Hwang, S. M., Le, D., Kim, J., & Kim, S. J. (2022). Relaxation induced by imprint phenomena in low-temperature (400° C) processed $Hf_{0.5}Zr_{0.5}O_2$-based metal-ferroelectric-metal capacitors. *ACS Applied Electronic Materials*, *4*(4), 1405-1414.

[12] Deng, S., Zhao, Z., Kim, Y. S., Duenkel, S., MacMahon, D., Tiwari, R., Chowdhury, N., Beyer, S., Gong, X., Kurinec, S., & Ni, K. (2022). Unraveling the dynamics of charge trapping and de-trapping in ferroelectric FETs. *IEEE Transactions on Electron Devices*, *69*(3), 1503-1511.

[13] Fichtner, S., Wolff, N., Lofink, F., Kienle, L., & Wagner, B. (2019). AlScN: A III-V semiconductor based ferroelectric. *Journal of Applied Physics*, *125*(11), 114103.

[14] Zhu, W., He, F., Hayden, J., Yang, J. I., Tipsawat, P., Maria, J-P., & Trolier-McKinstry, S. (2023). Exceptional high temperature retention in $Al_{0.93}B_{0.07}N$ films. *Applied Physics Letters*, *122*(24), 242902.

[15] Hayden, J., Hossain, M. D., Xiong, Y., Ferri, K., Zhu, W., Imperatore, M. V., Giebink, N., Trolier-McKinstry, S., Dabo, I., & Maria, J-P. (2021). Ferroelectricity in boron-substituted aluminum nitride thin films. *Physical Review Materials*, *5*(4), 044412.

[16] Zhu, W., Hayden, J., He, F., Yang, J. I., Tipsawat, P., Hossain, M. D., Maria, J-P., & Trolier-McKinstry, S. (2021). Strongly temperature dependent ferroelectric switching in AlN, $Al_{1-x}Sc_xN$, and $Al_{1-x}B_xN$ thin films. *Applied Physics Letters*, *119*(6).

[17] Ferri, K., Bachu, S., Zhu, W., Imperatore, M., Hayden, J., Alem, N., Giebink, N., Trolier-McKinstry, S., & Maria, J-P. (2021). Ferroelectrics everywhere: Ferroelectricity in magnesium substituted zinc oxide thin films. *Journal of Applied Physics*, *130*(4), 044101.

[18] Gupta, A. (2021). *Zinc Oxide Thin Film Transistor (ZnO TFT)- Lipid Membrane Based Electronic Biosensor* (Doctoral Dissertation, The Pennsylvania State University).

[19] de Castro Monsores, K. G., da Silva, A. O., Oliveira, S. D. S. A., Rodrigues, J. G. P., & Weber, R. P. (2019). Influence of ultraviolet radiation on polymethylmethacrylate (PMMA). *Journal of Materials Research and Technology*, *8*(5), 3713-3718.

[20] Zhu, W., He, F., Hayden, J., Fan, Z., Yang, J. I., Maria, J-P., & Trolier-McKinstry, S. (2022). Wake-up in $Al_{1-x}B_xN$ ferroelectric films. *Advanced Electronic Materials*, *8*(6), 2100931.

[21] Kolosov, O., Gruverman, A., Hatano, J., Takahashi, K., & Tokumoto, H. (1995). Nanoscale visualization and control of ferroelectric domains by atomic force microscopy. *Physical Review Letters*, *74*(21), 4309.

[22] Buragohain, P., Erickson, A., Kariuki, P., Mittmann, T., Richter, C., Lomenzo, P. D., Lu, H., Schenk, T., Mikolajick, T., Schroeder, U., & Gruverman, A. (2019). Fluid imprint and inertial switching in ferroelectric La:HfO_2 capacitors. *ACS Applied Materials & Interfaces*, *11*(38), 35115-35121.

[23] Warren, W. L., Dimos, D., Pike, G. E., Tuttle, B. A., Raymond, M. V., Ramesh, R., & Evans Jr, J. T. (1995). Voltage shifts and imprint in ferroelectric capacitors. *Applied Physics Letters*, *67*(6), 866-868.

[24] Yeargan, J. R., & Taylor, H. L. (1968). The Poole-Frenkel effect with compensation present. *Journal of Applied Physics*, *39*(12), 5600-5604.

[25] Chang, W. Y., Lai, Y. C., Wu, T. B., Wang, S. F., Chen, F., & Tsai, M. J. (2008). Unipolar resistive switching characteristics of ZnO thin films for nonvolatile memory applications. *Applied Physics Letters*, *92*(2), 022110.

[26] Zu, R., Ryu, G., Kelley, K. P., Baksa, S. M., Jacques, L. C., Wang, B., Ferri, K., He, J., Chen, L.-Q., Dabo, I., Trolier-McKinstry, S., Maria, J-P., & Gopalan, V. (2023). Large enhancements in optical and piezoelectric properties in ferroelectric $Zn_{1-x}Mg_xO$ thin films through engineering electronic and ionic anharmonicities. *Advanced Physics Research*, *2*(12), 2300003.

[27] Lin, T. T., Young, S. L., Kung, C. Y., Chen, H. Z., Kao, M. C., Chang, M. C., & Ou, C. R. (2013). Variable-range hopping and thermal activation conduction of Y-doped ZnO nanocrystalline films. *IEEE Transactions on Nanotechnology*, *13*(3), 425-430.

[28] Ju, S., Li, J., Pimparkar, N., Alam, M. A., Chang, R. P. H., & Janes, D. B. (2007). N-type field-effect transistors using multiple Mg-doped ZnO nanorods. *IEEE Transactions on nanotechnology*, *6*(3), 390-395.

[29] Lien, C. C., Wu, C. Y., Li, Z. Q., & Lin, J. J. (2011). Electrical conduction processes in ZnO in a wide temperature range 20–500 K. *Journal of Applied Physics*, *110*(6), 063706.

[30] Look, D. C. (2001). Recent advances in ZnO materials and devices. *Materials Science and Engineering: B*, *80*(1-3), 383-387.

[31] Schifano, R., Monakhov, E. V., Svensson, B. G., Mtangi, W., van Rensburg, P. J., & Auret, F. D. (2009). Shallow levels in virgin hydrothermally grown n-type ZnO studied by thermal admittance spectroscopy. *Physica B: Condensed Matter*, *404*(22), 4344-4348.

[32]Kılınç, N., Arda, L., Öztürk, S., & Öztürk, Z. Z. (2010). Structure and electrical properties of Mg-doped ZnO nanoparticles. *Crystal Research and Technology*, *45*(5), 529-538.

[33] Zhang, L. Q., Ye, Z. Z., Huang, J. Y., Lu, B., He, H. P., Lu, J. G., Zhang, Y. Z., Jiang, J., Zhang, J., Wu, K. W., & Zhang, W. G. (2011). Fabrication and properties of p-type K doped $Zn_{1-x}Mg_xO$ thin film. *Journal of Alloys and Compounds*, *509*(27), 7405-7409.

[34] Murkute, P., Ghadi, H., Sushama, S., & Chakrabarti, S. (2021). Realization of high-quality RF sputtered ZnMgO (x= 15%) thin films by post-growth annealing treatment. *Superlattices and Microstructures*, *156*, 106977.

[35] Coşkun, M., Polat, Ö., Coşkun, F. M., Durmuş, Z., Çağlar, M., & Türüt, A. (2018). The electrical modulus and other dielectric properties by the impedance spectroscopy of $LaCrO_3$ and $LaCr_{0.90}Ir_{0.10}O_3$ perovskites. *RSC Advances*, *8*(9), 4634-4648.

[36] Viehland, D., & Chen, Y. H. (2000). Random-field model for ferroelectric domain dynamics and polarization reversal. *Journal of Applied Physics*, *88*(11), 6696-6707.

[37] Ofuonye, B., Lee, J., Yan, M., Sun, C., Zuo, J. M. & Adesida, I. (2014). Electrical and microstructural properties of thermally annealed Ni/Au and Ni/Pt/Au Schottky contacts on AlGaN/GaN heterostructures. *Semiconductor science and technology*, *29*(9), 095005.

[38] Jacobs, R., Morgan, D. & Booske, J. (2017). Work function and surface stability of tungsten-based thermionic electron emission cathodes. *APL Materials*, *5*(11).

[39] Wang, J., Nguyen, M. D., Gauquelin, N., Verbeeck, J., Do, M. T., Koster, G., Rijnders, G. & Houwman, E. (2020). On the importance of the work function and electron carrier

density of oxide electrodes for the functional properties of ferroelectric capacitors. *Physica Status Solidi (RRL)–Rapid Research Letters*, *14*(3), 1900520.

Chapter 5

Switching Kinetics n Ferroelectric Zinc Magnesium Oxide Thin Films

This chapter is reproduced from Jacques, L., Behrendt, D., Ozdemir, E., Yousefian, P., Spurling, R. J., Tipsawat, P., Akkopru-Akgun, B., Rappe, A. M., Maria, J-P., Yazawa, K., & Trolier-McKinstry, S. (2025). Switching Kinetics in Ferroelectric Zinc Magnesium Oxide Thin Films. (In submission).

5.1 Introduction

The 2019 report[1] of ferroelectricity in (Al,Sc)N with the wurtzite structure has spawned a flurry of activity in demonstrating ferroelectricity in other wurtzites, including (Al,B)N,[2] (Zn,Mg)O,[3] (Ga,Sc)N,[4,5] (Al,Y)N,[6,7] as well as exploring their functionality as piezoelectric,[8,9] electrooptic,[10,11,12,13] and non-volatile memory devices.[14,15,16] In particular, ferroelectric wurtzite nitrides such as (Al,Sc)N and (Al,B)N show promise for in-compute memory due to their low processing temperatures[3,2] and scalability to thicknesses below 10 nm.[14,17] Ferroelectric wurtzites have large, reversible spontaneous polarizations along the crystallographic *c*-axis, and exceptional retention properties up to 600°C.[17,18] Both same state and opposite state retention are excellent at temperatures up to 200°C for over 1,000 hours.[18] For current generation films, the cycling endurance is on the order of 10^3 to 10^8 cycles,18 likely due to high defect concentrations and large coercive fields (E_c) of 3 to 5 MV cm^{-1}.

In terms of the switching process, the pseudo-activation energies for E_c are 20 – 40 meV, similar to perovskite ferroelectrics, suggesting polarization reversal in wurtzite ferroelectrics occurs by domain nucleation and growth.[17] Both charged and uncharged domain walls have been

directly imaged.[19,20] In some cases, the switching pathways occur through non-polar intermediate phases.[19,21,22]

Traditionally, switching kinetics in ferroelectrics based on nucleation and growth can be modeled by the Kolmogorov-Avrami-Ishibashi (KAI) equation (derived from the JMAK equation) which considers a constant nucleation rate or a Dirac delta function rate and constant growth rate in all directions of growth: [23,24,25,26,27]

$$f(t) = 1 - \exp\left(-\left(\frac{t}{t_0}\right)^n\right) \quad (1)$$

where $f(t)$is the fraction of switched polarization, t is time, t_0 is the characteristic switching time, and n is the rate constant (n_{KAI}). The value of n corresponds to the number of growth dimensions D plus 1 if a constant nucleation rate is included. For a given ferroelectric material, one can gain information about the mechanism and dimensionality of observed growth by fitting an n value for given samples and field strengths.

To go beyond KAI, there are a modest number of reports on kinetic models for nucleation and growth that describe polarization reversal in (Al,B)N and (Al,Sc)N, using a modified Johnson-Mehl-Avrami-Kolmogorov (JMAK) equation, called the Simultaneous Non-linear Nucleation and Growth (SNNG) model:[28,29]

$$f(t) = 1 - exp\left[-2\pi d v^2 N(\infty)\alpha m \int_0^t \tau^{m-1}(t-\tau)^2 \exp(-\alpha t^m)\, d\tau\right] \quad (2)$$

where t is time, d is the film thickness, v is the domain wall velocity, $N(\infty)$ is the saturated nucleation density, τ is the nucleation time, and α and m are fitting parameters for the nucleation curve position and slope, respectively. The SNNG model has been used to fit switching processes where the traditional KAI model cannot reasonably fit the data, usually when the best-fit n_{KAI} is higher than 4. The SNNG model augments the KAI equation for describing ferroelectric switching kinetics by including a changing nucleation rate.[30,23]The SNNG model attributes the excess dimensionality in the transformation rate constant n (from here on denoted n_{KAI}), the

Avrami exponent in the KAI model,[24252627]to a higher order of this time dependent nucleation rate, where $m = n_{KAI} - D$, and D is the dimensionality of the growth rate – which is assumed to be 2 in thin films. This provides an explanation for fits involving $n_{KAI} > 3$ in thin films of (Al,B)N and (Al,Sc)N when fitting experimental data to the original JMAK equation, but it introduces a time dependent nucleation rate that is not fully justified yet in wurtzite ferroelectrics. Note that theoretically, *n* can be as large as 4, but in thin film metal-insulator-metal capacitor structures, only two dimensions of growth (D = 2) can generally be measured. This means that a rate law of $n_{KAI} = 2$ indicates that nucleation obeys a Dirac delta function at the onset of switching, and transformation is dominated by growth. In thin films, $n_{KAI} = 3$, or $m = 1$ for the SNNG model, is measurable when a constant nucleation rate is present throughout switching, assuming 1 dimension for nucleation. Rate laws $n_{KAI} > 3$ imply that switching cannot be completely described by constant nucleation and growth rates for a uniform sample with spherical/cylindrical domains.

The nucleation-limited switching (NLS) model was initially presented by Tagantsev et al.[31] and later modified by Jo et al.[32] to model a system with nuclei that form after a broad distribution of waiting times. They use this model to describe polarization reversal in $PbZr_{0.3}Ti_{0.7}O_3$ with a substantial concentration of defect dipoles which acted as domain pinning sites. The NLS model is described by the following equation:

$$f(t) = \int_{-\infty}^{+\infty} \left[1 - e^{-\left(\frac{t}{t_0}\right)^n}\right] \cdot F(\log t_0) d(\log t_0) \quad (3)$$

where t is the time, t_0 is the characteristic switching time, *n* is the dimensionality of growth (from here on denoted n_{NLS}), and $F(\log t_0)$ is a distribution function of the waiting times.[31,32] Effectively, the NLS model proposes a regime where many small independent domains are guided locally by individual KAI-like kinetics, but each domain is limited by the initial nucleation time in that region which does not lead the domain wall motion propagation beyond the elementary region. Thus, for most ferroelectric thin films, the value of n_{NLS} in the NLS model

is assumed to be 2, for the 2-dimensional growth experienced in each local region[32,33] usually modeled as a Lorentzian distribution: $F(\log t_0)$

$$F(\log t_0) = \frac{A}{\pi} \cdot \frac{w}{(\log t - \log t_1)^2 + w^2} \quad (4)$$

where A is a normalization constant, t is the time, t_1 is the position of the center of the distribution function, and w describes the half-width at half-maximum.[69] In most cases, this growth is approximated to be extremely fast relative to the time to nucleate a domain, so the limiting factor in switching is purely domain nucleation. A key aspect of this model is that the variance for nucleation time in each region depends on the field strength; at low fields there is a high variation in possible nucleation times whereas at high fields more uniform switching of the domains is expected.[69]

Guido et al. applied the nucleation-limited switching (NLS) model to (Al,Sc)N films at low applied fields and the SNNG model at intermediate applied fields.[33] Several additional reports applied the NLS model to (Al,Sc)N and observed a reasonable transition between switching mechanisms with an increase in the applied field from NLS to the KAI model.[34,3527] Separately, the domain structures of (Al,Sc)N films during the switching process were mapped using piezoresponse force microscopy. Nucleation was found to be sparse, indicating the significant role of domain growth in the polarization reversal process. Switching times spanned 5 orders of magnitude, from 10^{-6} to 10^{-1} seconds, by varying the applied field.[35] Notably, Tagantsev et al. indicated that the NLS model pertains to films with relatively few nuclei, compared to scenarios where the KAI model applies.[31]

Multiple reports[33,34,35,36] suggest that in wurtzite films, domains grow more rapidly through the film thickness, relative to sideways motion, and that the relative growth rates differ by several orders of magnitude. This last observation is consistent with the large energy penalty

that would be associated with head-to-head or tail-to-tail domain walls in wurtzite films with low free carrier concentrations.[36]

This growth anisotropy in wurzites was confirmed quantitatively with the molecular dynamics and Monte Carlo models of Behrendt et al., which demonstrated an order of magnitude faster out-of-plane domain wall velocity relative to the in-plane velocity in AlN-based wurtzites[36] (note that wedge-shaped domains, with faster growth along the end of the needle than along its diameter is also reported in perovskites).[37] The model predicts a nonspherical domain growth over the course of the switching process, which leads to deviations from the KAI-predicted kinetics through changes in the effective domain wall velocities observed through differences in real versus expected switched area in agreement which is consistent with Guido et al.,[33] and differing from the SNNG model.[23] Nonlinear growth has also been reported in $LiNbO_3$.[38] Behrendt et al.'s model describes fractal-like growth in wurtzites[35] where the dimensionality of the fractals $D \approx 1.3$ is due to the stability of domain walls and the fact that the growth morphology develops as a result of each column having only three neighboring columns. Fractal-like growth was also observed in the ferroelectric switching of thin $Pb(Zr,Ti)O_3$ films at applied fields near E_c, which produced in-plane domain wall velocities which vary by up to two orders of magnitude due to interaction of domain walls with microstructural/defect features, such as grain boundaries.[39] This supports the creation of a kinetic model wherein switching occurs via individual columns of atoms along the polar axis. Furthermore, the fractal nature of the switched domains disobeys the assumptions in the KAI model, which leads to faster polarization switching as the fractal domains form and combine.

Data for the switching speeds and their evolution throughout the switching process are not yet reported for ZMO. Baska et al.[22] and Sepehrinezhad et al. [40] simulated ferroelectric switching in ZMO at various compositions and temperatures. They note ***i.*** the preponderance of out-of-plane domain wall motion in ZMO, ***ii.*** the kinetics-slowing effects of Mg clusters for $x \gtrsim$

0.4, and ***iii.*** the coercive-field dependence of the distribution of Mg atoms in ZMO. These observations for ZMO suggest that the columnar switching and fractal domains found in Behrendt et al. for AlN-based ferroelectrics will also hold for wurtzite ZMO. Preferential out-of-plane domain wall motion suggests that an individual-column switching (ICS) mechanism applies, where individual columns of ZMO switch polarity, with each column either starting a nucleus to begin switching from an electrode interface or a defect, or facilitating growth when added to an

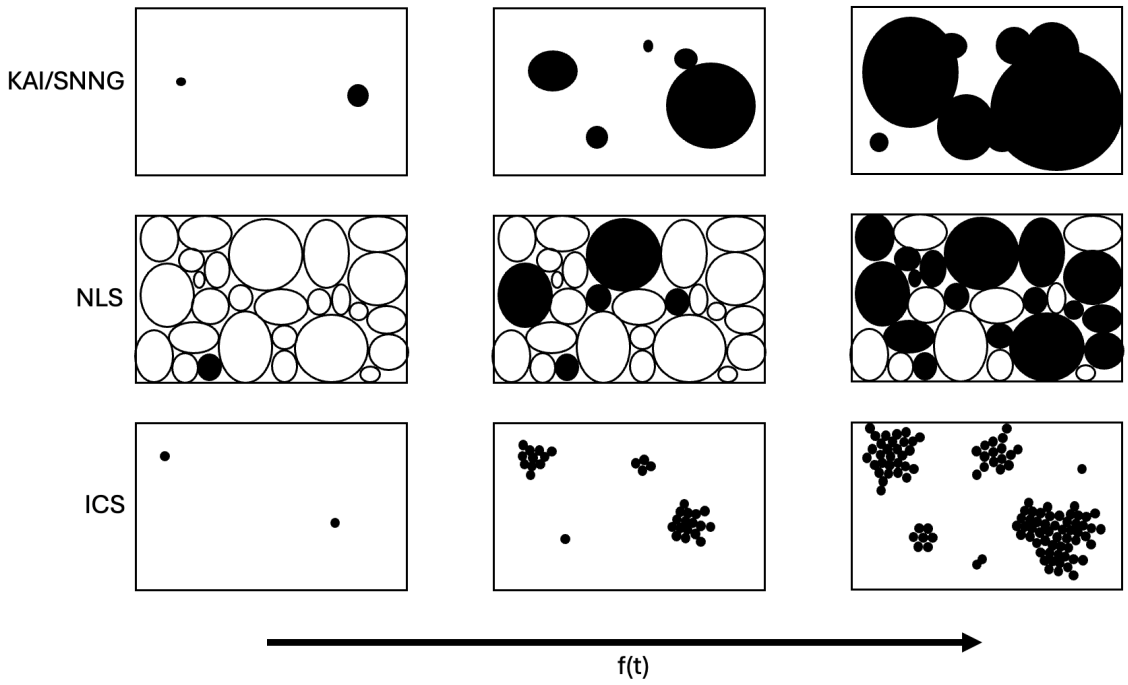

Figure **5-1**: A comparison between KAI/SNNG, NLS and ICS switching modes. Switching is viewed along the polar axis for each case with the black area representing flipped domains that propagate all the way through the sample. For KAI and SNNG models, nuclei appear (linearly or not) and grow with a constant rate until the space is filled. For NLS, domains in elementary regions nucleate and switch at different times. For ICS, individual columns of atoms flip at a varying rate based on the local environment of each column.

existing domain wall. These individual columns of atoms serve to grow domains as shown in Figure 5-1, but here can be modelled individually without the constraints of the KAI assumptions.

The ICS model proposed in this work differs fundamentally from the NLS model proposed by Tagantsev et al. because the NLS model deals with inhomogeneous samples with domains that nucleate at different rates. In this work, nucleation and growth is possible in all regions with all individual columns contributing to polarization change as they switch.

The ICS model proposed in this work differs fundamentally from the NLS model proposed by Tagantsev et al, but maintains one of the four key assumptions ***iii.*** the time to switch a column is the waiting time for the first atoms to begin the process (i.e. vertical domain wall motion though the film thickness must occur first, and the domain is considered switched when the domain wall completes its travel to the interface).[31,] However, as is addressed in this paper, the first and second assumptions ***i.*** the film is an ensemble of elementary regions, and ***ii.*** that there is only one nuclei per elementary region does not apply in ICS switching because all columns of atoms along the polar axis switch individually whether they are a new nuclei or contributing to domain growth. The fourth assumption ***iv.*** that switching times should span several decades, does not apply for ZMO and this is a major reason that the NLS model fails for wurtzite switching. Instead, at applied fields near E_c ($E \lesssim 1.1\ E_c$), ZMO obeys the KAI model, where $n_{KAI} = 2$, similar to other ferroelectrics. At $n_{KAI} = 2$, nucleation is expected to obey a Dirac delta function – meaning all the nuclei are pre-existing, and no nucleation takes place after the onset of switching. NLS is expected to apply when $n_{KAI} < 1$, and when nuclei are sparse such that there is only one nuclei per elementary region.[23,31,35]

When $n_{KAI} > 1$, growth becomes important. Traditionally, domain walls move by single unit cell steps at low applied fields, and by larger steps at larger applied fields.[41] This definition of growth can apply to the KAI and SNNG models ($m \leq 1$). In the ICS model ($n_{KAI} > 3$), individual line switching occurs at the domain wall boundaries. In wurtzites, this individual

column switching accounts for a significantly faster polarization reversal than the radial growth defined in the KAI model. This is depicted in Figure 5-1. At higher applied fields ($E \gtrsim 1.2\ E_c$) switching occurs within a single decade of time, and the switching is no longer captured with the traditional KAI model. This individual line mechanism becomes a greater contributor to polarization reversal on increasing the applied field.

To investigate this, various statistical models were applied to switching transients of ZMO and compared, including the SNNG[23] and NLS[32] models. A cumulative distribution function combining fits using combinations of Gaussian and Inverse Gamma distributions to describe the individual column flipping rate were found to fit switching curves in ZMO. Here, individual column switching which primarily occurs at the sidewalls of switched domains in ZMO at applied fields $\gtrsim 1.2\ E_c$ (to reverse ~80% of the spontaneous polarization) was assessed by comparing distribution functions of nucleation from the SNNG model to Gaussian models fitted to the switching transients. The Gaussian model obeys the central limit theorem, which describes a large number of independent and evenly distributed events – and is phenomenologically consistent with ICS.[42]

Furthermore, this paper presents an analysis of the ICS kinetics in ZMO during wake-up and throughout fatigue using multi-function fitting to show how the switching character changes as a function of both dopant concentration and field cycling. Switching was analyzed in both 41 mol% Mg and 27 mol% Mg ZMO thin films with thicknesses of ~220 nm up to 900 cycles.

5.2 Methods

$Zn_{1-x}Mg_xO$ films were deposited via RF magnetron co-sputtering from Zn and Mg elemental metal targets (Zn: 99.99%, Mg: 99.95%, 2-in. diameter, Kurt J. Lesker) onto as-received, well-oriented 50 nm Pt(111)/ 5 nm $Ti/SiO_2/Si$ substrates (Applied Materials). The target-substrate working distance was maintained at ~4 cm, with guns (MeiVac 2” cathodes)

opposite each other and both inclined at 45° incident angles relative to the substrate. All depositions were conducted at the same total pressure (1 mTorr) during constant flow of 18 sccm Ar and 3 sccm 10% O_3/90% O_2. All depositions were conducted without intentional substrate heating. The relative Mg composition was controlled by changing the power supplied to the Zn and Mg guns with a total combined power constant at 120 W. Additional details can be found in the references.[3]

Crystallinity in as-deposited ZMO films was assessed using a Panalytical Empyrean II X-ray diffractometer (Bragg-Brentano geometry, Cu kα λ = 1.54 Å). *c*-axis oriented wurtzite ZMO was confirmed via X-ray diffraction (XRD) by Bragg-Brentano and Omega (ω) scans with Cu Kα radiation. The microstructure and composition were characterized with a field emission scanning electron microscope (FESEM) (Merlin, Zeiss) with an attached energy dispersive spectroscopy (EDS) detector (Oxford Instruments). A 5 kV accelerating voltage and 216 pA beam current were used for imaging, and 10 kV and 2 nA, respectively, for EDS. ImageJ software was used to determine the lateral grain sizes by counting the number of grains over a known length in an FESEM micrograph and averaging 5 measurements.[43]

Circular IrO_2 top electrodes ranging from 20 to 100 μm diameter and 70 nm thick were patterned via a non-aqueous lithographic patterning process described elsewhere.[18] The surface was gently cleaned with plasma immediately before depositing the top electrode. IrO_2 top electrodes were RF magnetron sputtered in a Kurt J. Lesker CMS-18 from a 3" pure Ir target at a power of 70 W and in an Ar/O_2 flow ratio of 10:1 at a process pressure of 5 mTorr. The target-substrate distance was 4", and the substrate was kept at room temperature.

The switching kinetics apparatus consisted of an Agilent 33220A 20 MHz function generator, a 50x Trek Model 2100HF amplifier (without overshoot), and a Tektronix TBS 2000B Series Oscilloscope with 1 ns precision. Further details are provided elsewhere.[44] A Python script was used to apply a custom PUND waveform sequence with a 12.5 μs pulse width/delay to the

function generator. Data curation and fitting experimental data to the simulated models was performed in MATLAB using an iterative fitting technique to minimize error in the slope and position of the curves, thus minimizing the residual sum of squares (SSR) error.

Temperatures were varied between room temperature and 100°C using a Micromanipulator heated plate. Corresponding polarization-electric field (P-E) hysteresis loops were generated using a Radiant Technologies Precision Multiferroic tester. P-E loops were measured in the triangle wave mode at 1 kHz, with the applied field sequence of ↑↓ relative to the ZMO as-grown poled-down state (↓) (O-polar).

5.3 Results and Discussion

5.3.1 Structural Characterization

ZMO films with 41% Mg and 27% Mg (referred to as x=0.41 and x=0.27, respectively, from here on) were sputter deposited in an $Ar/O_3/O_2$ mixture. The ZMO films were studied via X-ray diffraction in the Bragg-Brentano θ-2θ geometry to determine the phases present in the films. Both films are strongly 001 oriented with the *c*-axis out of plane. Crystallinity of the ZMO was generally found to improve with the introduction of ozone into the deposition chamber, compared to ZMO deposited in oxygen. Although films with x=0.41 are near the upper boundary for metastability in sputtered ZMO,[3] no MgO phase was detected in the XRD pattern (see Figure 5-2). The average grain sizes were 70 ± 3 nm and 63 ± 9 nm for x = 0.41 and x = 0.27, respectively, and both samples had homogeneous morphologies.

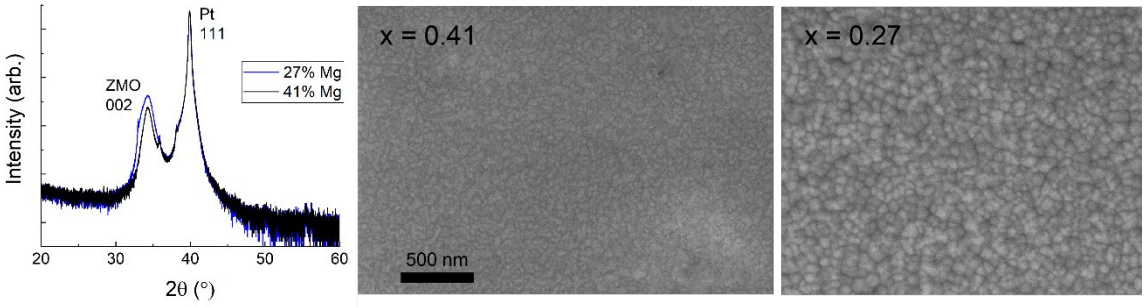

Figure **5-2**: X-ray diffraction patterns of x = 0.41 and x = 0.27 ZMO (left). FESEM micrographs of x = 0.41 (middle) and x = 0.27 (right) ZMO reveal the difference in morphology between the two compositions.

5.3.2 Ferroelectric Characterization

Both ZMO film compositions are ferroelectric with maximum remanent polarizations of approximately 80 μC cm^{-2}, in agreement with DFT calculations,[21,22] and E_c between 4 and 5 MV cm^{-1} at room temperature and 1 kHz. Corresponding Polarization-Electric field (P-E) hysteresis loops are shown in Figure 5-3 for various temperatures and applied fields (see Table 5-1). Sharply pointed tips on the hysteresis loops indicate saturation of the polarization response with low leakage currents, which is desirable for switching speed measurements. Higher applied fields tend to incur larger leakage currents. However, the larger Mg content of x=0.41 mitigates the leakage contributions even though the required fields are ~ 1 MV cm^{-1} greater than for x=0.27.[45] Previous reports suggest that incorporation of Mg into ZnO raises the band gap and thus lowers the conductivity.[18,46] Applied fields are larger for x=0.41 because E_c increases for Mg contents above ~30% Mg in ZMO, in agreement with theoretical predictions, and possibly because x-ray peaks broaden in 2θ and ω and because the microstructural features become finer, both indicating additional structural disorder.[22,40] For this reason, applied fields in excess of 5 MV/cm are

required to switch the whole spontaneous polarization of ± 80 μC cm^{-2}. These large fields cause the current draw to exceed the amplifier's maximum power output, distorting the switching curves. To address this, the highest applied field that could be used at each temperature without exceeding the amplifier's capabilities was determined. The results are presented in Table 5-1, with the corresponding P-E hysteresis loops shown in Figure 5-3.

Table **5-1**: Coercive fields (E_c) and testing parameters for the switching kinetics measurements.

Sample	Temperature	Switching Polarity	Applied Field (E_A) (MV cm^{-1})	Coercive Field (E_c) at 1 kHz (MV cm^{-1})	E_A/E_c
$Zn_{0.59}Mg_{0.41}O$	20°C	+	4.9	3.8	1.29
		-	-5.1	-3.9	1.31
	60°C	+	4.6	3.5	1.31
		-	-4.7	-3.6	1.31
	100°C	+	4.3	3.1	1.39
		-	-4.6	-3.2	1.44
$Zn_{0.73}Mg_{0.27}O$	20°C	+	4.1	3.4	1.21
		-	-3.9	-3.2	1.22
	60°C	+	3.8	2.9	1.31
		-	-3.6	-2.8	1.29
	100°C	+	3.4	2.8	1.21
		-	-3.6	-2.5	1.44

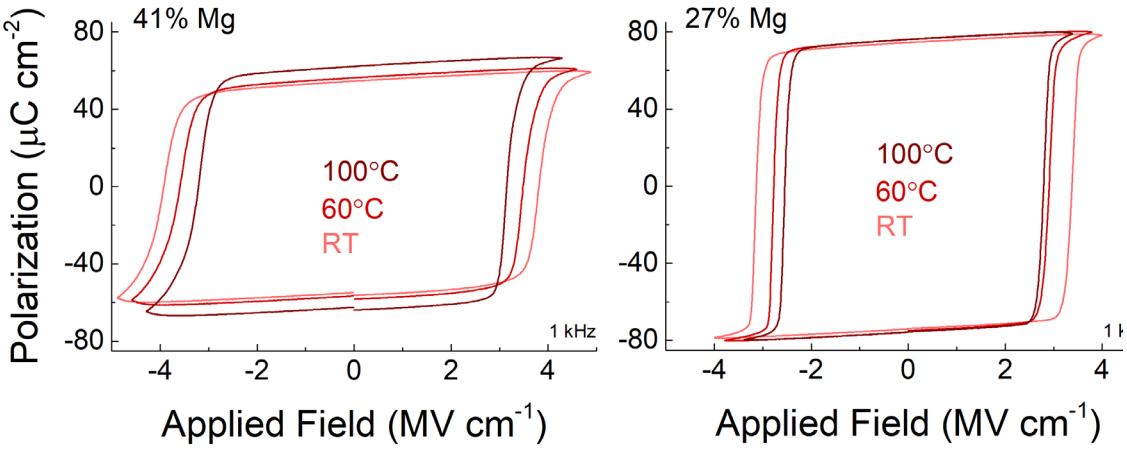

Figure **5-3**: P-E hysteresis loops of x=0.41 and x=0.27 at various applied fields and temperatures. Maximum applied fields for the P-E loops are reported in Table 5-1, as the value of the (+) applied field for each temperature. The apparent increase in polarization at 100°C for the x = 0.41 samples is an artifact associated with the maximum output of the amplifier.

In addition to the coercive field (E_c), the breakdown field also increased from 5 to 7 MV cm^{-1} by increasing the Mg content. Both samples display imprint in the P-E loops, but in opposite directions. For x=0.27, switching to the opposite polarity from the as-grown state requires a larger coercive field (i.e., the magnitude of the positive E_c exceeds that of the negative E_c), while the opposite is true for the x=0.41 films. The magnitude of the imprint is larger for the sample x=0.41, as indicated by larger differences in the + and – E_c (see Table 5-1). The reason for this is unknown.

5.3.3 Switching Speed Measurements

Switching speed measurements were performed at room temperature, 60°C, and 100°C. The driving field amplitudes were adjusted for each temperature and field direction to account for changes in E_c, as described in Table 5-1. A summary of the polarization responses from the

switching kinetics measurement module at each temperature and respective field amplitude are presented in Figure 5-4. Additional data are presented in Supplemental Figure 5-S4.

Wake-up of the switched polarization is observed for the film with x=0.27 within the first 10 switching cycles (Figure 5-4a). Wake-up is hardly observed for the film with x=0.41 due to the higher E_A/E_c ratio for switching, where E_A is the applied field. Despite applying higher E_A for the film with x=0.41, the switched polarization values are lower compared to x=0.27, due to the high Mg content.[40] Switching beyond 100 cycles results in the reduction of the switched polarization in films with x=0.27, which is likely due to the formation of irreversible regions of film at the fixed driving voltage amplitude. A sharp reduction in switched polarization on cycling is not observed for films with x=0.41. Finally, the films experience electrical breakdown between 700 and 900 cycles, regardless of the composition, temperature ($20 \leq T(°C) \leq 100$), or applied field ($1.2 < E_A/E_c < 1.5$).

Switching is completed hundreds of nanoseconds faster in films with x=0.41 compared to those with x=0.27, due to the higher applied fields (see Table 5-1). Note that the applied fields for switching in films with x=0.41 are approximately 1 MV cm^{-1} larger than in films with x=0.27 due to the larger E_c. Switching times generally decreased with cycling until breakdown (see Figures 5-4b,c,e,f), indicating that switching in ZMO occurs faster with the progression of cycling and fatigue. Trends in switching transients for reversal to O-polarity are in agreement with the observation by Yazawa et al. in (Al,B)N, where switching is delayed in the first 20 cycles due to a decrease in the population of pre-existing oppositely oriented nuclei with switching.[23] For switching to the M-polar state, significantly fewer oppositely oriented nuclei are expected to exist in pristine films. Therefore, the data in Fig. 3 demonstrate that the existence of pre-existing nuclei hastens the switching kinetics in ZMO.

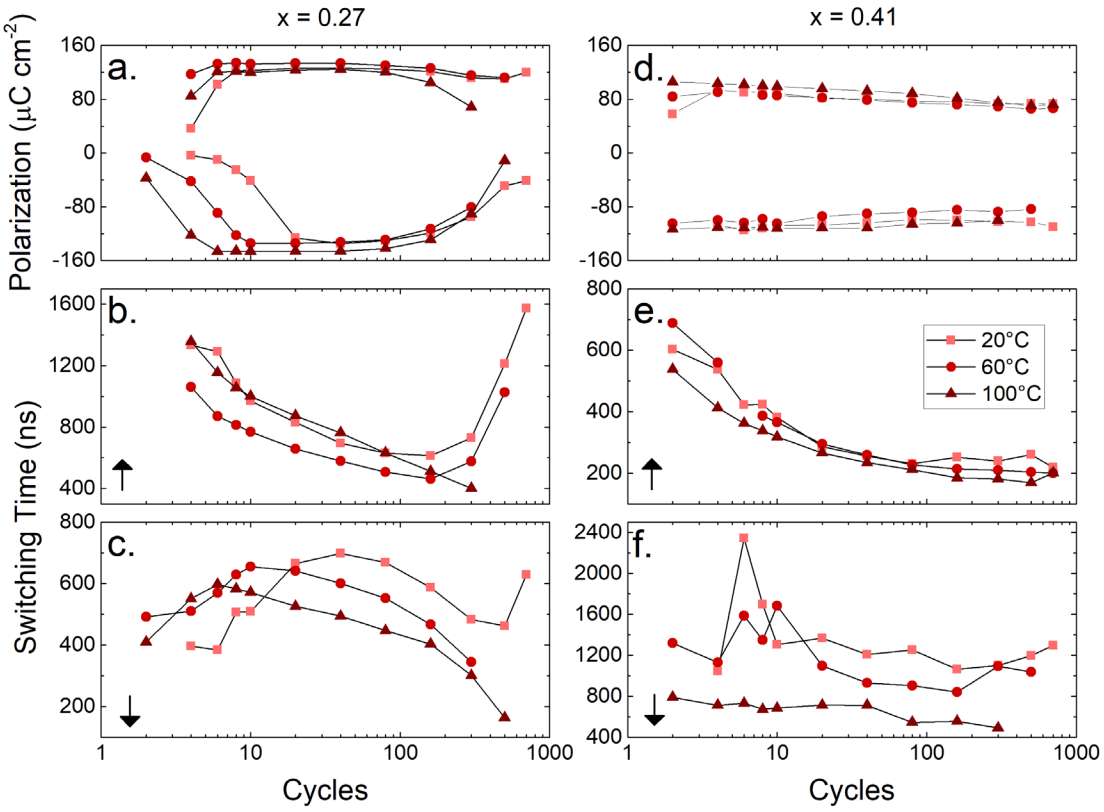

Figure **5-4**: The switched polarizations as a function of the number of switching cycles for ZMO for films with compositions x=0.27 and x=0.41 are presented in parts (a) and (d), respectively. The corresponding switching times to 90% of the switched polarization value are presented in (b), (c), (e), and (f). The direction of the applied field relative to the as-grown polarity (↓) are indicated by the arrows. The switching curves are presented in the Supplemental Section (Figure 5-S4). The applied fields for each condition are listed in Table 5-1.

Out-of-plane domain wall speeds in ZMO are ~ 1 m s^{-1} due to the approximately 200 ns time for polarization reversal to begin after the switching field is reached. This out-of-plane domain wall speed is in agreement with that observed for (Al,Sc)N.[35]

Notably, in ZMO, the kinetics of polarization reversal are history-dependent; this is manifested by changes in the switched polarization and the switching times over the film's

electrical lifetime. While the origin of these changes will be explored in future work, they are likely due to changes in defect chemistry and defect distribution. Large applied fields and switching currents may accelerate defect migration, leading to the formation of defect complexes that concentrate fields enough to cause breakdown within 1,000 switching cycles.

While solid solution of Mg at concentrations greater than a few mol% is metastable in ZMO,[47] there was virtually no difference in the fatigue lifetimes between the two samples with different mol% Mg. Both samples experienced breakdown between 700 and 900 cycles; breakdown in these measurements often occurs directly underneath the probe tips.[48] As switching occurs sooner with increased number of cycles, the magnitude of the switching current continues to increase until breakdown. Wurtzite-structured (Al,B)N and (Al,Sc)N films show similar evolution in the switching kinetics, accompanied by much greater cycling endurance lifetimes.[21,33,49] These changes resemble the "hot atom" effect described by Guido et al.[50] who noted that defects introduced by the bond-breaking process associated with switching can simultaneously decrease the energy barrier for nucleation and act as domain wall pinning sites. This manifests in the switching data as faster switching and reduced switched polarization, respectively, with cycling (see Figure 5-4).

5.3.4 Activation Energy

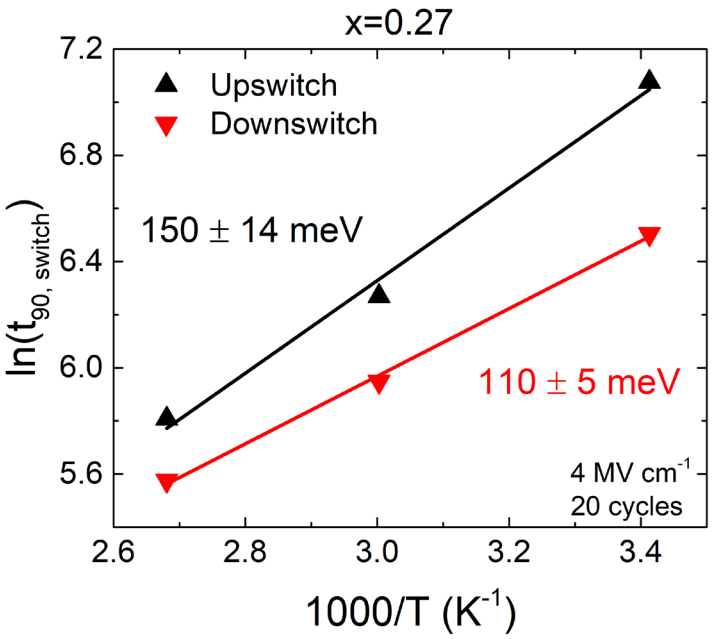

Figure **5-5**: The activation energy for ferroelectric switching was determined for a film with x=0.27 at 20 switching cycles and a fixed applied field of 4 MV cm^{-1}.

The activation energy for switching was determined from the switching times to 90 % of the switched polarization, $t_{90,\,switch}$, as shown in Figure 5-5. An Arrhenius relationship between switching at 20, 60 and 100°C, at 4 MV cm^{-1} and at the 20th switching cycle in sample x=0.27, confirming that NCS in ZMO is a thermally activated process. In particular, the activation energy was calculated from:

$$k = A\exp\left(-\frac{E_a}{k_B T}\right) \quad (5)$$

$$\ln(k) = \ln(A) + \left(-\frac{E_a}{k_B}\right)\left(\frac{1}{T}\right) \quad (6)$$

Using data as a function of temperature, activation energies for switching were determined for sample x=0.27 to be 150 ± 14 meV for switching to the M-polar state, and 110 ± 5 meV for switching to the O-polar state. The activation energy for switching to the M-polar state is greater than for switching to the O-polar state, which is consistent with a slight forward skew

for switching to the O-polar state, which was not observed for switching to the M-polar state (see Figure 5-S11). The forward skew is likely due to pre-existing nuclei accelerating the switching kinetics. Differences in the values between switching to the O- and M-polar states reveal the difference between nucleating from pre-existing sidewalls (as in the case of switching to the O-polar state), and from the electrode interfaces, which is necessary at the onset of switching when switching to the M-polar state (see Figure 5-1).

5.3.5 Individual-Column Switching in ZMO

Ferroelectric switching of ZMO at ~ 1.1 E_c obeys the KAI model well, however, only ± 42 μC cm^{-2} of polarization switched, which is about half of the spontaneous polarization of ZMO.[22] Therefore the initial reversal kinetics can be described as KAI-like. A similar phenomenon was reported in $BiFeO_3$ at low applied fields, where switching kinetics appeared to obey the KAI model, but only half of the spontaneous polarization reversed.[51] In order to switch more of the spontaneous polarization, the sample must be subjected to a larger applied field. At ~ 1.2 E_c, ± 66 μC cm^{-2} of polarization switches, however, the rate law n_{KAI} is > 3 which indicates a change in the switching mechanism at the higher applied fields necessary to switch most of the spontaneous polarization (here, about 80% of the spontaneous polarization was reversed at 1.2 E_c,

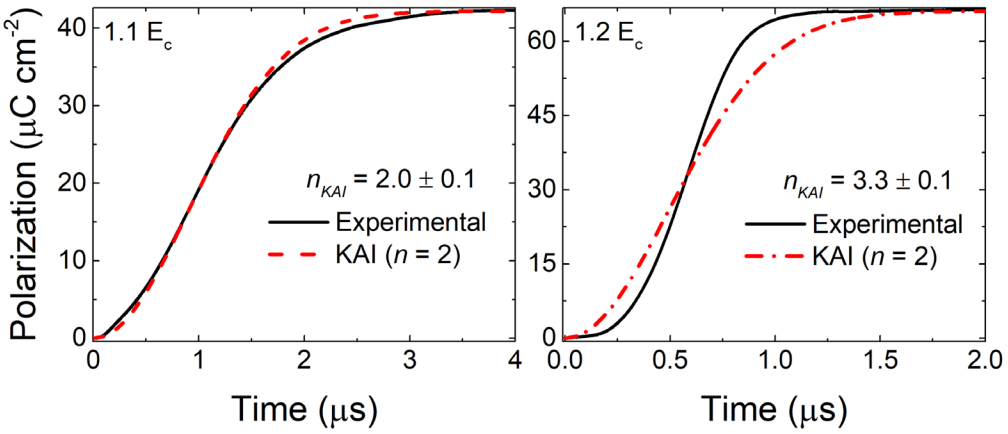

Figure **5-6**: Ferroelectric switching of ZMO at 1.1 E_c (left) nearly obeys the KAI kinetics model where $n_{KAI} = 2 \pm 0.1$, although the total switching amounts to ± 42 μC cm^{-2} which is half of the spontaneous polarization. Switching at 1.2 E_c (right) deviates more from KAI and resulted in a larger-than-physical rate law, where $n_{KAI} = 3.3 \pm 0.1$. This corresponds to ± 66 μC cm^{-2} of switched polarization. The value of n_{KAI} was obtained by finding the least-error fit of the KAI model to the switching curve.

to avoid over-driving the power supply).

To understand switching in the high field regime, several statistical models were explored. The fit based on a Gaussian distribution of switching rates vs. time and the SNNG model were found to fit the switching transients (polarization vs time) in ZMO. The SNNG model had the lowest regression sum of squares error (SSR) (3.7×10^{-5}), shown in Figure 5-7. The Gaussian distribution applied nearly as well as the SNNG model, with a SSR of 9×10^{-5}.

The successful application of the Gaussian model to fitting the switching transients in ZMO provides guidance for future development of physical models. The pairing of individual randomized events and a rapidly changing nucleation rate suggest the importance of local environment and growth processes in switching. In addition, the successful application of the

KAI model at applied fields of $E_A \lesssim 1.1\ E_c$ and the SNNG model at higher fields also suggests that both nucleation and growth are important contributors to the switching response. Taking the following two assumptions, a distribution function for individual-column switching was extracted from the nucleation rate for the SNNG model:

i. Switching is dominated by individual columns of atoms

ii. Switching of a new column of atoms is treated equally whether it occurs at the electrode interface or the sidewall of a switched domain.

As noted above, physical modeling emphasizes the importance of local environment. The above assumptions aggregate over nucleation and growth in order to develop a simple and a tractable fit. Simulations of the distribution function for the flipping of individual columns were performed in MATLAB (see Supplemental Section) using the nucleation rate for the SNNG model:

$$\frac{\dot{N}(\tau)}{N(\infty)} = \alpha m \tau^{m-1} \exp(-\alpha \tau^m) \quad (7)$$

where $\frac{\dot{N}(\tau)}{N(\infty)}$ is the relative nucleation rate. As usual, phantom nuclei – nuclei which do not contribute to polarization reversal and are stochastically generated in already switched domains – were subtracted from the nucleation rate.[29] Calculations for this are in the Supplemental Section.

In-plane diameters of the domains were varied between 1 and 50 nm, and the distribution of nucleation events calculated from the SNNG model agree reasonably with the Gaussian distribution when the size of columns are < 10 nm in diameter (see Figure 5-7). Atomistic simulations of related materials strongly suggest that individual atomic columns play a preeminent role in nucleation and growth. Here, the column diameter is used as an additional fitting parameter to incorporate additional aspects of growth phenomenologically. Therefore, the SNNG model can provide nearly equivalent fits to the Gaussian distribution if the changing nucleation rate from SNNG is used as the rate for individual column flipping. If domains (or

columns) are < 10 nm in diameter, nucleation sites must exist at a concentration of > $4x10^{11}$ cm^{-2}

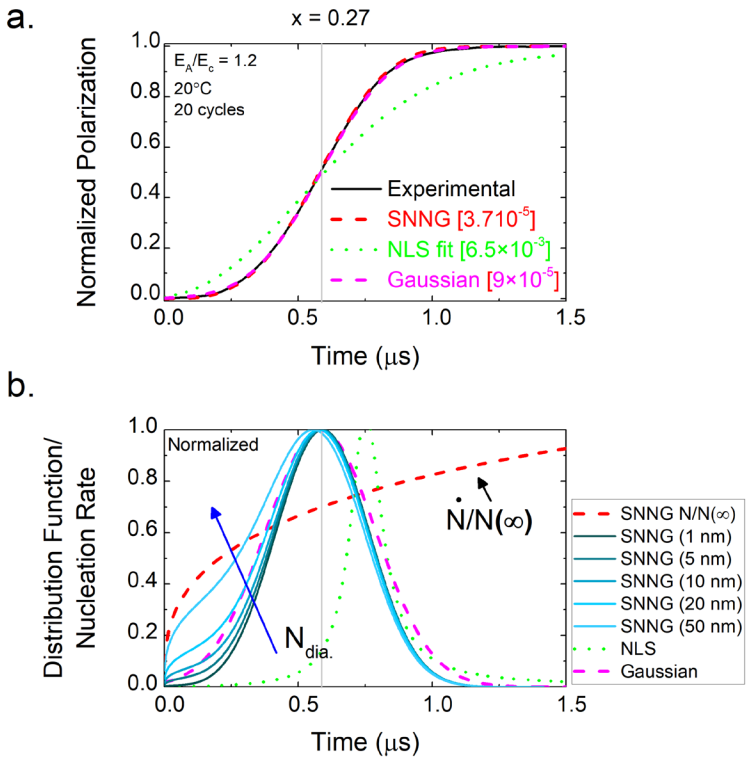

Figure **5-7**: A comparison of the SNNG and ICS model fits with the experimental room temperature switching transient of $Zn_{0.73}Mg_{0.27}O$. This sample was switched 20 times at room temperature, and the switching response from the O- to M-polar state is shown. The residual sum of squares for each of the fitted curves is in [brackets] in the legend. The gray line marks the time at which 50% of the polarization is reversed. In (b) the distribution function is normalized for the Lorentzian function in the NLS curve and for the Gaussian curve. The nucleation rate curve, $\dot{N}/N(\infty)$, from the SNNG model is normalized in the plot. m = 1.33 for the SNNG model, which corresponds to n_{KAI} = 3.3 ± 0.1. The same data produced n_{NLS} = 4.8 ± 0.2.

to fully switch the film. The nuclei generated at high applied fields are likely associated with crystallographic defects and local strains induced by the Zn/Mg solid solution.[22]

The NLS model was used by Jo et al. to fit the switching curves of PZT (equation 3), and employs the Lorentzian distribution of long waiting times to describe nucleation where an n_{NLS} value of 2 describes 2-dimensional domain growth in the plane of the film. However, this model did not adequately fit the switching transients in ZMO. Only when the rate constant n_{NLS} was increased well beyond 2, (e.g. up to n_{NLS} ~5) did the slopes of the simulated NLS curve begin to align to the experimental polarization reversal curve. This implies that the strong heterogeneity implicit in the NLS model is not crucial for explaining polarization reversal in ZMO when $E_A \gtrsim 1.2\ E_c$.

When a column becomes active, the domain wall travels through the thickness rapidly in the out-of-plane direction. Newly switched columns form with a non-uniform (not convex) spatial distribution at the domain walls, leading to roughening of the domain wall, rather than radial growth (see Figure 5-1). As shown above, the polarization reversal can be modeled as individual events throughout the capacitor volume. For ZMO, this process follows either the normal (Gaussian) or the inverse gamma distribution (described later). In scenarios where insufficient fields are supplied to the sample to switch the whole polarization, a fraction of the domains does not reverse due to incomplete coalescence.

5.3.6 Bi-modal Ferroelectric Switching in high-Mg content ZMO

Ferroelectric switching of ZMO with higher Mg contents (x=0.41) differs from ZMO with moderate Mg content (x=0.27). The two main differences are (1) switching is faster and (2) switching of ZMO with high Mg content is bi-modal; it cannot be fit with a single distribution

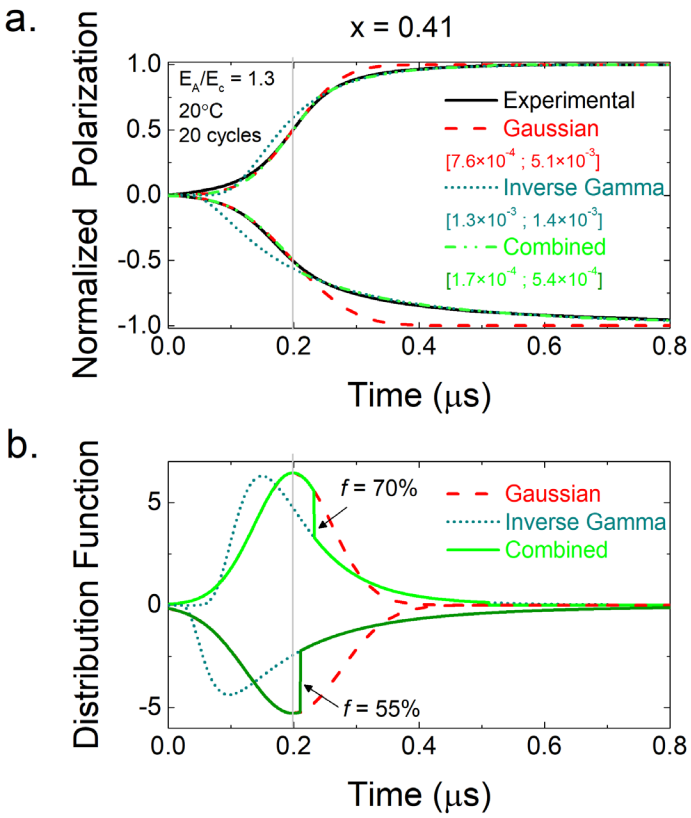

Figure **5-8**: Ferroelectric switching of $Zn_{0.59}Mg_{0.41}O$ (x=0.41), showing a comparison of the Gaussian and inverse gamma distributions fitted to the experimental switching curve. This sample was switched 20 times at room temperature, and the responses from switching in both directions are presented. The residual sum of squares for each of the fitted curves are in brackets for switching in the respective polarities [↑ (M-polar); ↓ (O-polar)] in the legend. The distribution functions are presented in (b). The abrupt drop in the combined curve is from the transition to the inverse gamma function; the relevant polarization fractions where this occurs are marked with arrows. The gray line is a reference for 50% reversed polarization, which is at the same time (199 ns) for switching to both polarities. The curve for the SNNG model is similar to the Gaussian distribution in (a) and is shown in the Supplemental Section (Figure 5-S9). $n_{KAI} = 3.8 \pm 0.1$ for switching to the M-polar state and $n_{KAI} = 3.1 \pm 0.1$ for switching to the O-polar state.

function. Both findings are consistent with simulations by Sepehrinezhad et al.,[40] where high Mg concentrations are associated with larger E_c, and faster switching occurs in local regions where there is Mg clustering (see Figure 5-3). DFT calculations show that strain fluctuations in ZMO promoted by Mg clustering locally reduce the E_c.[22] ReaxFF simulations suggest that Mg-rich regions are the first to switch in ZMO, followed by the Mg-deficient regions; the Mg-deficient regions complete polarization reversal first, before the Mg-rich regions reverse their polarization to the opposite state from the intermediate phase.[40] This retards the latter portion of switching.

Bimodal switching in x=0.41 is described by two distribution functions, as shown in Figure 5-8. The first 50 to 75% of polarization reversal is fit well by the Gaussian distribution, similar to ZMO with moderate Mg concentrations (x=0.27), while the latter part of polarization reversal is fit better by the inverse gamma distribution. The transition from the normal distribution occurs within $f(t)$ = 50 – 55% of the switched polarization when switching to the O-polar state, and the transition can occur as late as $f(t)$ = 80% when switching to the M-polar state. The delay in the latter part of switching is believed to be due to Mg clustering, as described above.[40]

A similar transition from one mode to another was reported in the polarization reversal of some lead zirconate titanate films for memory applications.[52] In that work, the initial portion of the switching transient was described as nucleation and the latter portion as growth, although neither the KAI nor the NLS models properly fit the kinetics of the end of the switching process. Piezoresponse force microscopy suggested a fractal-like growth where domain wall velocities vary by up to two orders of magnitude in different directions; this was believed to be responsible for the tail of the curve. Fractal-like *growth*, for which no model exists to describe the kinetics, is also reported[36] for ferroelectric wurtzites. In ZMO, the latter portion of switching in the bimodal behavior observed was fitted with the inverse gamma distribution. The inverse gamma distribution is described elsewhere,[53] which resists coming to 0 (coming to completion) and has a

substantial tail – which in this case – means resisting completing the polarization reversal. This is in agreement with observations by Sepehrinezhad et al. where Mg clusters retard the tail of the switching transient.[40]

5.3.7 Fatigue in ZMO

For x=0.27, switching to the M-polar state, the Gaussian distribution describes switching from wake-up through 80 cycles. By 160 cycles, the tail described by the inverse gamma function appears (see Figure 5-10a). This suggests reorganization of defects in ZMO – also improving the switching times. Interstitial cations are a common defect in ZMO.[54,55] This response was consistent for all temperatures (20, 60 and 100°C) switching to the M-polar state. When switching to the ↓ polarity, the Gaussian distribution applies to polarization reversal, but experiences a slight forward skew (see Figure 5-S11). This is presumably due to pre-existing nuclei for switching to that state because the film was grown in that polarity.

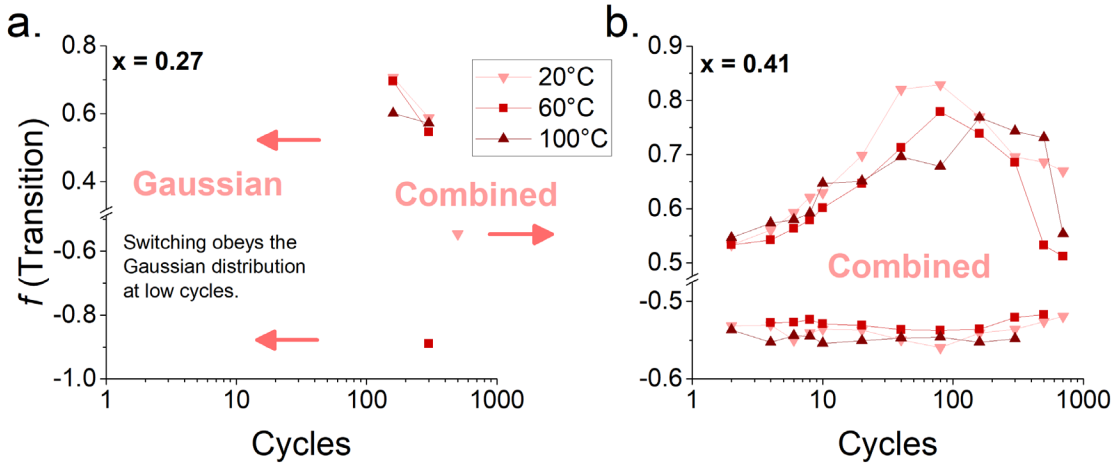

Figure **5-9**: Description of the mode of ferroelectric switching as either Gaussian or combined Gaussian with transition to the inverse gamma distribution. The y-axis contains transition points for switching between the O- and M-polar states, respectively.

The film with x=0.41 was fit with the combined Gaussian and inverse gamma distributions at temperatures between 20 and 100°C, as shown in Figure 5-9. The combined distribution described switching from wake-up until breakdown for both polarities of switching (see Figure 5-9b). When switching to the M-polar state, the transition to the inverse gamma distribution occurs later in the switching after wakeup, which implies that nucleation plays a greater role in switching to that state. This trend continues until 80 cycles, beyond which the Gaussian portion of switching diminishes and the transition to the inverse gamma distribution shifts to earlier times. Switching to the O-polar state shows that about half of the polarization switched by the nucleation of individual columns throughout fatigue.

5.3.8 Domains and Domain Walls in ZMO

In order to understand the nature of domain walls throughout fatigue, Rayleigh-like behavior of the dielectric constant was assessed in ZMO (see Figure 5-10b).[56] Here, the Rayleigh law is used to categorize contributions of the polarization response as reversible or irreversible, and to qualitatively assess the combination of domain wall density and mobility.[56,57]

$$\varepsilon = \alpha E + \varepsilon_{init} \quad (8)$$

The slope of the relative dielectric constant, ε, with respect to the applied field, E, was used to determine the irreversible contributions to the dielectric constant (α), and the y-intercept or ε_{init} describes the reversible contribution. These values were measured with the progression of cycling. The increase of α with the number of cycles indicates the population of domain walls and/or their mobility is increasing. Therefore, cycling the polarization induces an increase in α which suggests that more shallowly trapped domain walls contribute to the dielectric constant.

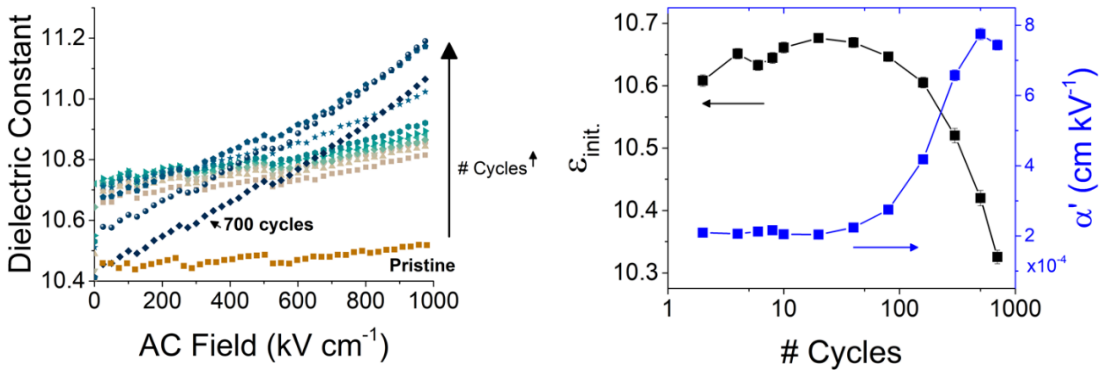

Figure **5-10**: (left) Rayleigh like behavior is observed in the dielectric constant of ZMO. (right) Rayleigh law indicates that the irreversible contributions to the dielectric constant (α‘) increase with cycling. The reversible contribution (ε_{init}) initially increases during the first few cycles after wake-up, followed by decreasing throughout cycling.

The reversible contribution ε_{init} decreases with increasing cycles, presumably due to a reduction of the number of domain walls that are trapped in deep potential wells. The Rayleigh data suggest that the population of nuclei, and mobile domain walls increase with continued cycling in ZMO, which is consistent with the observation of individual-column switching, and the hot atom effect.[50]

Similar to (Al,B)N, the reversible contribution to the permittivity increases during the wake-up process, up to 20 cycles.[24] Likewise, α increases initially and becomes constant until 20 cycles, and at values twice those reported for (Al,B)N.[24] Beyond 20 cycles, the increase in ε_{init} is coupled with decrease in α, suggesting the domains are dislodged from deep potential wells as the domain state is re-written during cycling.

5.4 Conclusions

In conclusion, ferroelectric switching of $Zn_{1-x}Mg_xO$ obeys KAI-like switching at low applied fields and violates KAI at higher applied fields. Switching of ZMO with moderate Mg

contents, near x = 0.27 is well fit by independent switching events and a Gaussian distribution of switching rate vs. time or by a distribution function from a simplified form of the SNNG model. Switching becomes bimodal in ZMO with Mg contents of x = 0.41, where the first ½ to ⅔ of switching occurs quickly and obeys the Gaussian distribution, and is followed by a slow tail which obeys the inverse gamma distribution. It is suggested that the tail is due to Mg clustering which retards the latter portion of switching in high Mg-content ZMO ($x \gtrsim 0.4$). Ferroelectric switching beyond 100 cycles results in fatiguing of ZMO, possibly due to the "hot atom" effect which was described in (Al,Sc)N. Rayleigh analysis reveals a simultaneous increase in the irreversible and decrease in the reversible contributions to the dielectric constant on cycling, due to an increase in the density of mobile domain walls. This causes faster switching with cycling in ZMO until breakdown.

5.5 Supplementary Materials

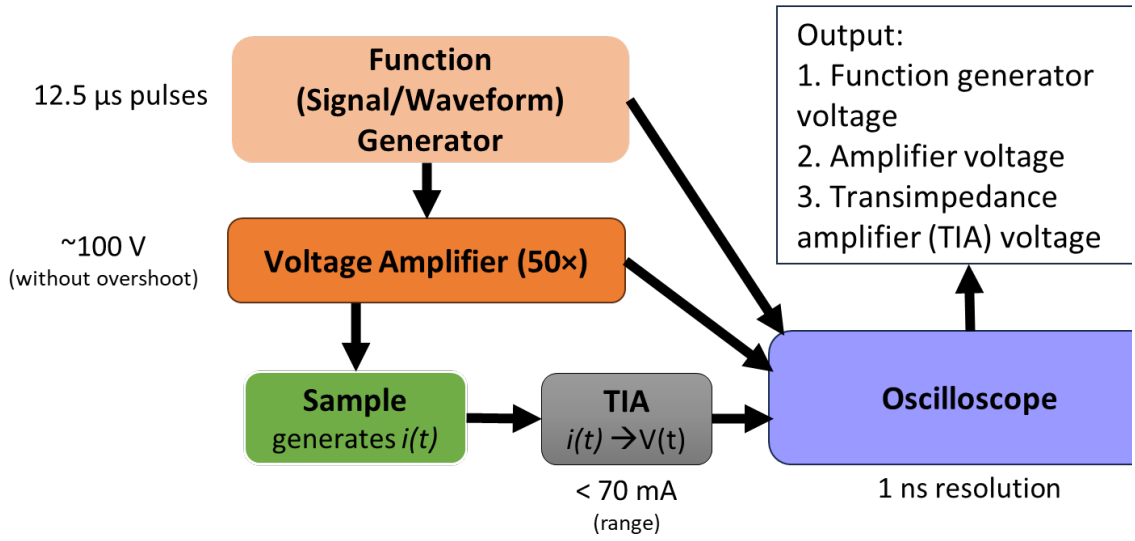

Figure **5-S1**: The experimental set-up with relevant parameters assigned to the components.

Python was used to customize a double-PUND waveform with 12.5 μs pulse widths and delays as the function (or signal) generator output. The output of the function generator was the input to the Trek 50x voltage amplifier. The function generator output, amplifier output, and transimpedance amplifier output were recorded on the oscilloscope with 1 ns precision (see Figure 5-S1). The rise time for the function generator to achieve 2 V output was approximately 35 ns, and the corresponding rise time of the 50x amplifier to 100 V was approximately 200 ns. There was no observed delay between the amplifier output and the (TIA) response, even when using cables of different lengths. Amplifier rise times were prolonged when switching occurred at a rate that exceeded the amplifier slew rate. Exceedingly fast switching could also result in ringing in the TIA output. To avoid this, small capacitors (60 μm in diameter) and appropriate field amplitudes were chosen to avoid exceeding the slew rate of the amplifier and to avoid ringing of the TIA.

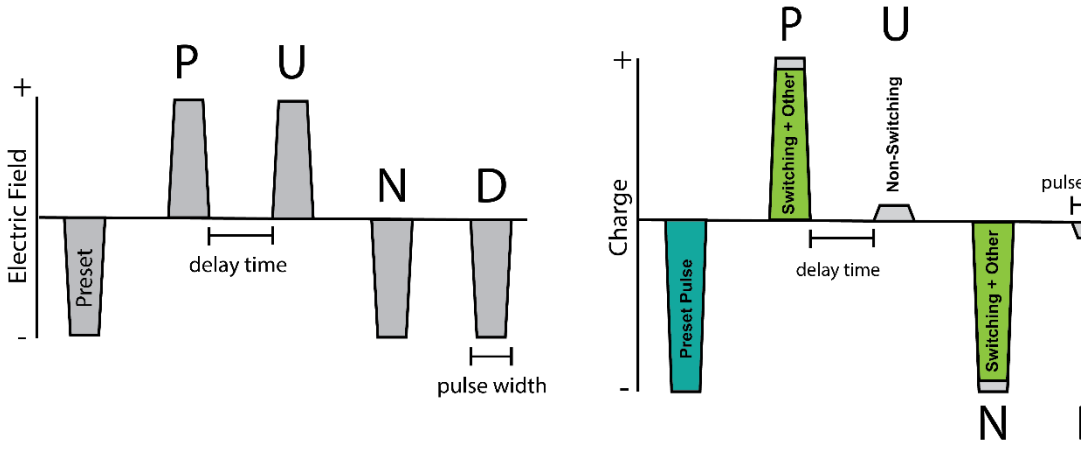

Figure **5-S2**: A diagram of the PUND (Positive Up Negative Down) measurement.

The ferroelectric samples responded with capacitive current at the onset of voltage output from the amplifier, followed by polarization reversal once the coercive field was reached. This capacitive response existed in both the switching and the non-switching responses. Therefore, for

all measurements, the non-switching responses (U and D in PUND, or $P_{non-switching}$) were subtracted from the switching responses (P and N, respectively, or P_{total}).[23]

$$P_{polarization} = P_{total} - P_{non-switching} \quad \text{(S1)}$$

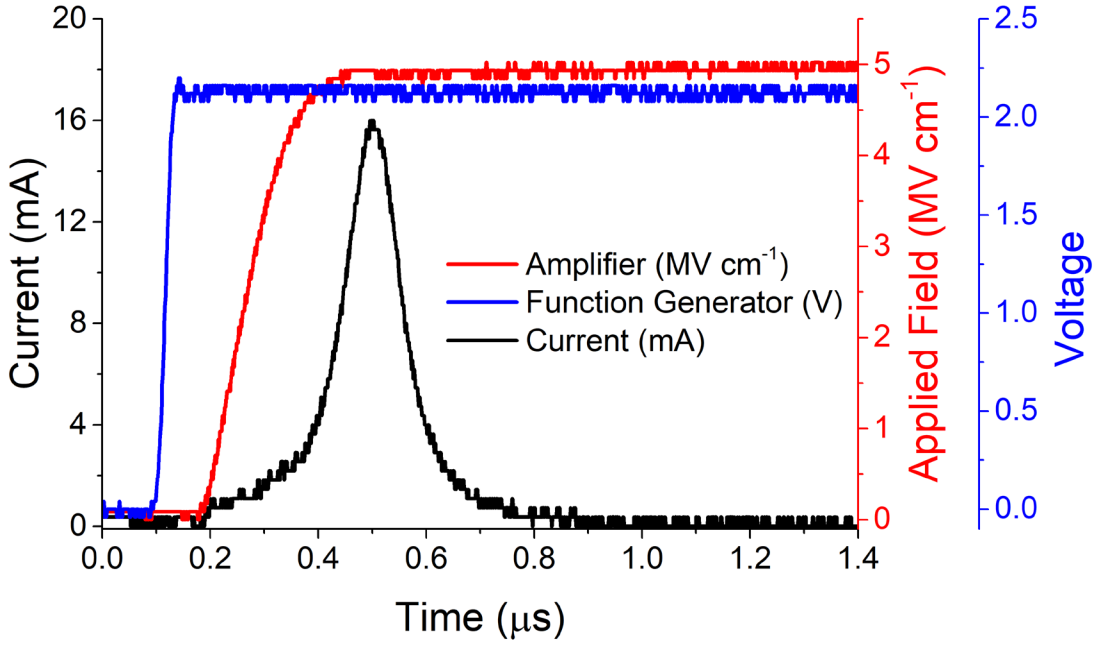

Figure **5-S3**: A ZMO film with x=0.41, 20°C, ↑ (indicating switching to the M-polar state) 20 cycles. The polarization (black), amplifier (red) and function generator (blue) responses were collected by the oscilloscope.

In addition to this, slightly larger post-switching leakage currents were observed in ZMO, which did not exist in the non-switching curves, so they were subtracted from the switching curves separately. The leakage currents between 3 μs and 9 μs after switching, where polarization reversal had completed, were averaged and subtracted from the post-switching response beginning at the point at which the polarization reversal concluded. Depiction of the PUND waveform is shown in Figure 5-S2, where pulse widths and delays were set to 12.5 μs, each.

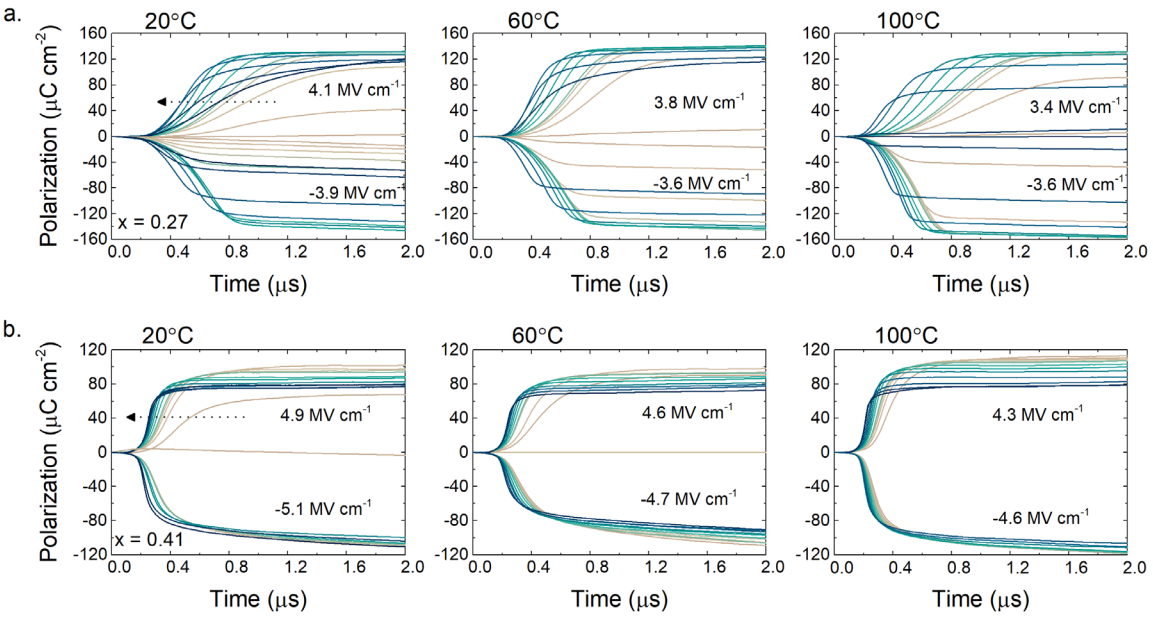

Figure **5-S4**: The switching polarization curves for samples x=0.27 and x=0.41 are presented, here.

To determine the switching kinetics, t_0 where the onset of polarization reversal occurs, was set to 70% of the set-point voltage. In reports for (Al,B)N and for (Al,Sc)N, t_0 was set at 90% of the set-point voltage.[23,32] This was not suitable for ZMO because several μC cm^{-2} of polarization had switched before 90% of the setpoint voltage, due to more rapid polarization reversal in ZMO than in the aluminum nitrides. Therefore, t_0 was set at 70% of the set-point voltage. This was reliable for all switching measurements in this study.

Iterative fitting in MATLAB was performed to determine fitting parameters for the simultaneous non-linear nucleation and growth (SNNG) model, modified NLS model from Jo et al. (Lorentzian), the Gaussian distribution and the inverse-gamma distribution by minimizing error in the slopes and the positions of the curves.

5.5.1 Simultaneous Non-Linear Nucleation and Growth (SNNG) Model

The SNNG model[23] is described below:

$$f(t) = 1 - exp\left[-2\pi d v^2 N(\infty)\alpha m \int_0^t \tau^{m-1}(t-\tau)^2 \exp(-\alpha t^m)\, d\tau\right] \quad \text{(S2)}$$

where $f(t)$ is the fraction of switched polarization, d is the film thickness, v is the domain wall velocity, $N(\infty)$ is the saturated nucleation density, *t* is the time (also called the nucleation time), and α and m are fitting parameters for the curve position and slope, respectively. The parameters $N(\infty)$ and α were varied with iterative fitting to match the slope and position of the simulated polarization curve with the experimental curve. The $N(\infty)$ and v could not be determined experimentally, but because these terms are coupled, they do not need to be known to fit the SNNG model to experimental data. However, knowledge of one of the terms from subsequent experiments would provide quantitative information to calculate the value of the other term.

The term *m* describes the shape of the nucleation curve, and was set to $m = n_{KAI} - 2$ (assuming 2-dimensional growth), where n_{KAI} is the rate law and was determined by the Avrami-Erofeev equation:[30]

$$f(t) = 1 - \exp(-kt^n) \quad \text{(S3)}$$

$$\ln\left(\ln\frac{1}{1-f(t)}\right) = \ln k + n \ln t \quad \text{(S4)}$$

$f(t)$ is the fraction of transformed polarization, *n* is the rate law (n_{KAI}), and *k* is the rate constant. The value of n_{KAI} was determined within ± 10 ns of the current maximum in the switching curve, which is at approximately 50% of the switching time. The nucleation curve is described by the following equation:

$$\frac{\dot{N}(\tau)}{N(\infty)} = \alpha m \tau^{m-1} \exp(-\alpha \tau^m) \quad \text{(S5)}$$

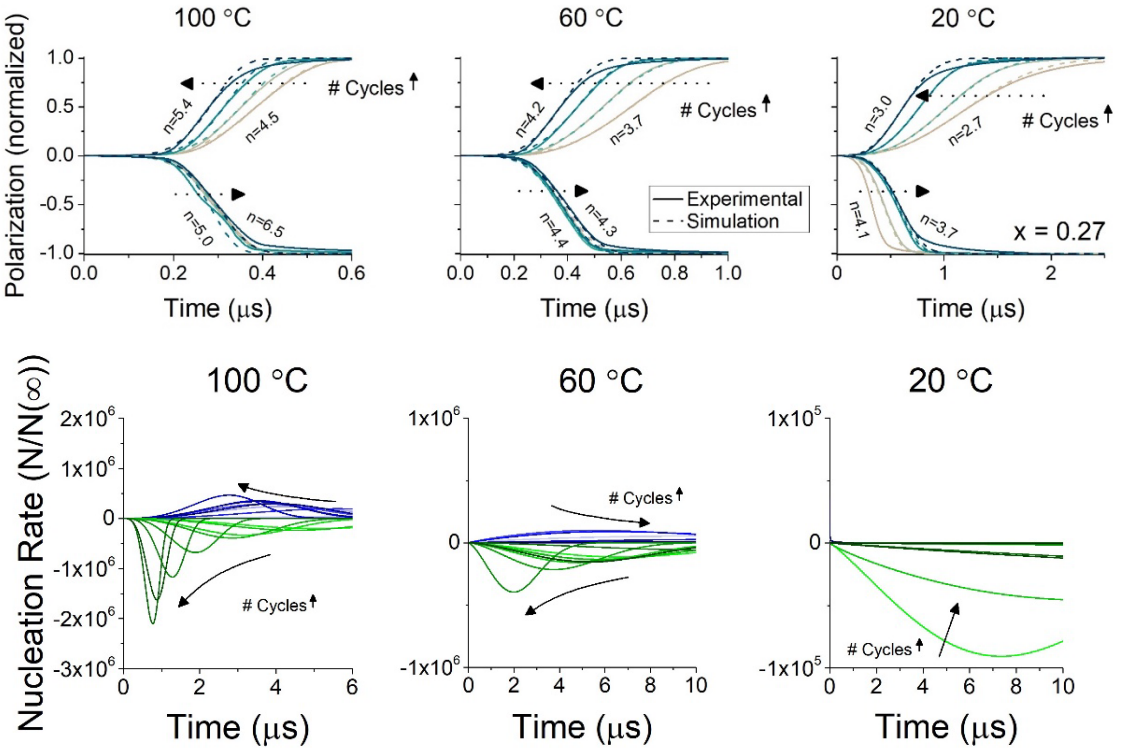

Figure **5-S5**: Sample x=0.27 was switched at 4 MV cm^{-1} at various temperatures. The SNNG model was fit to the polarization reversal curves (top), and the nucleation rates are presented (bottom).

The SNNG model was found to have low regression sum of squares error (SSR) values of < 0.0001 at low number of switching cycles when switching was not bi-modal, as shown in Figure 5-S3, suggesting that the SNNG model applies well. Increasing nucleation rates with the number of switching cycles are consistent with "hot atom" effects in ZMO, as was reported for other wurtzite ferroelectrics.[50]

5.5.2 Kolmogorov-Avrami-Ishibashi (KAI) Model

The Kolmogorov-Avrami-Ishibashi (KAI) Model was also applied to the switching data.[24,25,26,27]

$$f(t) = 1 - \exp\left(-\left(\frac{t}{t_0}\right)^n\right) \quad \text{(S6)}$$

where t is the elapsed time, t_0 is the characteristic switching time, and n is the rate law (n_{KAI}). In thin films it is expected that domains should propagate quickly through the thickness and grow outward radially, and should be described by a rate law of 2. However, rate laws greater than 2 describe a complicated nucleation and growth pathway, and the maximum theoretical rate law for processes in thin films is 3. Therefore, at applied field greater than 1.2 E_c, the KAI model does not provide an understanding of the nucleation and growth phenomenon in ZMO. Rather, the Gaussian distribution accurately describes transformation processes in ZMO as these high fields, suggesting that switching is governed by the probability of nucleation, rather than nucleation followed by radial growth, which occurs when $n_{KAI} = 2$ (see Figure 5-S6a and Figure 5-6a).

5.5.3 Nucleation Limited Switching (NLS) Model

The modified nucleation-limited switching (NLS) model presented by Jo et al. describes switching in the presence of defect dipoles which hinder domain wall motion.[69]

$$f(t) = \int_{-\infty}^{+\infty}\left[1 - e^{-\left(\frac{t}{t_0}\right)^n}\right] \cdot F(\log t_0)d(\log t_0) \quad \text{(S7)}$$

where t is the time, t_0 is the characteristic switching time, n is the dimensionality of growth (n_{NLS}), and $F(\log t_0)$ is a distribution function describing nucleation. For most ferroelectrics, the value of n_{NLS} in the NLS model is assumed to be 2, for 2-dimensional growth. However, measured values of n_{NLS} exceed 2 for ZMO, therefore the value of n_{NLS} in this work is assumed to be the calculated value of the Avrami constant $n_{KAI} - 1$ (for 1 dimension of nucleation).

Jo et al. presented a Lorentzian distribution for $F(\log t_0)$, described in the equation below.

$$F(\log t_0) = \frac{A}{\pi} \cdot \frac{w}{(\log t - \log t_1)^2 + w^2} \quad \text{(S8)}$$

where A is an arbitrary fitting constant (A≈1), t is the switching time, t_1 is the position of the center of the distribution function, and w describes the half-width at half-maximum by the relationship $w \cdot \log(t_1)$. However, a reasonable fit of the slope of the polarization reversal could not be applied without applying n_{NLS} constants greater than the Avrami n_{KAI} values. Therefore, the Lorentzian model used by Jo et al. for PZT with defect dipoles was not found to apply to ferroelectric switching in ZMO.

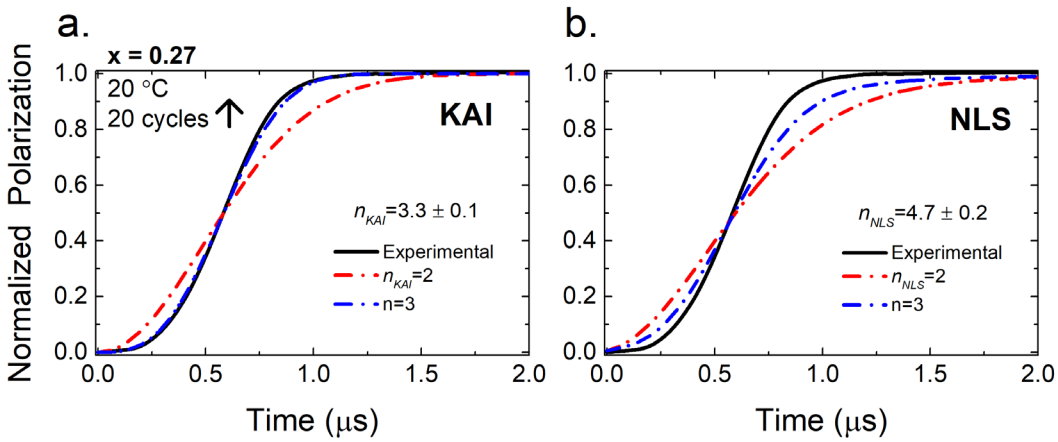

Figure **5-S6**: The KAI model, and the NLS model presented by Jo et al. with various n_{NLS} values are applied to the experimental switching curve from Figure 5-7. The value of n_{KAI} was obtained by finding least error fit, so error bars are not provided. The value of n_{NLS} was obtained by testing various values of n_{NLS}.

5.5.4 Gaussian Distribution Model

The cumulative distribution function of the Gaussian (or normal) distribution[58] was found to fit the switching curves in ZMO reasonably at moderate Mg concentrations. It is described as:

$$f\left(\frac{t-\tau_0}{\sigma}\right) = \frac{1}{2}\left[1 + \text{erf}\left(\frac{t-\tau_0}{\sigma\sqrt{2}}\right)\right] \quad \text{(S10)}$$

where $f\left(\frac{t-\tau_0}{\sigma}\right)$ is the fraction of switched polarization, t is the time, τ_0 is the mean of the Gaussian distribution (i.e. 50% of the switching transient), and σ is the standard deviation. The probability density function of the Gaussian distribution which describes the switching current transient, and the shape of the nucleation rate is:

$$f(t) = \frac{1}{\sqrt{2\pi\sigma^2}} e^{-\frac{(t-\tau_0)^2}{2\sigma^2}} \quad \text{(S10)}$$

The Gaussian distribution describes phenomena which are most probable near the mean, and occurs often in nature.[42] This distribution describes switching to the opposite state in films with x=0.27 up to 80 cycles before switching became bi-modal and the tail which obeys the inverse gamma distribution appears. A slightly skewed Gaussian distribution describes switching to the O-polar state in films with x=0.27.

5.5.5 Combined Gaussian and Inverse Gamma Model

Bi-modal switching in ZMO was predicted for high-Mg content ZMO films by Sepehrinezhad et al. where the latter part of switching is much slower than the initial part and suggests the formation of Mg-rich regions in the film.[40] For films with x=0.41, the Gaussian distribution fits the first ½ to ¾ of the polarization reversal well, before transitioning to a secondary switching mechanism described by the inverse gamma distribution, shown below.[59]

$$f(t;\alpha,\beta) = \frac{\beta^\alpha}{\Gamma(\alpha)} t^{-\alpha-1} \exp\left(-\frac{\beta}{t}\right) \quad \text{(S11)}$$

where β is a scale parameter, α is a shape parameter and *t* is the switching time. The inverse gamma model describes situations with high entropy. The Shannon entropy, which describes the level of uncertainty, can be calculated from α and β with the following equation[60]:

$$H = \alpha + \ln\big(\beta\Gamma(\alpha)\big) - (\alpha + 1)\psi(\alpha) \quad \text{(S12)}$$

The Shannon entropy was measured for the fitted inverse gamma distributions in films with x=0.41. The Shannon entropy changes with field cycling and generally increases to a maximum at 80 cycles and declines thereafter.

5.5.6 Curve Fitting in MATLAB

Iterative fitting was used to match the simulated curves of models and statistical distributions to the normalized experimental polarization curve. Generally, a parameter which modifies either the position or the slope of a curve is varied for each iteration. Whether the error between the position or slope of the simulated curve gets closer or further from the experimental curve determines which direction the value of the parameter changes for the next iteration. Once a minimum in the error is achieved, finer refinement is performed and variations become smaller, and the same process is performed. This was done repeatedly to minimize the regression sum of squares error (SSR) at the expense of computation time. For simulations which involve more than one parameter, such as the SNNG model, two parameters were used to match the slope and the position, α and $N(\infty)$. The flow of refinement is depicted schematically in Figure 5-S7.

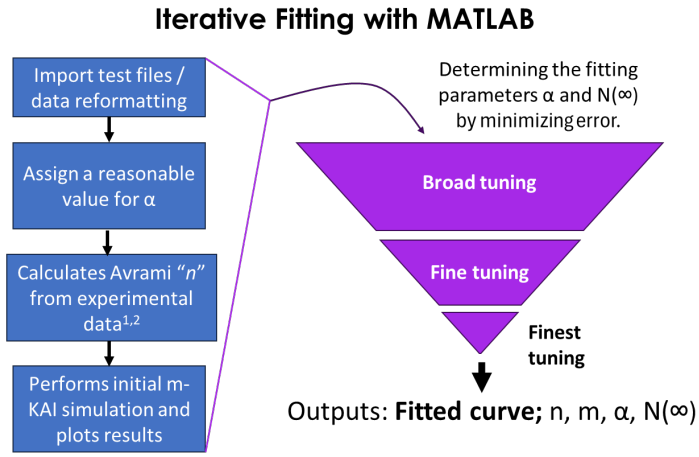

Figure **5-S7**: This schematic shows the logical order of the curve fitting code from top to bottom and from left to right.

5.5.7 The SNNG Model

To begin curve fitting, the starting value of α was underestimated and a reasonable value for $N(\infty)$ was chosen. The program then increased the value of α by an order of magnitude until the value of the slope (m) of the curve exceeded 0.5. Then, the iterative fitting process began. A local minimum was sought in each segment before moving to the next segment. Fitting the slope and position of the simulated curve to the experimental curve by toggling the values of α and $N(\infty)$ was performed in the order described in Figure 5-S3. The tolerances for error were reduced with successive segments. In the final tuning step, the position of the curve at $f \approx 0.5$ was matched to within 5 ns of the experimental curve; a representative output is shown in Figure 5-S5 and in Figure 5-S8.

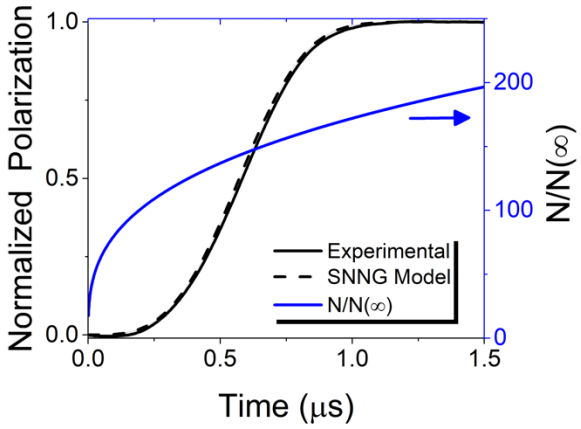

Figure **5-S8:** The output of iterative fitting in MATLAB. There is one data point for each nanosecond, with a total of 10 μs observation time for each switching instance. The script takes 1 – 2 minutes to run on average with an intel core i7 processor.

The MATLAB script is fully automatic and only requires the user to underestimate a starting value for α. Without additional information, such as *N(∞)* and domain wall velocity *v*, the average impingement time for domains can be calculated (see equation 2).[23]

$$\bar{t}_{imp} = \frac{1}{2v\sqrt{dN(\infty)}} \tag{S13}$$

where *d* is the film thickness. As described by Yazawa et al., the *N(∞)* and *v* terms are coupled and need not be known to simulate the curve.

5.5.8 Calculating the Distribution Function for Nucleation from the SNNG Model

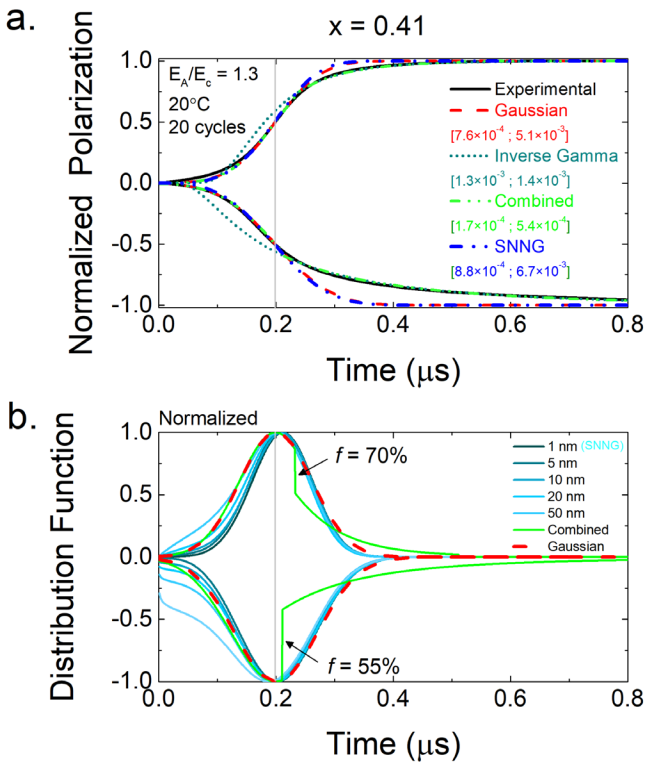

Figure **5-S9**: Ferroelectric switching of $Zn_{0.59}Mg_{0.41}O$ (x=0.41), showing a comparison of the Gaussian and inverse gamma distributions, and the SNNG model fitted to the experimental switching curve. This sample was switched 20 times at room temperature, and the responses from switching in both directions are presented. The residual sum of squares error (SSR) for each of the fitted curves are in brackets for switching in the respective polarities [↑ (M-polar); ↓ (O-polar)] in the legend. The distribution functions are presented in (b). The abrupt drop in the combined curve is from the transition to the inverse gamma function; the relevant polarization fractions where this occurs are marked with arrows. The light blue color gradients are the distribution functions for nucleation extracted from the SNNG model according to the assumptions in this work. The gray line is a reference for 50% of reversed polarization, which is at the same time (199 ns) for switching

to both polarities. n_{KAI} = 3.8 ± 0.1 for switching to the M-polar state and n_{KAI} = 3.1 ± 0.1 for switching to the O-polar state.

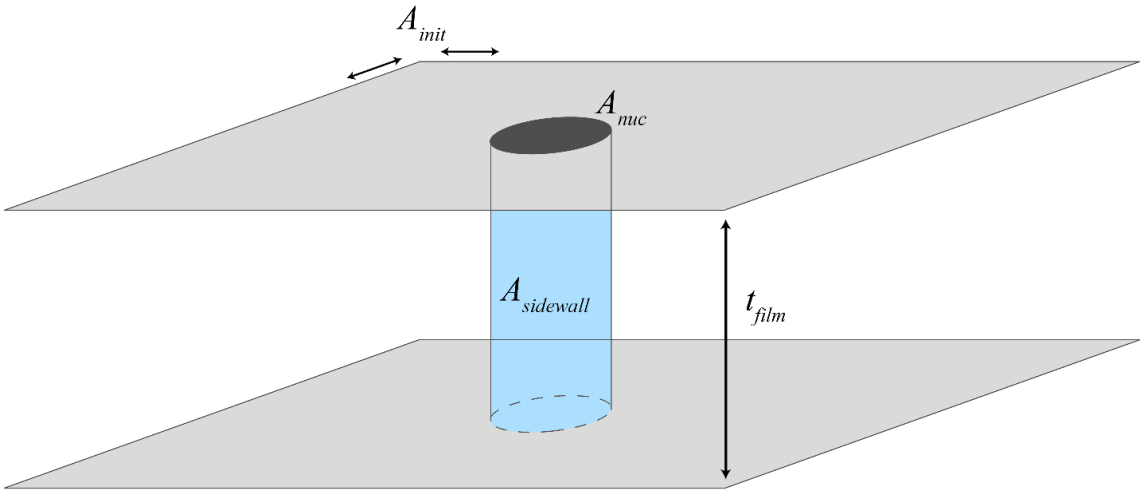

Figure **5-S**: Representation of the area parameters used for extracting the distribution function from the nucleation rate for the SNNG model, assuming only nucleation occurs. A_{init} incudes A_{nuc}. The cylinder is an ideal switched column sandwiched between the top and bottom electrodes, and surrounded by unswitched material.

Both the area of the remaining available sidewalls of switched domains and the remaining electrode areas were important for calculating the nucleation density (see Figure 5-S10). Nucleation at the sidewalls begins to dominate as switching progresses and the ratio of the domain sidewall area to the electrode surface area increases.

Sidewall areas were calculated as:

$$A_{sidewall} = 2dt_{film} \quad \text{(S14)}$$

where $A_{sidewall}$ is the surface area of the sidewall for a single column, d is the diameter of a column, and t_{film} is the film thickness.

$$A_{nuc} = \pi \left(\frac{d}{2}\right)^2 \quad \text{(S15)}$$

where A_{nuc} is the surface area of a column on the electrode surface.

$$A_{total} = (1 - f(t))(A_{init} + N_{nuc}A_{sidewall}) \quad \text{(S16)}$$

A_{total} is the total surface area in a capacitor where nuclei can form (both the remaining electrode surface area and remaining domain sidewalls), $f(t)$ is the fraction of transformed polarization, and A_{init} is the surface area of the top and bottom electrodes, and N_{nuc} is the number of nuclei, defined as:

$$N_{nuc} = \frac{f(t)\left(\frac{1}{2}A_{init}\right)}{A_{nuc}} \quad \text{(S17)}$$

The shape of the distribution function for nucleation is then calculated by:

$$D(t) = \frac{\dot{N}(t)}{N(\infty)} \cdot A_{total} \quad \text{(S18)}$$

where D(t) resembles the shape of the distribution function, and $\frac{\dot{N}(t)}{N(\infty)}$ is the nucleation rate from the SNNG model. D(t) was then normalized for plotting:

$$f(D(t)) = \frac{D(t)}{\max\left[D(t)\right]} \quad \text{(S19)}$$

MATLAB was used to calculate the distribution functions. It should be noted that self-consistency was not explicitly solved for. Instead, the effect of domain size on the shape of the nucleation curve was shown from 1 to 50 nm, to provide an estimate on the domain size.

5.5.9 The NLS Model

Fitting to the NLS model presented by Jo et al. was performed in two steps. First, the cumulative distribution function of the Lorentzian was fit to the normalized experimental curve

by varying the parameters t_1 and w, which are the center position and half-width half-maximum of the distribution function (see equation A7). The position of the curve was matched by varying t_1, and the slope of the curve was matched by varying w. Because the cumulative distribution function of the Lorentzian does not involve integration, this step is fast and can be completed in approximately 1 second. Fitting the CDF of the Lorentzian provided adequate initial values of the parameters t_1 and w for the next step. The second step was fitting the experimental curve to the NLS model in equation A7. The parameters were varied again. Because this step involves an integral, it is more computationally expensive and takes several minutes to complete. The parameter A is a scale factor that was varied in order to match the scale of the fitted NLS curve to the experimental curve.

5.5.10 The Gaussian Model

The Gaussian distribution is simple to fit to the experimental data. Only the position of the curve was varied to fit the experimental curve by modifying σ, which is the mode of the distribution function (see equation A9). As the Gaussian distribution does not involve any integrals, the final result of fitting is produced in less than 1 second.

5.5.11 The Combined Gaussian and Inverse Gamma Model

The combined model uses the Gaussian and inverse gamma distributions to fit the experimental curve. The Gaussian is initially fit to the curve. Between 50 and 80% of the total polarization reversal, the error between the Gaussian fit and the experimental curve exceeds 0.01 fraction of the total polarization. From that time, the inverse gamma distribution is applied to the experimental curve (see equation S11). The inverse gamma fit is generated independently from

the Gaussian fit, but uses the same t_0 setpoint. To fit the inverse gamma model, the scale parameter $\boldsymbol{\beta}$ was varied to match the y-axis (polarization fraction) tail of the curve at a position between 0.85 and 0.95 fraction of the total reversed polarization. The shape parameter $\boldsymbol{\alpha}$ was varied to match the body of the curve at a position on the x-axis (time) between 0.6 and 0.8 fraction of the total reversed polarization. As neither distribution involves an integral, the final result of fitting is produced in approximately 2 seconds.

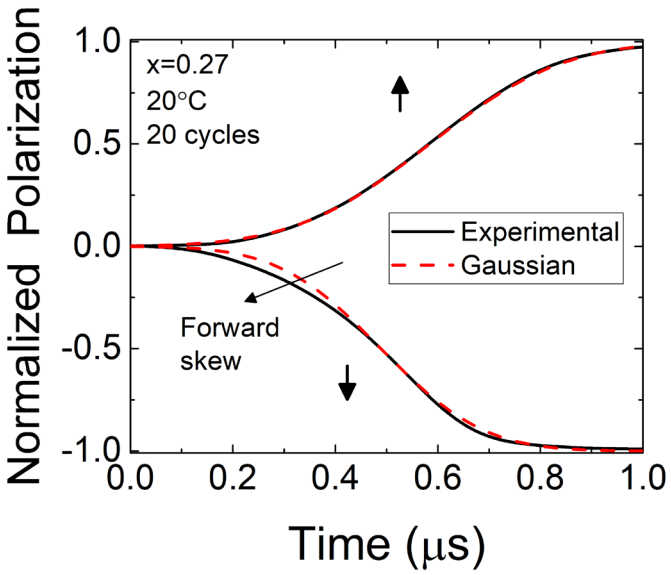

Figure **5-S11**: Forward skew in the Gaussian fit in films with x=0.27 when switching to the O-polar state suggests that the switching mechanism is slightly different than switching to the M-polar state, and may be influenced by pre-existing nuclei. The applied field for switching to the M-polar state was 4.1 MV cm^{-1}, and it was 3.9 MV cm^{-1} for switching to the O-polar state.

References

[1] Fichtner, S., Wolff, N., Lofink, F., Kienle, L., & Wagner, B. (2019). AlScN: A III-V semiconductor based ferroelectric. *Journal of Applied Physics*, *125*(11), 114103.

[2] Hayden, J., Hossain, M. D., Xiong, Y., Ferri, K., Zhu, W., Imperatore, M. V., Giebink, N., Trolier-McKinstry, S, Dabo, I. & Maria, J-P. (2021). Ferroelectricity in boron-substituted aluminum nitride thin films. *Physical Review Materials*, *5*(4), 044412.

[3] Ferri, K., Bachu, S., Zhu, W., Imperatore, M., Hayden, J., Alem, N., Giebink, N., Trolier-McKinstry, S. & Maria, J-P. (2021). Ferroelectrics everywhere: Ferroelectricity in magnesium substituted zinc oxide thin films. *Journal of Applied Physics*, *130*(4), 044101.

[4] Wang, D., Wang, P., Wang, B., & Mi, Z. (2021). Fully epitaxial ferroelectric ScGaN grown on GaN by molecular beam epitaxy. *Applied Physics Letters*, *119*(11), 111902.

[5] Uehara, M., Mizutani, R., Yasuoka, S., Shiraishi, T., Shimizu, T., Yamada, H., Akiyama, M., & Funakubo, H. (2021). Demonstration of ferroelectricity in ScGaN thin film using sputtering method. *Applied Physics Letters*, *119*(17), 172901.

[6] Wang, D., Mondal, S., Liu, J., Hu, M., Wang, P., Yang, S., Wang, D., Xiao, Y., Wu, Y., Ma, T., & Mi, Z. (2023). Ferroelectric YAlN grown by molecular beam epitaxy. *Applied Physics Letters, 123*(3), 033504.

[7] Moriwake, H., Yokoi, R., Taguchi, A., Ogawa, T., Fisher, C. A., Kuwabara, A., Sato, Y., Shimizu, T., Hamasaki, Y., Takashima, H., & Itoh, M. (2020). A computational search for wurtzite-structured ferroelectrics with low coercive voltages. *APL Materials*, *8*(12), 121102.

[8] Olsson, R. H., Tang, Z., & D'Agati, M. (2020, March). Doping of aluminum nitride and the impact on thin film piezoelectric and ferroelectric device performance. In *2020 IEEE Custom Integrated Circuits Conference* (CICC) (pp. 1-6). IEEE.

[9] Fujimura, J., Adachi, Y., Takahashi, T., & Kobayashi, T. (2022). Impact of piezo-phototronic effect on ZnMgO/Se heterojunction photovoltaic devices. *Nano Energy, 99*, 107385.

[10] Yuan, X., Yamada, T., & Meng, L. (2022). Strong electro-optic effect in Mg incorporated ZnO thin films. *Applied Physics Letters, 121*(15), 152903.

[11] Bose, S., Chevallier, C., Ould Saad Hamady, S., & Fressengeas, N. (2022). Optical and Electrical Properties of ZnMgO with High Mg Content Elaborated by Ultrasonic Spray Pyrolysis Using Water-Based Solutions. *Physica Status Solidi (a), 219*(16), 2200091.

[12] Zu, R., Ryu, G., Kelley, K. P., Baksa, S. M., Jacques, L. C., Wang, B., Ferri, K., He, J., Chen, L. Q., Dabo, I., Trolier-McKinstry, S., Maria, J-P., & Gopalan, V. (2023). Large Enhancements in Optical and Piezoelectric Properties in Ferroelectric $Zn_{1-x}Mg_xO$ Thin Films through Engineering Electronic and Ionic Anharmonicities. *Advanced Physics Research*, *2*(12), 2300003.

[13] Suceava, A., Hayden, J., Kelley, K. P., Xiong, Y., Fazlioglu-Yalcin, B., Dabo, I., Trolier-McKinstry, S., Maria, J-P., & Gopalan, V. (2023). Enhancement of second-order optical nonlinearities and nanoscale periodic domain patterning in ferroelectric boron-substituted aluminum nitride thin films. *Optical Materials Express*, *13*(6), 1522-1534.

[14] Kim, K. H., Han, Z., Zhang, Y., Musavigharavi, P., Zheng, J., Pradhan, D. K., Stach, E. A., Olsson, R. H., & Jariwala, D. (2024). Multi-State, Ultra-thin, BEOL-Compatible AlScN Ferroelectric Diodes. *ACS Nano, 18(24)*, 15925-15934.

[15] Qin, H., He, N., Han, C., Zhang, M., Wang, Y., Hu, R., Wu, J., Shao, W., Saadi, M., Zhang, H., Hu, Y., Liu, Y., Wang, X., & Tong, Y. (2024). Perspectives of Ferroelectric Wurtzite AlScN: Material Characteristics, Preparation, and Applications in Advanced Memory Devices. *Nanomaterials, 14*(11), 986.

[16] Schönweger, G., Wolff, N., Islam, M. R., Gremmel, M., Petraru, A., Kienle, L., Kohlstedt, H., & Fichtner, S. (2023). In-grain ferroelectric switching in sub-5 nm thin $Al_{0.74}Sc_{0.26}N$ films at 1 V. *Advanced Science, 10*(25), 2302296.

[17]Pradhan, D. K., Moore, D. C., Kim, G., He, Y., Musavigharavi, P., Kim, K. H., Sharma, N., Han, Z., Du, X., Puli, V. S., Stach, E. A., Kennedy, W. J., Glavin, N. R., Olsson, R. H., & Jariwala, D. (2024). A scalable ferroelectric non-volatile memory operating at 600° C. *Nature Electronics*, *7*, 348-355.

[18] Jacques, L., Ryu, G., Goodling, D., Bachu, S., Taheri, R., Yousefian, P., Shetty, S., Akkopru-Akgun, B., Randall, C., Alem, N., Maria, J. P., & Trolier-McKinstry, S. (2023). Wake up and retention in zinc magnesium oxide ferroelectric films. *Journal of Applied Physics, 133*(22), 224102.

[19] Calderon, S., Hayden, J., Baksa, S. M., Tzou, W., Trolier-McKinstry, S., Dabo, I., Maria, J. P., & Dickey, E. C. (2023). Atomic-scale polarization switching in wurtzite ferroelectrics. *Science, 380*(6649), 1034-1038.

[20] Wolff, N., Schönweger, G., Streicher, I., Islam, M. R., Braun, N., Straňák, P., Kirste, L., Prescher, M., Lotnyk, A., Kohlstedt, H., Leone, S., Kienle, L., & Fichtner, S. (2024). Demonstration and STEM Analysis of Ferroelectric Switching in MOCVD-Grown Single Crystalline $Al_{0.85}Sc_{0.15}N$. *Advanced Physics Research*, 2300113.

[21]Lee, C. W., Yazawa, K., Zakutayev, A., Brennecka, G. L., & Gorai, P. (2024). Switching it up: New mechanisms revealed in wurtzite-type ferroelectrics. *Science Advances*, *10*(20), eadl0848.

[22] Baksa, S. M., Gelin, S., Oturak, S., Trolier-McKinstry, S. E., Maria, J. P., Rappe, A. M., & Dabo, I. (2023). Strain fluctuations unlock ferroelectricity in wurtzites. *arXiv preprint arXiv:2311.05413*.

[23] Johnson, W. A., & Mehl, R. F. (1939) Reaction Kinetics in Processes of Nucleation and Growth. *Transaction Metallurgical Society AIME*, *135*, 416-442.

[24] Orihara, H., Hashimoto, S., & Ishibashi, Y. (1994). A theory of DE hysteresis loop based on the Avrami model. *Journal of the Physical Society of Japan*, *63*(3), 1031-1035.

[25] Kolmogorov, A. N. (1937). Izv Akad Nauk SSSR. *Ser Materm*, *3*, 355-359.

[26] Avrami, M. (1940). Kinetics of phase change. II transformation-time relations for random distribution of nuclei. *The Journal of Chemical Physics*, *8*(2), 212-224.

[27] Erofe'ev, B. V. (1946). Generalized equation of chemical kinetics and its application in reactions involving solids. *Comptes Rendus de l'Académie des Sciences de l'URSS*, *52*(51), 1-514.

[28] Yazawa, K., Hayden, J., Maria, J. P., Zhu, W., Trolier-McKinstry, S., Zakutayev, A., & Brennecka, G. L. (2023). Anomalously abrupt switching of wurtzite-structured ferroelectrics: simultaneous non-linear nucleation and growth model. *Materials Horizons*, *10*(8), 2936-2944.

[29] Yazawa, K., Drury, D., Hayden, J., Maria, J. P., Trolier-McKinstry, S., Zakutayev, A., & Brennecka, G. L. (2024). Polarity effects on wake-up behavior of $Al_{0.94}B_{0.06}N$ ferroelectrics. *Journal of the American Ceramic Society*, *107*(3), 1523-1532.

[30]Fanfoni, M., & Tomellini, M. (1998). The Johnson-Mehl-Avrami-Kolmogorov model: a brief review. *Il Nuovo Cimento D*, *20*, 1171-1182.

[31] Tagantsev, A. K., Stolichnov, I., Setter, N., Cross, J. S., & Tsukada, M. (2002). Non-Kolmogorov-Avrami switching kinetics in ferroelectric thin films. *Physical Review B*, *66*(21), 214109.

[32] Jo, J. Y., Han, H. S., Yoon, J. G., Song, T. K., Kim, S. H., & Noh, T. W. (2007). Domain switching kinetics in disordered ferroelectric thin films. *Physical Review Letters*, *99*(26), 267602.

[33] Guido, R., Lu, H., Lomenzo, P. D., Mikolajick, T., Gruverman, A., & Schroeder, U. (2024). Kinetics of N-to M-Polar Switching in Ferroelectric $Al_{1-x}Sc_xN$ Capacitors. *Advanced Science, 11*(16), 2308797.

[34] Gao, J., Chien, Y. C., Li, L., Lee, H. K., Samanta, S., Varghese, B., Xiang, H., Li, M., Liu, C., Zhu, Y., Chen, L., & Ang, K. W. (2024). Ferroelectric Aluminum Scandium Nitride Transistors with Intrinsic Switching Characteristics and Artificial Synaptic Functions for Neuromorphic Computing. *Small*, 2404711.

[35] Lu, H., Schönweger, G., Petraru, A., Kohlstedt, H., Fichtner, S., & Gruverman, A. (2024). Domain dynamics and resistive switching in ferroelectric $Al_{1-x}Sc_xN$ thin film capacitors. *Advanced Functional Materials*, *34*(28), 2315169.

[36] Behrendt, D., Samanta, A., & Rappe, A. M. (2024). Ferroelectric Fractals: Switching Mechanism of Wurtzite AlN. *arXiv preprint arXiv:2410.18816*.

[37] Merz, W. J. (1954). Domain formation and domain wall motions in ferroelectric $BaTiO_3$ single crystals. *Physical Review*, *95*(3), 690.

[38] Scrymgeour, D. A., & Gopalan, V. (2005). Nanoscale piezoelectric response across a single antiparallel ferroelectric domain wall. *Physical Review B—Condensed Matter and Materials Physics, 72*(2), 024103.

[39] Gruverman, A., Rodriguez, B. J., Dehoff, C., Waldrep, J. D., Kingon, A. I., Nemanich, R. J., & Cross, J. S. (2005). Direct studies of domain switching dynamics in thin film ferroelectric capacitors. *Applied Physics Letters*, *87*(8), 082902.

[40] Sepehrinezhad, A., Baksa, S. M., Dabo, I., & van Duin, A. C. (2024). ReaxFF Reactive Force Field for Exploring Electronically Switchable Polarization in $Zn_{1-x}Mg_xO$ Ferroelectric Semiconductors. *The Journal of Physical Chemistry C*, *128*(30), 12534-12543.

[41] Lines, M. E., & Glass, A. M. (2001). *Principles and applications of ferroelectrics and related materials*. Oxford university press.

[42] Weiss, N. A. (2012). *Introductory Statistics* (9th ed.). Pearson.

[43] Schneider, C. A., Rasband, W. S., & Eliceiri, K. W. (2012). NIH Image to ImageJ: 25 years of image analysis. *Nature Methods*, *9*(7), 671-675.

[44] Yazawa, K., Zakutayev, A., & Brennecka, G. L. (2022). High-speed and high-power ferroelectric switching current measurement instrument for materials with large coercive voltage and remanent polarization. *Sensors, 22*(24), 9659.

[45] Zhang, L. Q., Ye, Z. Z., Huang, J. Y., Lu, B., He, H. P., Lu, J. G., Zhang, Y. Z., Jiang, J., Zhang, J., Wu, K. W., & Zhang, W. G. (2011). Fabrication and properties of p-type K doped $Zn_{1-x}Mg_xO$ thin film. *Journal of Alloys and Compounds, 509*(27), 7405-7409.

[46] Ohtomo, A., Kawasaki, M., Koida, T., Masubuchi, K., Koinuma, H., Sakurai, Y., Yoshida, Y., Yasuda, T., & Segawa, Y. (1998). $Mg_xZn_{1-x}O$ as a II–VI widegap semiconductor alloy. *Applied Physics Letters*, *72*(19), 2466-2468.

[47]Bhattacharya, P., Das, R. R., & Katiyar, R. S. (2004). Comparative study of Mg doped ZnO and multilayer ZnO/MgO thin films. *Thin Solid Films*, *447*, 564-567.

[48] Zuo, Y., Lin, H., Guo, J., Yuan, Y., He, H., Li, Y., Xiao, Y., Li, X., Zhu, K., Wang, T., Jing, X., Wen, C., & Lanza, M. (2020). Effect of the pressure exerted by probe station tips in the electrical characteristics of memristors. *Advanced Electronic Materials*, *6*(3), 1901226.

[49] He, F., Zhu, W., Hayden, J., Casamento, J., Tran, Q., Kang, K., Song, Y., Akkopru-Akgun, B., Yang, J. I., Tipsawat, P., Brennecka, G., Choi, S., Jackson, T. N., Maria, J. P., & Trolier-McKinstry, S. (2024). Frequency dependence of wake-up and fatigue characteristics in ferroelectric $Al_{0.93}B_{0.07}N$ thin films. *Acta Materialia, 266*, 119678.

[50] Guido, R., Mikolajick, T., Schroeder, U., & Lomenzo, P. D. (2023). Role of Defects in the Breakdown Phenomenon of $Al_{1-x}Sc_xN$: From Ferroelectric to Filamentary Resistive Switching. *Nano Letters, 23*(15), 7213-7220.

[51] Pantel, D., Chu, Y. H., Martin, L. W., Ramesh, R., Hesse, D., & Alexe, M. (2010). Switching kinetics in epitaxial $BiFeO_3$ thin films. *Journal of Applied Physics*, *107*(8).

[52] Gruverman, A., Rodriguez, B. J., Dehoff, C., Waldrep, J. D., Kingon, A. I., Nemanich, R. J., & Cross, J. S. (2005). Direct studies of domain switching dynamics in thin film ferroelectric capacitors. *Applied Physics Letters*, *87*(8), 082902.

[53] Gelman, A., Carlin, J. B., Stern, H. S., Dunson, D. B., Vehtari, A., & Rubin, D. B. (2003). *Bayesian Data Analysis* (2nd ed.). Taylor & Francis.

[54] Tatsumi, T., Fujita, M., Kawamoto, N., Sasajima, M., & Horikoshi, Y. (2004). Intrinsic defects in ZnO films grown by molecular beam epitaxy. *Japanese Journal of Applied Physics*, *43*(5R), 2602.

[55] Park, S. H., Kim, K. B., Seo, S. Y., Kim, S. H., & Han, S. W. (2006). Structural and optical properties of $Zn_{1-x}Mg_xO$ thin films synthesized with metal organic chemical vapor deposition. *Journal of Electronic Materials*, *35*, 1680-1684.

[56] Bassiri-Gharb, N., Fujii, I., Hong, E., Trolier-McKinstry, S., Taylor, D. V., & Damjanovic, D. (2007). Domain wall contributions to the properties of piezoelectric thin films. *Journal of Electroceramics*, *19*, 49-67.

[57] Keech, R., Shetty, S., Kuroda, M. A., Hu Liu, X., Martyna, G. J., Newns, D. M., & Trolier-McKinstry, S. (2014). Lateral scaling of Pb $(Mg_{1/3}Nb_{2/3})O_3$-$PbTiO_3$ thin films for piezoelectric logic applications. *Journal of Applied Physics*, *115*(23).

[58] Gauss, C. F. (1857). *Theory of the motion of the heavenly bodies moving about the sun in conic sections: a translation of Gauss's" Theoria Motus." with an appendix*. Little, Brown.

[59] Wolfram Language. (2008). InverseGammaDistribution. Wolfram Language & System Documentation Center. Retrieved from https://reference.wolfram.com/language/ref/InverseGammaDistribution.html

[60] Abid, S. H., & Al-Hassany, S. A. (2016). On the inverted gamma distribution. *International Journal of Systems Science and Applied Mathematics*, *1*(3), 16-22.

Chapter 6

A Non-aqueous Process for Remote Probe Contact on (Zn,Mg)O

6.1 Introduction

It was routinely observed in ZMO thin films that the dielectric breakdown channel forms directly underneath the probe contact to the top electrode. One possible reason is due to stress from the probe contact. For example, lower breakdown strengths and anomalous leakage current characteristics were reported for metal-insulator-metal memristor devices when the probe tip was applied to the surface of the active layer, as opposed to when it was not (see Figure 6-1).[1] In addition, the heat generated during dielectric breakdown is enough to melt and/or to vaporize both the ZMO and the top and bottom electrode materials, as shown in Figure 6-2 (see relevant calculations and justifications in Appendix B-1). This degrades low-field measurements. Therefore, it became desirable to remotely contact small capacitors of ZMO (≤ 20 μm in diameter) to ensure accurate data collection.

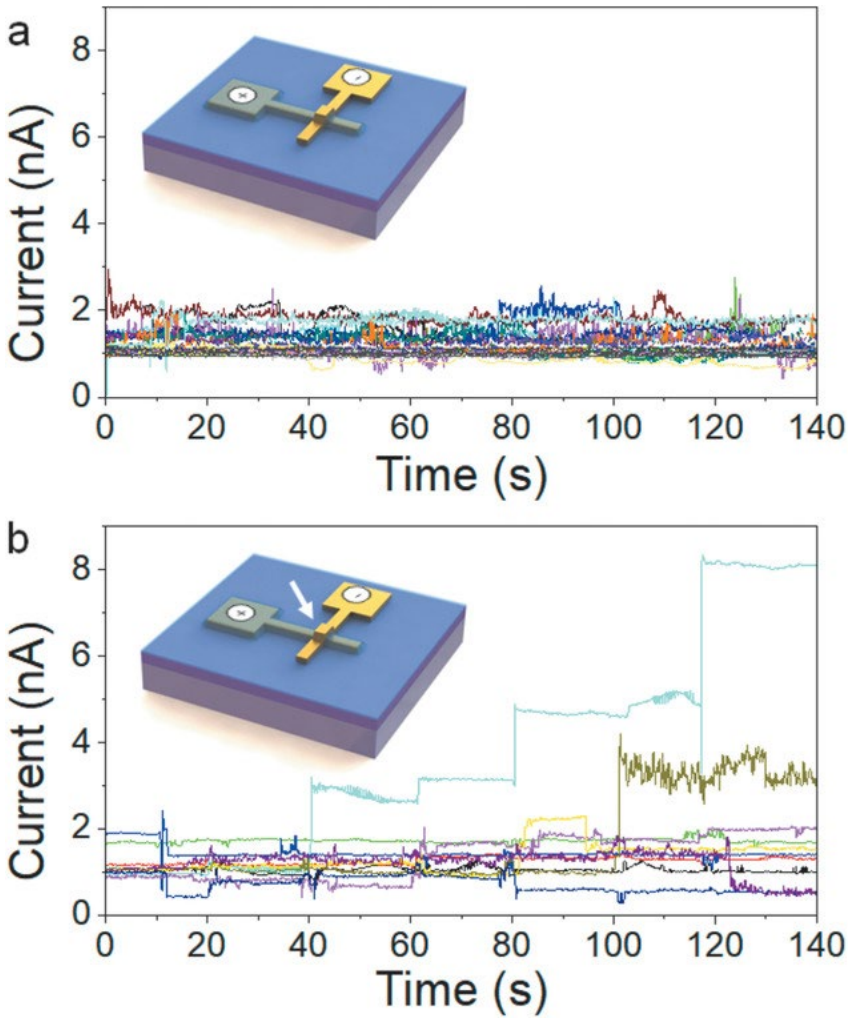

Figure 6-**1**: Current vs. time plots for $Ag/Al_2O_3/Au$ memristors. The top plot (a) shows the memristor performance without the application of the probe tip on the active area. The bottom plot (b) shows memristor performance with a probe tip applied to the memristor surface. The probe tip is indicated by the white arrow.[1]

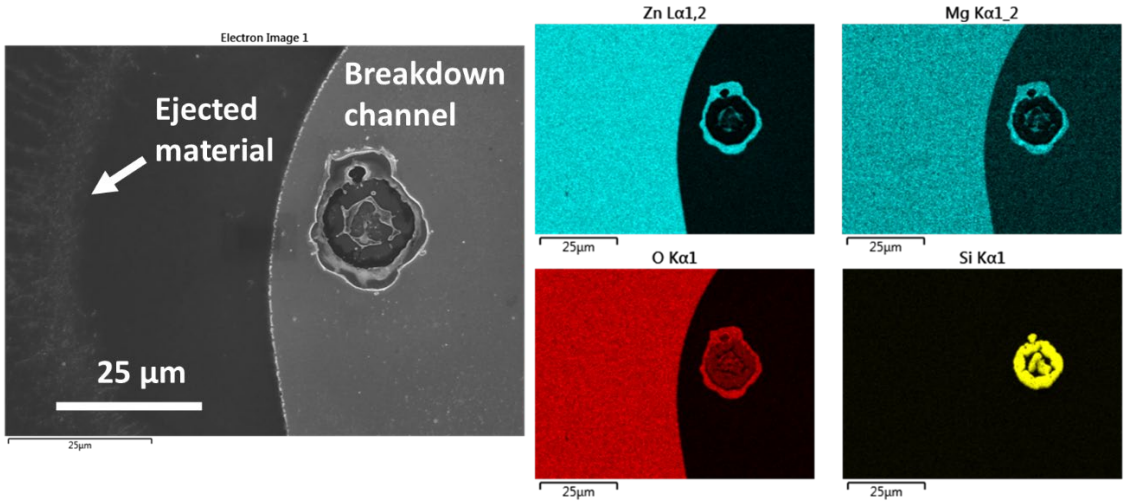

Figure 6-**2**: A dielectric breakdown channel observed in ZMO.

Fabricating a device for ZMO poses some challenges. First, the process must be non-aqueous – that is, water must not contact the surface of ZMO throughout the process. Second, reactive ion etching (RIE) of the ZMO layer was to be avoided in order to protect the ferroelectric layer and prevent unwanted surface conductivity.[2] Thus, in this chapter is demonstrated a 3-layer process to fabricate a remote probe contact device via a non-aqueous process, and without RIE, as shown in Figures 6-3 and 6-4.

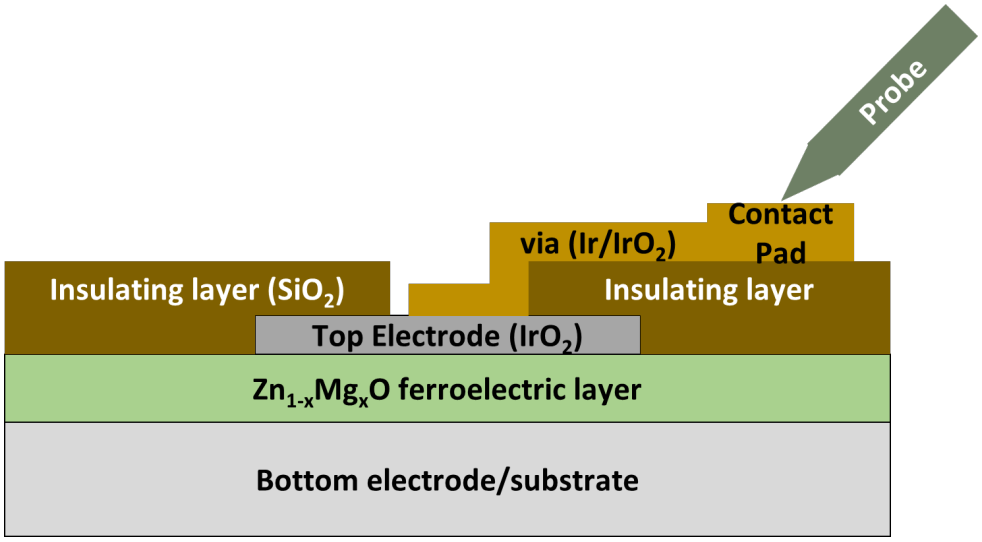

Figure 6-**3**: A schematic of the non-contact pad device.

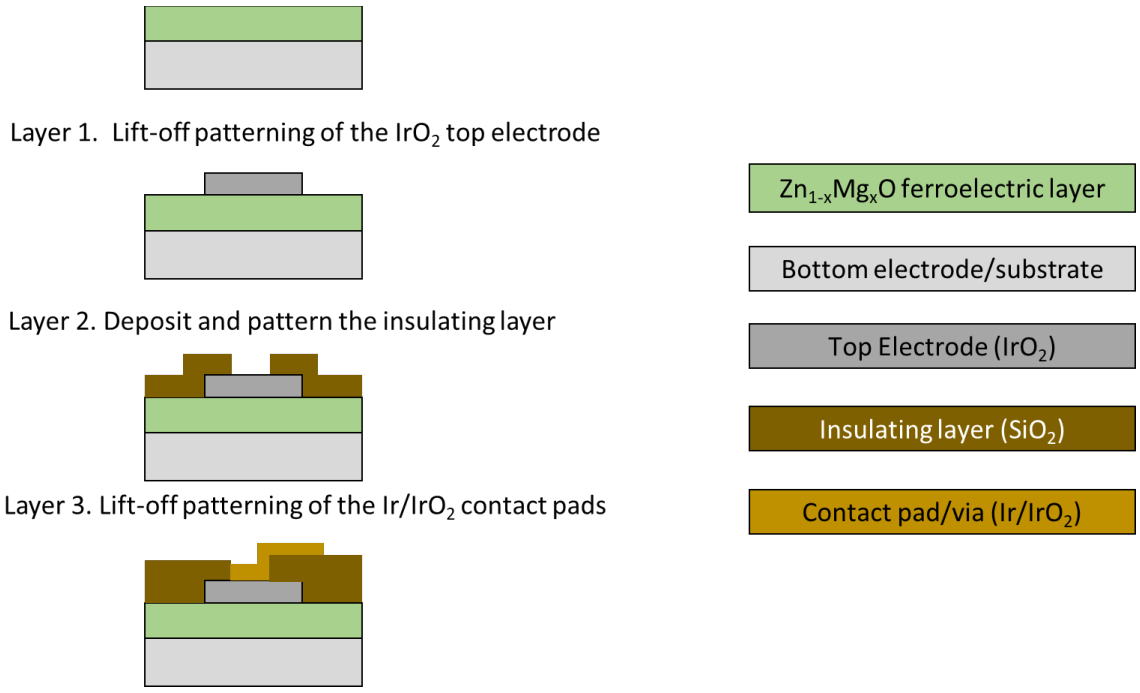

Figure 6-**4**: A schematic of the layer-by-layer progress of the non-contact pad device.

6.2 Layer One

The first layer in the three-layer device fabrication process is the deposition of the IrO_2 top electrode. Choice of top electrode is critical not only for device performance, but because it also acts as an HF etch stop during the next layer, layer 2. Therefore, it is critical that the IrO_2 top electrode be dense enough to prevent HF from penetrating the top electrode to the underlying ZMO.

The non-aqueous lithographic patterning procedure listed in Table B-1 of the Appendix was used to pattern the top electrodes. The MLA non-contact alignment tool was used for exposure. IrO_2 was reactively sputtered as outlined in Table 3-3 of the experimental procedure chapter. The IrO_2 top electrodes were patterned according to the design in Figure 6-5. Top electrodes were positioned with centers 200 µm apart in both the vertical and horizontal directions (see Figure 6-5). Spacings were designed to maximize yield while mitigating interference between capacitors due to dielectric breakdown events (see Appendix C). The top electrode diameters were 20 µm, and thicknesses were 70 nm. Exposures and non-contact alignments were performed using a Heidelberg MLA 150 Direct Write Exposure Tool, and laser energies 200 mJ at a wavelength of 375 nm.

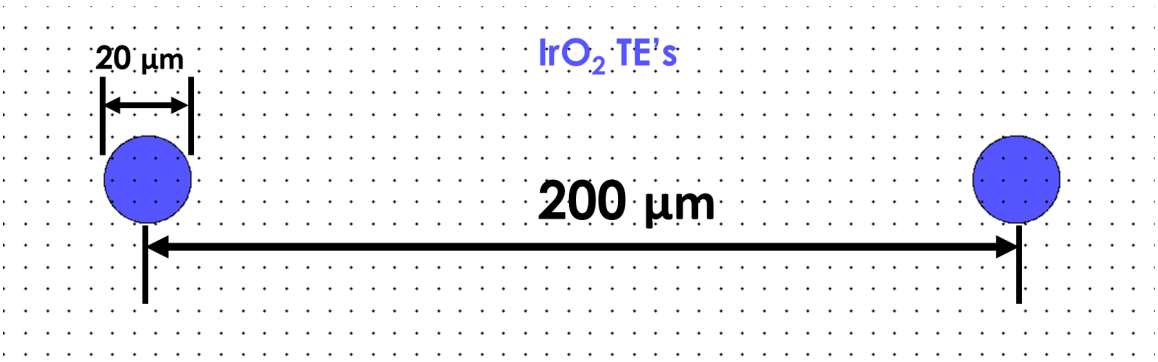

Figure **6-5**: A diagram of the IrO_2 top electrode diameters and inter-electrode spacing.

6.3 Layer Two

Layer 2 involves:

1) The deposition of a SiO_2 insulating layer that is thick enough to mitigate parasitic capacitive contributions to the ferroelectric response from the layer.
2) Patterning and etching of vias through the SiO_2 layer and to the top electrode.

Thus, after this layer the ZMO layer is totally covered by SiO_2 and IrO_2 to form a hermetic seal. This should also encourage preservation of ZMO should the samples be exposed to humid environments.

A 500 nm thick layer of SiO_2 was deposited using the Temescal F-2000 E-beam evaporator to evaporate pure SiO_2 pellets. Two options were considered for depositing the SiO_2 layer:

1) Patterning followed by deposition of the SiO_2 layer and lift-off to form vias to the top electrode. (1^{st} generation device)
2) Blanket deposition of SiO_2 followed by etching vias to the top electrode. (2^{nd} generation device)

For the first option, the process outlined in Table 6-1 was used. LOR 10B was used to provide a 1 μm height for the undercut profile, which was necessary for the 500 nm thick SiO_2 layer.

This process was unsuccessful due to peel-back of the SiO_2 layer at the end of the lift-off process (see Figure 6-6). It was discovered that the combination of PMMA and LOR series lift-off resists causes an interphase layer that is not easily removed by CD-26 or toluene during the development steps. This layer forms a lip that, when removed, forces the SiO_2 layer to peel (see Figure 6-7). For this reason, wet etching of the SiO_2 layer was chosen for the 2^{nd} generation device in order to form vias through the insulating layer and to the top electrode.

Table 6-**1**: Non-aqueous patterning and lift-off procedure for the SiO_2 layer.

	Non-aqueous Lift-Off Procedure
1	PMMA A3 in pipette, and spin @ 4,000 RPM for 60 s (sample should be clean before this step)
2	Bake for 10 minutes @ 190°C on hotplate.
3	LOR 10B in pipette, and spin @ 4,000 RPM for 40 s
4	Bake for 3 minutes @ 180°C on hotplate
5	SPR 3012 in pipette, and spin @ 4,000 RPM for 40 s
6	Bake for 1 minute @ 95°C on hotplate
7	Exposure with the Heidelberg MLA 200 mJ/cm^2 exposure (λ = 375 nm)
8	Develop in 50/50 ratio of Microposit/DI water for 60 seconds.
9	Hard bake at 120°C for 5 minutes
10	Develop the undercut in 50/50 ratio of Microposit/DI water for 150 seconds.
9	Expose the film to high power UV (SRP 3012 acts as a UV mask) →Fusion UV (λ = 260 nm, 385 mW/cm^2) 60 seconds exposure (use the ENG-2 recipe)
10	Expose to toluene for 3 minutes, followed by rinse in IPA
12	M4L Plasma Ash to clean the surface of residual PMMA Power: 300 W, 20 minutes**; He 50 mTorr; O_2 150 mTorr; Regulate: 550 mTorr
	Check with the optical microscope to make sure all the residual resist and PMMA is removed.
Deposition	Temescal E-beam evaporator; 0.2 Å/s for the first 20 nm and 2 Å/s for the remaining 480 nm.
	Lift-Off Procedure
1	Leave samples in a sonicating acetone bath for 15 minutes, or until the SiO_2 plugs are removed. They will appear as numerous small floating specs after sonication.
2	M4L Plasma Ash to clean the TE's of residual PMMA Power: 300 W, xx minutes; He 50 mTorr; O_2 150 mTorr; Regulate: 550 mTorr

** This was split into three steps. The sample will get hot.

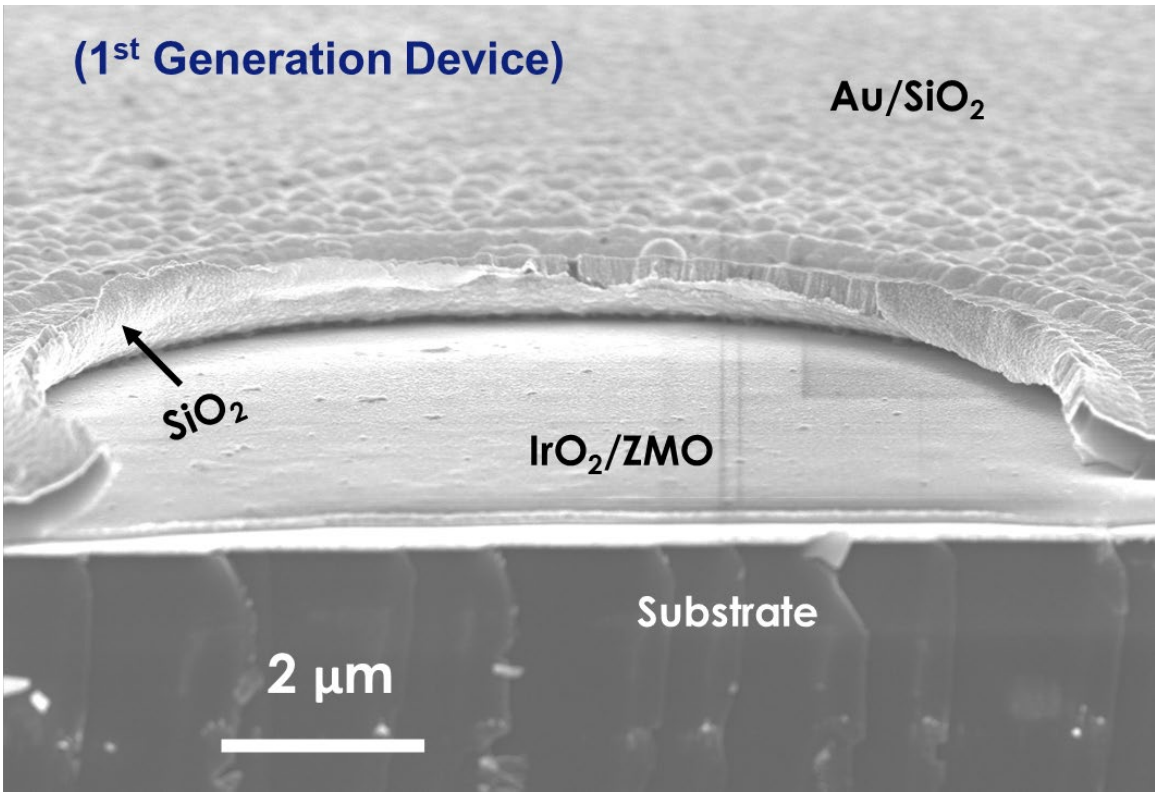

Figure **6-6**: FESEM image of peel-back of the SiO_2 layer in a finished 1st generation device.

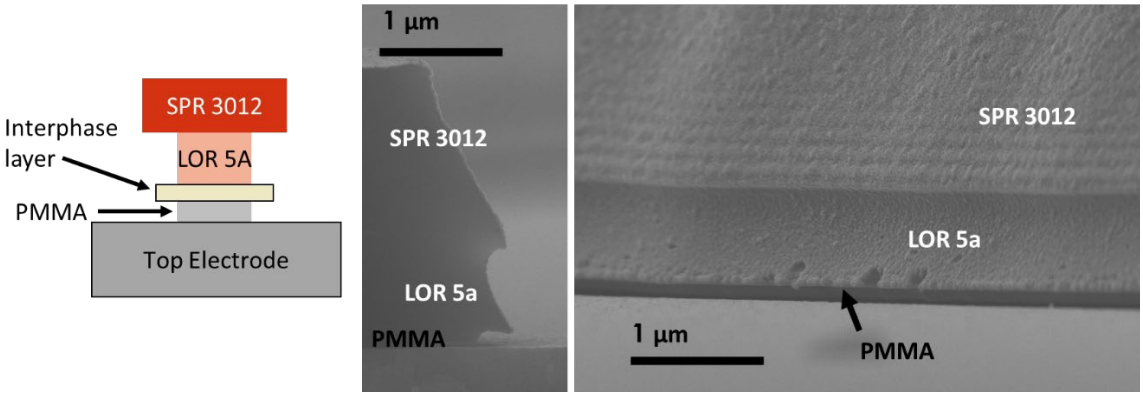

Figure **6-7**: Peel-back of the SiO_2 layer is caused by the liftoff profile and the interphase layer between LOR and PMMA.

Buffered oxide etchant (BOE) with a ratio of 10:1 (NH_4F:HF) was the preferred etchant for etching through SiO_2. To pattern the etch, Microposit S1827 photoresist (2.7 μm thick) was used due to its superior resistance towards chemical etching compared to SPR photoresists. The etch was performed at room temperature and lasted for 10 minutes, with an expected etch rate of ≥ 50 nm/minute.[3] For this reason, the etching pattern was designed to accommodate for several microns of undercut into the SiO_2 layer, and 8 μm diameter vias were patterned over the 20 μm diameter top electrodes, as shown in Figures 6-8 and 6-9.

Figure **6-8**: Pattern of the 8 μm diameter wet etch vias over the top electrodes.

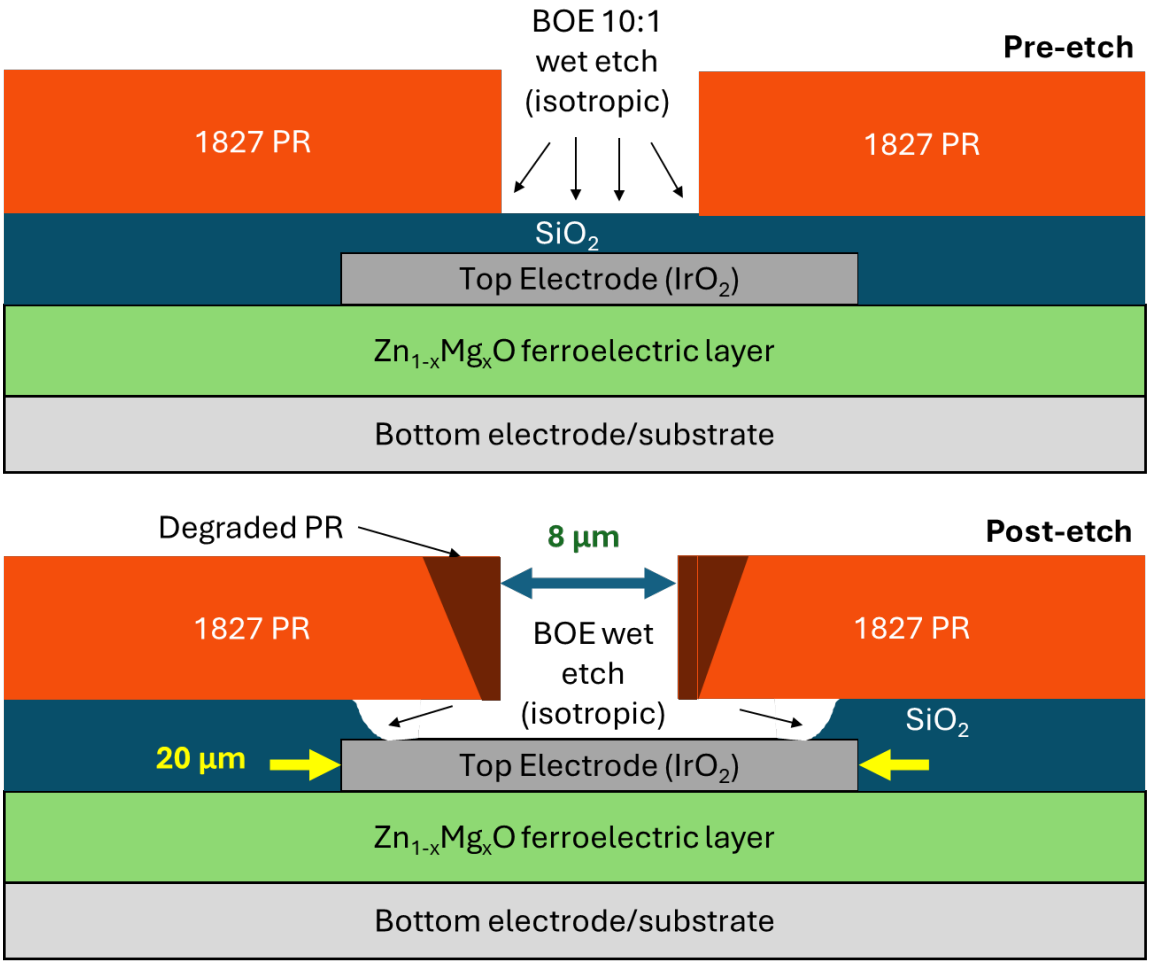

Figure **6-9**: Cross-sectional schematic of the wet etching profile for layer 2.

The highly reactive BOE 10:1 was found to degrade the photoresist at the edges of the pattern. However, the 8 µm pattern area was small enough to accommodate for this, and for misalignment of the write exposure tool (MLA), without exposing the ZMO layer to BOE and consequently destroying the device. The successful etch profile is shown in Figure 6-10. The diagonal edge profile is desirable for sputtering the probing contact pad in the next layer, and results of the etch are shown in Table 6-2.

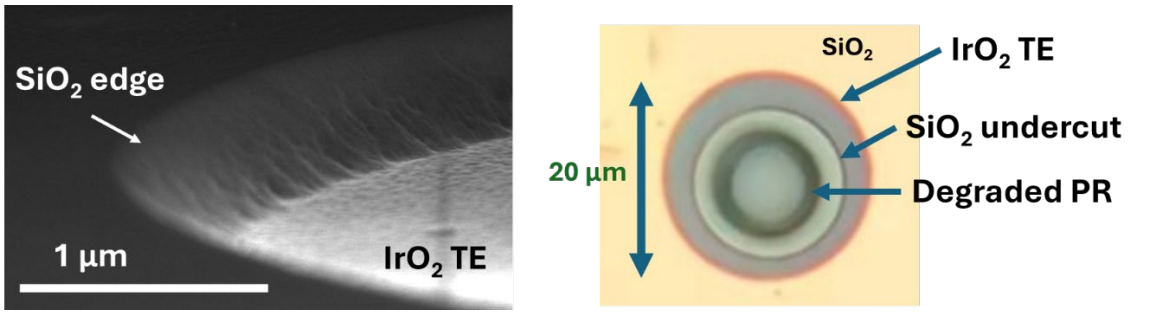

Figure **6-10**: FESEM image (left) reveals the desirable edge profile of the BOE etch on SIO_2, and the IrO_2 top electrode as an effective etch stop (left). Optical microscope (right) reveals the patterned S1827 resist, degraded resist area, and SiO_2 undercut, over the IrO_2 top electrode.

Table **6-2**: Results etching in BOE 10:1 for 10 minutes.

Feature	Size
IrO_2 TE	10 µm radius
SiO_2 undercut	~ 3.8 µm radius
Degraded PR	~ 1.8 µm radius

The procedures for this process are shown in Table 6-3. It is of note that when working with HF, it is important to remove the photoresist as soon as the etching process is completed. The reason for this is because HF will continue to etch the photoresist after the etching process is completed, and if left long enough, it can eat through the photoresist and destroy the device. Extra precaution was taken in this case to first perform an O_2 plasma ash immediately after the etch process to remove the most heavily contaminated photoresist from the sample. Then the remaining photoresist was removed by spraying acetone on the sample held vertically until all the photoresist was removed. Lastly, the sample was subjected to a second O_2 plasma ash to ensure

no HF remained on the sample surface. The procedure for layer 2 for the 2nd generation device is outlined in Table 6-3.

The choice of wet etching circumvented a complicated PMMA removal step from the trench surrounded by SiO_2 as was the case for the process for the 1st generation device. The removal of remaining resists required an approximately 30 minute long O_2 plasma ash step, which was split into 3 steps to mitigate heating of the sample. Therefore, wet etching was a more facile avenue of fabrication for layer 2. The top electrode for this step can be scaled down to 15 μm diameter along with appropriate scaling of the wet etch via, without the need for more careful measures taken such as control of exposure tool misalignment and preservation of the photoresist layer during etching, which could be accomplished by diluting the BOE 10:1.

Table **6-3**: Wet-etch procedure for the SiO_2 layer.

	SiO_2 Etch Procedure
1	M4L Plasma Ash: 150 sccm O_2, 50 sccm He, 550 mTorr, 300 W, 2 min (immediately before step 2, chamber vented)
2	Temescal E-beam Evaporation: SiO_2; 0.5 Å/s, first 10 nm; 2 Å/s, remaining 490 nm
3	Spin: HMDS, 2500 RPM, 30 s, bake 105 °C, 1 min
4	Spin: 1827 PR, 4000 RPM, 45 s, bake 110 °C, 2 min
5	MLA exposure: 280 mJ/cm^2, 375 nm
6	Develop: CD-26, 80 s
7	Apply1827 PR to sample edges to protect them
8	Hardbake: 115 °C, 5 min
9	Wet etch: BOE 10:1, 10 minutes MAX
10	M4L Plasma Ash: 150 sccm O_2, 50 sccm He, 550 mTorr, 300 W, 5 min
11	Strip resist in acetone, rinse in IPA
12	M4L Plasma Ash: 150 sccm O_2, 50 sccm He, 550 mTorr, 200 W, 2 min

6.4 Layer Three

The third and final layer involves deposition of the probe landing pad and the contact via (see Figure 6-11) in a process similar to the first layer. The PMMA, LOR 5a and SPR 3012 stack was used for patterning the contact pads and via. The PMMA was used even though the ZMO was completely covered because the resist developer (CD-26) dissolves SiO_2. So, the PMMA layer served to protect the SiO_2 layer from CD-26.

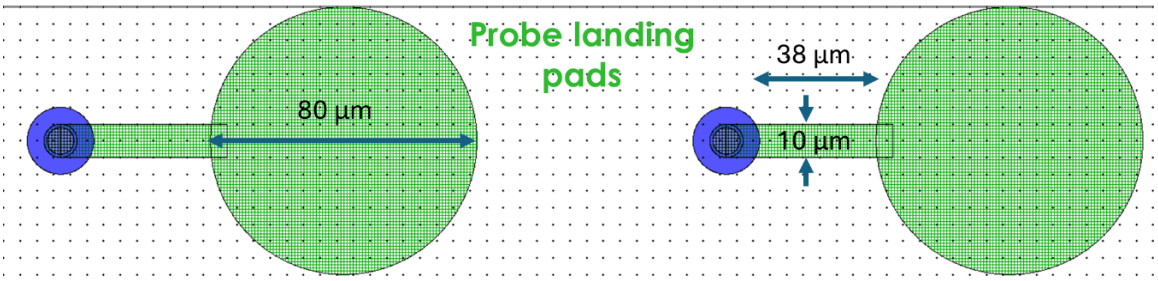

Figure **6-11**: A diagram of the probe landing/contact pad and via to the top electrode (green pattern).

This step was relatively straightforward. A slightly longer O_2 plasma ash (6 minutes total) was required before depositing the top electrode to remove remaining PMMA in the trench (refer to Table A-1). An EDS map of the final device is shown in Figure 6-12. In the 1st generation device, 2 nm of Ti were sputtered at 2.5 mTorr for 20 s, followed by 100 nm of Au at 7.5 mTorr for 150 s. The Ti served as an adhesion layer for gold on SiO_2 and the electrode did not experience delamination even when heated to 200°C. However, for the 2nd generation device, 20 nm of IrO_2 was deposited first, followed by 50 nm of Ir. It was expected that IrO_2 should act as an adhesion layer for the Ir, but delamination of the contact pad occurred in a device when heated to 200°C. This suggests that Ti/Au layer is superior in forming adhesive electrode contact on SiO_2, when compared with IrO_2/Ir.

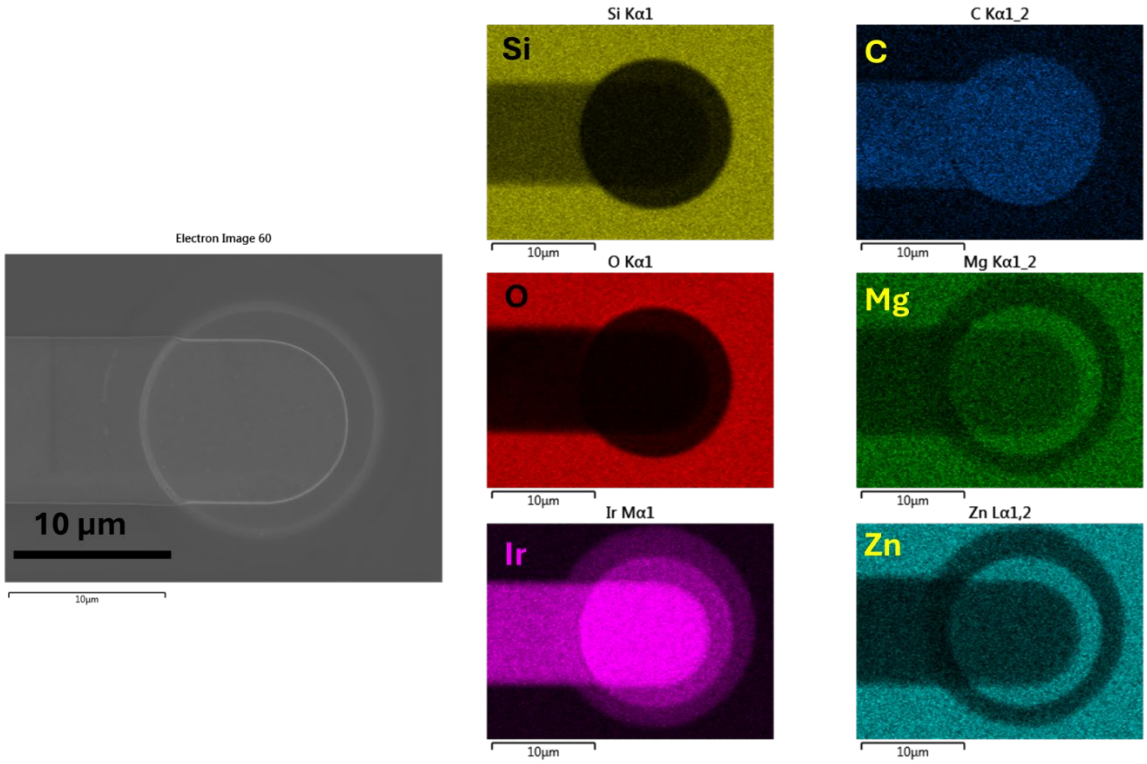

Figure 6-**12**: FESEM/EDS images of the completed 2nd generation device. Carbon is observed due to surface adsorption as the sample is exposed to atmosphere.

6.5 Ferroelectric Properties

Generation 2-devices were successfully fabricated, with the exception that they could not be heated to 200°C lest the contact pads delaminate from the SiO_2 insulating layer. Polarization-electric field (P-E) hysteresis loops were measured for the 1st and 2nd generation devices, and parasitic capacitances from the SiO_2 were found to have significant contributions to the saturated polarization. The parasitic capacitance could be subtracted from the polarization values and a reasonable P-E hysteresis loop for ZMO could be obtained (see Figure 6-13, and Appendix B-2

for calculations). Nonetheless, generation 1 devices were especially leaky, and polarization values were inflated.

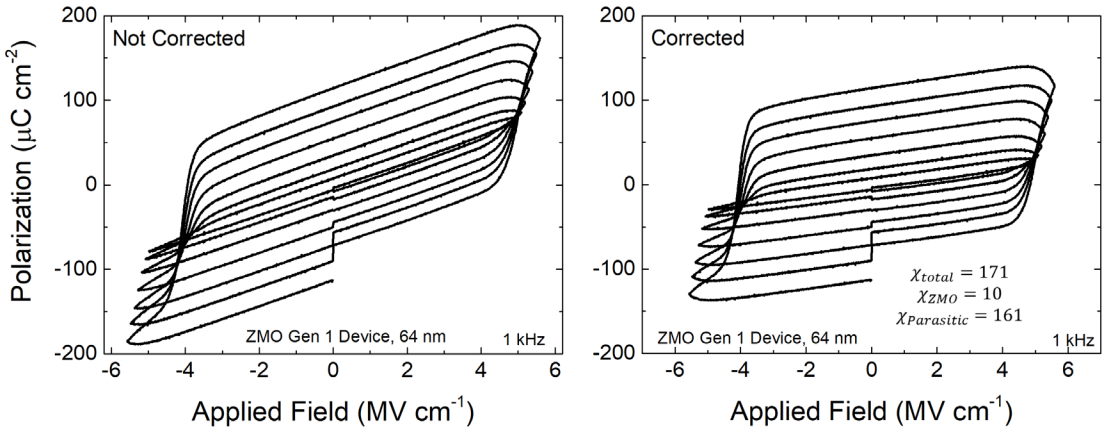

Figure **6-13**: Parasitic capacitance subtractions were performed successfully on 1st generation ZMO device with a 64 nm thick ferroelectric layer.

2nd generation devices did not experience artificial inflation of the remanent polarization, albeit the P-E hysteresis loop exhibited leakage at high applied fields (> 6 MV cm^{-1}) beyond those necessary to switch the spontaneous polarization. In this way, scaling of the ZMO thin films was demonstrated down to 43 nm thickness of the ferroelectric ZMO layer, as shown in Figure 6-14. The relative contribution of the capacitive currents decreased with decreasing layer thickness of ZMO due to increasing capacitance of the ferroelectric layer.

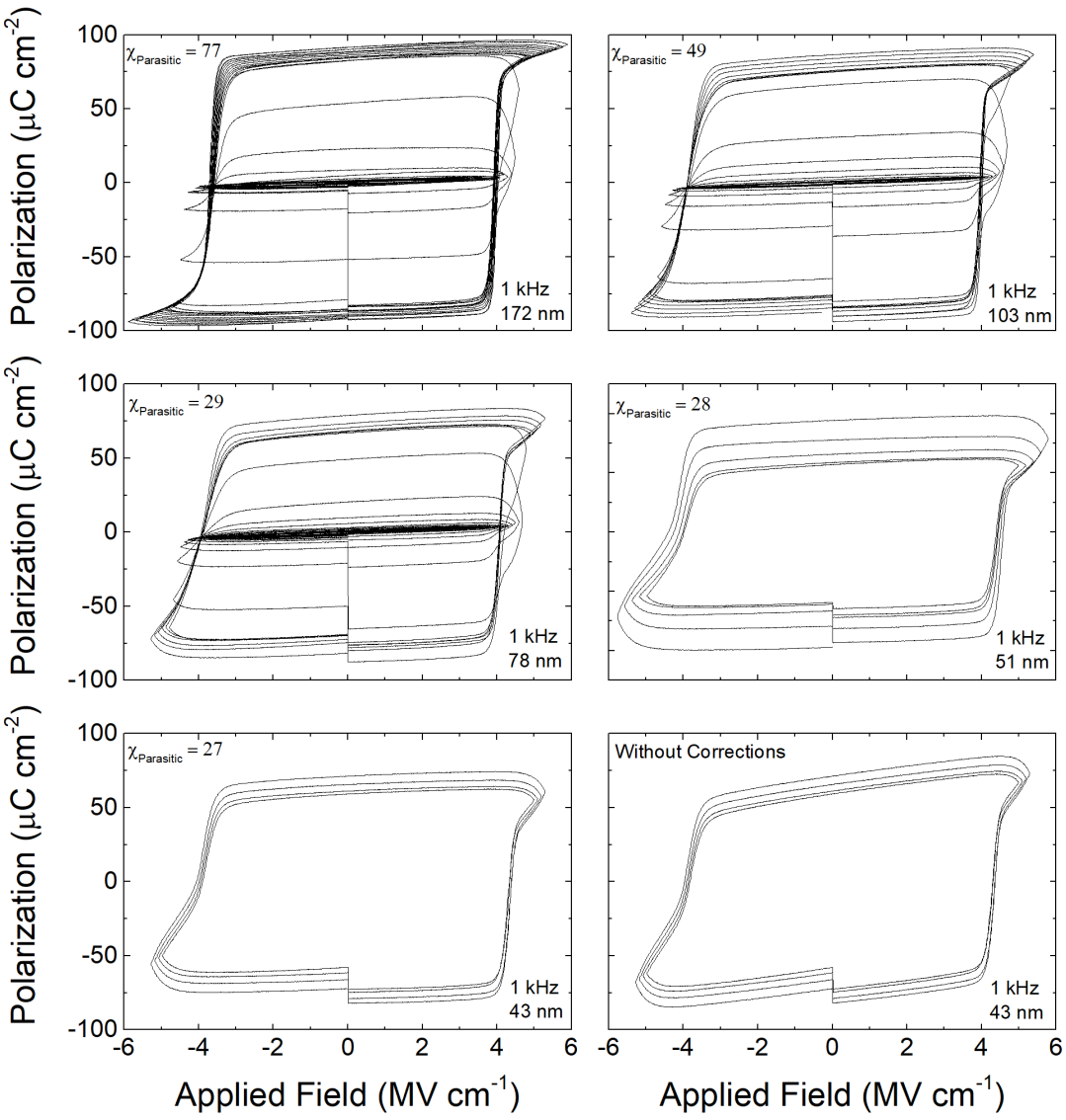

Figure **6-14**: Ferroelectric P-E hysteresis loops of 2nd generation $Zn_{0.63}Mg_{0.37}O$ devices scaled down to ferroelectric layer thickness of 43 nm. The parasitic capacitances of the devices were subtracted from data in these plots. The effective parasitic susceptibility is shown in the upper left corner of each plot.

As the film thickness decreases, the film's breakdown field relative to the coercive field decreases, and less of the polarization can be switched. This is one contributor to the apparent

reduction in switchable polarization with film thickness. Compositional gradients at thicknesses < 30 nm may also contribute to changes in the coercive field, [4] as local strains responsible for lowering the coercive field are also altered.[5] Extensive scaling to ≤ 6 atomic layers thick results in a graphitic ZnO structure where the tetrahedra flatten.[6] In thicker ZnO films, there is expected to be a barrierless transition to the puckered hexagonal wurtzite structure.

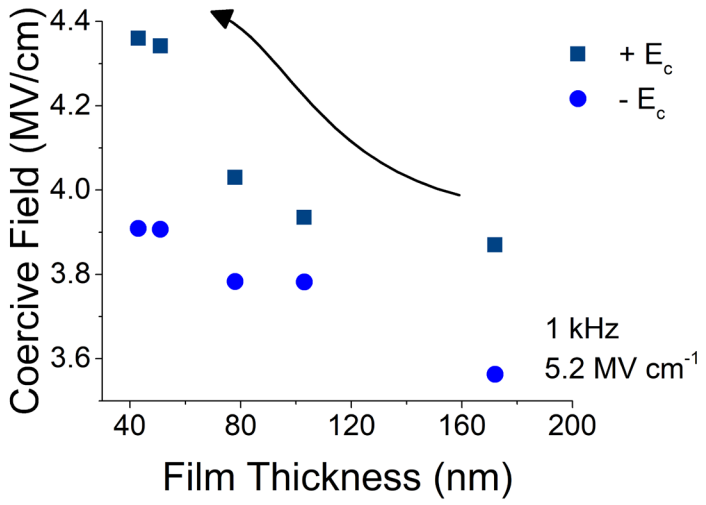

Figure **6-15**: The dependence of coercive field on ZMO thickness.

The coercive fields plateaued between 51 nm and 43 nm, as shown in Figure 6-15. This may be due to several factors, including lower concentrations of nuclei in the thinner ZMO films.[5] Another factor that may contribute to the change in coercive field with film thickness is that the films were grown at room temperature, and rising substrate temperature throughout the deposition may alter the bulk film properties. As was reported in previous chapters, the coercive fields are lower for switching to the as grown polarization orientation, relative to switching to the opposite polarization orientation. This may be due to pre-existing nuclei which facilitate polarization reversal at lower fields when switching to the as-grown, initial polarization state of the samples.

In chapter 5, it was shown that KAI-like kinetics apply to switching in ZMO at applied fields below 4 MV cm^{-1}. For the KAI-like kinetics to take place in ZMO, there must be a population of nuclei or germs existing in the film, and the amount of polarization that reverses is dependent on the concentration of nuclei (or germs) in the film. Generating new nuclei demands a larger energy penalty and thus requires higher applied fields to activate and reverse them. Recall that the ICS model presented in Chapter 5 applies at higher fields, whereas at lower fields switching appears to obey the KAI kinetics model.

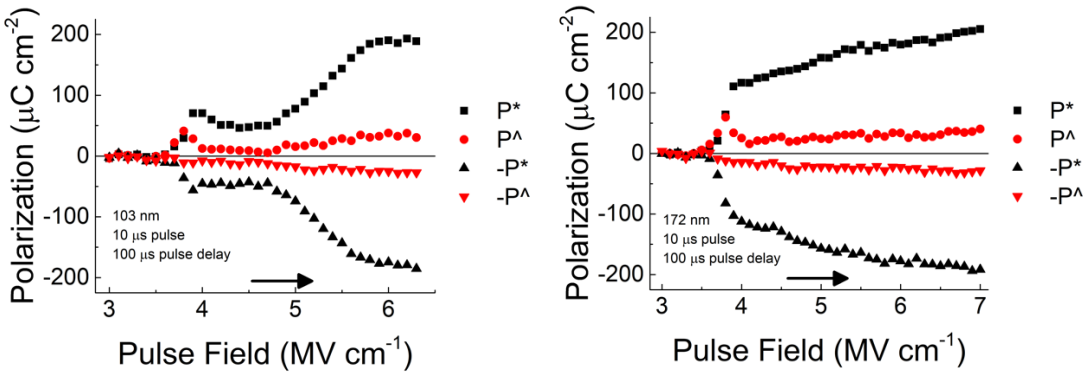

Figure **6-16**: PUND with increasing applied field in 2nd generation ZMO devices. P* is the total polarization and P^ is polarization arising from the non-switching pulse and can represent non-ferroelectric components of switching, including leakage currents and capacitive currents.

In Figure 6-16, larger applied fields are required to switch the polarization in a 103 nm thick film compared to a 172 nm thick film. In the 103 nm thick ZMO film, a finite amount of polarization switches at 4 MV cm^{-1}, and the switched polarization does not increase further until 5 MV cm^{-1} is applied to the sample. In a thicker 172 nm thick ZMO film, this phenomenon is less pronounced, but the positive correlation between applied field and switched polarization still exists, suggesting more nuclei are generated at higher applied fields.

In kinetics models such as the KAI, NLS, and SNNG models, all the polarization should reverse at 4 MV cm^{-1}, given enough time, since a significant amount of polarization has already begun to reverse. However, at 4 MV cm^{-1}, the amount of switched polarization plateaus, and does not increase any more beyond 20 μs, as shown in Figure 6-17a. This contrasts behavior at 5 MV cm^{-1}, in Figure 6-17b, where switching is bimodal with a prolonged tail of its switching transient, as described in chapter 5.

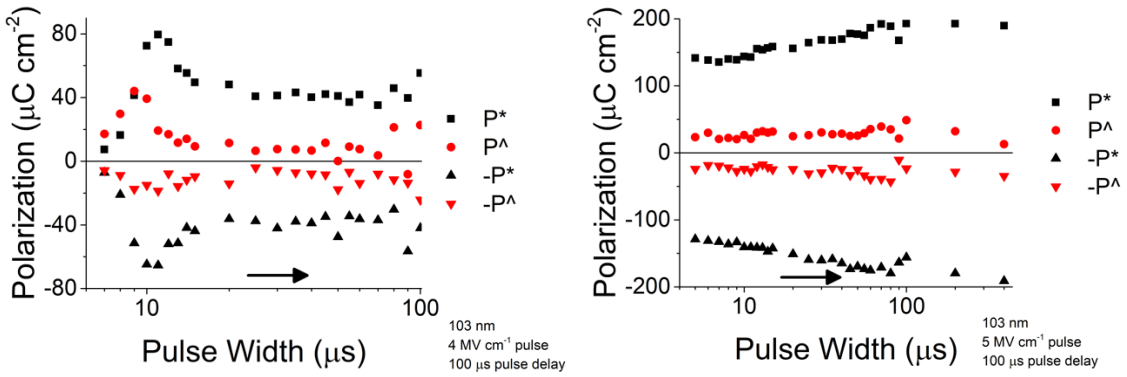

Figure **6-17**: PUND with increasing pulse width in 2nd generation ZMO devices.

Another strange phenomenon that occurs in ZMO films is that at high applied fields and longer pulse widths, the P^ value decreases, signifying the leakage current contribution in ZMO decreases. Simultaneously, the apparent switched polarization increases beyond the spontaneous polarization for ZMO. This is due to increased leakage currents at fields near the breakdown field in ZMO, and is a likely indicator of damage.

6.6 Conclusions

A process flow was successfully demonstrated with ZMO that allowed for the observation of P-E hysteresis loops with reasonable P_r values > 40 μC cm^{-2} in sub-50 nm thick ZMO for the first time. Further scaling of ZMO could be applied, albeit with changes to the

growth conditions, such as increasing the deposition temperature. In addition, this device structure acts as a hermetic seal which protects the ferroelectric ZMO layer from atmospheric effects that could degrade the film quality over time.

References

[1] Zuo, Y., Lin, H., Guo, J., Yuan, Y., He, H., Li, Y., Xiao, Y., Li, X., Zhu, K., Wang, T., Jing, X., Wen, C., & Lanza, M. (2020). Effect of the pressure exerted by probe station tips in the electrical characteristics of memristors. *Advanced Electronic Materials*, *6*(3), 1901226.

[2] Hinkov, B., Hoang, H. T., Hugues, M., Chauveau, J. M., & Strasser, G. (2021). Etching of m-plane Zn(Mg)O epitaxial films and its impact on surface leakage currents. *Semiconductor Science and Technology*, *36*(3), 035023.

[3] BOE Buffered Oxide Etchants. (n.d.). *Technical Data*. Rochester Institute of Technology. Available at: http://www.smfl.rit.edu/pdf/productinfo/productinfo_General_Chem_BOE.pdf. Accessed 2018.

[4] Yang, J., Ievlev, A. V., Morozovska, A. N., Eliseev, E. A., Poplawsky, J. D., Goodling, D., Spurling, R. J., Maria, J-P., Kalinin, S. V., & Liu, Y. (2024). Coexistence and interplay of two ferroelectric mechanisms in $Zn_{1-x}Mg_xO$. *Advanced Materials*, *36*(39), 2404925.

[5] Baksa, S. M., Gelin, S., Oturak, S., Spurling, R. J., Sepehrinezhad, A., Jacques, L., Trolier-McKinstry, S., van Duin, A. C. T., Maria, J-P., Rappe, A., & Dabo, I. (2024). Strain fluctuations unlock ferroelectricity in wurtzites. *Advanced Electronic Materials*, 2400567. Early view

[6] Claeyssens, F., Freeman, C. L., Allan, N. L., Sun, Y., Ashfold, M. N., & Harding, J. H. (2005). Growth of ZnO thin films—experiment and theory. *Journal of Materials Chemistry*, *15*(1), 139-148.

Chapter 7

Conclusions and Future Work

7.1 Conclusions

The wake-up and retention performance of ferroelectric wurtzite structure ZMO films is reported. Strong field dependence of the wake-up is observed, where higher fields require fewer cycles for the film to fully awaken. High quality ZMO films with breakdown strengths in excess of 5 MV cm^{-1} can be fully woken in a single P-E loop. Fluid imprint was found to affect the coercive field and wake-up of aged samples. A strong imprint effect on the coercive field was also observed after DC I-V experiments at high temperatures. Ferroelectric switching is kinetically limited, whereby slower switching frequencies yield a lower coercive field for polarization reversal. Strong temperature dependence of the coercive field is observed, with a pseudo-activation energy of 23.2 ± 0.3 meV at room temperature and of 40.6 ± 0.6 meV between 120 and 240°C. Over this same temperature range, there was also a transition in the activation energy for electrical conduction. The minimum observed coercive field was 1.5 MV cm^{-1} at temperatures above 240°C. The same-state and opposite-state polarization retention was excellent, showing no reduction in the polarization margin, even for bakes at temperatures up to 200°C, making ZMO an interesting candidate for high temperature memory applications.

Ferroelectric switching of ZMO obeys KAI-like switching at low applied fields, and ICS at higher applied fields. Switching of ZMO with moderate Mg contents, near x = 0.27 obeys the cumulative Gaussian distribution. The reliance of switching on nucleation was confirmed by

extracting a distribution function from an SNNG model assuming only nucleation, which agreed well with the Gaussian distribution. Switching becomes bimodal in ZMO with Mg contents of x = 0.41, where the first ½ to ⅔ of switching occurs quickly and obeys the Gaussian distribution, and is followed by a slow tail which obeys the inverse gamma distribution. It is suggested that the tail is due to Mg clustering which retards the latter portion of switching in high Mg-content ZMO ($x \gtrsim 0.4$). Ferroelectric switching beyond 100 cycles results in fatiguing of ZMO, possibly due to the "hot atom" effect which was described in (Al,Sc)N. Rayleigh analysis reveals a simultaneous increase in the irreversible and decrease in the reversible contributions to the dielectric constant on cycling, due to an increase in the density of mobile domain walls. This is associated with faster switching with cycling in ZMO until breakdown.

A process flow was successfully demonstrated with ZMO that allowed for the observation of P-E hysteresis loops with reasonable P_r values > 40 μC cm^{-2} in sub-50 nm thick films for the first time. Further scaling of ZMO is possible. In addition, the device structure acts as a hermetic seal which protects the ferroelectric ZMO layer from atmospheric effects that could degrade the film quality over time.

7.2 Future Work

ZMO is a unique ferroelectric material with highly modifiable ferroelectric properties. Domain engineering may provide a pathway to increase cycling endurance lifetimes by avoiding higher applied fields which cause the films to degrade appreciably.

The rather large coercive fields in (Zn.Mg)O thin films are undesirable for memory applications unless extensive scaling can be achieved to sub-5 nm thicknesses. At the time of writing, the thinnest ZMO film which experienced robust ferroelectricity with moderate values for the remanent polarization (P_r) were 43 nm thick. Switching of a finite value of the

spontaneous polarization (± 3 μC cm^{-2}) was observed in 36 nm thick (early generation) ZMO grown on platinized *c*-sapphire substrates (see Figure 7-1). However, ferroelectric switching in those early generation ZMO films at sub-100 nm thicknesses was not repeatable, and the capacitors would break down easily.

One means to reduce the coercive field of ZMO was attempted by seeding the nucleation. It is hypothesized that by seeding the nucleation with insulating nanodots on the surface of ZMO, pre-existing domains can be forced into existence due to the presence of unswitchable regions of film.[1] For example, an insulating material with a low carrier concentration like SiO_2 does not have enough carriers to compensate for the spontaneous polarization of ~80 μC cm^2 in ZMO. By nature of the charge balance, ZMO at the interface of SiO_2 will have a host of structural anomalies due to the frustrated polarization states which consequentially becomes a nucleation promoter in the presence of large applied fields.

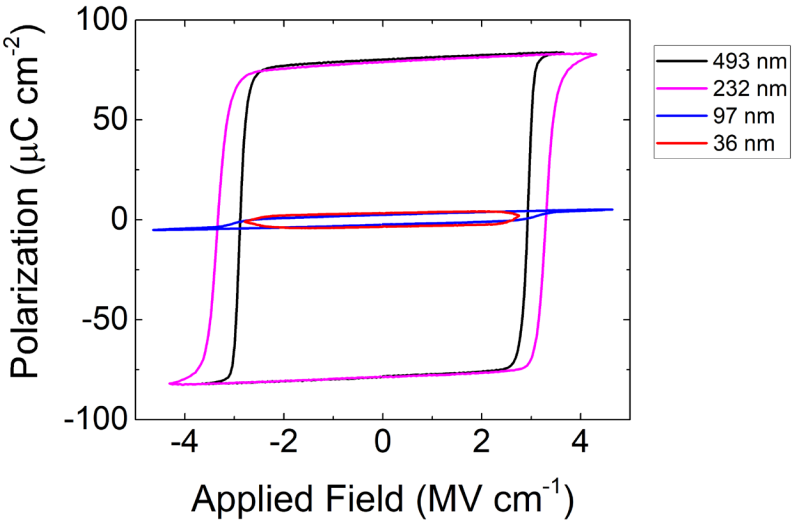

Figure **7-1**: Scaling of ferroelectric switching behavior in early generation Pt/ZMO/Pt(111)/c-Al_2O_3 thin films, down to 36 nm thickness.

As improvements in the quality of ZMO and re-optimization of the deposition process may bring its own benefits to the end of producing a viable candidate for ferroelectric memory, it is of interest to investigate whether ZMO films could be modified to reduce the coercive field. As switching in ZMO was proven to occur by nucleation and growth, it was hypothesized early during this work that introducing nuclei to the surface of ZMO could facilitate switching at lower applied fields, thus reducing the coercive field. Later on, as discussed in Chapter 5, it was determined that nuclei are abundant in ZMO, and seeding in fact had no effect on the coercive field (c.f. Appendix A).

In other materials, however, the pre-existing concentration of nuclei may be small.[2] In this case, a method to introduce nuclei to the exposed (top electrode) surface of the ferroelectric might be deposition of insulating nanodots, composed of a material with a low carrier concentration (SiO_2). If this could be accomplished, the interface between the insulating nanodots and the ferroelectric would produce field concentrations that might favor nucleation.[1] Moreover, unswitched regions of film should exist in the vicinity of the insulating nanodots, which would act as nuclei for switching to the opposite state. In addition, the density of nuclei present on the thin film surface could be controlled simply by modifying the e-beam lithography pattern.

7.3 Domain Engineering

Interesting hysteretic effects on the domain state of ~200 nm thick $Zn_{0.61}Mg_{0.39}O$ films were observed in sub-coercive field switching between 2.4 and 3.2 MV cm^{-1}. Switching at sub-coercive fields was observed in ZMO after applying the P-E loop sequence shown in Figure 7-2. That is, the film was first switched through the entire hysteresis loop at 5 MV cm^{-1}. Then a second pre-conditioning P-E loop at the sub-coercive field of 3 MV cm^{-1} and at 100 Hz was conducted. It is speculated that during this second step, that residual oppositely oriented domains

were left in the material. Following the second pre-conditioning P-E loop, substantial amounts of remanent polarization switch at sub-coercive fields. Without the second pre-conditioning loop, switching does not occur at sub-coercive fields, as shown in Figure 7-3. To optimize the pre-treatment conditions, Preisach distributions of the switching should be constructed.

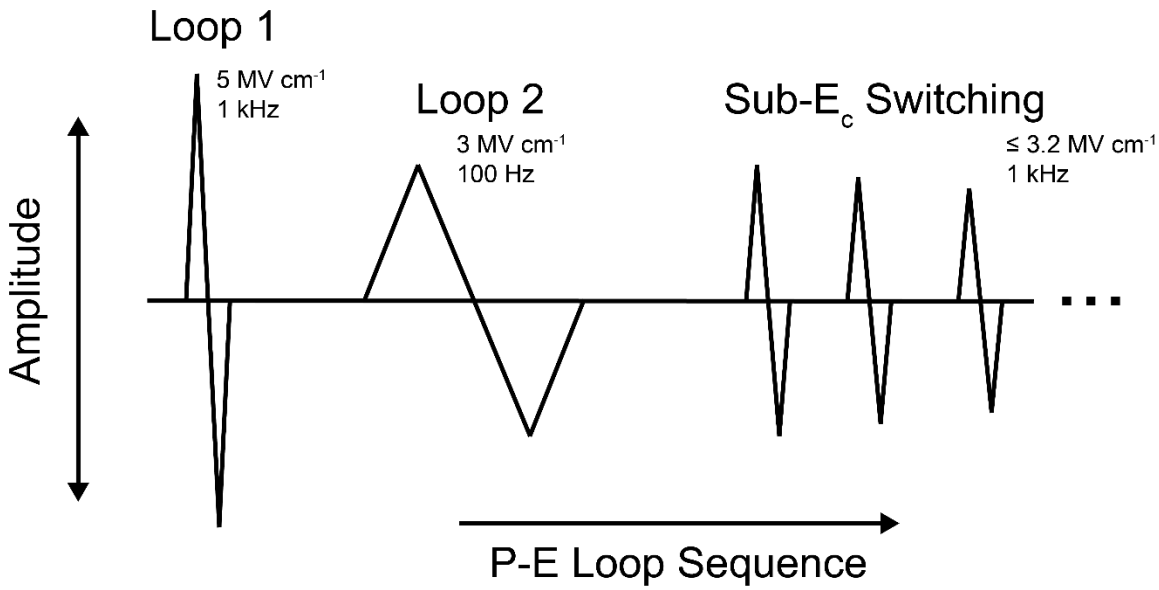

Figure **7-2**: A sequence of P-E loops used to pre-condition ZMO thin films for switching at sub-coercive fields.

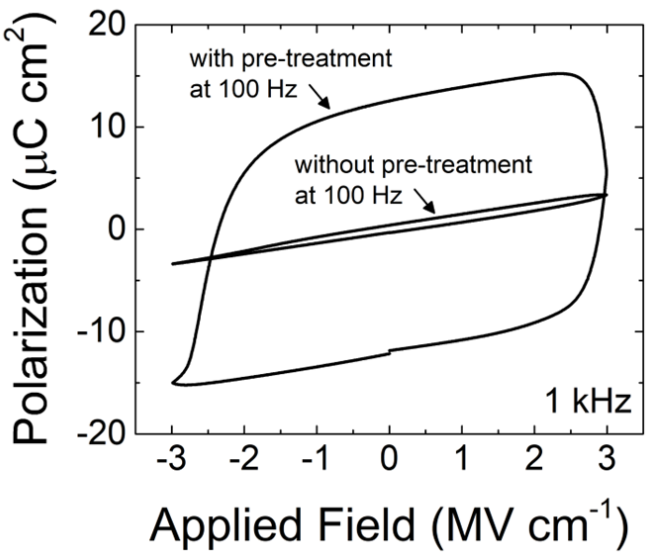

Figure **7-3**: Differences in switching of a $Zn_{0.61}Mg_{0.39}O$ thin film preconditioning at 5 MV cm^{-1} @ 1 kHz, followed by a second preconditioning step at 3 MV cm^{-1} @ 100 Hz. P-E loops at 3 MV cm^{-1} @ 1 kHz with and without the 2nd preconditioning step are shown. It is speculated that the difference is due to a difference in the domain states of the films induced by the pre-conditioning.

More complete switching occurs when switching to the as-grown state, ↓, which is indicative of more facile switching to that polarity, likely due to a larger concentration of nuclei present. The P_r of the sub-coercive P-E loops increases with up to 8 pre-treatment P-E loops at 5 MV cm^{-1}, after which the P_r degrades for the sub-coercive P-E loops, as shown in Figure 7-4. Before 8 pre-treatment loops at 5 MV cm^{-1}, no degradation in the sub-coercive P_r values was observed in the first 15 loops. Beyond 8 pre-treatment loops, it is speculated that there is a trade-off between the generation of nuclei and generation of new defects. This is manifested by the P_r for the 1st loop at 3 MV cm^{-1} (black) continuing to increase until 12 pre-treatment loops at 5 MV cm^{-1}, while the P_r degrades with continued cycling at 3 MV cm^{-1} until the 15th loop (red). This suggests that the spontaneous polarization can switch at at < 3 MV cm^{-1} if impediments to switching (possibly domain wall pinning at defects) are removed. Further experiments using

photoluminescence spectroscopy are suggested in order to quantify the presence of defects in ZMO after cycling at 5 MV cm^{-1} which may be responsible for trends in sub-coercive field switching behavior.

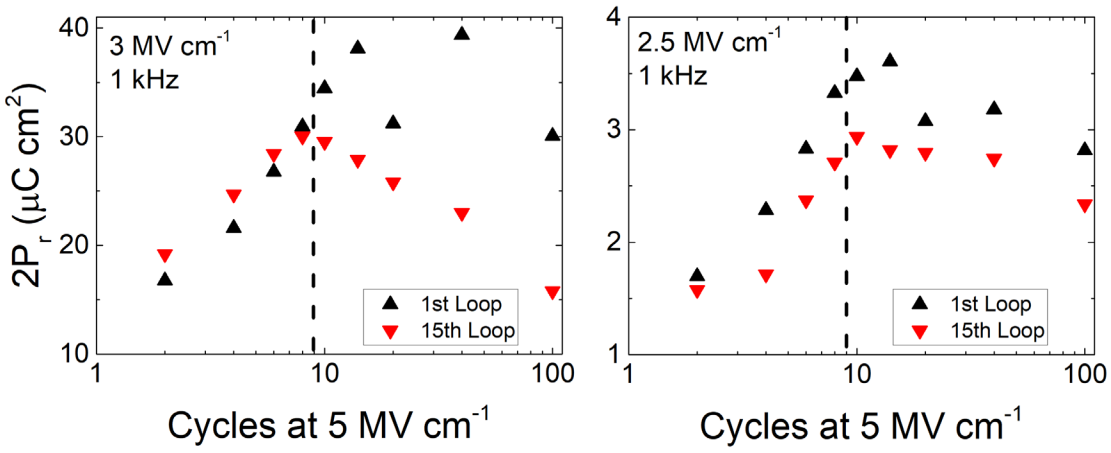

Figure **7-4**: $2P_r$ values of P-E loops at 3 MV cm^{-1} (left) and 2.5 MV cm^{-1} (right) as a function of the number of preconditioning loops at 5 MV cm^{-1}. "1st Loop" and "15th Loop" indicate the number of P-E loops at sub-coercive field specified in the upper left corner of each plot.

The relationship $P_r = e^{\alpha E} + C$ where $\alpha = 4.8 \pm 0.1$ cm MV^{-1} was observed where $\ln(2P_r)$ scaled linearly with the applied sub-coercive fields between 2.4 and 3.2 MV cm^{-1}, as plotted in Figure 7-5.

In order to achieve ZMO films with large fatigue cycling endurance, measures must be taken to mitigate the change in defect populations in the film. As reported in the literature review, GIZO is effective at blocking oxygen vacancy migration which is possible in ferroelectric switching of ZMO.[3] Oxygen vacancy migration has been reported in ZnO memristors, where oxygen absorption and desorption occurred at the electrode interface.[4] Incorporation of an extremely thin GIZO barrier layer at the electrode interface may permit switching while blocking oxygen vacancy migration in ZMO, and hence increase the cycling endurance characteristics.[5]

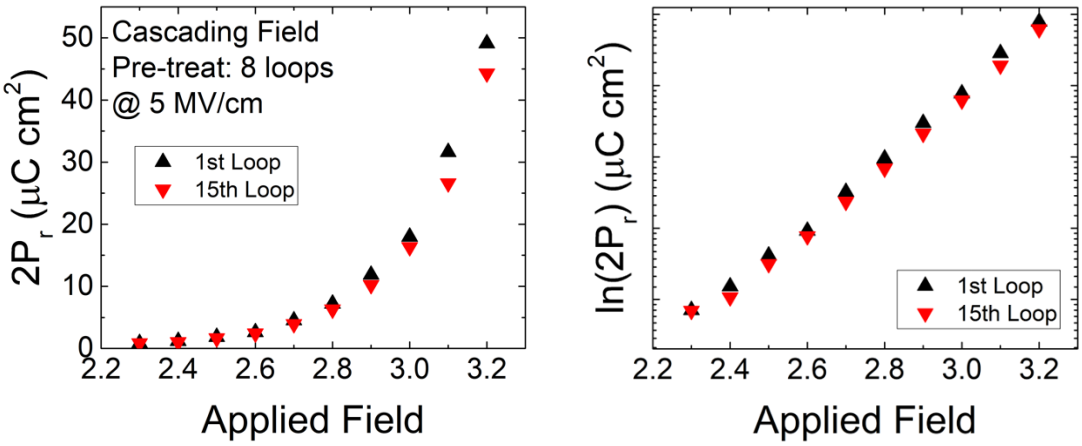

Figure **7-5**: A linear relationship between the log of $2P_r$ and the applied field at sub-coercive fields is depicted.

First order reversal curves (FORC) were measured to qualitatively observe the distribution of hysterons in ZMO (see Figure 7-6). Domains in ZMO do not switch until a threshold applied field is reached. Therefore, the hysteron distribution is far narrower in ZMO than in many other ferroelectrics. The first 120 μC cm^{-2} switches before polarization reversal requires either more time or higher fields. The Preisach distributions in Figure 7-7 indicate that switching in ZMO initially has a narrow distribution of switching (coercive) fields,[6,7] followed by a broad distribution of hysterons at higher fields indicated by the roughness in the distribution. The negative values of p(α, β) are due to the continued rise in polarization as the applied field begins to decrease. For similar occurrences in magnetic materials, the "moving Preisach distribution" was proposed.[8] However, application of a moving Preisach distribution can be quite complicated and is outside the scope of this dissertation. Maxima in the Preisach distribution in Figure 7 are located at (α, β) values of (2.8 MV/cm, -2.6 MV/cm) for plot a and (3.1 MV/cm, -2.8 MV/cm) for plot b.

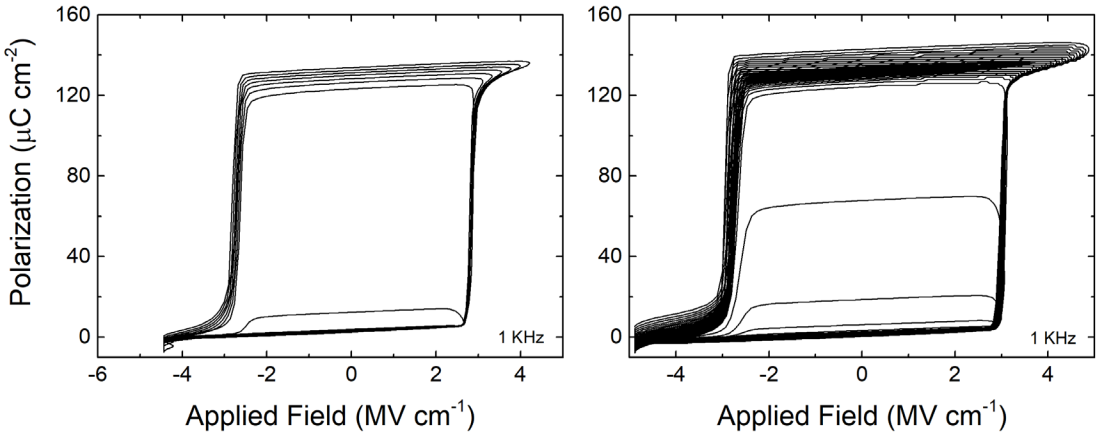

Figure **7-6**: FORC curves at moderate applied fields (left) and at high applied fields (right). 40 P-E loops were measured for each experiment using a sine wave function at 1 kHz frequency. Applied fields ranged from 0 to 4 MV cm^{-1} (left) and from 2.5 to 5 MV cm^{-1} (right).

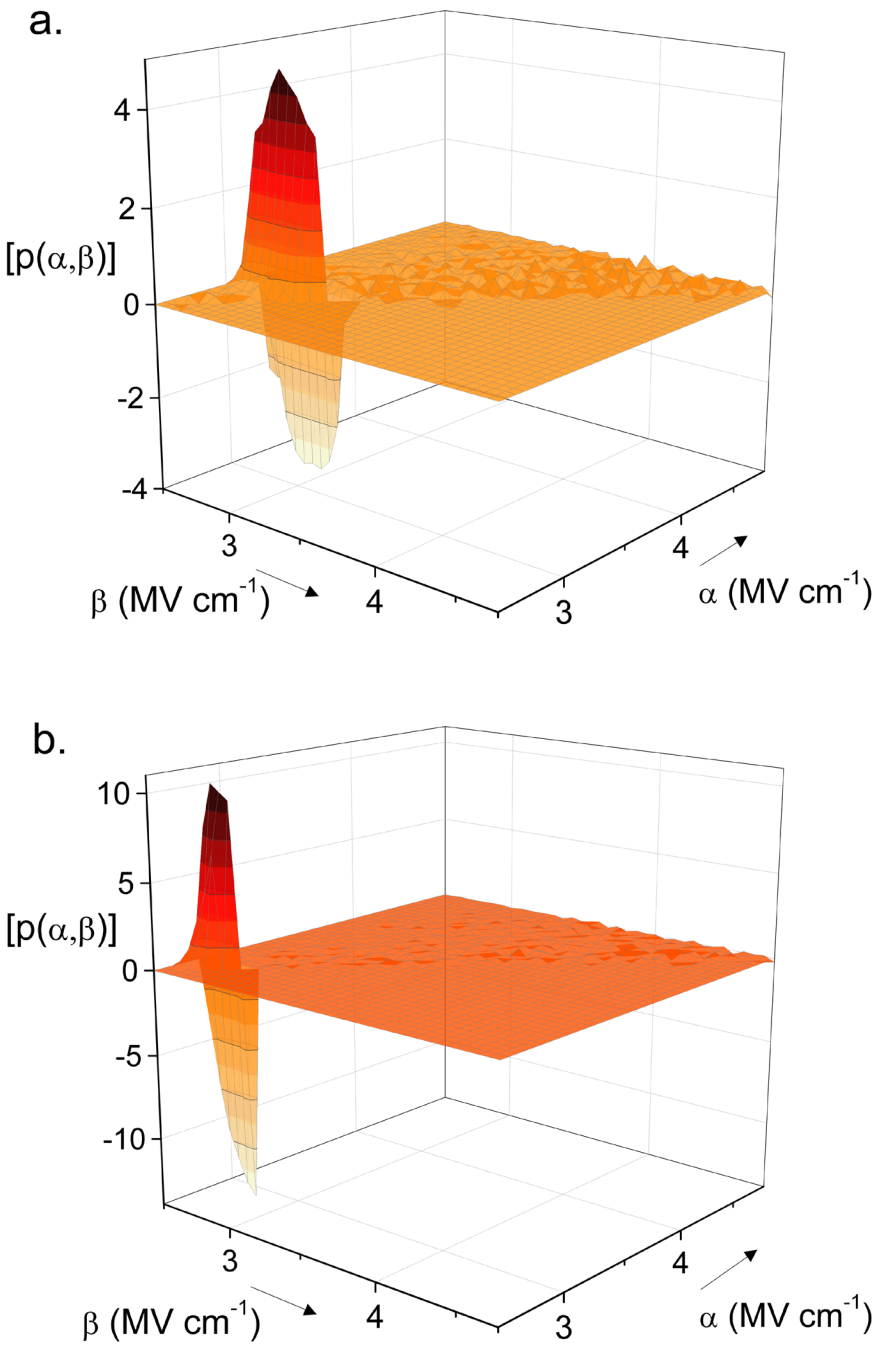

Figure **7-7**: The Preisach distribution plot indicates switching in ZMO is dominated by a narrow distribution of hysterons. The distribution of hysterons during wake-up (a) is broader than

switching after wake-up (b). The apparent negative hysteron distribution is an artefact. (Credit: Herb McKinstry for assistance with Preisach calculations)

7.4 Alternative Deposition Methods

As of now, scaling ZMO is a challenge which is necessary to overcome in order to achieve switching voltages of ~ 1 V in ZMO thin films. Scaled sputtered ZMO may be challenging to sputter deposit because of composition gradients at thicknesses less than 30 nm. As shown in Figure 7-8,[9] ToF-SIMS measurements indicate that at least some sputtered films grow Zn-rich at the onset of growth. At <6 atomic layers, ZnO is more stable as gZnO than the wurtzite structure. After the first few seconds of deposition ZnO should adopt the wurtzite structure and facilitate Mg substitution on Zn sites. As will be shown in section 7.3.2, Mg does not incorporate into gZnO under equilibrium conditions. Likewise, if nucleation of ZnO is favorable during sputter growth it could cause Mg to be expelled to the surface in the initial stages of growth. This may explain the increase in Mg concentration in the following 5 – 25 nm of growth with respect to the Mg concentration at greater thicknesses. It is important to know if this always occurs in ZMO thin films.

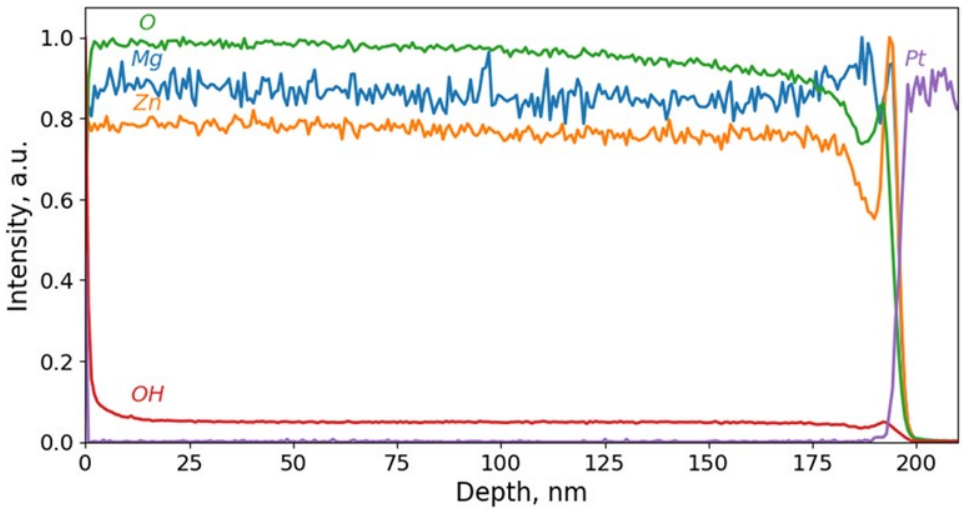

Figure **7-8**: ToF-SIMS composition profile of a rf magnetron sputtered 200 nm thick $Zn_{0.68}Mg_{0.32}O$ film.[9]

As an alternative to sputtering, sol-gel deposition of ZMO and a reduced graphene oxide intercalation technique could be utilized to deposit thin ZMO and ZnO, as described elsewhere.[10,11] Initial exploration along these lines is described below.

7.4.1 Sol-gel ZMO

Thin, homogeneous ZMO films can be grown via sol-gel methods. To accomplish this, appropriate choice of precursors must be made. Zn acetate dihydrate and Mg acetate tetrahydrate are two common sources for Zn and Mg,[12,13] so it is tempting to use those precursors to deposit ZMO. However, differences in the thermal decomposition of precursors can lead to segregation of MgO at low mol fractions of substitution.[10] This can be addressed by choosing precursors with similar decomposition temperatures.

Zn acetate dihydrate is reported to decompose around 250°C, and Mg acetate is reported to decompose at approximately 350°C.[14,15] The difference between these two decomposition

temperatures is significant. Although use of like precursors (i.e. acetates with acetates) seems, at first blush, as though it would promote homogeneity, that is not necessarily the case during the pyrolysis step. During that step, Zn and Mg can segregate as the Zn acetate will decompose and form a metal oxide matrix before the Mg precursor decomposes. However, Mg ethoxide decomposes at approximately 270°C,[16] which is close to the decomposition temperature of Zn acetate dihydrate. Therefore, choosing an appropriate pyrolysis temperature can reduce composition segregation during that step. Likewise, this prevents homogeneity from being destroyed due to low diffusion distance.

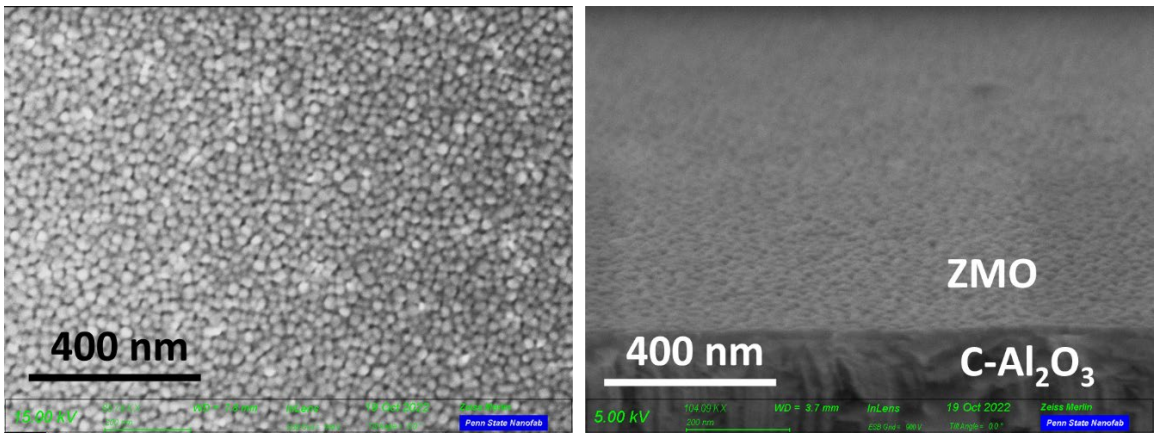

Figure 7-9: (left) FESEM image of the top surface of 3-layer $Zn_{0.74}Mg_{0.26}O$ grown via sol-gel. (right) Cross-sectional view of the microstructure.

Therefore, a process to deposit homogeneous ZMO films was employed, which was adapted from Ohyama et al.[13] To make the solution, 2-methoxyethanol was added to a 150 mL Erlenmeyer flask. The flask was set on a hot plate set to 60°C, with a magnetic stir bar. Zn acetate dihydrate and Mg ethoxide were added to the flask while stirring to from a 0.2 M solution for $Zn_{0.74}Mg_{0.26}O$. Diethanolamine was added to the solution dropwise while stirring until a 2:3 ratio

to Zn+Mg was achieved. Alternatively, monoethanolamine could be added until a 1:1 ratio to Zn+Mg is achieved. The solution was then stirred overnight capped in parafilm, then stored.

The solution was dynamically spin coated at 3,000 RPM for 40 s, immediately followed by drying at 200°C for 3 minutes. The dried film was pyrolyzed at 350°C for 3 minutes, followed by annealing in a rapid thermal annealer at 500°C for 5 minutes. This process yielded a dense, transparent, and homogeneous film with a thickness of approximately 9 nm/layer, as shown in Figure 7-9. The target composition of $Zn_{0.74}Mg_{0.26}O$ was confirmed by EDS, as shown in Figure 7-10.

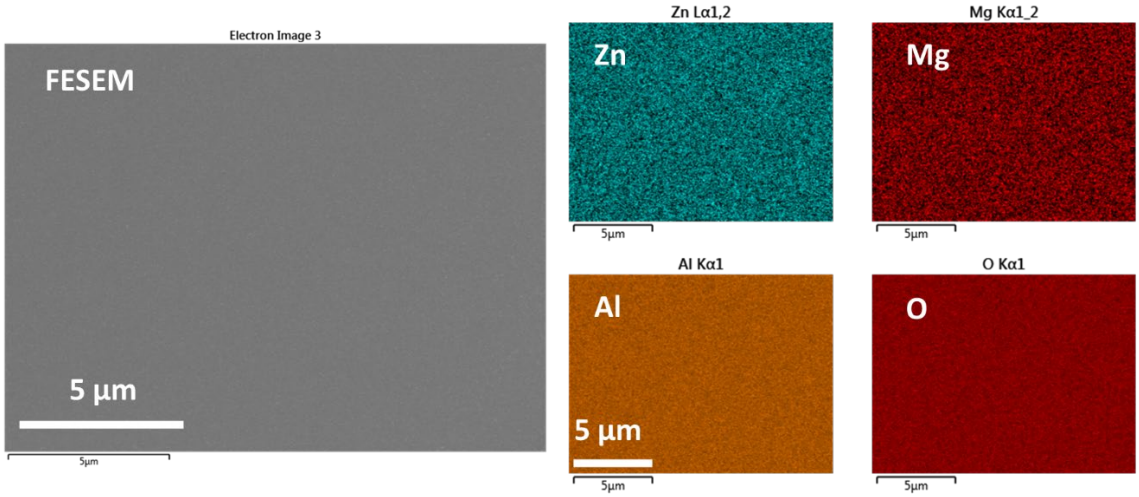

Figure 7-10: FESEM-EDS spatial mapping of the composition of $Zn_{0.74}Mg_{0.26}O$ grown via sol-gel.

However, weak 002 orientation was observed in the XRD patterns for these films. Choosing MEA as a stabilizer instead of DEA is reported to improve the 002 orientation of sol-gel deposited ZnO films.[17] Optimization of this process with MEA may facilitate further study into thin ZMO films < 50 nm in thickness.

7.4.2 Graphitic ZnO

Another method to potentially reduce the coercive field in ZMO is to flatten the cation tetrahedra, which has been demonstrated in utrathin graphitic ZnO (gZnO) grown from a graphitic oxide conversion technique.[11] Stability of the polar wurtzite structure is necessary for a spontaneous polarization to exist, but more distorted tetrahedra could then be switched at a lower coercive field than ZMO.

In an attempt to accomplish this, graphitic oxide solution was drop-cast to form a graphene oxide (GO) film on a platinized silicon substrate.[18] The deposited solution was dried on a hotplate at 80°C for 10 minutes in a cleanroom. After drying, the GO film was placed in an aqueous solution of zinc acetate (10 wt.%) at room temperature for at least 8 hours to intercalate Zn in the hexagonal GO structure. The sample was then removed and rinsed thoroughly in DI water for at least 2 minutes. Next, the film was reduced in a box furnace with 300 sccm nitrogen flow with a ramp to 300°C at 5°C/s for 4 hours. After this step carbon was visible on the surface of the reduced GO film. Finally, the sample was annealed at 400°C for 1 hour in standing air to

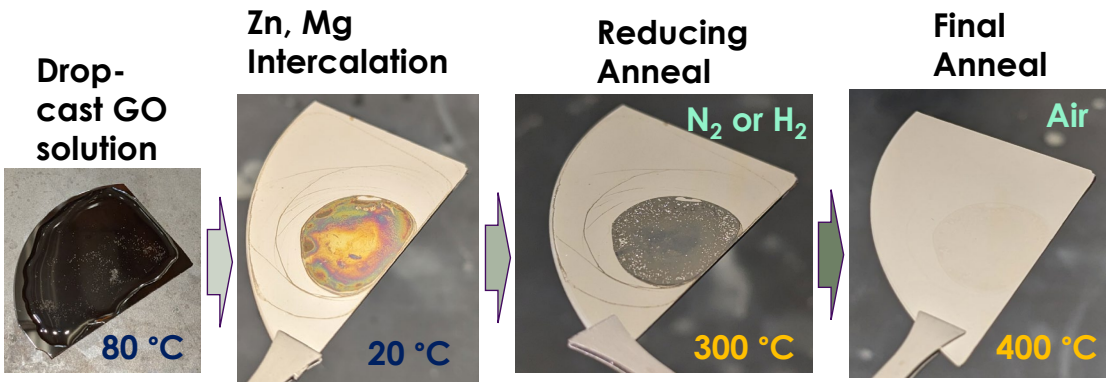

Figure 7-11: The g-ZMO process is outlined above. The reducing anneals are 4 hours long, and the final anneal is 1 hour.

remove the carbon. At the end of this process, transparent gZnO was produced, as shown in Figure 7-11. The gZnO has a wider bandgap than bulk ZnO, and is chemically stable in air above 400°C.[11,19]

The stoichiometry of the solution used for intercalation can be modified to yield other compositions.[19] To this end, Mg acetate tetrahydrate was introduced to the intercalation solution at a ratio of 7:3 for Zn:Mg. However, negligible amounts of Mg incorporated into the structure even though several mol% MgO is expected to form a solid solution with ZnO at 400°C (see

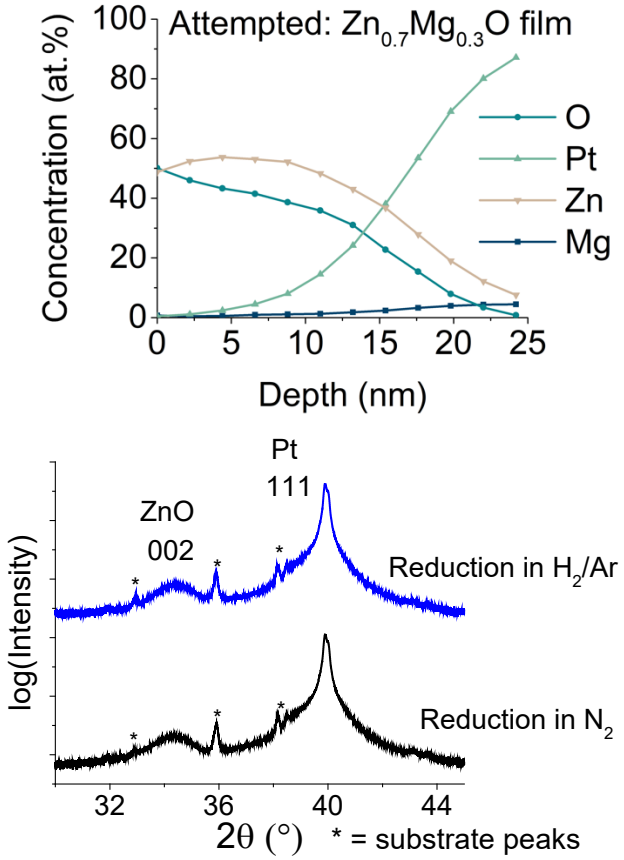

Figure 7-**12**: Top: X-ray Photoelectron Spectroscopy (XPS) depth profile of the composition of g-ZMO films. Bottom: X-ray diffraction patterns of gZnO films which were reduced in forming gas and in nitrogen.

Figure 7-12).[20] Instead, phase pure {002} oriented ZnO films were grown following this method using either nitrogen or forming gas in the reducing step. The composition of ZnO films was confirmed by X-ray photoelectron spectroscopy (XPS), and films were approximately 10 nm thick, as shown in Figure 7-12. The apparent detection of Pt in the ZnO layer are believed to be an artifact associated with both the interaction depth in XPS measurements (up to 10 nm) and inhomogeneous thickness in the g-ZnO films.[21]

Top electrodes were deposited on the gZnO films, however due to pinholes in the film, none of the capacitors were insulating. Further work is recommended here, especially an attempt to probe for ferroelectric regions with piezoforce response microscopy.[22] Growth of pinhole-free GO films from solution has been reported;[23] this was accomplished by removing small GO flakes from the solution GO solution by a series of titrations to alter the solution pH and precipitate out smaller flakes. An alternative method to drop casting is chemical vapor deposition to grow reduced GO films.[24] Therefore, depositing conformal GO films is a technological barrier that must be overcome in order to test the feasibility of gZnO thin films.

7.5 Use of the Non-contact Probe Device with Other Materials

The design of a non-contact probe pad for ZMO was presented in the previous chapter. This concept and fabrication methodology can be extended to other compositions such as (Al,Sc)N and (Al,B)N which are susceptible to oxygen incorporation. It is of interest to observe ferroelectric switching in inert environments. For that purpose, highly insulating layers such as amorphous boron nitride (a-BN) may serve as a replacement for the SiO_2 layer because of its compatible deposition method, high breakdown strength of ~ 10 MV cm^{-1}, and its chemical resistance.[25,26] For this same reason, BN is difficult to etch, and reactive ion etching in CF_4 plasma would likely be necessary to form a via to the top electrode.[27] Or, a process similar to that

used for the 1st generation device without the PMMA layer may allow for adequate undercut to ensure good lift-off without experiencing peel back of the a-BN layer. TiN which is both conducting and an excellent barrier layer can replace IrO_2 as the top electrode.[28] Since the films are nitrides, the O_2 plasma ash steps can be replaced with Ar^+ ion etches.

References

[1] Lines, M. E. & Glass, A. M. (2001). *Principles and Applications of Ferroelectrics and Related Materials*. Oxford University Press.

[2] Lu, H., Schönweger, G., Petraru, A., Kohlstedt, H., Fichtner, S., & Gruverman, A. (2024). Domain dynamics and resistive switching in ferroelectric $Al_{1-x}Sc_xN$ thin film capacitors. *Advanced Functional Materials*, *34*(28), 2315169.

[3] Nomura, K., Ohta, H., Ueda, K., Kamiya, T., Hirano, M., & Hosono, H. (2003). Thin-film transistor fabricated in single-crystalline transparent oxide semiconductor. *Science*, *300*(5623), 1269-1272.

[4] Li, C., Vaynzof, Y., Lakhwani, G., Beirne, G. J., Wang, J., & Greenham, N. C. (2017). Observation of oxygen vacancy migration in memory devices based on ZnO nanoparticles. *Journal of Applied Physics, 121*(14), 144503.

[5] Nomura, K., Ohta, H., Ueda, K., Kamiya, T., Hirano, M., & Hosono, H. (2003). Thin-film transistor fabricated in single-crystalline transparent oxide semiconductor. *Science*, *300*(5623), 1269-1272.

[6] Preisach, F. (1935). Über die magnetische Nachwirkung. *Zeitschrift für Physik*, *94*(5), 277-302.

[7] Fujii, I. (2010). *Dielectric Nonlinearity of Ferroelectrics* (Doctoral Dissertation, The Pennsylvania State University).

[8] Salling, C., & Schultz, S. (1987). Experimental determination of the shift of the Preisach distribution with magnetization. *Journal of Applied Physics*, *61*(8), 4010-4012.

[8] Yang, J., Ievlev, A. V., Morozovska, A. N., Eliseev, E. A., Poplawsky, J. D., Goodling, D., Spurling, R. J., Maria, J-P., Kalinin, S. V., & Liu, Y. (2024). Coexistence and interplay of two ferroelectric mechanisms in $Zn_{1-x}Mg_xO$. *Advanced Materials*, *36*(39), 2404925.

[10] Huang, K., Tang, Z., Zhang, L., Yu, J., Lv, J., Liu, X., & Liu, F. (2012). Preparation and characterization of Mg-doped ZnO thin films by sol–gel method. *Applied Surface Science*, *258*(8), 3710-3713.

[11] Tom, K. B., Lin, S., Wan, L. F., Wang, J., Ahlm, N., N'Diaye, A. T., Bustillo, K., Huang, J., Liu, Y., Lou, S., Chen, R., Yan, S., Wu, H., Jin, D., Yuan, H., Prendergast, D. & Yao, J. (2018). Solution-based, template-assisted realization of large-scale graphitic ZnO. *ACS Nano*, *12*(8), 7554-7561.

[12] Foo, K. L., Kashif, M., Hashim, U., & Liu, W. W. (2014). Effect of different solvents on the structural and optical properties of zinc oxide thin films for optoelectronic applications. *Ceramics International*, *40*(1), 753-761.

[13] Ohyama, M., Kozuka, H., Yoko, T., & Sakka, S. (1996). Preparation of ZnO films with preferential orientation by sol-gel method. *Journal of the Ceramic Society of Japan*, *104*(1208), 296-300.

[14] Ghule, A. V., Lo, B., Tzing, S. H., Ghule, K., Chang, H., & Ling, Y. C. (2003). Simultaneous thermogravimetric analysis and in situ thermo-Raman spectroscopic investigation of thermal decomposition of zinc acetate dihydrate forming zinc oxide nanoparticles. *Chemical Physics Letters*, *381*(3-4), 262-270.

[15] Niu, S., Han, K., Lu, C., & Sun, R. (2010). Thermogravimetric analysis of the relationship among calcium magnesium acetate, calcium acetate and magnesium acetate. *Applied Energy*, *87*(7), 2237-2242.

[16] Fisher Scientific. (n.d.). *Magnesium ethoxide, Mg 21-22%, Thermo Scientific Chemicals*. Fisher Scientific. https://www.fishersci.pt/shop/products/magnesium-ethoxide-mg-21-22-thermo-scientific/11397847

[17] Malek, M. F., Alfah, M., Khusaimi, Z., Mamat, M. H., Sahdan, M. Z., & Rusop, M. (2009, June). Effect of Mg Dopant Percentage on the Photoluminescence Property of Nano-Structured ZnO Thin Films Deposited on Si Substrate. In *AIP Conference Proceedings* (Vol. 1136, No. 1, pp. 616-620). American Institute of Physics.

[18] Zuo, C., Scully, A. D., Tan, W. L., Zheng, F., Ghiggino, K. P., Vak, D., Weerasinghe, H., McNeil, C. R., Angmo, D., Chesman, A. S. R., & Gao, M. (2020). Crystallisation control of drop-cast quasi-2D/3D perovskite layers for efficient solar cells. *Communications Materials*, *1*(1), 33.

[19] Chen, R., Luo, F., Liu, Y., Song, Y., Dong, Y., Wu, S., Cao, J., Yang, F., N'Diaye, A., Shafer, P., Liu, Y., Lou, S., Huang, J., Chen, X., Fang, Z., Wang, Q., Jin, D., Cheng, R., Yuan, H., Birgeneau, R. & Yao, J.

(2021). Tunable room-temperature ferromagnetism in Co-doped two-dimensional van der Waals ZnO. *Nature Communications*, *12*(1), 3952.

[20] Segnit, E. R., & Holland, A. E. (1965). The System MgO-ZnO-SiO_2. *Journal of the American Ceramic Society*, *48*(8), 409-413.

[21] Stevie, F. A., & Donley, C. L. (2020). Introduction to x-ray photoelectron spectroscopy. *Journal of Vacuum Science & Technology A*, *38*(6), 063204.

[22] Yang, J., Ievlev, A. V., Morozovska, A. N., Eliseev, E. A., Poplawsky, J. D., Goodling, D., Spurling, R. J., Maria, J-P., Kalinin, S. V., & Liu, Y. (2024). Coexistence and Interplay of Two Ferroelectric Mechanisms in $Zn_{1-x}Mg_xO$. *Advanced Materials*, *36*(39), 2404925.

[23] Chi, C., Wang, X., Peng, Y., Qian, Y., Hu, Z., Dong, J., & Zhao, D. (2016). Facile preparation of graphene oxide membranes for gas separation. *Chemistry of Materials*, *28*(9), 2921-2927.

[24] Kim, K. S., Zhao, Y., Jang, H., Lee, S. Y., Kim, J. M., Kim, K. S., Ahn, J-H., Kim, P., Choi, J-Y., & Hong, B. H. (2009). Large-scale pattern growth of graphene films for stretchable transparent electrodes. *Nature*, *457*(7230), 706-710.

[25] Abbas, Q., Liang, H., Shi, J., Chen, Y., Xia, X., Ul Ahmad, A., Liu, J., & Du, G. (2018). Growth and characterization of amorphous boron nitride dielectric films on Si via RF sputtering at room temperature. *Materials Letters*, *227*, 284-288.

[26] Hong, S., Lee, C. S., Lee, M. H., Lee, Y., Ma, K. Y., Kim, G., Yoon, S. I., Ihm, K., Kim, K. -J., Shin, T. J., Kim, S. W., Jeon, E. C., Jeon, H., Kim, J. Y., Lee, H. I., Lee, Z., Antidormi, A., Roche, S., Chhowalla, M., Shin, H. J., & Shin, H. S. (2020). Ultralow-dielectric-constant amorphous boron nitride. Nature, 582(7813), 511-514.

[27] Neureither, B., Cote, D., Nguyen, S., Dobuzinsky, D., & Basa, C. (1994). High selectivity magnetically enhanced reactive ion etching of boron nitride films. IBM Technology Products, 1850 Rt. 52, Hopewell Junction, NY 12533.

[28] Sunal, P., Messier, R., & Horn, M. W. (2006). Reactive co-deposition of TiN_x/SiN_x nanocomposites using pulsed direct current magnetron sputtering. Thin solid films, 515(4), 2185-2191.

Appendix A

Deposition of SiO_2 Nanodots to Reduce the Coercive Field in ZMO

It was hypothesized that if switching occurs by domain nucleation and growth in ZMO, then forcing the existence of pre-existing nuclei could bypass the need to generate nuclei and reduce the coercive field. An interface engineering method was explored to demonstrate the feasibility of this idea. The speculation was that if insulating nanodots were placed on the surface, the material would form a dense array of oppositely oriented domains underneath the nanodots to reduce the polarization discontinuity. 30 nm thick SiO_2 nanodots were patterned with e-beam lithography and deposited on ZMO films via

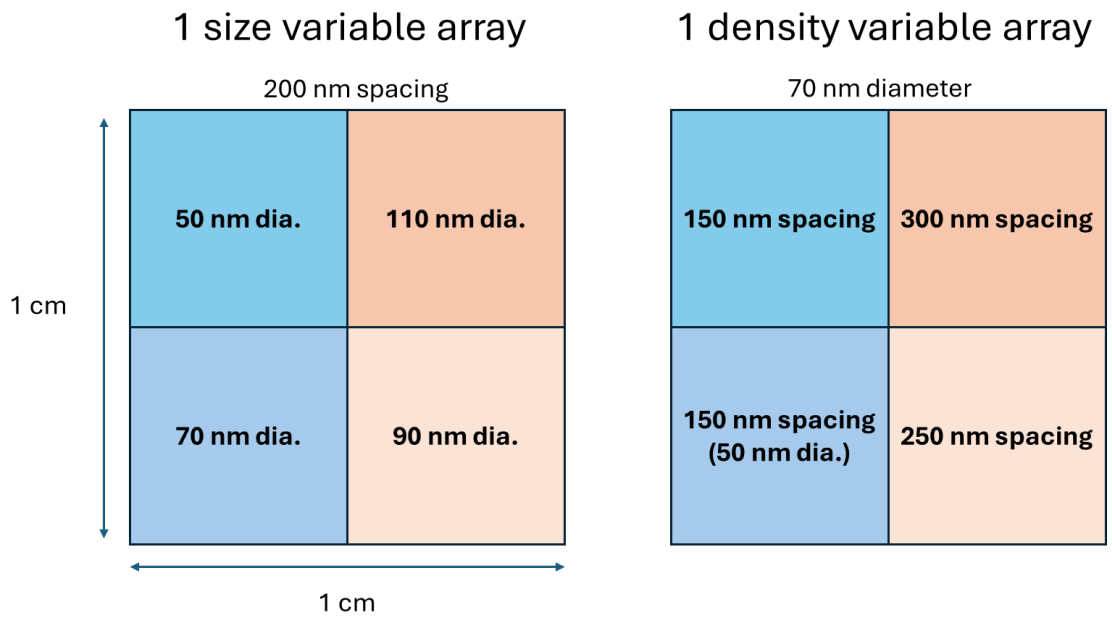

Figure **A**-1: A schematic describing choices of nanodot spacing and diameters for testing the effectiveness of SiO_2 nanodots deposited on ZMO.

e-beam evaporation (c.f. Experimental Methods section) according to the pattern details in Figure A-1. The films were capped with IrO_2 electrodes that were 70 nm thick.

Nanodots were all larger than intended and attempts to deposit nanodots with diameters < 70 nm were mostly unsuccessful. Figures A-2 and A-3 show the deposited nanodots on ZMO in AFM images for the two designs in Figure A-1.

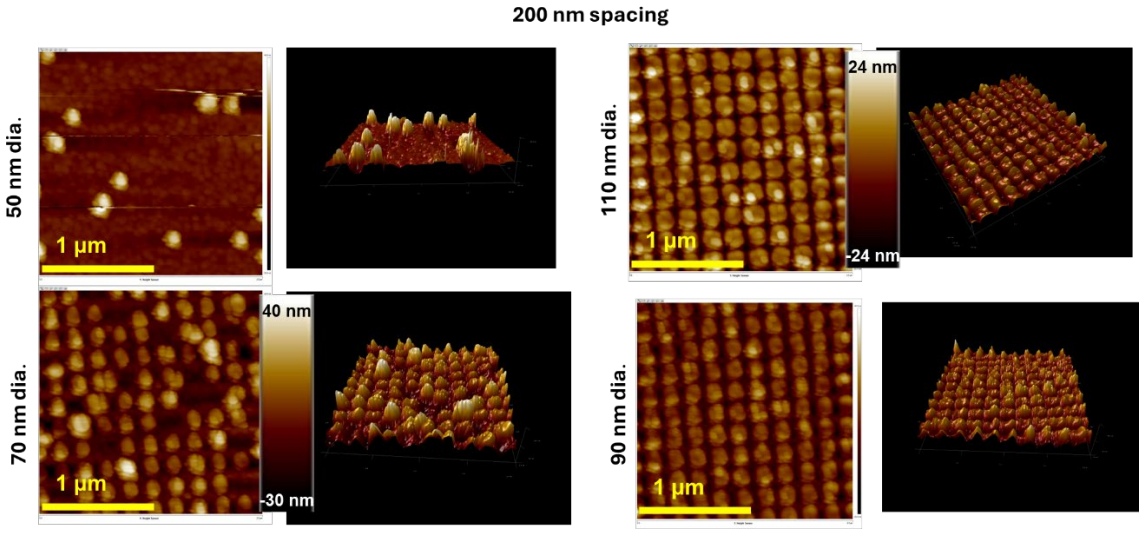

Figure **A**-2: AFM images of SiO_2 nanodots on ZMO with diameters ranging from 50 nm to 110 nm, with 200 nm spacing. All plots are 2 µm × 2 µm. The color scale is the same for the 2-D and 3-D contour plots. The plot for 110 nm diameter spacing has a different color (height) scale from the other plots.

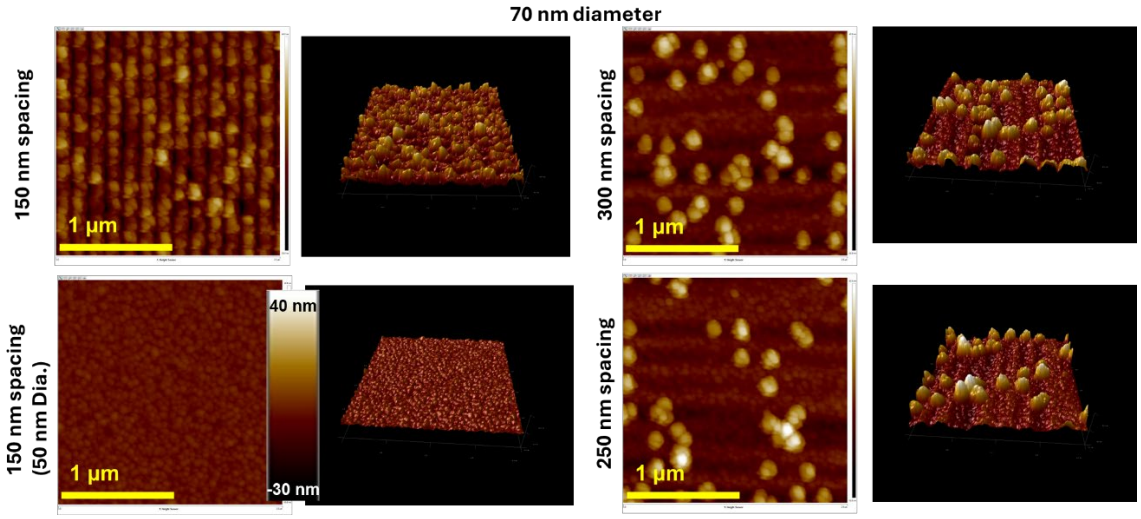

Figure **A**-3: AFM images of SiO_2 nanodots on ZMO with intended 70 nm diameter and spacing ranging from 150 nm to 300 nm. All plots are 2 µm × 2 µm. The color scale is the same for the 2-D and 3-D contour plots.

The presence of nanodots did not improve switching kinetics in ZMO. Instead, the presence of nanodots limited the maximum switching currents to ~ 4.5 mA in a capacitor patterned (incompletely) with 70 nm diameter nanodots and 200 nm spacing (see Figure A-4). Here, the introduction of SiO_2 nanodots reduced the switched polarization by 16 µC cm^{-2} from 89 to 73 µC cm^{-2} at 180 cycles. If the nanodots were 70 nm as patterned, the nanodots should cover 10% of the sample, and the switched polarization would be expected to reduce by 10%. However, an 18% reduction in the switched polarization is observed, which correlates to an effective diameter of 96 nm for the SiO_2 nanodots if there is 100% yield of the pattern. The switched polarization decreases further to 45 µC cm^{-2} at same number of cycles for the patterned 110 nm diameter dots (see Figure A-5), which corresponds to nanodots with an effective diameter of 160 nm.

The disparity in the increase of effective diameter of the SiO_2 nanodots is likely due to lower coverage of the nanodots patterned with a 70 nm diameter. The reductions in switched polarization are likely due to the highly insulating nature of SiO_2, which was too thick for tunneling and was not able to charge compensate the spontaneous polarization of ZMO at the interface. Polarization was likely compensated by generating arrays of oppositely oriented domains underneath the nanodots.

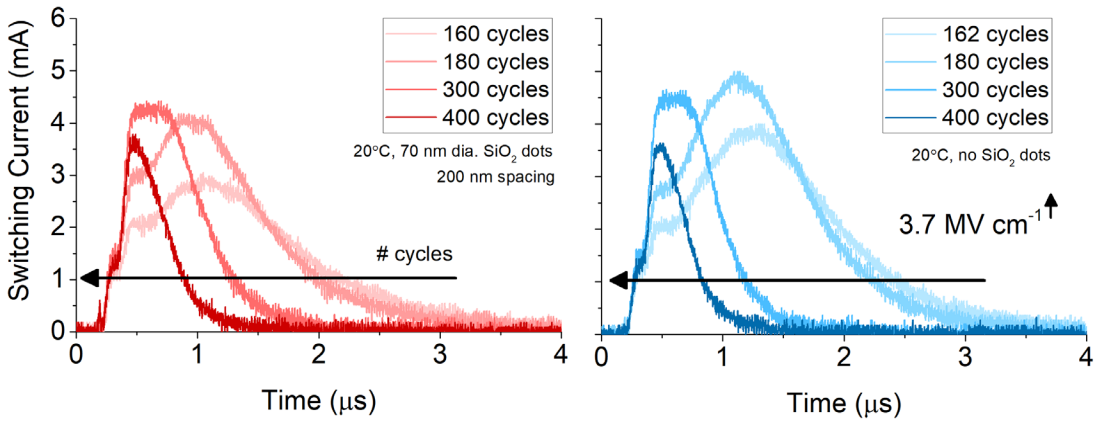

Figure **A-4**: A comparison between switching transients ZMO with (right) and without (left) nanodots after various numbers of cycles, with subtraction of the capacitive current peak.

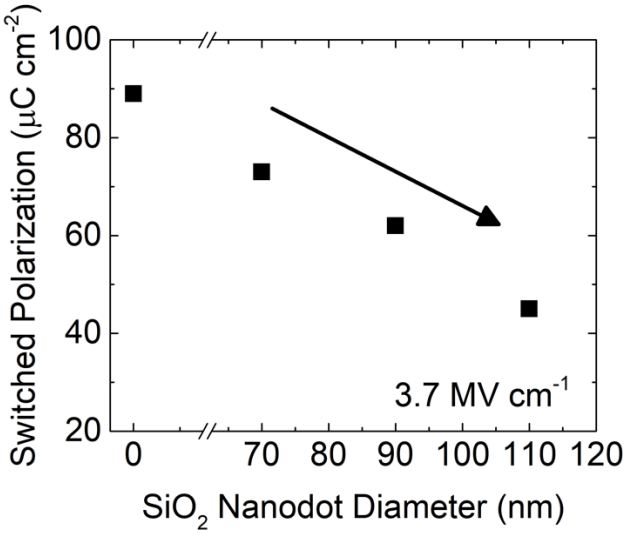

Figure **A**-5: Switched polarizations decreased according to the amount of SiO_2 at the top electrode interface.

Switching in these films and at 3.7 MV cm^{-1} obeyed the KAI kinetics model with n_{KAI}=2, although only a fraction of the spontaneous polarization switched. The first peak that is observed at the onset of polarization reversal in Figure A-4 is the nucleation peak which obeys a Dirac delta function. Differences in the switching times between samples with and without the nanodots were not statistically significant. Therefore, the SiO_2 nanodots were effective in preventing portions of the ferroelectric from switching. However, this does not benefit the switching kinetics in ZMO, possibly because of the significant quantity of nuclei in ZMO. Interface engineering of this type may benefit other wurtzite structure ferroelectrics where there is difficulty in generating nuclei at an interface.[1]

COMSOL Multiphysics was used to simulate the voltage profile through the SiO_2 nanodot/ZMO structure (see Figure A-6), neglecting the existence of the spontaneous

polarization in ZMO. As expected, there was a reduced voltage directly underneath the SiO_2 nanodots due to the lower permittivity of SiO_2 relative to ZMO. This also prevented switching underneath the nanodots. Parameters for the COMSOL Multiphysics simulation are in Table A-1.

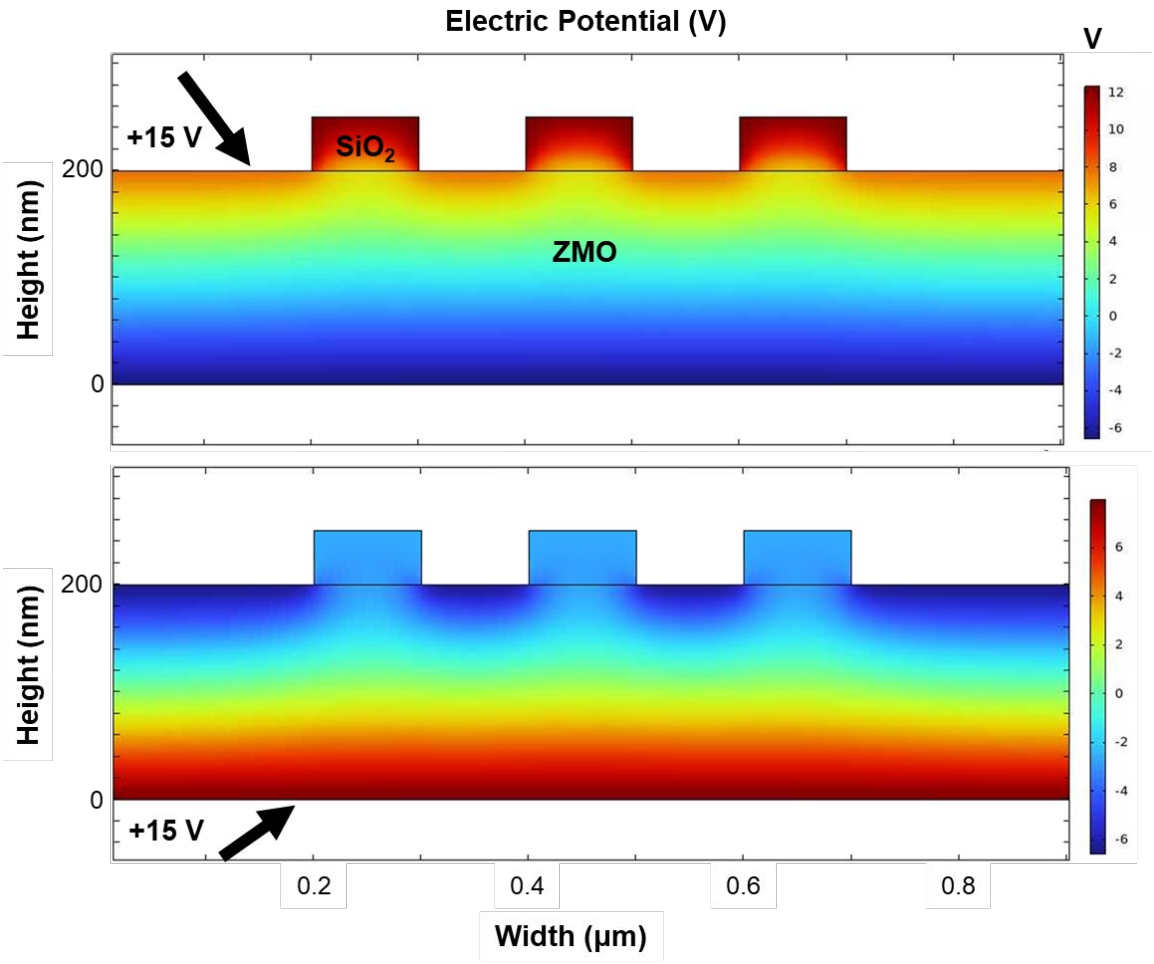

Figure **A-6**: COMSOL multiphysics simulations of electric potential profiles in ZMO with 100 nm diameter SiO_2 nanodots and equipotential regions covering the top and bottom surfaces of the structure. The arrow indicates the surface with applied +15 V. The opposing surface is held at 0 V. Relevant materials parameters are in Table A-1.

Table **A-1**: Materials parameters for ZMO and SiO_2 in COMSOL. The resistivity for ZMO was determined experimentally by the van der Pauw method with 4-point probe contact.

Parameter	ZMO	SiO_2
Temperature	293 K	293 K
Resistivity	10^{11} Ω·m	10^{16} Ω·m [7]
Temperature Coefficient of Resistivity	3×10^{-3} Ω·m/K [2]	3×10^{-6} [8]
Band gap	4 eV [3]	8.9 eV [9]
Electron Affinity	4.8 eV [4]	0.8 eV [10]
Electron Mobility	7.7×10^{-4} $m^2/V\cdot s$ [5]	3×10^{-3} $m^2/V\cdot s$ [11]
Hole Mobility	10^{-7} $m^2/V\cdot s$ [6]	10^{-8} $m^2/V\cdot s$ [12]
N_C	10^{22} m^{-3}	10^{16} m^{-3}
N_V	10^{21} m^{-3}	10^{10} m^{-3}

References

[1] Wolff, N., Schönweger, G., Islam, R. M., Ding, Z., Kübel, C., Fichtner, S., & Kienle, L. (2025). Interfacial Polarization Switching in $Al_{0.92}Sc_{0.08}N$/GaN Heterostructures Grown by Sputter Epitaxy. *arXiv preprint arXiv:2502.09090*.

[2] Zhang, Y., & Han, J. (2006). Microstructure and temperature coefficient of resistivity for ZnO ceramics doped with Al_2O_3. *Materials Letters*, *60*(20), 2522-2525.

[3] Ferri, K., Bachu, S., Zhu, W., Imperatore, M., Hayden, J., Alem, N., Giebink, N., Trolier-McKinstry, S., & Maria, J-P. (2021). Ferroelectrics everywhere: Ferroelectricity in magnesium substituted zinc oxide thin films. *Journal of Applied Physics*, *130*(4), 044101.

[4] Rajbhandari, P. P., Bikowski, A., Perkins, J. D., Dhakal, T. P., & Zakutayev, A. (2017). Combinatorial sputtering of Ga-doped (Zn,Mg)O for contact applications in solar cells. *Solar Energy Materials and Solar Cells*, *159*, 219-226.

[5] Ma, T. Y., & Choi, M. H. (2013). Optical and electrical properties of Mg-doped zinc tin oxide films prepared by radio frequency magnetron sputtering. *Applied Surface Science*, *286*, 131-136.

[6] Heo, Y. W., Kwon, Y. W., Li, Y., Pearton, S. J., & Norton, D. P. (2004). p-type behavior in phosphorus-doped (Zn,Mg)O device structures. *Applied Physics Letters*, *84*(18), 3474-3476.

[7] Bartzsch, H., Glöß, D., Böcher, B., Frach, P., & Goedicke, K. (2003). Properties of SiO_2 and Al_2O_3 films for electrical insulation applications deposited by reactive pulse magnetron sputtering. *Surface and Coatings Technology*, *174*, 774-778.

[8] Microwaves101. (n.d.). *Silicon Dioxide*. https://www.microwaves101.com/encyclopedias/silicon-dioxide

[9] Bersch, E., Rangan, S., Bartynski, R. A., Garfunkel, E., & Vescovo, E. (2008). Band offsets of ultrathin high-κ oxide films with Si. *Physical Review B—Condensed Matter and Materials Physics*, *78*(8), 085114.

[10] Astašauskas, V., Bellissimo, A., Kuksa, P., Tomastik, C., Kalbe, H., & Werner, W. S. (2020). Optical and electronic properties of amorphous silicon dioxide by single and double electron spectroscopy. *Journal of Electron Spectroscopy and Related Phenomena*, *241*, 146829.

[11] Goodman, A. M. (1967). Electron Hall effect in silicon dioxide. *Physical Review*, *164*(3), 1145.

[12] Hughes, R. C. (1975). Hole mobility and transport in thin SiO_2 films. *Applied Physics Letters*, *26*(8), 436-438.

Appendix B

A Non-aqueous Lithographic Process for ZMO

This section contains detailed processes and methodologies pertinent and supplemental to Chapter 3.

Table B-**1**: A non-aqueous lithographic process for depositing top electrodes on ZMO.

	Non-aqueous Lift-Off Procedure
1	Clean the sample surface with acetone and IPA.
2	M4L Plasma clean (Ash Process): He 50 mTorr ; O_2 150 mTorr ; Power 200 W ; Regulate to 550 mTorr ; 2 minutes
3	PMMA A5 in pipette, and spin @ **4,000 RPM for 60 s**
4	Bake for 10 **minutes @ 200°C** on hotplate (Do Not Exceed 200°C, is ok to be a couple degrees below temp.)
5	LOR 5a in pipette, and spin @ **4,000 RPM for 40 s**
6	Bake for **2 minutes @ 190°C** on hotplate
7	SPR 3012 in pipette, and spin **@ 4,000 RPM** for **40 s**
8	Bake for **1 minute @ 95°C** on hotplate
9	Ready for patterning For the MA/BA6 Gen 4: **60 mJ/cm^2** exposure, Use Hard Contact For the Heidelberg MLA: **200 mJ/cm^2** exposure (λ = 375 nm)

10	Prepare one bath of CD-26 to expose the patterned surface - total exposure time to CD-26 ≤ **60** seconds. DO NOT OVER-DEVELOP IN CD-26!!! (it is ok to take stop the develop prematurely to check the progress under an optical microscope, then resume the develop)
11	**IMMEDIATELY rinse samples with water** after developing in CD-26, then **blow samples with nitrogen**.
12	Expose the film to high power UV (SRP 3012 acts as a UV mask) →Fusion UV (λ = 260 nm, 385 mW/cm^2) **120 seconds** exposure. • The ENG-2 recipe can be modified for this. It is usually set to 180 seconds.
13	Expose to **toluene** for 120 seconds, with gentle agitation.
14	Immediately follow with a rinse in IPA, and dry with nitrogen.
15	M4L Plasma Ash to clean the surface of debris and residual resist. Power: 300 W, 2 minutes; He 50 mTorr ; O_2 150 mTorr ; Regulate: 550 mTorr ** Larger electrode areas may require a longer Plasma Ash step. Check the patterns with an optical microscope if you are unsure of the removal of remaining residuals. ** Alternatively, a pre-sputter etch in Ar at 20 mTorr and 100 W for 10 minutes can be used.
16	Deposit the desired top electrode material.

	For the best results, if you are confident of the residuals removal, place samples in the sputter vacuum immediately after the plasma ash process. This will prevent the clean surface from adsorbing atmospheric species.
	Resist Removal Procedure
1	Let the samples stand in acetone for 10 to 15 minutes. You should see an outline of the pattern begin to lift off of the sample. This is the remaining electrode layer. If you deposit a thick electrode of ~100 nm thickness, you may not see the metal lift off. This is not a cause for worry. You may proceed to the next step. It will just take longer to complete the removal process.
2	Wrap the beaker in parafilm and seal it with tape. Then, place the samples in a sonicating bath of acetone for 40 minutes, or until all the photoresist is removed. This step may take over an hour long in difficult cases.
3	Rise the samples with fresh acetone, then let them sit in IPA for 2 minutes. Finally, blow dry with compressed air or nitrogen.
	Finished.

Notes:

- **MAXIMUM top electrode thickness**: **100 nm**
- This process does involve aqueous CD-26 developer and steps with rinses in water, however the surface of interest is protected by PMMA which is spun on first until it is removed by toluene in step 13. After that step the sample should not be exposed to water or other aqueous species.

- This process was modified from an existing process used by Prof. Tom Jackson's group, with the help of MRI staff Kathy Gehoski and Mike LaBella. The citation is shown below:

Gupta, A. (2021). *Zinc Oxide Thin Film Transistor (Zno TFT)–Lipid Membrane Based Electronic Biosensor*. The Pennsylvania State University.

Appendix C

Calculations

C-1 Dielectric Energy Storage and Breakdown Calculations

During dielectric breakdown, all the dielectric energy stored in the capacitor is released at once. In order to calculate the energy released during breakdown, the dielectric energy stored in a capacitor at a given applied field is determined by the equation below:

$$E = \frac{1}{2}(\varepsilon_r - 1)\varepsilon_o E_{max}^2$$

where E is the energy stores in Joules, ε_r is the dielectric constant, ε_o is the permittivity of free space ($8.85 \cdot 10^{-12}\,\frac{s^4A^2}{m^3kg}$), and E_{max} is the applied field in V m^{-1}.

Here is an example calculation for a 100 nm thick ZMO capacitor with a 20 μm diameter, and a dielectric constant of 11:

$$E = \frac{1}{2}(11 - 1)\left(8.85 \cdot 10^{-12}\,\frac{s^4A^2}{m^3kg}\right)\left(5 \cdot 10^8\,\frac{V}{m}\right)$$

$$E = 1.11 \cdot 10^7\,\frac{J}{m^3}$$

Next, the volume of the capacitor must be calculated:

$$V = \pi r^2 t$$

$$V = \pi(10^{-5}\,m)^2(10^{-7}\,m)$$

$$V = 3.14 \cdot 10^{-17}\,m^3$$

Then, the energy stored in the capacitor can be determined:

$$E \times V$$

$$1.11 \cdot 10^7\,\frac{J}{m^3} \times 3.14 \cdot 10^{-17}\,m^3 = 3.47 \cdot 10^{-10}\,J$$

Suppose a single breakdown channel that is 2 μm in diameter is formed:

$$3.47 \cdot 10^{-10} J \div \pi(1 \cdot 10^{-4}\ cm)^2 = 11\ \mathrm{mJ/cm^2}$$

If breakdown occurs over a 15 μm diameter area:

$$3.47 \cdot 10^{-10} J \div \pi(7.5 \cdot 10^{-4}\ cm)^2 = 0.2\ \mathrm{mJ/cm^2}$$

The energy density of a breakdown event is significantly lower when it occurs over a larger area (see Figure C-3). The reason energy density is important is because non-trivial shockwaves can be produced in capacitors where energy density is > 10 mJ cm^2 (see Figures C-1 and C-2).[1] This can potentially cause spalling of the SiO_2 layer in ZMO remote probe contact devices, especially if the breakdown channel forms beneath the SiO_2 layer.

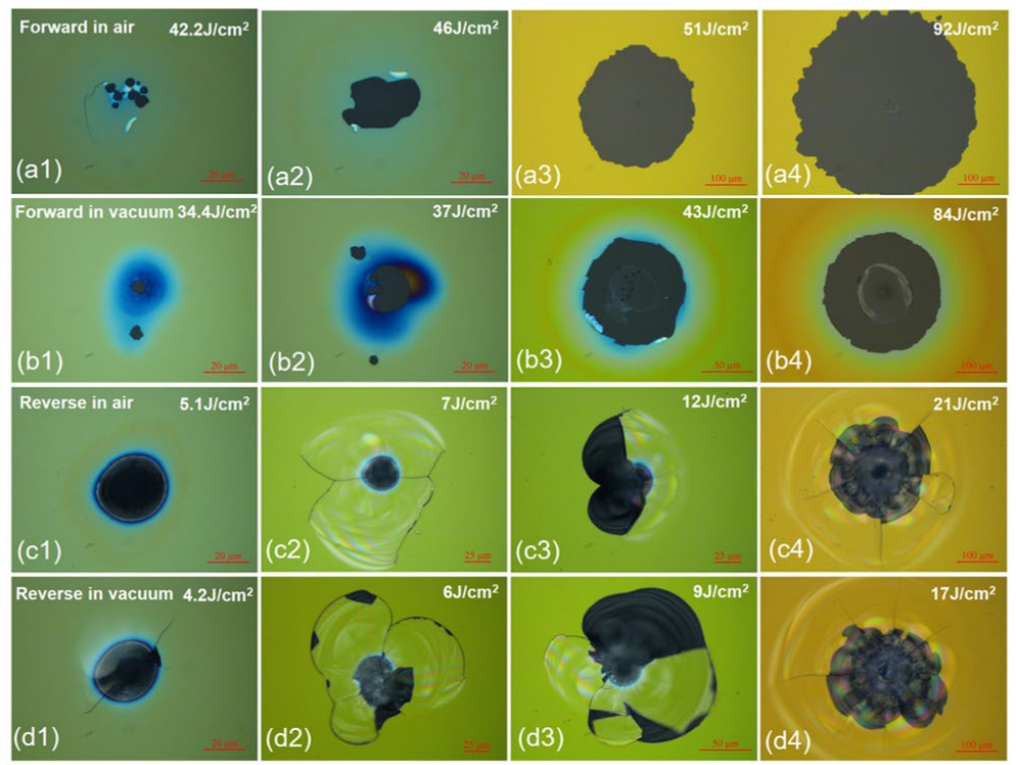

Figure **C-1**: HfO_2/SiO_2 coatings with laser-induced damage at the specified energy densities. "Forward" indicates laser incident on the surface of the coating. "Reverse" indicates laser incident on the backside of the coating. Cracking can occur at energy densities > 7 mJ cm^{-2}.[1]

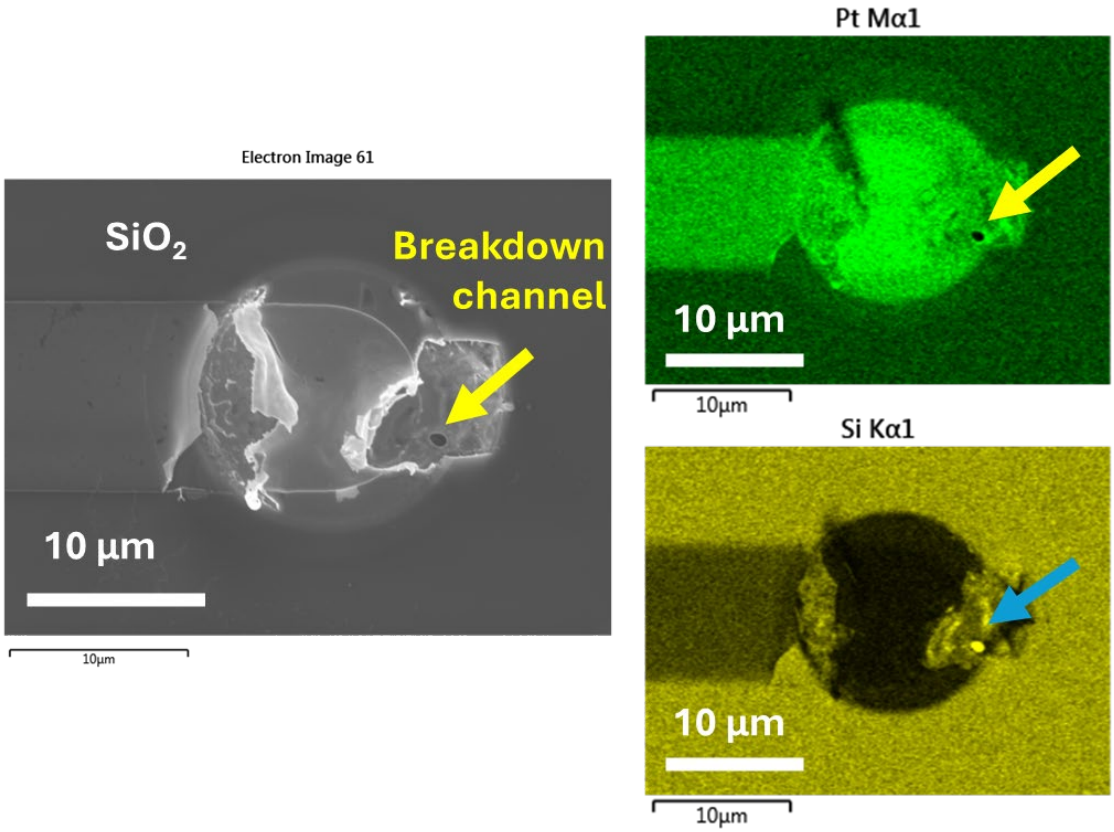

Figure **C-2**: Spalling was observed in ZMO generation 2 non-contact probe devices because of thermal breakdown. In this case, the breakdown channel was at the edge of the SiO_2 layer, and part of the Ir via peeled back. This caused the SiO_2 to peel as well.

In addition, enough heat is released during breakdown to melt portions of the ferroelectric layer. The relevant calculations are shown below.

$$V = \frac{E_{Br}}{H_{ZnO}\rho_{ZnO}} = \frac{3.47 \cdot 10^{-10}\, J}{\left(230\frac{J}{g}\right)\left(5.61\frac{g}{cm^3}\right)} = 2.6 \times 10^{-13} cm^3 = 0.26\, \mu m^3$$

where V is the volume of melted material (ZnO), E_{Br} is the energy released during breakdown, and H_{ZnO} is the enthalpy of fusion of ZnO,[2] and ρ_{ZnO} is the density of ZnO. Enough energy is released

during breakdown to decompose nearly 0.3 μm^3 of ZnO, which is in reasonable agreement with the observation of 1 μm wide breakdown craters in 100 – 200 nm thick ZMO (see Figure C-2).

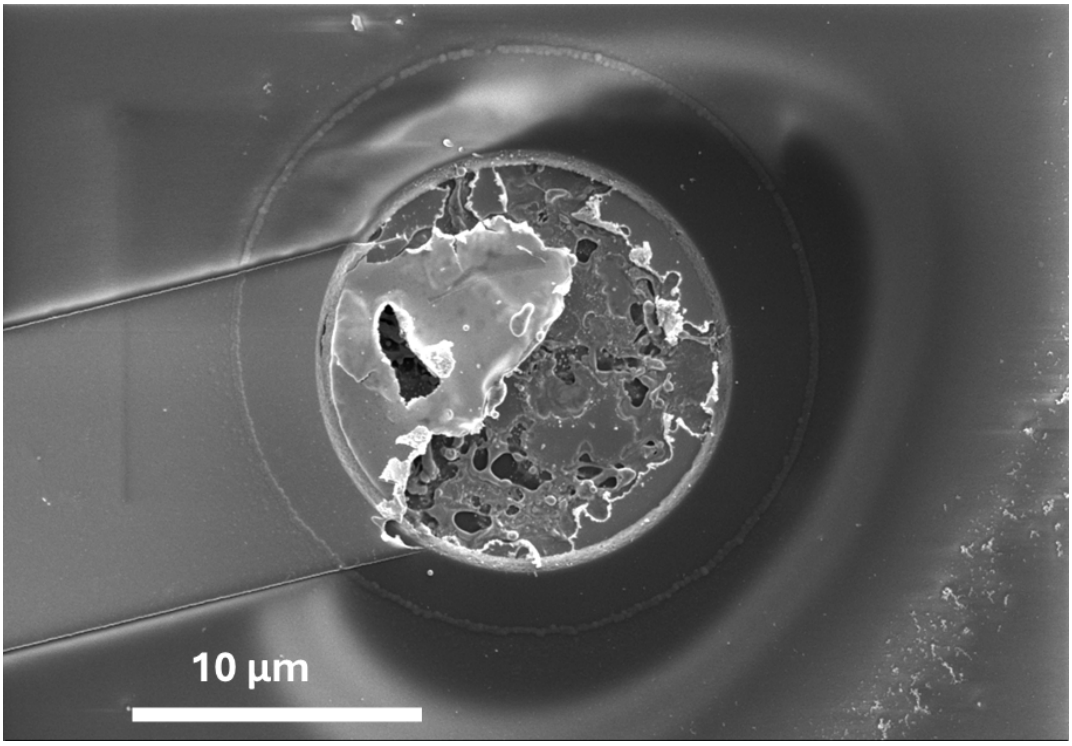

Figure **C-3**: Breakdown energy is spread over the breadth of the exposed electrode area in a generation 2 ZMO device.

References

[1] Zhou, Q., Qiu, F., Ma, P., Pu, Y., Qiao, Z., Lv, L., Zhang, M., & Die, J. (2023). Investigating the material properties of HfO_2/SiO_2-based anti-reflection coatings during 1064 nm laser-induced breakdown in air and vacuum conditions. Optics & Laser Technology, 157, 108645.

[2] MatWeb. (n.d.). *Material property data for zinc oxide, ZnO, Zincite*. MatWeb. https://www.matweb.com/search/datasheet.aspx?matguid=173a8f1e7cec4ce7af5dc3b90d10f756C

-2 Parasitic Capacitance Subtractions (Analytical Method)

C-2 Calculations to Subtract Parasitic Capacitance

The parasitic capacitance can be subtracted from ZMO devices. The known relative permittivity of ZMO ~ 11 was used for the parasitic capacitance subtraction. The equation relating the polarization (P), electric field (E, in V/m) and the dielectric constant (ε_r) in a P-E hysteresis loop is below:

$$\mathrm{P} = \varepsilon_0 \chi \times E$$

$$\mathrm{P} = \varepsilon_0 (\varepsilon_r - 1) \times E$$

Modifying this equation to consider the parasitic capacitance:

$$\mathrm{P} = \varepsilon_0 \chi_{total} \times E \left(\frac{V}{m}\right)$$

$$\mathrm{P} = \varepsilon_0 \left(\chi_{parasitic} + \chi\right) \times E \left(\frac{V}{m}\right)$$

From the above equation, the contribution of the parasitic capacitance ($\chi_{parasitic}$) can be determined. LINEST was used to measure the slope of the P-E hysteresis loop near the remanent polarization, and determine χ_{total}. From this, $\chi_{parasitic}$ was determined. The polarization values of the adjusted hysteresis loop were corrected according to the following equation:

$$\mathrm{P_{corrected}} = \mathrm{P_{exp}} - (\varepsilon_0 \chi_{parasitic} \times E \left(\frac{V}{m}\right))$$

Where $\mathrm{P_{corrected}}$ is the corrected polarization value, and $\mathrm{P_{exp}}$ is the experimental polarization value (c.f. Figure 6.13).

C-3 MATLAB Codes

These are the working MATLAB codes as of December 31, 2024. These programs are designed to find the least error fit of experimental data. The programming methodology used is

original and was not informed from other sources except for the MathWorks website to find useful MATLAB functions.

C-3-1 SNNG Model (now available on Github)

```
%% Leonard Jacques
% December 2024

% For determining the extended KAI (SNNG) model kinetics applicable to
% polarization reversal in the ferroelectric switching of wurtzite
% structure ferroelectrics such as doped AlN or ZnO systems.

% ref. Yazawa et al. (2023). Mater. Hrz., 10(8), 2936-2944.

clear
%% User Inputs
%% Import from File:
xfrac = readtable('TEK00768.CSV'); % Imports data from a .txt file that is tab delimited performs the function of "text to columns"
nsxfrac = readtable(['TEK00767.CSV']); % Imports non-switching data, later to be subtracted from the switching data. Variables specific to non-switching data have "ns" in front of it.
d = 220; % sample thickness in nanometers
thickness = d*10^-7; % film thickness (cm)
area = 2.8*10^-5; % sample area in cm^2 7.85*10^-5 for 100 micron dia., 2.83*10^-5 for 60 micron dia.
AvraminMod = 0; % for modifying the location of where n is determined (in ns)
tzerosp = 70*0.01; % the fraction of the setpoint voltage to call t0
ErrorStop = 100*0.01; % The percentage of the polarization where to stop calculating for the error in the regression calculations at the end of this script
dNuc = 10*10^-7; % The surface/in-plane diameter of nuclei in the film in units of centimeters

%% Fitting Parameters
v = 0.01; % growth speed (cm/s)  **  The domain wall speed is a function of both the applied field and the temperature. This value is unknown at the moment, so the speed of sound of 34,300 cm/s is used.
Ninf = 5*10^25; % initial guess for the saturated density of nuclei (/cm^3)
a=10^1; % use a larger initial value of "a" to save time and iterations when the switching occurs earlier
% Ninf, a and m are automatically determined later in this script. m = n-2
% v and Ninf can be coupled together as v*Ninf^(1/2)

%% imported data management
% for the switching data
xfrac = table2array(xfrac); % converts the imported data type from "table' to "array"
nsxfrac = table2array(nsxfrac); % for the non-switching data
% finding where the function generator output begins
xa = xfrac(:,2); % calling CH1, the function generator output
xa = abs(xa); % making all values positive for referencing applications to follow
xaloc = find(xa==0.12); % 0.10 to 0.24V is the function generator output that signifies the output has begun !!! CHECK THIS VALUE IF THE CODE DOES NOT WORK !
n=isempty(xaloc); % this series of if loops is used to determine where the function generator input begins for the switching data
if n==1
   xaloc = find(xa==0.12);
   n=isempty(xaloc);
end
if n==1
   xaloc = find(xa==0.14);
   n=isempty(xaloc);
end
if n==1
   xaloc = find(xa==0.16);
   n=isempty(xaloc);
end
```

```
if n==1
   xaloc = find(xa==0.18);
   n=isempty(xaloc);
end
if n==1
   xaloc = find(xa==0.20);
   n=isempty(xaloc);
end
pos1 = xaloc(1) +100 -2; % holds the value where to start accepting points. +100 is for neglecting the first 100 ns before the amplifier
output begins.
% ps 1 also governs the position of t0
% for the non-switchng data (ns)
nsxa = nsxfrac(:,2); % calling CH1, the function generator output
nsxa = abs(nsxa);
nsxaloc = find(nsxa==0.18); % > 0.10 V is the function generator output that signifies the output has begun  !!! CHECK THIS
VALUE IF THE CODE DOES NOT WORK !!!
n=isempty(nsxaloc);
if n==1  % this series of if loops is used to determine where the function generator input begins for the non-switching data
   nsxaloc = find(nsxa==0.12);
   n=isempty(nsxaloc);
end
if n==1
   nsxaloc = find(nsxa==0.14);
   n=isempty(nsxaloc);
end
if n==1
   nsxaloc = find(nsxa==0.16);
   n=isempty(nsxaloc);
end
if n==1
   nsxaloc = find(nsxa==0.18);
   n=isempty(nsxaloc);
end
if n==1
   nsxaloc = find(nsxa==0.20);
   n=isempty(nsxaloc);
end
nspos1 = nsxaloc(1) +100 - 2; % holds the value where to start accepting points. +100 is for neglecting the first 100 ns before the
amplifier output begins.

%% Adjusting for t0, and choosing the data to simulate
t0adjust = xfrac(pos1:end,3);
maxamp = mode(t0adjust); % assumes the mode (most common value) in the amplifier output is the voltage setpoint
fract0 = tzerosp*maxamp; % calculates the voltage where to start accepting
fract0 = abs(fract0); % for handling negative values
t0adjust = abs(t0adjust); % for handling negative values
t0pos = find(t0adjust>fract0); % finds the position of t0 in the amplifier output greater than the defined percentage of the setpoint
voltage where to start the simulation

pos1 = pos1 + t0pos(1); % adjusts the pos1 time for the voltage where t0 is assigned
nspos1 = nspos1 + t0pos(1);

% shortens the arrays for the function generator (fg), amplifier (amp) and
% TIA (tia) switching curves
fg = xfrac(pos1:end,2);
amp = xfrac(pos1:end,3);
tia = abs(xfrac(pos1:end,4).*1000./22); % TIA output (in mA)
l = length(tia);

%% setting the time at polarization saturation
[maxtiaval,maxTIApos] = max(tia); % maximum current value and position from the TIA
tiafind = tia(maxTIApos:end);
zeroTIApos = find(tiafind < 0.5); % to index the zero positions after the TIA current peak
timelimit = maxTIApos + zeroTIApos(1) + 400; % to identify the location where the polarization is considered to have saturated

% non-switching curve
nsfg = nsxfrac(nspos1:end,2);
```

```
nsamp = nsxfrac(nspos1:end,3);
nstia = abs(nsxfrac(nspos1:end,4).*1000./22); % TIA output (in mA)
nsl = length(nstia);

% to set the proper array length of data to calculate
if l <= nsl
   l = l;
elseif l > nsl
   l = nsl;
end
l=9000;% sets the length scale to stop at 9 microseconds
%% Leakge current subtration from the TIA output
NetLeakageCurrent = mean(tia(3000:9000))-mean(nstia(3000:9000)); % calculated the mean of the TIA output beyond the switching
transient from 3 to 9 microseconds
tia = tia(1:9000)-nstia(1:9000);
if NetLeakageCurrent > 0
   tia(timelimit+400:end) = tia(timelimit+400:end)-NetLeakageCurrent;
end
%% Imported data mamagement and calculation of experimental volume fraction transformed
% calculates the experimental polarization by subtracting a switching curve
% from the non-switching curve

time = 0.001:0.001:0.001*l; % sets the time in microseconds
time = transpose(time);

i=1;
po = 0;
while i <= l
   polarization(i,1) = po + 10^3*((tia(i,1)-nstia(i,1))*(10^-9))/area; % solves for the polarization by subtracting the switching curve
from the non-switching curve
   po = polarization(i);
   i=i+1;
end

expfraction = polarization./polarization(timelimit); % calls the sets the volume fraction of polarization
tcorrection = 0.2; % A correction factor which simultaneously shifts the ext. KAI model and projected nucleation rate forward to a
lower time (in order to match the slope) and adjusts the x-axis limit of the plot accordingly.
time2 = [0.001:0.001:l*0.001]-tcorrection; % Sets the array for plotting of the ext. KAI model and the projected nucleation rate peak.

%% Finding maximum value of the current to assign the Avrami constant, n

maxCurrent = max(tia);
maxCurrent = find(tia==maxCurrent); % Assigns the position of the max current in the array
Begin = maxCurrent(1) - 10;
Last = maxCurrent(1) + 10;

timevar = log((10^-9).*time(Begin:Last)); % changes unit of time from nanooseconds to seconds
polarizationvar = log(log(1./(1-expfraction([Begin:Last]+AvraminMod))));
Avramin = polyfit(timevar,polarizationvar,1);
lnK = Avramin(2);
Avramin = Avramin(1);

m = Avramin-2 % Avramin-2; % sets the fitting parameter "m" to n-2.

%% Auto determination of the fitting paramenter "a"
j=1;
while j<70
   %% Simulated KAI model
   % setting up the integral
   t = 10^-9; % (beginning of) time in the upper integrand (s)
   i=1;
   while i<=l
      fun = @(tnuc) tnuc.^(m-1).*(t-tnuc).^2.*exp(-1.*a.*t.^m); % setting up the integral in the modofied KAI formula
      x = integral(fun,0,t);
      f = 1-exp(-2*pi*thickness*v^2*Ninf*a*m*x);
      Pfraction(i) = f; % sets values in an array for transformation fraction
      t=t+(10^-9); % adds 1 nanosecond to the time
```

```
    i=i+1;
  end

  % adds to the power of a
  powera = ceil(log10(a));
  if max(Pfraction) < 0.5
    a = 10^(powera+1);
  elseif max(Pfraction) >= 0.5
    break % exits teh while loop when conditions are met
  end
  j=j+1;
end

%% Nucleation rate peak calculation
i = 1;
t = 10^-9; %
while i<=l
  Nrp = a*m*t^(m-1)*exp(-1*a*t^m); % relative nucleation rate peak
  NucRatePeak(i) = Nrp; % sets values in an array for the nucleation rate peak
  t=t+(10^-9); % adds 1 nanosecond to the time
  i=i+1;
end
y = transpose(Pfraction); % transposed the Pfraction into columnar data which can be used later for exporting


%figure % for plotting the data used to determine the Avrami n
%plot(timevar,polarizationvar)

%% Plot the extended KAI model vs. Experimental data
figure % creates a new figure
yyaxis left % sets up the left yaxis
p = plot(time,expfraction,(time),Pfraction,'k'); % plotted data for the left y-axis
title('Extended KAI model comparison with experimental data') % plot title
xlabel('Time (microseconds)') % generates axis titles
ylabel('fraction of polarization reversal')
ylim([-0.01 1]) % sets bounds for the left y-axis
xlim([0 (2-tcorrection)])
p(1).LineWidth = 3; % sets the width of lines in the plot
p(2).LineWidth = 2;
caption = sprintf(' n = %1.2s \n m = %1.2s \n a = %1.1s \n Ninf = %1.1s',Avramin,m,a,Ninf); % text for the caption, limited to one
decimal place by %1.1s
text(0.1,0.6,caption); % generates a text box at the coordinates (x,y,caption) according to the left y-axis
%setting up the right y-axis
yyaxis right % sets up the right y axis. syntax below will correspond to the right y-axis.
plot(time2,NucRatePeak); % plotted data for the right y-axis
ylabel('N/N(\infty)')
ylim([0 10^4])
legend('experimental','ext. KAI model','Nuc. rate') % creates a legend for both the left and right y-axes in one box

%% Automatic determination of the fitting parameters a and Ninf

%% Slope matching with a
% Modifying the fitting parameter, a
j=1;
while j<40 % the number of iterations to run
  j
  Pfloc = find(Pfraction>=0.5); % holds the index values where the value of Pfraction, the calculated KAI curve, is greater than 0.5,
in order to calculate the n value there.
  Begin = Pfloc(1) - 10;
  Last = Pfloc(1) + 10;
  % Determinining the slope of the simulated curve in order to compare it to
  % the experimental volume fracton transformed.
  KAIvar = log(log(1./(1-Pfraction(Begin:Last))));
  KAIn = polyfit(timevar,KAIvar,1);
  % for modifying the power exponent of a
  powera = ceil(log10(a));
  if KAIn(1)<Avramin
```

```
        a = 10^(powera+1)+1;
    elseif KAIn(1)>Avramin
        a = 10^(powera-1)+1;
    elseif KAIn(1)==Avramin
        sprintf('KAIn(1)=Avramin')
    end
testm = [KAIn(1),Avramin]
a
    % Simulated KAI model
    % setting up the integral
    t = 10^-9; % (beginning of) time in the upper integrand (s)
    i=1;

    if m<0
        m=0.01;
    end

    while i<=l
        fun = @(tnuc) tnuc.^(m-1).*(t-tnuc).^2.*exp(-1.*a.*t.^m); % setting up the integral in the modofied KAI formula
        x = integral(fun,0,t);
        f = 1-exp(-2*pi*thickness*v^2*Ninf*a*m*x);
        Pfraction(i) = f; % sets values in an array for transformation fraction
        t=t+(10^-9); % adds 1 nanosecond to the time
        i=i+1;
    end

    % calculates the n value for the KAI model
    KAIvar = log(log(1./(1-Pfraction(Begin:Last))));
    KAIn = polyfit(timevar,KAIvar,1);
    % this will end the while loop when the values begin to toggle
    testKAI(j) = KAIn(1); % stores and array of values of the slopes of the simulated curve
    if j>2
        if testKAI(j)==testKAI(j-2)
            break
        end
    end
    j=j+1;
end
clear testKAI
%% Slope matching with Ninf
% Modifying the saturated density of nuclei, Ninf
j=1;
while j<40
    Pfloc = find(Pfraction>=0.5); % holds the index values where the value of Pfraction, the calculated KAI curve, is greater than 0.5,
in order to calculate the n value there.
    Begin = Pfloc(1) - 10;
    Last = Pfloc(1) + 10;
    % Determinining the slope of the simulated curve in order to compare it to
    % the experimental volume fracton transformed.
    KAIvar = log(log(1./(1-Pfraction(Begin:Last))));
    KAIn = polyfit(timevar,KAIvar,1);
    % for modifying the power exponent of a
    powerNinf = ceil(log10(Ninf)-1);
    if KAIn(1)<Avramin
        Ninf = Ninf + 10^powerNinf;
    elseif KAIn(1)>Avramin
        Ninf = Ninf - 10^powerNinf;
    elseif KAIn(1)==Avramin
        sprintf('KAIn(1)=Avramin')
    end
testm = [KAIn(1),Avramin]
a
    % Simulated KAI model
    % setting up the integral
    t = 10^-9; % (beginning of) time in the upper integrand (s)
    i=1;
    while i<=l
```

```
    fun = @(tnuc) tnuc.^(m-1).*(t-tnuc).^2.*exp(-1.*a.*t.^m); % setting up the integral in the modofied KAI formula
    x = integral(fun,0,t);
    f = 1-exp(-2*pi*thickness*v^2*Ninf*a*m*x);
    Pfraction(i) = f; % sets values in an array for transformation fraction
    t=t+(10^-9); % adds 1 nanosecond to the time
    i=i+1;
  end

  % this will end the while loop when the values begin to toggle
  testKAI(j) = KAIn(1); % stores and array of values of the slopes of the simulated curve
  if j>2
    if testKAI(j)==testKAI(j-2)
      break
    end
  end
  j=j+1;
end
clear testKAI

exploc = find(expfraction>=0.5);
%% Position finding with a
j=1;
while j<20
  Pfloc = find(Pfraction>=0.5); % holds the index values where the value of Pfraction, the calculated KAI curve, is greater than 0.5,
in order to calculate the n value there.
  powera = ceil(log10(a))-1;
  if Pfloc(1)<exploc(1)
    a = a - 9*10^(powera-1);
  elseif Pfloc(1)>exploc(1)
    a = a + 9*10^(powera-1);
  elseif Pfloc(1)==exploc(1)
    sprintf('Pfloc(1) = exploc(1)')
  end
testm = [KAIn(1),Avramin]
test2peakloc= [Pfloc(1),exploc(1)]
  % Simulated KAI model
  % setting up the integral
  t = 10^-9; % (beginning of) time in the upper integrand (s)
  i=1;
  while i<=l
    fun = @(tnuc) tnuc.^(m-1).*(t-tnuc).^2.*exp(-1.*a.*t.^m); % setting up the integral in the modofied KAI formula
    x = integral(fun,0,t);
    f = 1-exp(-2*pi*thickness*v^2*Ninf*a*m*x);
    Pfraction(i) = f; % sets values in an array for transformation fraction
    t=t+(10^-9); % adds 1 nanosecond to the time
    i=i+1;
  end

  % calculates the n value for the KAI model
  KAIvar = log(log(1./(1-Pfraction(Begin:Last))));
  KAIn = polyfit(timevar,KAIvar,1);
  % this will end the while loop when the values begin to toggle
  testKAI(j) = KAIn(1); % stores and array of values of the slopes of the simulated curve
  if j>2
    if testKAI(j)==testKAI(j-2)
      break
    end
  end
  j=j+1;
end
clear testKAI
%% Slope matching with Ninf (2nd time)
% Modifying the saturated density of nuclei, Ninf
j=1;
while j<20
  Pfloc = find(Pfraction>=0.5); % holds the index values where the value of Pfraction, the calculated KAI curve, is greater than 0.5,
in order to calculate the n value there.
```

```
    Begin = Pfloc(1) - 10;
    Last = Pfloc(1) + 10;
    % Determinining the slope of the simulated curve in order to compare it to
    % the experimental volume fracton transformed.
    KAIvar = log(log(1./(1-Pfraction(Begin:Last))));
    KAIn = polyfit(timevar,KAIvar,1);
    % for modifying the power exponent of a
    powerNinf = ceil(log10(Ninf)-2);
    if KAIn(1)<Avramin
        Ninf = Ninf + 10^powerNinf;
    elseif KAIn(1)>Avramin
        Ninf = Ninf - 10^powerNinf;
    elseif KAIn(1)==Avramin
        sprintf('KAIn(1)=Avramin')
    end
testm = [KAIn(1),Avramin]
test2peakloc = [Pfloc(1),exploc(1)]
    % Simulated KAI model
    % setting up the integral
    t = 10^-9; % (beginning of) time in the upper integrand (s)
    i=1;
    while i<=l
        fun = @(tnuc) tnuc.^(m-1).*(t-tnuc).^2.*exp(-1.*a.*t.^m); % setting up the integral in the modofied KAI formula
        x = integral(fun,0,t);
        f = 1-exp(-2*pi*thickness*v^2*Ninf*a*m*x);
        Pfraction(i) = f; % sets values in an array for transformation fraction
        t=t+(10^-9); % adds 1 nanosecond to the time
        i=i+1;
    end

    % this will end the while loop when the values begin to toggle
    testKAI(j) = KAIn(1); % stores and array of values of the slopes of the simulated curve
    if j>2
        if testKAI(j)==testKAI(j-2)
            break
        end
    end
    j=j+1;
end
clear testKAI
exploc = find(expfraction>=0.5);
%% Position finding with a (2nd time) (Finer tuning)
j=1;
while j<20
    Pfloc = find(Pfraction>=0.5); % holds the index values where the value of Pfraction, the calculated KAI curve, is greater than 0.5,
in order to calculate the n value there.
    powera = ceil(log10(a))-1;
    if Pfloc(1)<exploc(1)
        a = a - 9*10^(powera-1);
    elseif Pfloc(1)>exploc(1)
        a = a + 9*10^(powera-1);
    elseif Pfloc(1)==exploc(1)
        sprintf('Pfloc(1) = exploc(1)')
    end
testm = [KAIn(1),Avramin]
test2peakloc= [Pfloc(1),exploc(1)]
    % Simulated KAI model
    % setting up the integral
    t = 10^-9; % (beginning of) time in the upper integrand (s)
    i=1;
    while i<=l
        fun = @(tnuc) tnuc.^(m-1).*(t-tnuc).^2.*exp(-1.*a.*t.^m); % setting up the integral in the modofied KAI formula
        x = integral(fun,0,t);
        f = 1-exp(-2*pi*thickness*v^2*Ninf*a*m*x);
        Pfraction(i) = f; % sets values in an array for transformation fraction
        t=t+(10^-9); % adds 1 nanosecond to the time
        i=i+1;
```

```
    end

    % calculates the n value for the KAI model
    KAIvar = log(log(1./(1-Pfraction(Begin:Last))));
    KAIn = polyfit(timevar,KAIvar,1);
    % this will end the while loop when the values begin to toggle
    testKAI(j) = KAIn(1); % stores and array of values of the slopes of the simulated curve
    if j>2
       if testKAI(j)==testKAI(j-2)
          break
       end
    end
    j=j+1;
end
clear testKAI
%% Slope matching with Ninf (3rd time) (Finer Tuning)
% Modifying the saturated density of nuclei, Ninf
j=1;
while j<20
    Pfloc = find(Pfraction>=0.5); % holds the index values where the value of Pfraction, the calculated KAI curve, is greater than 0.5,
in order to calculate the n value there.
    Begin = Pfloc(1) - 10;
    Last = Pfloc(1) + 10;
    % Determinining the slope of the simulated curve in order to compare it to
    % the experimental volume fracton transformed.
    KAIvar = log(log(1./(1-Pfraction(Begin:Last))));
    KAIn = polyfit(timevar,KAIvar,1);
    % for modifying the power exponent of a
    powerNinf = ceil(log10(Ninf)-1);
    if KAIn(1)<Avramin
       Ninf = Ninf + 10^(powerNinf-1);
    elseif KAIn(1)>Avramin
       Ninf = Ninf - 10^(powerNinf-1);
    elseif KAIn(1)==Avramin
       sprintf('KAIn(1)=Avramin')
    end
testm = [KAIn(1),Avramin]
test2peakloc= [Pfloc(1),exploc(1)]
    % Simulated KAI model
    % setting up the integral
    t = 10^-9; % (beginning of) time in the upper integrand (s)
    i=1;
    while i<=l
       fun = @(tnuc) tnuc.^(m-1).*(t-tnuc).^2.*exp(-1.*a.*t.^m); % setting up the integral in the modofied KAI formula
       x = integral(fun,0,t);
       f = 1-exp(-2*pi*thickness*v^2*Ninf*a*m*x);
       Pfraction(i) = f; % sets values in an array for transformation fraction
       t=t+(10^-9); % adds 1 nanosecond to the time
       i=i+1;
    end

    % this will end the while loop when the values begin to toggle
    testKAI(j) = KAIn(1); % stores and array of values of the slopes of the simulated curve
    if j>2
       if testKAI(j)==testKAI(j-2)
          break
       end
    end
    j=j+1;
end
clear testKAI
%% Slope matching with a (Finer tuning)
% Modifying the fitting parameter, a
j=1;
while j<20 % the maximum number of iterations to run
    Pfloc = find(Pfraction>=0.5); % holds the index values where the value of Pfraction, the calculated KAI curve, is greater than 0.5,
in order to calculate the n value there.
```

```
    Begin = Pfloc(1) - 10;
    Last = Pfloc(1) + 10;
    % Determinining the slope of the simulated curve in order to compare it to
    % the experimental volume fracton transformed.
    KAIvar = log(log(1./(1-Pfraction(Begin:Last))));
    KAIn = polyfit(timevar,KAIvar,1);
    % for modifying the power exponent of a
    powera = ceil(log10(a))-1;
    if KAIn(1)<Avramin
        a = a + 10^(powera-1);
    elseif KAIn(1)>Avramin
        a = a - 10^(powera-1);
    elseif KAIn(1)==Avramin
        sprintf('KAIn(1)=Avramin')
    end
testm = [KAIn(1),Avramin]
test2peakloc= [Pfloc(1),exploc(1)]
    % Simulated KAI model
    % setting up the integral
    t = 10^-9; % (beginning of) time in the upper integrand (s)
    i=1;
    while i<=l
        fun = @(tnuc) tnuc.^(m-1).*(t-tnuc).^2.*exp(-1.*a.*t.^m); % setting up the integral in the modofied KAI formula
        x = integral(fun,0,t);
        f = 1-exp(-2*pi*thickness*v^2*Ninf*a*m*x);
        Pfraction(i) = f; % sets values in an array for transformation fraction
        t=t+(10^-9); % adds 1 nanosecond to the time
        i=i+1;
    end

    % calculates the n value for the KAI model
    KAIvar = log(log(1./(1-Pfraction(Begin:Last))));
    KAIn = polyfit(timevar,KAIvar,1);
    % this will end the while loop when the values begin to toggle
    testKAI(j) = KAIn(1); % stores and array of values of the slopes of the simulated curve
    if j>2
        if testKAI(j)==testKAI(j-2)
            break
        end
    end
    j=j+1;
end
clear testKAI
%% Slope matching with Ninf (3rd time) (Finest Tuning)
% Modifying the saturated density of nuclei, Ninf
j=1;
while j<20
    Pfloc = find(Pfraction>=0.5); % holds the index values where the value of Pfraction, the calculated KAI curve, is greater than 0.5,
in order to calculate the n value there.
    Begin = Pfloc(1) - 10;
    Last = Pfloc(1) + 10;
    % Determinining the slope of the simulated curve in order to compare it to
    % the experimental volume fracton transformed.
    KAIvar = log(log(1./(1-Pfraction(Begin:Last))));
    KAIn = polyfit(timevar,KAIvar,1);
    % for modifying the power exponent of a
    powerNinf = ceil(log10(Ninf)-1);
    if KAIn(1)<Avramin
        Ninf = Ninf + 10^(powerNinf-2);
    elseif KAIn(1)>Avramin
        Ninf = Ninf - 10^(powerNinf-2);
    elseif KAIn(1)==Avramin
        sprintf('KAIn(1)=Avramin')
    end
testm = [KAIn(1),Avramin]
test2peakloc= [Pfloc(1),exploc(1)]
    % Simulated KAI model
```

```
    % setting up the integral
    t = 10^-9; % (beginning of) time in the upper integrand (s)
    i=1;
    while i<=l
        fun = @(tnuc) tnuc.^(m-1).*(t-tnuc).^2.*exp(-1.*a.*t.^m); % setting up the integral in the modofied KAI formula
        x = integral(fun,0,t);
        f = 1-exp(-2*pi*thickness*v^2*Ninf*a*m*x);
        Pfraction(i) = f; % sets values in an array for transformation fraction
        t=t+(10^-9); % adds 1 nanosecond to the time
        i=i+1;
    end

    % this will end the while loop when the values begin to toggle
    testKAI(j) = KAIn(1); % stores and array of values of the slopes of the simulated curve
    if j>2
        if testKAI(j)==testKAI(j-2)
            break
        end
    end
    j=j+1;
end
clear testKAI
%% Slope matching with a (Finest tuning)
% Modifying the fitting parameter, a
j=1;
while j<20 % the number of iterations to run
    Pfloc = find(Pfraction>=0.5); % holds the index values where the value of Pfraction, the calculated KAI curve, is greater than 0.5,
in order to calculate the n value there.
    Begin = Pfloc(1) - 10;
    Last = Pfloc(1) + 10;
    % Determinining the slope of the simulated curve in order to compare it to
    % the experimental volume fracton transformed.
    KAIvar = log(log(1./(1-Pfraction(Begin:Last))));
    KAIn = polyfit(timevar,KAIvar,1);
    % for modifying the power exponent of a
    powera = ceil(log10(a))-1;
    if KAIn(1)<Avramin
        a = a + 10^(powera-2);
    elseif KAIn(1)>Avramin
        a = a - 10^(powera-2);
    elseif KAIn(1)==Avramin
        sprintf('KAIn(1)=Avramin')
    end
testm = [KAIn(1),Avramin]
test2peakloc= [Pfloc(1),exploc(1)]
    % Simulated KAI model
    % setting up the integral
    t = 10^-9; % (beginning of) time in the upper integrand (s)
    i=1;
    while i<=l
        fun = @(tnuc) tnuc.^(m-1).*(t-tnuc).^2.*exp(-1.*a.*t.^m); % setting up the integral in the modofied KAI formula
        x = integral(fun,0,t);
        f = 1-exp(-2*pi*thickness*v^2*Ninf*a*m*x);
        Pfraction(i) = f; % sets values in an array for transformation fraction
        t=t+(10^-9); % adds 1 nanosecond to the time
        i=i+1;
    end

    % calculates the n value for the KAI model
    KAIvar = log(log(1./(1-Pfraction(Begin:Last))));
    KAIn = polyfit(timevar,KAIvar,1);
    % this will end the while loop when the values begin to toggle
    testKAI(j) = KAIn(1); % stores and array of values of the slopes of the simulated curve
    if j>2
        if testKAI(j)==testKAI(j-2)
            break
        end
```

```
    end
    j=j+1;
end
clear testKAI
%% Position finding with a (3rd time) (Finest tuning)
Ni = Ninf*area*thickness; % Saturated number of nuclei in the defined capacitor volume
j=1;
while j<100
    Pfloc = find(Pfraction>=0.5); % holds the index values where the value of Pfraction, the calculated KAI curve, is greater than 0.5,
in order to calculate the n value there.
    powera = ceil(log10(a))-1;
    if Pfloc(1)<exploc(1)
        a = a - 0.9*10^(powera-1);
    elseif Pfloc(1)>exploc(1)
        a = a + 0.9*10^(powera-1);
    elseif Pfloc(1)==exploc(1)
        sprintf('Pfloc(1) = exploc(1)')
    end
testm = [KAIn(1),Avramin]
test2peakloc= [Pfloc(1),exploc(1)]
    % Simulated KAI model
    % setting up the integral
    t = 10^-9; % (beginning of) time in the upper integrand (s)
    i=1;
    while i<=l
        fun = @(tnuc) tnuc.^(m-1).*(t-tnuc).^2.*exp(-1.*a.*t.^m); % setting up the integral in the modofied KAI formula
        x = integral(fun,0,t);
        f = 1-exp(-2*pi*thickness*v^2*Ninf*a*m*x);
        Pfraction(i) = f; % sets values in an array for transformation fraction
        t=t+(10^-9); % adds 1 nanosecond to the time
        i=i+1;
    end

    y = transpose(Pfraction); % transposed the Pfraction into columnar data which can be used later for exporting
    % calculates the n value for the KAI model
    KAIvar = log(log(1./(1-Pfraction(Begin:Last))));
    KAIn = polyfit(timevar,KAIvar,1);
    % intended for this last step to run until the position of the
    % simulated curve is within the threshold of 5 ns from the experimental
    % curve.
    mer = KAIn(1); % for calculating error in the experimental and fitted values for n later on
    if abs(Pfloc(1)-exploc(1)) <= 5
        %% Nucleation rate peak calculation
    i = 1;
    t = 10^-9; %
    ActualN = 0; % sets the initial value for ActualNuc, the nucleation rate
    while i<=l % this is the letter "l", not the numbner "1" !!!
        Nrp = a*m*t^(m-1)*exp(-1*a*t^m); % relative nucleation rate peak
        NucRatePeak(i) = Nrp; % sets values in an array for the nucleation rate peak
        NucAdd(i) = Ni*Nrp*10^(-9);
        ActualN(i+1) = ActualN(i) + NucAdd(i); % stores the number of actual nuclei which have formed during the polarization
reversal process in the capacitor
        ActualNuc(i) = ActualN(i+1); % stores the number of actual nuclei which have formed during the polarization reversal process in
the capacitor - FOR PLOTTING
        t=t+(10^-9); % adds 1 nanosecond to the time
        i=i+1;
    end

% This loop calclautes the actual nucleation rate (without phantoms)
    i = 1;
    t = 10^-9;
    SA = 2*dNuc*thickness; % Surface area of one nuclei where other nuclei may grow (units are in meters)
    ANuc = 3.14159*(dNuc/2)^2; % Area of a nuclei on the electrode surface
    AreaInit = 2*area; % Consider both electrode surfaces as the area where nuclei can form. This may be wrong and only one surface
is important.
    while i<=timelimit % Sets the end of the data points at the max time of the loop
```

```
        nNuc = Pfraction(i)*area/ANuc; % the number of nuclei of the chosen diameter (dNuc) existing in the capacitor at a given time
during the switching process.
        TotalNucArea = (1-Pfraction(i))*(AreaInit + nNuc*SA); % Sums the total area where nuclei may form. * this is a hypothetical
situation and an estimation based on a guess of the uniform diameter of existing nuclei.
        TrueNuc(i) = NucAdd(i)*TotalNucArea; % Calculates the nucleation distribution throughout the switcing process, while
subtracting the phantom nuclei (assuming a random nucleation process)
        timeadj(i) = t*10^6; % sets up adjusted time variable
        t=t+(10^-9); % adds 1 nanosecond to the time
        i=i+1;
    end
        break
    end
    % this will end the while loop when the values begin to toggle
    testKAI(j) = KAIn(1); % stores and array of values of the slopes of the simulated curve
    if j>2
        if testKAI(j)==testKAI(j-2)
            %break
        end
    end
    j=j+1;
end
maxN = max(ActualNuc); % Holds the maximum value for nucleation
NucPercent = ActualNuc./maxN; % Holds the percentage of nucleation completed
NormalizedTrueNuc = TrueNuc./max(TrueNuc);

% SA = 2*dNuc*thickness; % Surface area of one nuclei where other nuclei may grow (units are in meters)
% ANuc = 3.14159*(dNuc/2)^2; % Area of a nuclei on the electrode surface
% nNuc = Pfraction(i)*area/ANuc; % the number of nuclei of the chosen diameter (dNuc) existing in the capacitor at a given time
during the switching process.
% AreaInit = 2*area; % Consider both electrode surfaces as the area where nuclei can form. This may be wrong and only one surface
is important.
% TotalNucArea = AreaInit*(1-Pfraction(i)) + nNuc*ANuc;

ErStop = find(expfraction > ErrorStop); % Holds the positions of the polarization fractions over a certain fraction that was
transformed. The first value in this array is the position where to stop calcualting the fitting errors.

% Solving for the regression sum of squares
i=1;
while i <= ErStop(1)
    SSRcal = (Pfraction(i) - expfraction(i))^2; % Regression sum of squares
    SSRhold(i) = SSRcal; % holds the value in a array
    i=i+1;
end
SSR = sum(SSRhold)/ErStop(1); % Regression sum of squares

timelimitadj = (timelimit*0.001);

% Plot the extended KAI model vs. Experimental data after automatic fitting
% corrections
figure % creates a new figure
yyaxis left % sets up the left yaxis
p = plot(time,expfraction,time,Pfraction,'k'); % plotted data for the left y-axis
title('SNNG model comparison with experimental data') % plot title
xlabel('Time (microseconds)') % generates axis titles
ylabel('fraction of polarization reversal')
ylim([-0.01 1]) % sets bounds for the left y-axis
%xlim([0 (2-tcorrection)])
xlim([0 1])
p(1).LineWidth = 3; % sets the width of lines in the plot
p(2).LineWidth = 2;
caption = sprintf(' n = %1.2s \n m = %1.2s \n a = %1.2s \n # Nuclei = %1.2s \n t_0 voltage s.p. = %1.1s \n SSR =
%1.3s',Avramin,m,a,maxN,tzerosp,SSR); % text for the caption, limited to one decimal place by %1.1s
text(0.1,0.6,caption); % generates a text box at the coordinates (x,y,caption) according to the left y-axis
%setting up the right y-axis
yyaxis right % sets up the right y axis. syntax below will correspond to the right y-axis.
plot(timeadj,NormalizedTrueNuc); % plotted data for the right y-axis
ylabel('Nucleation Distribution')
```

```
legend('experimental','ext. KAI model','Nuc. rate') % creates a legend for both the left and right y-axes in one box

figure % creates a new figure
yyaxis left % sets up the left yaxis
p = plot(time,expfraction,time,Pfraction,'k'); % plotted data for the left y-axis
title('SNNG model comparison with experimental data') % plot title
xlabel('Time (microseconds)') % generates axis titles
ylabel('fraction of polarization reversal')
ylim([-0.01 1]) % sets bounds for the left y-axis
%xlim([0 (2-tcorrection)])
xlim([0 1])
p(1).LineWidth = 3; % sets the width of lines in the plot
p(2).LineWidth = 2;
caption = sprintf(' n = %1.2s \n m = %1.2s \n a = %1.2s \n # Nuclei = %1.2s \n t_0 voltage s.p. = %1.1s \n SSR =
%1.3s',Avramin,m,a,maxN,tzerosp,SSR); % text for the caption, limited to one decimal place by %1.1s
text(0.1,0.6,caption); % generates a text box at the coordinates (x,y,caption) according to the left y-axis
%setting up the right y-axis
yyaxis right % sets up the right y axis. syntax below will correspond to the right y-axis.
plot(time,NucPercent); % plotted data for the right y-axis
ylabel('# Nuclei')
legend('experimental','ext. KAI model','# Nuclei') % creates a legend for both the left and right y-axes in one box

% Outputs the experimetal v.f., simulated v.f., and N/Ninf nucleation rate
% peak data in an array.
Pfraction = transpose(Pfraction);
NucRatePeak = transpose(NucRatePeak);
NucPercent=transpose(NucPercent);
PrOutput = [time,expfraction,Pfraction,NucRatePeak,NucPercent];
[maxNuc,maxNucPos] = max(NucRatePeak);
mer = 100*abs(mer-Avramin)/Avramin; % percent error in the resulting value of n between the experimental curve and the fitted
curve
amp = abs(amp); % used to calcualte the amplitude of the applied field
AppliedField = (max(amp)/(10^6))/thickness; % The calculated applied field in MV/cm
Properties = [AppliedField,Avramin,m,Ninf,maxNuc,maxNucPos,a,(timelimit/1000),mer,SSR,AvraminMod]; % a set of output
properties
```

C-3-2 NLS Model (with Lorentzian Distribution)

```
%% Leonard Jacques
% November 2024

% For determining the NLS model kinetics applicable to
% polarization reversal in the ferroelectric switching of any material.

% Refs:  1.  (Supplemental Information) Guido et al. (2024) Adv. Sci., 11(16), 2308797.
%        2.  Jo et al. (2007) Phys. Rev. Lett., 99(26), 267602.

% The first long while loop that spans several hundred lines used the
% arctan approximation for the NLS model which is much faster and helps to
% get parameters close to ideal.
% Then, the real NLS model with the integral is run in iterations with the
% appriximated fitting terms as initial conditions. Since the integral is
% more expensive to runs, it is efficient to start with the approximated
% values.
clc
clear
%% User Inputs
%% Import from File:
xfrac = readtable('TEK00872.CSV'); % Imports data from a .txt file that is tab delimited performs the function of "text to columns"
nsxfrac = readtable(['TEK00900.CSV']); % Imports non-switching data, later to be subtracted from the switching data. Variables
specific to non-switching data have "ns" in front of it.
d = 236; % sample thickness in nanometers
```

```
thickness = d*10^-7; % film thickness (cm)
area = 7.85*10^-5; % sample area in cm^2 7.85*10^-5
tzerosp = 70*0.01; % the fraction of the setpoint voltage to call t0
ErrorStop = 100*0.01; % The percentage of the polarization where to stop calculating for the error in the regression calculations at the end of this script

%% Fitting Parameters
w = 0.2; % half-width, half-maximum of the Lorentzian distribution (in nano-seconds)
A = 1.02; % A normalization constant for fitting the NLS distribution to the experimental data
t1 = 900*10^-9; % center of the distribution function

%% imported data management
% for the switching data
xfrac = table2array(xfrac); % converts the imported data type from "table' to "array"
nsxfrac = table2array(nsxfrac); % for the non-switching data
% finding where the function generator output begins
xa = xfrac(:,2); % calling CH1, the function generator output
xa = abs(xa); % making all values positive for referencing applications to follow
xaloc = find(xa==0.12); % 0.10 to 0.24V is the function generator output that signifies the output has begun !!! CHECK THIS VALUE IF THE CODE DOES NOT WORK !
n=isempty(xaloc); % this series of if loops is used to determine where the function generator input begins for the switching data
if n==1
   xaloc = find(xa==0.12);
   n=isempty(xaloc);
end
if n==1
   xaloc = find(xa==0.14);
   n=isempty(xaloc);
end
if n==1
   xaloc = find(xa==0.16);
   n=isempty(xaloc);
end
if n==1
   xaloc = find(xa==0.18);
   n=isempty(xaloc);
end
if n==1
   xaloc = find(xa==0.20);
   n=isempty(xaloc);
end
pos1 = xaloc(1) +100 -2; % holds the value where to start accepting points. +100 is for neglecting the first 100 ns before the amplifier output begins.
% ps 1 also governs the position of t0
% for the non-switchng data (ns)
nsxa = nsxfrac(:,2); % calling CH1, the function generator output
nsxa = abs(nsxa);
nsxaloc = find(nsxa==0.18); % > 0.10 V is the function generator output that signifies the output has begun  !!! CHECK THIS VALUE IF THE CODE DOES NOT WORK !!!
n=isempty(nsxaloc);
if n==1  % this series of if loops is used to determine where the function generator input begins for the non-switching data
   nsxaloc = find(nsxa==0.12);
   n=isempty(nsxaloc);
end
if n==1
   nsxaloc = find(nsxa==0.14);
   n=isempty(nsxaloc);
end
if n==1
   nsxaloc = find(nsxa==0.16);
   n=isempty(nsxaloc);
end
if n==1
   nsxaloc = find(nsxa==0.18);
   n=isempty(nsxaloc);
end
if n==1
```

```
   nsxaloc = find(nsxa==0.20);
   n=isempty(nsxaloc);
end
nspos1 = nsxaloc(1) +100 - 2; % holds the value where to start accepting points. +100 is for neglecting the first 100 ns before the amplifier output begins.

%% Adjusting for t0, and choosing the data to simulate
t0adjust = xfrac(pos1:end,3);
maxamp = mode(t0adjust); % assumes the mode (most common value) in the amplifier output is the voltage setpoint
fract0 = tzerosp*maxamp; % calculates the voltage where to start accepting
fract0 = abs(fract0); % for handling negative values
t0adjust = abs(t0adjust); % for handling negative values
t0pos = find(t0adjust>fract0); % finds the position of t0 in the amplifier output greater than the defined percentage of the setpoint voltage where to start the simulation

pos1 = pos1 + t0pos(1); % adjusts the pos1 time for the voltage where t0 is assigned
nspos1 = nspos1 + t0pos(1);

% shortens the arrays for the function generator (fg), amplifier (amp) and
% TIA (tia) switching curves
fg = xfrac(pos1:end,2);
amp = xfrac(pos1:end,3);
tia = abs(xfrac(pos1:end,4).*1000./22); % TIA output (in mA)
l = length(tia);

%% setting the time at polarization saturation
[maxtiaval,maxTIApos] = max(tia); % maximum current value and position from the TIA
tiafind = tia(maxTIApos:end);
zeroTIApos = find(tiafind < 0.5); % to index the zero positions after the TIA current peak
timelimit = maxTIApos + zeroTIApos(1) + 400; % to identify the location where the polarization is considered to have saturated

% non-switching curve
nsfg = nsxfrac(nspos1:end,2);
nsamp = nsxfrac(nspos1:end,3);
nstia = abs(nsxfrac(nspos1:end,4).*1000./22); % TIA output (in mA)
nsl = length(nstia);

% to set the proper array length of data to calculate
if l <= nsl
   l = l;
elseif l > nsl
   l = nsl;
end
l=9000; % sets the time time limit to 9 microseconds

%% Leakge current subtration from the TIA output
NetLeakageCurrent = mean(tia(3000:9000))-mean(nstia(3000:9000)); % calculated the mean of the TIA output beyond the switching transient from 3 to 9 microseconds
if NetLeakageCurrent > 0
   tia(timelimit+800:end) = tia(timelimit+800:end)-NetLeakageCurrent; % Can MODIFY the term here to modify where the begin the leakage current contributions
end

%% Imported data mamagement and calculation of experimental volume fraction transformed
% calculates the experimental polarization by subtracting a switching curve
% from the non-switching curve

time = [0.001:0.001:0.001*(l)]; % sets the time in microseconds
time = transpose(time);

i=1;
po = 0;
while i <= l
   polarization(i,1) = po + 10^3*((tia(i,1)-nstia(i,1))*(10^-9))/area; % solves for the polarization by subtracting the switching curve from the non-switching curve
   po = polarization(i);
   i=i+1;
```

```
end

expfraction = polarization./polarization(timelimit); % calls the sets the volume fraction of polarization
tcorrection = 0.2; % A correction factor which simultaneously shifts the ext. KAI model and projected nucleation rate forward to a
lower time (in order to match the slope) and adjusts the x-axis limit of the plot accordingly.
time2 = [0.001:0.001:l*0.001]-tcorrection; % Sets the array for plotting of the ext. KAI model and the projected nucleation rate peak.

%% Finding maximum value of the current to assign the Avrami constant, n

maxCurrent = max(tia);
maxCurrent = find(tia==maxCurrent); % Assigns the position of the max current in the array
Begin = maxCurrent(1) - 10;
Last = maxCurrent(1) + 10;

timevar = log((10^-9).*time([Begin:Last])); % changes unit of time from nanooseconds to seconds
polarizationvar = log(log(1./(1-expfraction([Begin:Last]))));
Avramin = polyfit(timevar,polarizationvar,1);
lnK = Avramin(2);
Avramin = Avramin(1);

m = Avramin-1 % Avramin-2; % sets the fitting parameter "m" to n-2.
m
%% Initial fitting of the NLS model
t = 10^-9; % (beginning of) time in the upper integrand (s)
i=1;
while i<=l
   f = (A/pi)*(atan((log(t) - log(t1))/w) + (pi/2));
   Pfraction(i) = f; % sets values in an array for transformation fraction
   t=t+(10^-9); % adds 1 nanosecond to the time
   i=i+1;
end

%% Nucleation Lorentzian calculation
i = 1;
t = 10^-9; %
while i<=l
   NucLorentz = (A/pi)*(w/((log(t)-log(t1))^2 + w^2)); % Lorentzian distribution of nucleation
   NucRatePeak(i) = NucLorentz; % sets values in an array for the nucleation rate peak
   t=t+(10^-9); % adds 1 nanosecond to the time
   i=i+1;
end
y = transpose(Pfraction); % transposed the Pfraction into columnar data which can be used later for exporting


%figure % for plotting the data used to determine the Avrami n
%plot(timevar,polarizationvar)

%% Plot the extended KAI model vs. Experimental data
%figure % creates a new figure
%yyaxis left % sets up the left yaxis
%p = plot(time,expfraction,(time),Pfraction,'k'); % plotted data for the left y-axis
%title('NLS model comparison with experimental data') % plot title
%xlabel('Time (microseconds)') % generates axis titles
%ylabel('fraction of polarization reversal')
%ylim([-0.01 1]) % sets bounds for the left y-axis
%xlim([0 (2-tcorrection)])
%p(1).LineWidth = 3; % sets the width of lines in the plot
%p(2).LineWidth = 2;
%caption = sprintf(' n = %1.2s \n w = %1.2s sec \n t1 = %1.1s sec',Avramin,w,t1); % text for the caption, limited to one decimal place
by %1.1s
%text(0.1,0.6,caption); % generates a text box at the coordinates (x,y,caption) according to the left y-axis
%setting up the right y-axis
%yyaxis right % sets up the right y axis. syntax below will correspond to the right y-axis.
%plot(time2,NucRatePeak); % plotted data for the right y-axis
%ylabel('Distribution Function')
%legend('experimental','NLS model','Distribution Function') % creates a legend for both the left and right y-axes in one box
```

```
%% Automatic determination of the fitting parameters t1 and w

% calculates the n value for the KAI model
KAIvar = log(log(1./(1-Pfraction([Begin:Last]))));
KAIn = polyfit(timevar,KAIvar,1);

%% Position finding with t1
exploc = find(expfraction>=0.5);
j=1;
while j<20
   Pfloc = find(Pfraction>=0.5); % holds the index values where the value of Pfraction, the calculated KAI curve, is greater than 0.5,
in order to calculate the n value there.
   if Pfloc(1)<exploc(1)
      t1 = t1 + (t1/15);
   elseif Pfloc(1)>exploc(1)
      t1 = t1 - (t1/15);
   elseif Pfloc(1)==exploc(1)
      sprintf('Pfloc(1) = exploc(1)')
   end
testm = [KAIn(1),Avramin]
test2peakloc= [Pfloc(1),exploc(1)]
   % Simulated KAI model
   % setting up the integral
   t = 10^-9; % (beginning of) time in the upper integrand (s)
   i=1;
   while i<=l
      f = (A/pi)*(atan((log(t) - log(t1))/w) + (pi/2));
      Pfraction(i) = f; % sets values in an array for transformation fraction
      t=t+(10^-9); % adds 1 nanosecond to the time
      i=i+1;
   end

   % calculates the n value for the KAI model
   KAIvar = log(log(1./(1-Pfraction([Begin:Last]))));
   KAIn = polyfit(timevar,KAIvar,1);
   % this will end the while loop when the values begin to toggle
   testKAI(j) = KAIn(1); % stores and array of values of the slopes of the simulated curve
   if j>2
      if testKAI(j)==testKAI(j-2)
         break
      end
   end
   j=j+1;
end
clear testKAI

%% Position finding with t1
j=1;
while j<20
   Pfloc = find(Pfraction>=0.5); % holds the index values where the value of Pfraction, the calculated KAI curve, is greater than 0.5,
in order to calculate the n value there.
   if Pfloc(1)<exploc(1)
      t1 = t1 + (t1/50);
   elseif Pfloc(1)>exploc(1)
      t1 = t1 - (t1/50);
   elseif Pfloc(1)==exploc(1)
      sprintf('Pfloc(1) = exploc(1)')
   end
testm = [KAIn(1),Avramin]
test2peakloc= [Pfloc(1),exploc(1)]
   % Simulated KAI model
   % setting up the integral
   t = 10^-9; % (beginning of) time in the upper integrand (s)
   i=1;
   while i<=l
      f = (A/pi)*(atan((log(t) - log(t1))/w) + (pi/2));
      Pfraction(i) = f; % sets values in an array for transformation fraction
```

```
    t=t+(10^-9); % adds 1 nanosecond to the time
    i=i+1;
  end

  % calculates the n value for the KAI model
  KAIvar = log(log(1./(1-Pfraction([Begin:Last]))));
  KAIn = polyfit(timevar,KAIvar,1);
  % this will end the while loop when the values begin to toggle
  testKAI(j) = KAIn(1); % stores and array of values of the slopes of the simulated curve
  if j>2
    if testKAI(j)==testKAI(j-2)
      break
    end
  end
  j=j+1;
end
clear testKAI
%% Position finding with t1
j=1;
while j<20
  Pfloc = find(Pfraction>=0.5); % holds the index values where the value of Pfraction, the calculated KAI curve, is greater than 0.5,
in order to calculate the n value there.
  if Pfloc(1)<exploc(1)
    t1 = t1 + (t1/250);
  elseif Pfloc(1)>exploc(1)
    t1 = t1 - (t1/250);
  elseif Pfloc(1)==exploc(1)
    sprintf('Pfloc(1) = exploc(1)')
  end
testm = [KAIn(1),Avramin]
test2peakloc= [Pfloc(1),exploc(1)]
  % Simulated KAI model
  % setting up the integral
  t = 10^-9; % (beginning of) time in the upper integrand (s)
  i=1;
  while i<=l
    f = (A/pi)*(atan((log(t) - log(t1))/w) + (pi/2));
    Pfraction(i) = f; % sets values in an array for transformation fraction
    t=t+(10^-9); % adds 1 nanosecond to the time
    i=i+1;
  end

  % calculates the n value for the KAI model
  KAIvar = log(log(1./(1-Pfraction([Begin:Last]))));
  KAIn = polyfit(timevar,KAIvar,1);
  % this will end the while loop when the values begin to toggle
  testKAI(j) = KAIn(1); % stores and array of values of the slopes of the simulated curve
  if j>2
    if testKAI(j)==testKAI(j-2)
      break
    end
  end
  j=j+1;
end
clear testKAI
%% Position finding with t1
j=1;
while j<20
  Pfloc = find(Pfraction>=0.5); % holds the index values where the value of Pfraction, the calculated KAI curve, is greater than 0.5,
in order to calculate the n value there.
  if Pfloc(1)<exploc(1)
    t1 = t1 + (t1/1000);
  elseif Pfloc(1)>exploc(1)
    t1 = t1 - (t1/1000);
  elseif Pfloc(1)==exploc(1)
    sprintf('Pfloc(1) = exploc(1)')
  end
```

```
testm = [KAIn(1),Avramin]
test2peakloc= [Pfloc(1),exploc(1)]
   % Simulated KAI model
   % setting up the integral
   t = 10^-9; % (beginning of) time in the upper integrand (s)
   i=1;
   while i<=l
      f = (A/pi)*(atan((log(t) - log(t1))/w) + (pi/2));
      Pfraction(i) = f; % sets values in an array for transformation fraction
      t=t+(10^-9); % adds 1 nanosecond to the time
      i=i+1;
   end

   % calculates the n value for the KAI model
   KAIvar = log(log(1./(1-Pfraction([Begin:Last]))));
   KAIn = polyfit(timevar,KAIvar,1);
   % this will end the while loop when the values begin to toggle
   testKAI(j) = KAIn(1); % stores and array of values of the slopes of the simulated curve
   if j>2
      if testKAI(j)==testKAI(j-2)
         break
      end
   end
   j=j+1;
end
%% Slope matching with w - modifying the fitting parameter, w
j=1;
while j<40 % the maximum number of iterations to run
   Pfloc = find(Pfraction>=0.5); % holds the index values where the value of Pfraction, the calculated KAI curve, is greater than 0.5,
in order to calculate the n value there.
   Begin = Pfloc(1) - 10;
   Last = Pfloc(1) + 10;
   % Determinining the slope of the simulated curve in order to compare it to
   % the experimental volume fracton transformed.
   KAIvar = log(log(1./(1-Pfraction([Begin:Last]))));
   KAIn = polyfit(timevar,KAIvar,1);
   % for modifying the power exponent of a
   if KAIn(1)<Avramin
      w = w - (w/15);
   elseif KAIn(1)>Avramin
      w = w + (w/15);
   elseif KAIn(1)==Avramin
      sprintf('KAIn(1)=Avramin')
   end
testm = [KAIn(1),Avramin]
w
   % Simulated KAI model
   % setting up the integral
   t = 10^-9; % (beginning of) time in the upper integrand (s)
   i=1;
   while i<=l
      f = (A/pi)*(atan((log(t) - log(t1))/w) + (pi/2));
      Pfraction(i) = f; % sets values in an array for transformation fraction
      t=t+(10^-9); % adds 1 nanosecond to the time
      i=i+1;
   end

   % calculates the n value for the KAI model
   KAIvar = log(log(1./(1-Pfraction([Begin:Last]))));
   KAIn = polyfit(timevar,KAIvar,1);
   % this will end the while loop when the values begin to toggle
   testKAI(j) = KAIn(1); % stores and array of values of the slopes of the simulated curve
   if j>2
      if testKAI(j)==testKAI(j-2)
         break
      end
   end
```

```
   j=j+1;
end
clear testKAI

%% Slope matching with w - modifying the fitting parameter, w
j=1;
while j<40 % the maximum number of iterations to run
   Pfloc = find(Pfraction>=0.5); % holds the index values where the value of Pfraction, the calculated KAI curve, is greater than 0.5,
in order to calculate the n value there.
   Begin = Pfloc(1) - 10;
   Last = Pfloc(1) + 10;
   % Determinining the slope of the simulated curve in order to compare it to
   % the experimental volume fracton transformed.
   KAIvar = log(log(1./(1-Pfraction([Begin:Last]))));
   KAIn = polyfit(timevar,KAIvar,1);
   % for modifying the power exponent of a
   if KAIn(1)<Avramin
      w = w - (w/50);
   elseif KAIn(1)>Avramin
      w = w + (w/50);
   elseif KAIn(1)==Avramin
      sprintf('KAIn(1)=Avramin')
   end
testm = [KAIn(1),Avramin]
w
   % Simulated KAI model
   % setting up the integral
   t = 10^-9; % (beginning of) time in the upper integrand (s)
   i=1;
   while i<=l
      f = (A/pi)*(atan((log(t) - log(t1))/w) + (pi/2));
      Pfraction(i) = f; % sets values in an array for transformation fraction
      t=t+(10^-9); % adds 1 nanosecond to the time
      i=i+1;
   end

   % calculates the n value for the KAI model
   KAIvar = log(log(1./(1-Pfraction([Begin:Last]))));
   KAIn = polyfit(timevar,KAIvar,1);
   % this will end the while loop when the values begin to toggle
   testKAI(j) = KAIn(1); % stores and array of values of the slopes of the simulated curve
   if j>2
      if testKAI(j)==testKAI(j-2)
         break
      end
   end
   j=j+1;
end
clear testKAI

%% Slope matching with w - modifying the fitting parameter, w
j=1;
while j<40 % the maximum number of iterations to run
   Pfloc = find(Pfraction>=0.5); % holds the index values where the value of Pfraction, the calculated KAI curve, is greater than 0.5,
in order to calculate the n value there.
   Begin = Pfloc(1) - 10;
   Last = Pfloc(1) + 10;
   % Determinining the slope of the simulated curve in order to compare it to
   % the experimental volume fracton transformed.
   KAIvar = log(log(1./(1-Pfraction([Begin:Last]))));
   KAIn = polyfit(timevar,KAIvar,1);
   % for modifying the power exponent of a
   if KAIn(1)<Avramin
      w = w - (w/250);
   elseif KAIn(1)>Avramin
      w = w + (w/250);
   elseif KAIn(1)==Avramin
```

```
      sprintf('KAIn(1)=Avramin')
   end
testm = [KAIn(1),Avramin]
w
   % Simulated KAI model
   % setting up the integral
   t = 10^-9; % (beginning of) time in the upper integrand (s)
   i=1;
   while i<=l
      f = (A/pi)*(atan((log(t) - log(t1))/w) + (pi/2));
      Pfraction(i) = f; % sets values in an array for transformation fraction
      t=t+(10^-9); % adds 1 nanosecond to the time
      i=i+1;
   end

   % calculates the n value for the KAI model
   KAIvar = log(log(1./(1-Pfraction([Begin:Last]))));
   KAIn = polyfit(timevar,KAIvar,1);
   % this will end the while loop when the values begin to toggle
   testKAI(j) = KAIn(1); % stores and array of values of the slopes of the simulated curve
   if j>2
      if testKAI(j)==testKAI(j-2)
         break
      end
   end
   j=j+1;
end
clear testKAI

%%% Height matching with A - modifying the fitting parameter, A
%j=1;
%while j<40 % the maximum number of iterations to run
%Pfloc = find(Pfraction>=0.5); % holds the index values where the value of Pfraction, the calculated KAI curve, is greater than 0.5, in
order to calculate the n value there.
%Begin = Pfloc(1) - 10;
%   Last = Pfloc(1) + 10;
%   % Determinining the slope of the simulated curve in order to compare it to
%   % the experimental volume fracton transformed.
%   KAIvar = log(log(1./(1-Pfraction([Begin:Last]))));
%   KAIn = polyfit(timevar,KAIvar,1);
%   % for modifying the power exponent of a
%   if Pfraction(timelimit) < expfraction(timelimit)
%      A = A + 0.005;
%   elseif Pfraction(timelimit) > expfraction(timelimit)
%      A = A - 0.005;
%   elseif Pfraction(timelimit) == expfraction(timelimit)
%      sprintf('Pfraction(timelimit) == expfraction(timelimit)')
%   end
%testm = [KAIn(1),Avramin]
%w
%   % Simulated KAI model
%   % setting up the integral
%   t = 10^-9; % (beginning of) time in the upper integrand (s)
%   i=1;
%   while i<=l
%      f = (A/pi)*(atan((log(t) - log(t1))/w) + (pi/2));
%      Pfraction(i) = f; % sets values in an array for transformation fraction
%      t=t+(10^-9); % adds 1 nanosecond to the time
%      i=i+1;
%   end
%
%   % calculates the n value for the KAI model
%   KAIvar = log(log(1./(1-Pfraction([Begin:Last]))));
%   KAIn = polyfit(timevar,KAIvar,1);
%   % this will end the while loop when the values begin to toggle
%   testKAI(j) = Pfraction(timelimit); % stores and array of values of the simulated curve at the "timelimit" where the response is
condisered to have saturated
```

```
%    if j>2
%        if testKAI(j)==testKAI(j-2)
%            break
%        end
%    end
%    j=j+1;
%end
%clear testKAI

%% Slope matching with w - modifying the fitting parameter, w
j=1;
while j<40 % the maximum number of iterations to run
    Pfloc = find(Pfraction>=0.5); % holds the index values where the value of Pfraction, the calculated KAI curve, is greater than 0.5,
in order to calculate the n value there.
    Begin = Pfloc(1) - 10;
    Last = Pfloc(1) + 10;
    % Determinining the slope of the simulated curve in order to compare it to
    % the experimental volume fracton transformed.
    KAIvar = log(log(1./(1-Pfraction([Begin:Last]))));
    KAIn = polyfit(timevar,KAIvar,1);
    % for modifying the power exponent of a
    if KAIn(1)<Avramin
        w = w - (w/250);
    elseif KAIn(1)>Avramin
        w = w + (w/250);
    elseif KAIn(1)==Avramin
        sprintf('KAIn(1)=Avramin')
    end
testm = [KAIn(1),Avramin]
w
    % Simulated KAI model
    % setting up the integral
    t = 10^-9; % (beginning of) time in the upper integrand (s)
    i=1;
    while i<=l
        f = (A/pi)*(atan((log(t) - log(t1))/w) + (pi/2));
        Pfraction(i) = f; % sets values in an array for transformation fraction
        t=t+(10^-9); % adds 1 nanosecond to the time
        i=i+1;
    end

    % calculates the n value for the KAI model
    KAIvar = log(log(1./(1-Pfraction([Begin:Last]))));
    KAIn = polyfit(timevar,KAIvar,1);
    % this will end the while loop when the values begin to toggle
    testKAI(j) = KAIn(1); % stores and array of values of the slopes of the simulated curve
    if j>2
        if testKAI(j)==testKAI(j-2)
            break
        end
    end
    j=j+1;
end
clear testKAI

%% Position finding with t1
j=1;
while j<100
    Pfloc = find(Pfraction>=0.5); % holds the index values where the value of Pfraction, the calculated KAI curve, is greater than 0.5,
in order to calculate the n value there.
    if Pfloc(1)<exploc(1)
        t1 = t1 + (t1/300);
    elseif Pfloc(1)>exploc(1)
        t1 = t1 - (t1/100);
    elseif Pfloc(1)==exploc(1)
        sprintf('Pfloc(1) = exploc(1)')
    end
```

```
testm = [KAIn(1),Avramin]
test2peakloc= [Pfloc(1),exploc(1)]
   % Simulated KAI model
   % setting up the integral
   t = 10^-9; % (beginning of) time in the upper integrand (s)
   i=1;
   while i<=l
      f = (A/pi)*(atan((log(t) - log(t1))/w) + (pi/2));
      Pfraction(i) = f; % sets values in an array for transformation fraction
      t=t+(10^-9); % adds 1 nanosecond to the time
      i=i+1;
   end
   y = transpose(Pfraction); % transposed the Pfraction into columnar data which can be used later for exporting
   % calculates the n value for the KAI model
   KAIvar = log(log(1./(1-Pfraction([Begin:Last]))));
   KAIn = polyfit(timevar,KAIvar,1);
   % this will end the while loop when the values begin to toggle
   testKAI(j) = KAIn(1); % stores an array of values of the slopes of the simulated curve
   if j>2
      if testKAI(j)==testKAI(j-2)
         break
      end
   end
   j=j+1;
end

%% reconverting from the approximation with the arctan to the actual NLS
% model using the obtained parameters

% ngrow=Avramin-1; % this sets the exponent "n" in the integral to the Avrami n constant from the experimental curve
ngrow=3;

%% Position finding with t1
j=1;
while j<20
   Pfloc = find(Pfraction>=0.5); % holds the index values where the value of Pfraction, the calculated KAI curve, is greater than 0.5,
in order to calculate the n value there.
   if Pfloc(1)<exploc(1)
      t1 = t1 + (t1/30);
   elseif Pfloc(1)>exploc(1)
      t1 = t1 - (t1/30);
   elseif Pfloc(1)==exploc(1)
      sprintf('Pfloc(1) = exploc(1)')
   end
testm = [KAIn(1),Avramin]
test2peakloc= [Pfloc(1),exploc(1)]
   % Simulated KAI model
   % setting up the integral
   t = 10^-9; % (beginning of) time in the upper integrand (s)
   i=1;
   while i<=l
      fun = @(logt) (1-exp(-(t./exp(logt)).^ngrow)).*(A./pi).*(w./((logt-log(t1)).^2 + w.^2));
      f = integral(fun,-Inf,Inf);
      Pfraction(i) = f; % sets values in an array for transformation fraction
      t=t+(10^-9); % adds 1 nanosecond to the time
      i=i+1;
   end

   % calculates the n value for the KAI model
   KAIvar = log(log(1./(1-Pfraction([Begin:Last]))));
   KAIn = polyfit(timevar,KAIvar,1);
   % this will end the while loop when the values begin to toggle
   testKAI(j) = test2peakloc(1); % stores and array of values of the slopes of the simulated curve
   if j>2
      if test2peakloc(1)==testKAI(j-2)
         break
      end
```

```
    end
    j=j+1;
end
clear testKAI

%% Position finding with t1
j=1;
while j<5
    Pfloc = find(Pfraction>=0.5); % holds the index values where the value of Pfraction, the calculated KAI curve, is greater than 0.5,
in order to calculate the n value there.
    if Pfloc(1)<exploc(1)
        t1 = t1 + (t1/90);
    elseif Pfloc(1)>exploc(1)
        t1 = t1 - (t1/90);
    elseif Pfloc(1)==exploc(1)
        sprintf('Pfloc(1) = exploc(1)')
    end
testm = [KAIn(1),Avramin]
test2peakloc= [Pfloc(1),exploc(1)]
    % Simulated KAI model
    % setting up the integral
    t = 10^-9; % (beginning of) time in the upper integrand (s)
    i=1;
    while i<=l
        fun = @(logt) (1-exp(-(t./exp(logt)).^ngrow)).*(A./pi).*(w./((logt-log(t1)).^2 + w.^2));
        f = integral(fun,-Inf,Inf);
        Pfraction(i) = f; % sets values in an array for transformation fraction
        t=t+(10^-9); % adds 1 nanosecond to the time
        i=i+1;
    end

    % calculates the n value for the KAI model
    KAIvar = log(log(1./(1-Pfraction([Begin:Last]))));
    KAIn = polyfit(timevar,KAIvar,1);
    % this will end the while loop when the values begin to toggle
%    testKAI(j) = test2peakloc(1); % stores and array of values of the slopes of the simulated curve
%    if j>2
%        if test2peakloc(1) == test2peakloc(1)
%            break
%        elseif test2peakloc(1)==testKAI(j-2)
%            break
%        end
%    end
    j=j+1;
end
clear testKAI

%% Slope matching with w - modifying the fitting parameter, w
j=1;
while j<40 % the maximum number of iterations to run
    Pfloc = find(Pfraction>=0.5); % holds the index values where the value of Pfraction, the calculated KAI curve, is greater than 0.5,
in order to calculate the n value there.
    Begin = Pfloc(1) - 10;
    Last = Pfloc(1) + 10;
    % Determinining the slope of the simulated curve in order to compare it to
    % the experimental volume fracton transformed.
    KAIvar = log(log(1./(1-Pfraction([Begin:Last]))));
    KAIn = polyfit(timevar,KAIvar,1);
    % for modifying the power exponent of a
    if KAIn(1)<Avramin
        w = w - (w/40);
    elseif KAIn(1)>Avramin
        w = w + (w/40);
    elseif KAIn(1)==Avramin
        sprintf('KAIn(1)=Avramin')
    end
testm = [KAIn(1),Avramin]
```

```
w
   % Simulated KAI model
   % setting up the integral
   t = 10^-9; % (beginning of) time in the upper integrand (s)
   i=1;
   while i<=l
      fun = @(logt) (1-exp(-(t./exp(logt)).^ngrow)).*(A./pi).*(w./((logt-log(t1)).^2 + w.^2));
      f = integral(fun,-Inf,Inf);
      Pfraction(i) = f; % sets values in an array for transformation fraction
      t=t+(10^-9); % adds 1 nanosecond to the time
      i=i+1;
   end

   % calculates the n value for the KAI model
   KAIvar = log(log(1./(1-Pfraction([Begin:Last]))));
   KAIn = polyfit(timevar,KAIvar,1);
   % this will end the while loop when the values begin to toggle
   testKAI(j) = KAIn(1); % stores and array of values of the slopes of the simulated curve
   if j>2
      if testKAI(j)==testKAI(j-2)
         break
      end
   end
   j=j+1;
end
clear testKAI

 % Nucleation rate peak calculation
i = 1;
   t = 10^-9; %
   ActualN = 0; % sets the initial value for ActualNuc, the nucleation rate
   while i<=l % this is the letter "l", not the numbner "1" !!!
      NucLorentz = (A/pi)*(w/((log(t)-log(t1))^2 + w^2)); % Lorentzian distribution of nucleation
      NucRatePeak(i) = NucLorentz; % sets values in an array for the nucleation rate peak
      ActualN(i+1) = ActualN(i) + NucLorentz*10^-9; % stores the number of actual nuclei which have formed during the polarization
reversal process in the capacitor
      ActualNuc(i) = ActualN(i+1); % stores the number of actual nuclei which have formed during the polarization reversal process in
the capacitor - FOR PLOTTING
      t=t+(10^-9); % adds 1 nanosecond to the time
      i=i+1;
   end
clear testKAI
% Solving for the regression sum of squares
ErStop = find(expfraction > ErrorStop); % Holds the positions of the polarization fractions over a certain fraction that was
transformed. The first value in this array is the position where to stop calcualting the fitting errors.
i=1;
while i <= ErStop(1)
   SSRcal = (Pfraction(i) - expfraction(i))^2; % Regression sum of squares
   SSRhold(i) = SSRcal; % holds the value in a array
   i=i+1;
end
SSR = sum(SSRhold)/ErStop(1); % Regression sum of squares

maxN = max(ActualNuc); % Holds the maximum value for nucleation
%NucPercent = ActualNuc./maxN; % Holds the percentage of nucleation completed
NucPercent = ActualNuc./ActualNuc(timelimit); % Holds the normalized percentage of nucleation completed

time = [0.001:0.001:0.001*(length(Pfraction))]; % sets the time in microseconds
time=transpose(time);
% Plot the extended KAI model vs. Experimental data after automatic fitting
% corrections
figure % creates a new figure
yyaxis left % sets up the left yaxis
p = plot(time,expfraction,time,Pfraction,'k'); % plotted data for the left y-axis
title('Automatic NLS model comparison with experimental data') % plot title
xlabel('Time (microseconds)') % generates axis titles
ylabel('fraction of polarization reversal')
```

```
ylim([-0.01 1]) % sets bounds for the left y-axis
%xlim([0 (2-tcorrection)])
xlim([0 1])
p(1).LineWidth = 3; % sets the width of lines in the plot
p(2).LineWidth = 2;
caption = sprintf(' n = %1.2s \n w = %1.2s sec \n t1 = %1.2s sec \n t_0 voltage s.p. = %1.1s \n A = %1.3s \n SSR =
%1.3s',Avramin,w,t1,tzerosp,A,SSR); % text for the caption, limited to one decimal place by %1.1s
text(0.1,0.6,caption); % generates a text box at the coordinates (x,y,caption) according to the left y-axis
%setting up the right y-axis
yyaxis right % sets up the right y axis. syntax below will correspond to the right y-axis.
plot(time,NucPercent); % plotted data for the right y-axis
ylabel('Fraction of Nucleation Progress')
ylim([-0.01 1]) % sets bounds for the right y-axis
legend('experimental','NLS model','# Nuclei') % creates a legend for both the left and right y-axes in one box

figure % creates a new figure
yyaxis left % sets up the left yaxis
p = plot(time,expfraction,time,Pfraction,'k'); % plotted data for the left y-axis
title('Automatic NLS model comparison with experimental data') % plot title
xlabel('Time (microseconds)') % generates axis titles
ylabel('fraction of polarization reversal')
ylim([-0.01 1]) % sets bounds for the left y-axis
%xlim([0 (2-tcorrection)])
xlim([0 1])
p(1).LineWidth = 3; % sets the width of lines in the plot
p(2).LineWidth = 2;
caption = sprintf(' n = %1.2s \n w = %1.2s sec \n t1 = %1.2s sec \n t_0 voltage s.p. = %1.1s \n A = %1.3s \n SSR =
%1.3s',Avramin,w,t1,tzerosp,A,SSR); % text for the caption, limited to one decimal place by %1.1s
text(0.1,0.6,caption); % generates a text box at the coordinates (x,y,caption) according to the left y-axis
%setting up the right y-axis
yyaxis right % sets up the right y axis. syntax below will correspond to the right y-axis.
plot(time,NucRatePeak); % plotted data for the right y-axis
ylabel('Distribution Function')
legend('experimental','NLS model','Nuc. rate') % creates a legend for both the left and right y-axes in one box

%maxamp = (maxamp/thickness)*10^-6; % converts "maxamp" from voltage to electric field (MV/cm)
% Calculating the theoretical values for t1 and w
%E0 = 15; % Threshold electric field for pinned domains (MV/cm)
%U = 0.07; % eV/function unit in ZMO (Baska et al., 2024)
%T = 273+19; % Temperature in Kelvin
%kb = 8.617*10^-5; % Boltzmann's constant in eV
%t1theo = 10^(U*E0/kb/T/maxamp)


% Outputs the experimetal v.f., simulated v.f., and N/Ninf nucleation rate
% peak data in an array.
Pfraction = transpose(Pfraction);
NucRatePeak = transpose(NucRatePeak);
NucPercent=transpose(NucPercent);
PrOutput = [time,expfraction,Pfraction,NucRatePeak,NucPercent];
[maxNuc,maxNucPos] = max(NucRatePeak);
amp = abs(amp); % used to calcualte the amplitude of the applied field
AppliedField = (max(amp)/(10^6))/thickness; % The calculated applied field in MV/cm
Properties = [tzerosp,A,Avramin,SSR]; % a set of output properties
```

C-3-3 KAI Model

```
%% Leonard Jacques
% December 2024

% For determining the NLS model kinetics applicable to
```

```
% polarization reversal in the ferroelectric switching of any material.

% Refs:  1.  (Supplemental Information) Guido et al. (2024) Adv. Sci., 11(16), 2308797.
%       2.  Jo et al. (2007) Phys. Rev. Lett., 99(26), 267602.

% The first long while loop that spans several hundred lines used the
% arctan approximation for the NLS model which is much faster and helps to
% get parameters close to ideal.
% Then, the real NLS model with the integral is run in iterations with the
% appriximated fitting terms as initial conditions. Since the integral is
% more expensive to runs, it is efficient to start with the approximated
% values.
clc
clear
%% User Inputs
%% Import from File:
xfrac = readtable('TEK00872.CSV'); % Imports data from a .txt file that is tab delimited performs the function of "text to columns"
nsxfrac = readtable(['TEK00810.CSV']); % Imports non-switching data, later to be subtracted from the switching data. Variables specific to non-switching data have "ns" in front of it.
d = 230; % sample thickness in nanometers
thickness = d*10^-7; % film thickness (cm)
area = 2.83*10^-5; % sample area in cm^2 7.85*10^-5
tzerosp = 90*.01; % the fraction of the setpoint voltage to call t0
ErrorStop = 100*0.01; % The percentage of the polarization where to stop calculating for the error in the regression calculations at the end of this script

%% For modifying the tail of the switching curve: (1) its location (TLadd), and (2) where to begin leakage current subtraction.
LeakageAdd = -100; % The number of nanoseconds before the timelimit for when to begin leakage current subtraction
TLadd = 400; % The number of nanoseconds to add to the "timelimit" variable. Value of 2,000 for situations where there is a long tail. Value of 400 or around that value is ok for Gaussian distribution switching in ZMO.

KAInUSE = 2.5; % The value of the Avrami n to use for the KAI model. "n" should be set to 2 for 2-dimensional (radial) growth of the nuclei.

%% imported data management
% for the switching data
xfrac = table2array(xfrac); % converts the imported data type from "table' to "array"
nsxfrac = table2array(nsxfrac); % for the non-switching data
% finding where the function generator output begins
xa = xfrac(:,2); % calling CH1, the function generator output
xa = abs(xa); % making all values positive for referencing applications to follow
xaloc = find(xa==0.12); % 0.10 to 0.24V is the function generator output that signifies the output has begun !!! CHECK THIS VALUE IF THE CODE DOES NOT WORK !
n=isempty(xaloc); % this series of if loops is used to determine where the function generator input begins for the switching data
if n==1
   xaloc = find(xa==0.12);
   n=isempty(xaloc);
end
if n==1
   xaloc = find(xa==0.14);
   n=isempty(xaloc);
end
if n==1
   xaloc = find(xa==0.16);
   n=isempty(xaloc);
end
if n==1
   xaloc = find(xa==0.18);
   n=isempty(xaloc);
end
if n==1
   xaloc = find(xa==0.20);
   n=isempty(xaloc);
end
pos1 = xaloc(1) +100 -2; % holds the value where to start accepting points. +100 is for neglecting the first 100 ns before the amplifier output begins.
% ps 1 also governs the position of t0
```

```
% for the non-switchng data (ns)
nsxa = nsxfrac(:,2); % calling CH1, the function generator output
nsxa = abs(nsxa);
nsxaloc = find(nsxa==0.18); % > 0.10 V is the function generator output that signifies the output has begun  !!! CHECK THIS VALUE IF THE CODE DOES NOT WORK !!!
n=isempty(nsxaloc);
if n==1  % this series of if loops is used to determine where the function generator input begins for the non-switching data
   nsxaloc = find(nsxa==0.12);
   n=isempty(nsxaloc);
end
if n==1
   nsxaloc = find(nsxa==0.14);
   n=isempty(nsxaloc);
end
if n==1
   nsxaloc = find(nsxa==0.16);
   n=isempty(nsxaloc);
end
if n==1
   nsxaloc = find(nsxa==0.18);
   n=isempty(nsxaloc);
end
if n==1
   nsxaloc = find(nsxa==0.20);
   n=isempty(nsxaloc);
end
nspos1 = nsxaloc(1) +100 - 2; % holds the value where to start accepting points. +100 is for neglecting the first 100 ns before the amplifier output begins.

%% Adjusting for t0, and choosing the data to simulate
t0adjust = xfrac(pos1:end,3);
maxamp = mode(t0adjust); % assumes the mode (most common value) in the amplifier output is the voltage setpoint
fract0 = tzerosp*maxamp; % calculates the voltage where to start accepting
fract0 = abs(fract0); % for handling negative values
t0adjust = abs(t0adjust); % for handling negative values
t0pos = find(t0adjust>fract0); % finds the position of t0 in the amplifier output greater than the defined percentage of the setpoint voltage where to start the simulation

pos1 = pos1 + t0pos(1)-300; % adjusts the pos1 time for the voltage where t0 is assigned
nspos1 = 9989;
% nspos1 + t0pos(1);

% shortens the arrays for the function generator (fg), amplifier (amp) and
% TIA (tia) switching curves
fg = xfrac(pos1:end,2);
amp = xfrac(pos1:end,3);
tia = abs(xfrac(pos1:end,4).*1000./22); % TIA output (in mA)
l = length(tia);

%% setting the time at polarization saturation
[maxtiaval,maxTIApos] = max(tia); % maximum current value and position from the TIA
tiafind = tia(maxTIApos:end);
zeroTIApos = find(tiafind < 0.5); % to index the zero positions after the TIA current peak
timelimit = maxTIApos + zeroTIApos(1) + TLadd; % to identify the location where the polarization is considered to have saturated

% non-switching curve
nsfg = nsxfrac(nspos1:end,2);
nsamp = nsxfrac(nspos1:end,3);
nstia = abs(nsxfrac(nspos1:end,4).*1000./22); % TIA output (in mA)
nsl = length(nstia);

% to set the proper array length of data to calculate
if l <= nsl
   l = l;
elseif l > nsl
   l = nsl;
end
```

```
l=9000;% sets the length scale to stop at 9 microseconds
%% Leakge current subtration from the TIA output

tia = tia(1:9000)-nstia(1:9000);
NetLeakageCurrent = mean(tia(5000:9000))-mean(nstia(5000:9000)); % calculated the mean of the TIA output beyond the switching
transient from 3 to 9 microseconds
if NetLeakageCurrent > 0
   tia(timelimit+LeakageAdd:end) = tia(timelimit+LeakageAdd:end)-NetLeakageCurrent;
end
%% Imported data mamagement and calculation of experimental volume fraction transformed
% calculates the experimental polarization by subtracting a switching curve
% from the non-switching curve

time = [0.001:0.001:0.001*(l)]; % sets the time in microseconds
time = transpose(time);

i=1;
po = 0;
while i <= l
   polarization(i,1) = po + 10^3*((tia(i,1)-nstia(i,1))*(10^-9))/area; % solves for the polarization by subtracting the switching curve
from the non-switching curve
   po = polarization(i);
   i=i+1;
end
expfraction = polarization./polarization(timelimit); % calls the sets the volume fraction of polarization

%% Finding maximum value of the current to assign the Avrami constant, n

maxCurrent = max(tia);
maxCurrent = find(tia==maxCurrent); % Assigns the position of the max current in the array
% maxCurrent = find(expfraction>=0.7);
Begin = maxCurrent(1) - 10;
Last = maxCurrent(1) + 10;

timevar = log((10^-9).*time([Begin:Last])); % changes unit of time from nanooseconds to seconds
polarizationvar = log(log(1./(1-expfraction([Begin:Last]))));
Avramin = polyfit(timevar,polarizationvar,1);
lnK = Avramin(2);
Avramin = Avramin(1)

%% Fitting of the KAI model
t0=1000; % initial value for t0
i=1;
while i<=l
      fKAI(i) = 1-(exp(-(i/t0)^2)); % KAI function
      i=i+1;
end

%% Automatic determination of the fitting parameters t1 and w

% calculates the n value for the KAI model
KAIvar = log(log(1./(1-fKAI([Begin:Last]))));
KAIn = polyfit(timevar,KAIvar,1);

%% Broad Position finding with t0
exploc = find(fKAI>=0.5);
j=1;
while j<80
   Pfloc = find(expfraction>=0.5); % holds the index values where the value of expfraction, the experimental curve, is greater than 0.5,
in order to calculate the n value there.
   KAIloc = find(fKAI>=0.5); % holds the index values where the value of fKAI, the calculated KAI curve, is greater than 0.5, in
order to calculate the n value there.
   if KAIloc(1)<Pfloc(1)
      t0 = t0 + 10;
   elseif KAIloc(1)>Pfloc(1)
      t0 = t0 - 10;
   elseif KAIloc(1)==Pfloc(1)
```

```
        sprintf('fKAI = expfraction')
    end
t0
test2peakloc= [KAIloc(1),Pfloc(1)]
    % Simulated NLS (Gaussian) model
    t = 10^-9; % (beginning of) time in the upper integrand (s)
    i=1;
    while i<=l
        fKAI(i) = 1-(exp(-(i/t0)^KAInUSE)); % KAI function
        i=i+1;
    end

    % this will end the while loop when the values begin to toggle
    testKAI(j) = KAIloc(1); % stores and array of values of the slopes of the simulated curve
    if j>2
        if testKAI(j)==testKAI(j-2)
            break
        end
    end
    j=j+1;
end
clear testKAI

%% Fine Position finding with t0
exploc = find(fKAI>=0.5);
j=1;
while j<80
    Pfloc = find(expfraction>=0.5); % holds the index values where the value of expfraction, the experimental curve, is greater than 0.5,
in order to calculate the n value there.
    KAIloc = find(fKAI>=0.5); % holds the index values where the value of fKAI, the calculated KAI curve, is greater than 0.5, in
order to calculate the n value there.
    if KAIloc(1)<Pfloc(1)
        t0 = t0 + 1;
    elseif KAIloc(1)>Pfloc(1)
        t0 = t0 - 1;
    elseif KAIloc(1)==Pfloc(1)
        sprintf('fKAI = expfraction')
    end
t0
test2peakloc= [KAIloc(1),Pfloc(1)]
    % Simulated NLS (Gaussian) model
    t = 10^-9; % (beginning of) time in the upper integrand (s)
    i=1;
    while i<=l
        fKAI(i) = 1-(exp(-(i/t0)^KAInUSE)); % KAI function
        i=i+1;
    end

    % this will end the while loop when the values begin to toggle
    testKAI(j) = KAIloc(1); % stores and array of values of the slopes of the simulated curve
    if j>2
        if testKAI(j)==testKAI(j-2)
            break
        end
    end
    j=j+1;
end
clear testKAI

% Solving for the regression sum of squares
ErStop = find(expfraction > ErrorStop); % Holds the positions of the polarization fractions over a certain fraction that was
transformed. The first value in this array is the position where to stop calcualting the fitting errors.
i=1;
while i <= ErStop(1)
    SSRcal = (fKAI(i) - expfraction(i))^2; % Regression sum of squares
    SSRhold(i) = SSRcal; % holds the value in a array
    i=i+1;
```

```
end
SSR = sum(SSRhold)/ErStop(1); % Regression sum of squares

time = [0.001:0.001:0.001*(length(fKAI))]; % sets the time in microseconds
time=transpose(time);
% Plot the extended KAI model vs. Experimental data after automatic fitting
% corrections

fKAI = transpose(fKAI);

figure % creates a new figure
yyaxis left % sets up the left yaxis
p = plot(time,expfraction,time,fKAI,'k'); % plotted data for the left y-axis
title('KAI comparison with experimental data') % plot title
xlabel('Time (microseconds)') % generates axis titles
ylabel('fraction of polarization reversal')
ylim([-0.01 1]) % sets bounds for the left y-axis
xlim([0 4])
p(1).LineWidth = 3; % sets the width of lines in the plot
p(2).LineWidth = 2;
caption = sprintf(' n = %1.2s \n t_0 voltage s.p. = %1.1s \n t_0 char = %1s \n SSR = %1.2s',KAInUSE,tzerosp,t0,SSR); % text for the
caption, limited to one decimal place by %1.1s
text(0.1,0.6,caption); % generates a text box at the coordinates (x,y,caption) according to the left y-axis
legend('experimental','KAI model') % creates a legend for both the left and right y-axes in one box
%maxamp = (maxamp/thickness)*10^-6; % converts "maxamp" from voltage to electric field (MV/cm)
% Calculating the theoretical values for t1 and w
%E0 = 15; % Threshold electric field for pinned domains (MV/cm)
%U = 0.07; % eV/function unit in ZMO (Baska et al., 2024)
%T = 273+19; % Temperature in Kelvin
%kb = 8.617*10^-5; % Boltzmann's constant in eV
%t1theo = 10^(U*E0/kb/T/maxamp)
switchingtime = find(expfraction >= 1);
PswitchValue = polarization(switchingtime(1));
clear switchingtime
switchingtime = find(expfraction >= 0.9);
A = [PswitchValue,switchingtime(1)];

% Outputs the experimetal v.f., simulated v.f., and N/Ninf nucleation rate
% peak data in an array.
PrOutput = [time,expfraction,fKAI];
amp = abs(amp); % used to calcualte the amplitude of the applied field
AppliedField = (max(amp)/(10^6))/thickness; % The calculated applied field in MV/cm
Properties = [tzerosp,Avramin,SSR]; % a set of output properties
```

C-3-4 Gaussian Distribution

```
%% Leonard Jacques
% 11/7/2024

% For determining the NLS model kinetics applicable to
% polarization reversal in the ferroelectric switching of any material.

% Refs:  1.  (Supplemental Information) Guido et al. (2024) Adv. Sci., 11(16), 2308797.
%        2.  Jo et al. (2007) Phys. Rev. Lett., 99(26), 267602.

% The first long while loop that spans several hundred lines used the
% arctan approximation for the NLS model which is much faster and helps to
% get parameters close to ideal.
% Then, the real NLS model with the integral is run in iterations with the
% appriximated fitting terms as initial conditions. Since the integral is
% more expensive to runs, it is efficient to start with the approximated
```

```
% values.
clc
clear
%% User Inputs
%% Import from File:
xfrac = readtable('Switching_Speed_Measurements\switching exported data\Raw_exported_data\TEK00791.CSV'); % Imports data from a .txt file that is tab delimited performs the function of "text to columns"
nsxfrac = readtable(['Switching_Speed_Measurements\switching exported data\Raw_exported_data\TEK00785.CSV']); % Imports non-switching data, later to be subtracted from the switching data. Variables specific to non-switching data have "ns" in front of it.
d = 236; % sample thickness in nanometers
thickness = d*10^-7; % film thickness (cm)
area = 7.85*10^-5; % sample area in cm^2 7.85*10^-5
tzerosp = 70*0.01; % the fraction of the setpoint voltage to call t0
ErrorStop = 100*0.01; % The percentage of the polarization where to stop calculating for the error in the regression calculations at the end of this script

%% Fitting Parameters
u = 900*10^-9; % half-width, half-maximum of the Lorentzian distribution (in nano-seconds)
s = 30*10^-9; % A normalization constant for fitting the NLS distribution to the experimental data (the middle of the distribution) - the position of this should be at the point of maximum current.

%% imported data management
% for the switching data
xfrac = table2array(xfrac); % converts the imported data type from "table' to "array"
nsxfrac = table2array(nsxfrac); % for the non-switching data
% finding where the function generator output begins
xa = xfrac(:,2); % calling CH1, the function generator output
xa = abs(xa); % making all values positive for referencing applications to follow
xaloc = find(xa==0.12); % 0.10 to 0.24V is the function generator output that signifies the output has begun !!! CHECK THIS VALUE IF THE CODE DOES NOT WORK !
n=isempty(xaloc); % this series of if loops is used to determine where the function generator input begins for the switching data
if n==1
   xaloc = find(xa==0.12);
   n=isempty(xaloc);
end
if n==1
   xaloc = find(xa==0.14);
   n=isempty(xaloc);
end
if n==1
   xaloc = find(xa==0.16);
   n=isempty(xaloc);
end
if n==1
   xaloc = find(xa==0.18);
   n=isempty(xaloc);
end
if n==1
   xaloc = find(xa==0.20);
   n=isempty(xaloc);
end
pos1 = xaloc(1) +100 -2; % holds the value where to start accepting points. +100 is for neglecting the first 100 ns before the amplifier output begins.
% ps 1 also governs the position of t0
% for the non-switchng data (ns)
nsxa = nsxfrac(:,2); % calling CH1, the function generator output
nsxa = abs(nsxa);
nsxaloc = find(nsxa==0.18); % > 0.10 V is the function generator output that signifies the output has begun  !!! CHECK THIS VALUE IF THE CODE DOES NOT WORK !!!
n=isempty(nsxaloc);
if n==1  % this series of if loops is used to determine where the function generator input begins for the non-switching data
   nsxaloc = find(nsxa==0.12);
   n=isempty(nsxaloc);
end
if n==1
   nsxaloc = find(nsxa==0.14);
   n=isempty(nsxaloc);
```

```
end
if n==1
   nsxaloc = find(nsxa==0.16);
   n=isempty(nsxaloc);
end
if n==1
   nsxaloc = find(nsxa==0.18);
   n=isempty(nsxaloc);
end
if n==1
   nsxaloc = find(nsxa==0.20);
   n=isempty(nsxaloc);
end
nspos1 = nsxaloc(1) +100 - 2; % holds the value where to start accepting points. +100 is for neglecting the first 100 ns before the
amplifier output begins.

%% Adjusting for t0, and choosing the data to simulate
t0adjust = xfrac(pos1:end,3);
maxamp = mode(t0adjust); % assumes the mode (most common value) in the amplifier output is the voltage setpoint
fract0 = tzerosp*maxamp; % calculates the voltage where to start accepting
fract0 = abs(fract0); % for handling negative values
t0adjust = abs(t0adjust); % for handling negative values
t0pos = find(t0adjust>fract0); % finds the position of t0 in the amplifier output greater than the defined percentage of the setpoint
voltage where to start the simulation

pos1 = pos1 + t0pos(1); % adjusts the pos1 time for the voltage where t0 is assigned
nspos1 = nspos1 + t0pos(1);

% shortens the arrays for the function generator (fg), amplifier (amp) and
% TIA (tia) switching curves
fg = xfrac(pos1:end,2);
amp = xfrac(pos1:end,3);
tia = abs(xfrac(pos1:end,4).*1000./22); % TIA output (in mA)
l = length(tia);

%% setting the time at polarization saturation
[maxtiaval,maxTIApos] = max(tia); % maximum current value and position from the TIA
tiafind = tia(maxTIApos:end);
zeroTIApos = find(tiafind < 0.5); % to index the zero positions after the TIA current peak
timelimit = maxTIApos + zeroTIApos(1) + 400; % to identify the location where the polarization is considered to have saturated

% non-switching curve
nsfg = nsxfrac(nspos1:end,2);
nsamp = nsxfrac(nspos1:end,3);
nstia = abs(nsxfrac(nspos1:end,4).*1000./22); % TIA output (in mA)
nsl = length(nstia);

% to set the proper array length of data to calculate
if l <= nsl
   l = l;
elseif l > nsl
   l = nsl;
end
l=9000;% sets the length scale to stop at 9 microseconds
%% Leakge current subtration from the TIA output
NetLeakageCurrent = mean(tia(3000:9000))-mean(nstia(3000:9000)); % calculated the mean of the TIA output beyond the switching
transient from 3 to 9 microseconds
tia = tia(1:9000)-nstia(1:9000);
if NetLeakageCurrent > 0
   tia(timelimit+400:end) = tia(timelimit+400:end)-NetLeakageCurrent;
end
%% Imported data mamagement and calculation of experimental volume fraction transformed
% calculates the experimental polarization by subtracting a switching curve
% from the non-switching curve

time = [0.001:0.001:0.001*(l)]; % sets the time in microseconds
time = transpose(time);
```

```
i=1;
po = 0;
while i <= l
   polarization(i,1) = po + 10^3*((tia(i,1)-nstia(i,1))*(10^-9))/area; % solves for the polarization by subtracting the switching curve
from the non-switching curve
   po = polarization(i);
   i=i+1;
end

expfraction = polarization./polarization(timelimit); % calls the sets the volume fraction of polarization
tcorrection = 0.2; % A correction factor which simultaneously shifts the ext. KAI model and projected nucleation rate forward to a
lower time (in order to match the slope) and adjusts the x-axis limit of the plot accordingly.
time2 = [0.001:0.001:l*0.001]-tcorrection; % Sets the array for plotting of the ext. KAI model and the projected nucleation rate peak.

%% Finding maximum value of the current to assign the Avrami constant, n

maxCurrent = max(tia);
maxCurrent = find(tia==maxCurrent); % Assigns the position of the max current in the array
% maxCurrent = find(expfraction>=0.7);
Begin = maxCurrent(1) - 10;
Last = maxCurrent(1) + 10;

timevar = log((10^-9).*time([Begin:Last])); % changes unit of time from nanooseconds to seconds
polarizationvar = log(log(1./(1-expfraction([Begin:Last]))));
Avramin = polyfit(timevar,polarizationvar,1);
lnK = Avramin(2);
Avramin = Avramin(1)

%% Initial fitting of the NLS model
meanFind = find(expfraction>=0.5);
u = meanFind(1)*10^-9;
t = 10^-9; % (beginning of) time in the upper integrand (s)
i=1;
while i<=l
   f = 0.5*(1+erf((t-u)/(s*(2^0.5))));
   Pfraction(i) = f; % sets values in an array for transformation fraction
   t=t+(10^-9); % adds 1 nanosecond to the time
   i=i+1;
end

%% Caussian Cumulative Distribution Function calculation
i = 1;
t = 10^-9; %
while i<=l
   NucGauss = (1/sqrt(2*pi*s^2))*exp(-((t-u)^2)/(2*s^2)); % Gaussian distribution of nucleation
   NucRatePeak(i) = NucGauss; % sets values in an array for the nucleation rate peak
   t=t+(10^-9); % adds 1 nanosecond to the time
   i=i+1;
end
y = transpose(Pfraction); % transposed the Pfraction into columnar data which can be used later for exporting

%% Automatic determination of the fitting parameters t1 and w

% calculates the n value for the KAI model
KAIvar = log(log(1./(1-Pfraction([Begin:Last]))));
KAIn = polyfit(timevar,KAIvar,1);

%% Position finding with s
exploc = find(Pfraction>=0.5);
j=1;
while j<80
   Pfloc = find(expfraction>=0.5); % holds the index values where the value of Pfraction, the calculated KAI curve, is greater than 0.5,
in order to calculate the n value there.
   if KAIn(1)<Avramin
      s = s - (s/30);
   elseif KAIn(1)>Avramin
```

```
        s = s + (s/30);
    elseif KAIn(1)==Avramin
        sprintf('KAIn(1) = Avramin')
    end
testm = [KAIn(1),Avramin]
test2peakloc= [Pfloc(1),exploc(1)]
    % Simulated NLS (Gaussian) model
    t = 10^-9; % (beginning of) time in the upper integrand (s)
    i=1;
    while i<=l
        f = 0.5*(1+erf((t-u)/(s*(2^0.5))));
        Pfraction(i) = f; % sets values in an array for transformation fraction
        t=t+(10^-9); % adds 1 nanosecond to the time
        i=i+1;
    end

    % calculates the n value for the KAI model
    KAIvar = log(log(1./(1-Pfraction([Begin:Last]))));
    KAIn = polyfit(timevar,KAIvar,1);
    % this will end the while loop when the values begin to toggle
    testKAI(j) = KAIn(1); % stores and array of values of the slopes of the simulated curve
    if j>2
        if testKAI(j)==testKAI(j-2)
            break
        end
    end
    j=j+1;
end
clear testKAI

 % Nucleation rate peak calculation
i = 1;
    t = 10^-9; %
    ActualN = 0; % sets the initial value for ActualNuc, the nucleation rate
    while i<=l % this is the letter "l", not the numbner "1" !!!
        NucGauss = (1/sqrt(2*pi*s^2))*exp(-((t-u)^2)/(2*s^2)); % Gaussian distribution of nucleation
        NucRatePeak(i) = NucGauss; % sets values in an array for the nucleation rate peak
        ActualN(i+1) = ActualN(i) + NucGauss*10^-9; % stores the number of actual nuclei which have formed during the polarization
reversal process in the capacitor
        ActualNuc(i) = ActualN(i+1); % stores the number of actual nuclei which have formed during the polarization reversal process in
the capacitor - FOR PLOTTING
        t=t+(10^-9); % adds 1 nanosecond to the time
        i=i+1;
    end
clear testKAI
% Solving for the regression sum of squares
ErStop = find(expfraction > ErrorStop); % Holds the positions of the polarization fractions over a certain fraction that was
transformed. The first value in this array is the position where to stop calcualting the fitting errors.
i=1;
while i <= ErStop(1)
    SSRcal = (Pfraction(i) - expfraction(i))^2; % Regression sum of squares
    SSRhold(i) = SSRcal; % holds the value in a array
    i=i+1;
end
SSR = sum(SSRhold)/ErStop(1); % Regression sum of squares
% Solving the Total Sum of Squares
i=1;
while i <= ErStop(1)
    SSTcal = (expfraction(i) - mean(expfraction))^2; % Regression sum of squares
    SSThold(i) = SSTcal; % holds the value in a array
    i=i+1;
end
SST = sum(SSThold)/ErStop(1); % Total sum of squares
%Rsquare = 1 - SSR/SST; % R^2 value
Rsquare = 1 - SSR; % not exactly R^2 value - because there is only 1 data point for each value on the simulated curve

maxN = max(ActualNuc); % Holds the maximum value for nucleation
```

```
%NucPercent = ActualNuc./maxN; % Holds the percentage of nucleation completed
NucPercent = ActualNuc./ActualNuc(timelimit); % Holds the normalized percentage of nucleation completed

time = [0.001:0.001:0.001*(length(Pfraction))]; % sets the time in microseconds
time=transpose(time);
% Plot the extended KAI model vs. Experimental data after automatic fitting
% corrections

figure % creates a new figure
yyaxis left % sets up the left yaxis
p = plot(time,expfraction,time,Pfraction,'k'); % plotted data for the left y-axis
title('NLS (Gaussian dist.) comparison with experimental data') % plot title
xlabel('Time (microseconds)') % generates axis titles
ylabel('fraction of polarization reversal')
ylim([-0.01 1]) % sets bounds for the left y-axis
%xlim([0 (2-tcorrection)])
xlim([0 1])
p(1).LineWidth = 3; % sets the width of lines in the plot
p(2).LineWidth = 2;
caption = sprintf(' n = %1.2s \n u(mean) = %1.2s sec \n sigma = %1.1s sec \n t_0 voltage s.p. = %1.1s \n SSR =
%1.2s',Avramin,u,s,tzerosp,SSR); % text for the caption, limited to one decimal place by %1.1s
text(0.1,0.6,caption); % generates a text box at the coordinates (x,y,caption) according to the left y-axis
%setting up the right y-axis
yyaxis right % sets up the right y axis. syntax below will correspond to the right y-axis.
plot(time,NucRatePeak); % plotted data for the right y-axis
ylabel('Distribution Function')
legend('experimental','NLS model','Nuc. rate') % creates a legend for both the left and right y-axes in one box

%maxamp = (maxamp/thickness)*10^-6; % converts "maxamp" from voltage to electric field (MV/cm)
% Calculating the theoretical values for t1 and w
%E0 = 15; % Threshold electric field for pinned domains (MV/cm)
%U = 0.07; % eV/function unit in ZMO (Baska et al., 2024)
%T = 273+19; % Temperature in Kelvin
%kb = 8.617*10^-5; % Boltzmann's constant in eV
%t1theo = 10^(U*E0/kb/T/maxamp)


% Outputs the experimetal v.f., simulated v.f., and N/Ninf nucleation rate
% peak data in an array.
Pfraction = transpose(Pfraction);
NucRatePeak = transpose(NucRatePeak);
NucPercent=transpose(NucPercent);
PrOutput = [time,expfraction,Pfraction,NucRatePeak,NucPercent];
[maxNuc,maxNucPos] = max(NucRatePeak);
amp = abs(amp); % used to calcualte the amplitude of the applied field
AppliedField = (max(amp)/(10^6))/thickness; % The calculated applied field in MV/cm
Properties = [tzerosp,Avramin,SSR]; % a set of output properties
```

C-3-5 Combined Gaussian and Inverse Gamma Distributions

```
%% Leonard Jacques
% 9/12/2024

% For determining the NLS model kinetics applicable to
% polarization reversal in the ferroelectric switching of any material.

% Refs:  1.  (Supplemental Information) Guido et al. (2024) Adv. Sci., 11(16), 2308797.
%        2.  Jo et al. (2007) Phys. Rev. Lett., 99(26), 267602.

% The first long while loop that spans several hundred lines used the
% arctan approximation for the NLS model which is much faster and helps to
```

```
% get parameters close to ideal.
% Then, the real NLS model with the integral is run in iterations with the
% appriximated fitting terms as initial conditions. Since the integral is
% more expensive to runs, it is efficient to start with the approximated
% values.

%% TROUBLESHOOTING:
%  the "j" variable inequalities for the while loops in lines 343 and 380
%  may have to be altered slightly to change the number of iterations so
%  the loops do not "run away" and produce obscure values. The values
%  should be whole integers and the number of iterations to performw would
%  likely be between 3 and 7 (j<4 and j<8) depending on the curcumstances,
%  but may be outside those bounds.
clc
clear
%% User Inputs
%% Import from File:
xfrac = readtable('TEK00768.CSV'); % Imports data from a .txt file that is tab delimited performs the function of "text to columns"
nsxfrac = readtable(['TEK00767.CSV']); % Imports non-switching data, later to be subtracted from the switching data. Variables specific to non-switching data have "ns" in front of it.
d = 227; % sample thickness in nanometers
thickness = d*10^-7; % film thickness (cm)
area = 7.85*10^-5; % sample area in cm^2 7.85*10^-5
tzerosp = 70*0.01; % the fraction of the setpoint voltage to call t0
ErrorStop = 100*0.01; % The percentage of the polarization where to stop calculating for the error in the regression calculations at the end of this script

%% For modifying the tail of the switching curve: (1) its location (TLadd), and (2) where to begin leakage current subtraction.
LeakageAdd = -400; % The number of nanoseconds to add to the "timelimit" variable. Value of 2,000 for situations where there is a long tail. Value of 400 or around that value is ok for Gaussian distribution switching in ZMO.
TLadd = 400; % The number of nanoseconds before the timelimit for when to begin leakage current subtraction

%% Initial Fitting Parameters / Matching Parameters
% Gaussian Distribution
u = 900*10^-9; % half-width, half-maximum of the Lorentzian distribution (in nano-seconds)
s = 30*10^-9; % A normalization constant for fitting the NLS distribution to the experimental data (the middle of the distribution) - the position of this should be at the point of maximum current.
% Inverse Gamma Distribution
a = 4; % initial value for alpha (describes the shape) - must be a positive number
B = 4.8*10^-7; % initial value for lambda (describes the scale) - must be a positive value between 0 and infinity
TailMatch = 87*0.01; % the position along the tail where to match the inverse gaussian distribution to the experimental curve
ShapeMatch = 60*0.01; % the position along the curve where to match the inverse gaussian distribution to the experimental curve
% Combined Distribution Distribution
DifferenceCondition = 0.01; % Holds the threshold difference between the experimental curve and the Gaussian fit
GaussPre = 0.5; % Holds the threshold difference between the experimental curve and the Gaussian fit

%% imported data management
% for the switching data
xfrac = table2array(xfrac); % converts the imported data type from "table' to "array"
nsxfrac = table2array(nsxfrac); % for the non-switching data
% finding where the function generator output begins
xa = xfrac(:,2); % calling CH1, the function generator output
xa = abs(xa); % making all values positive for referencing applications to follow
xaloc = find(xa==0.18); % 0.10 to 0.24V is the function generator output that signifies the output has begun !!! CHECK THIS VALUE IF THE CODE DOES NOT WORK !
n=isempty(xaloc); % this series of if loops is used to determine where the function generator input begins for the switching data
if n==1 % this series of if loops is used to determine where the function generator input begins for the switching data
   xaloc = find(xa==0.14);
   n=isempty(xaloc);
end
if n==1
   xaloc = find(xa==0.16);
   n=isempty(xaloc);
end
if n==1
   xaloc = find(xa==0.18);
   n=isempty(xaloc);
```

```
end
if n==1
   xaloc = find(xa==0.20);
   n=isempty(xaloc);
end
pos1 = xaloc(1) +100 -2; % holds the value where to start accepting points. +100 is for neglecting the first 100 ns before the amplifier
output begins.
% ps 1 also governs the position of t0
% for the non-switchng data (ns)
nsxa = nsxfrac(:,2); % calling CH1, the function generator output
nsxa = abs(nsxa);
nsxaloc = find(nsxa==0.18); % > 0.10 V is the function generator output that signifies the output has begun  !!! CHECK THIS
VALUE IF THE CODE DOES NOT WORK !!!
n=isempty(nsxaloc);
if n==1 % this series of if loops is used to determine where the function generator input begins for the non-switching data
   nsxaloc = find(nsxa==0.14);
   n=isempty(nsxaloc);
end
if n==1
   nsxaloc = find(nsxa==0.16);
   n=isempty(nsxaloc);
end
if n==1
   nsxaloc = find(nsxa==0.18);
   n=isempty(nsxaloc);
end
if n==1
   nsxaloc = find(nsxa==0.20);
   n=isempty(nsxaloc);
end
nspos1 = nsxaloc(1) +100 - 2; % holds the value where to start accepting points. +100 is for neglecting the first 100 ns before the
amplifier output begins.

%% Adjusting for t0, and choosing the data to simulate
t0adjust = xfrac(pos1:end,3);
maxamp = mode(t0adjust); % assumes the mode (most common value) in the amplifier output is the voltage setpoint
fract0 = tzerosp*maxamp; % calculates the voltage where to start accepting
fract0 = abs(fract0); % for handling negative values
t0adjust = abs(t0adjust); % for handling negative values
t0pos = find(t0adjust>fract0); % finds the position of t0 in the amplifier output greater than the defined percentage of the setpoint
voltage where to start the simulation

pos1 = pos1 + t0pos(1); % adjusts the pos1 time for the voltage where t0 is assigned
nspos1 = nspos1 + t0pos(1);

% shortens the arrays for the function generator (fg), amplifier (amp) and
% TIA (tia) switching curves
fg = xfrac(pos1:end,2);
amp = xfrac(pos1:end,3);
tia = abs(xfrac(pos1:end,4).*1000./22); % TIA output (in mA)
l = length(tia);

%% setting the time at polarization saturation
[maxtiaval,maxTIApos] = max(tia); % maximum current value and position from the TIA
tiafind = tia(maxTIApos:end);
zeroTIApos = find(tiafind < 0.5); % to index the zero positions after the TIA current peak
timelimit = maxTIApos + zeroTIApos(1) + TLadd; % to identify the location where the polarization is considered to have saturated

% non-switching curve
nsfg = nsxfrac(nspos1:end,2);
nsamp = nsxfrac(nspos1:end,3);
nstia = abs(nsxfrac(nspos1:end,4).*1000./22); % TIA output (in mA)
nsl = length(nstia);

% to set the proper array length of data to calculate
if l <= nsl
   l = l;
```

```
elseif l > nsl
   l = nsl;
end

l=9000; % sets the time time limit to 9 microseconds

%% Leakge current subtration from the TIA output
NetLeakageCurrent = mean(tia(3000:9000))-mean(nstia(3000:9000)); % calculated the mean of the TIA output beyond the switching
transient from 3 to 9 microseconds
if NetLeakageCurrent > 0
   tia(timelimit+LeakageAdd:end) = tia(timelimit+LeakageAdd:end)-NetLeakageCurrent; % Can MODIFY the term here to modify
where the begin the leakage current contributions
end

%% Imported data mamagement and calculation of experimental volume fraction transformed
% calculates the experimental polarization by subtracting a switching curve
% from the non-switching curve

time = [0.001:0.001:0.001*(l)]; % sets the time in microseconds
time = transpose(time);

i=1;
po = 0;
while i <= l
   polarization(i,1) = po + 10^3*((tia(i,1)-nstia(i,1))*(10^-9))/area; % solves for the polarization by subtracting the switching curve
from the non-switching curve
   po = polarization(i);
   i=i+1;
end

expfraction = polarization./polarization(timelimit); % calls the sets the volume fraction of polarization
tcorrection = 0.2; % A correction factor which simultaneously shifts the ext. KAI model and projected nucleation rate forward to a
lower time (in order to match the slope) and adjusts the x-axis limit of the plot accordingly.
time2 = [0.001:0.001:l*0.001]-tcorrection; % Sets the array for plotting of the ext. KAI model and the projected nucleation rate peak.

%% Finding maximum value of the current to assign the Avrami constant, n

maxCurrent = max(tia);
maxCurrent = find(tia==maxCurrent); % Assigns the position of the max current in the array
Begin = maxCurrent(1) - 10;
Last = maxCurrent(1) + 10;

timevar = log((10^-9).*time([Begin:Last])); % changes unit of time from nanooseconds to seconds
polarizationvar = log(log(1./(1-expfraction([Begin:Last]))));
Avramin = polyfit(timevar,polarizationvar,1);
lnK = Avramin(2);
Avramin = Avramin(1)

%% Gaussian Distribution

%% Initial fitting of the NLS model
meanFind = find(expfraction>=0.5);
u = meanFind(1)*10^-9;
t = 10^-9; % (beginning of) time in the upper integrand (s)
i=1;
while i<=l
   f = 0.5*(1+erf((t-u)/(s*(2^0.5))));
   Pfraction(i) = f; % sets values in an array for transformation fraction
   t=t+(10^-9); % adds 1 nanosecond to the time
   i=i+1;
end

%% Distribution Function calculation
i = 1;
t = 10^-9; %
while i<=l
   NucGauss = (1/sqrt(2*pi*s^2))*exp(-((t-u)^2)/(2*s^2)); % Gaussian distribution of nucleation
```

```
   NucRatePeak(i) = NucGauss; % sets values in an array for the nucleation rate peak
   t=t+(10^-9); % adds 1 nanosecond to the time
   i=i+1;
end
y = transpose(Pfraction); % transposed the Pfraction into columnar data which can be used later for exporting

%% Automatic determination of the fitting parameters t1 and w

% calculates the n value for the KAI model
KAIvar = log(log(1./(1-Pfraction([Begin:Last]))));
KAIn = polyfit(timevar,KAIvar,1);

%% Position finding with s
exploc = find(Pfraction>=0.5);
j=1;
while j<80
   Pfloc = find(expfraction>=0.5); % holds the index values where the value of Pfraction, the calculated KAI curve, is greater than 0.5,
in order to calculate the n value there.
   if KAIn(1)<Avramin
      s = s - (s/30);
   elseif KAIn(1)>Avramin
      s = s + (s/30);
   elseif KAIn(1)==Avramin
      sprintf('KAIn(1) = Avramin')
   end
testm = [KAIn(1),Avramin]
test2peakloc= [Pfloc(1),exploc(1)]
   % Simulated NLS (Gaussian) model
   t = 10^-9; % (beginning of) time in the upper integrand (s)
   i=1;
   while i<=l
      f = 0.5*(1+erf((t-u)/(s*(2^0.5))));
      Pfraction(i) = f; % sets values in an array for transformation fraction
      t=t+(10^-9); % adds 1 nanosecond to the time
      i=i+1;
   end

   % calculates the n value for the KAI model
   KAIvar = log(log(1./(1-Pfraction([Begin:Last]))));
   KAIn = polyfit(timevar,KAIvar,1);
   % this will end the while loop when the values begin to toggle
   testKAI(j) = KAIn(1); % stores and array of values of the slopes of the simulated curve
   if j>2
      if testKAI(j)==testKAI(j-2)
         break
      end
   end
   j=j+1;
end
clear testKAI

 % Nucleation rate peak calculation
i = 1;
   t = 10^-9; %
   ActualN = 0; % sets the initial value for ActualNuc, the nucleation rate
   while i<=l % this is the letter "l", not the numbner "1" !!!
      NucGauss(i) = (1/sqrt(2*pi*s^2))*exp(-((t-u)^2)/(2*s^2)); % Gaussian distribution of nucleation
      %NucRatePeak(i) = NucGauss; % sets values in an array for the nucleation rate peak
      ActualN(i+1) = ActualN(i) + NucGauss(i)*10^-9; % stores the number of actual nuclei which have formed during the
polarization reversal process in the capacitor
      ActualNuc(i) = ActualN(i+1); % stores the number of actual nuclei which have formed during the polarization reversal process in
the capacitor - FOR PLOTTING
      t=t+(10^-9); % adds 1 nanosecond to the time
      i=i+1;
   end
clear testKAI
% Solving for the regression sum of squares
```

```
ErStop = find(expfraction > ErrorStop); % Holds the positions of the polarization fractions over a certain fraction that was
transformed. The first value in this array is the position where to stop calcualting the fitting errors.
i=1;
while i <= ErStop(1)
   SSRcal = (Pfraction(i) - expfraction(i))^2; % Regression sum of squares
   SSRhold(i) = SSRcal; % holds the value in a array
   i=i+1;
end
SSRgauss = sum(SSRhold)/ErStop(1); % Regression sum of squares

% Plot the NLS Gaussian model vs. Experimental data after automatic fitting
% corrections
figure % creates a new figure
yyaxis left % sets up the left yaxis
p = plot(time,expfraction,time,Pfraction,'k'); % plotted data for the left y-axis
title('NLS (Gaussian dist.) comparison with experimental data') % plot title
xlabel('Time (microseconds)') % generates axis titles
ylabel('fraction of polarization reversal')
ylim([-0.01 1]) % sets bounds for the left y-axis
%xlim([0 (2-tcorrection)])
xlim([0 1])
p(1).LineWidth = 3; % sets the width of lines in the plot
p(2).LineWidth = 2;
caption = sprintf(' n = %1.2s \n u(mean) = %1.2s sec \n sigma = %1.1s sec \n t_0 voltage s.p. = %1.1s \n SSR =
%1.2s',Avramin,u,s,tzerosp,SSRgauss); % text for the caption, limited to one decimal place by %1.1s
text(0.1,0.6,caption); % generates a text box at the coordinates (x,y,caption) according to the left y-axis
%setting up the right y-axis
yyaxis right % sets up the right y axis. syntax below will correspond to the right y-axis.
plot(time,NucGauss); % plotted data for the right y-axis
ylabel('Fraction of Nucleation Progress')
%ylim([-0.01 1]) % sets bounds for the right y-axis
legend('experimental','NLS model','Distribution Function') % creates a legend for both the left and right y-axes in one box

% Store the Parameters for the Gaussian Distribution in this order: Polarization Fraction, Distribution Function, Reduced
% sum of squares
PfracGauss = Pfraction; % stores the Gaussian fit Pfraction data
Pfraction = transpose(Pfraction);
NucRatePeak = transpose(NucGauss);
PfracGauss = Pfraction;
GaussStore = [Pfraction,NucRatePeak];

%% Inverse Gamma Distribution

%% Initial fitting of the inv. gamma NLS model
t = 10^-9; % (beginning of) time in the upper integrand (s)
i=1;
while i<=l
   fun = @(t) t.^(a-1).*exp(-t); % partial CDF (cumulative distribution function) of gamma (Erlang) function
   f = integral(fun,B/t,Inf);
   Pfraction(i) = f; % sets values in an array for transformation fraction
   t=t+(10^-9); % adds 1 nanosecond to the time
   i=i+1;
end

%% Probability density function (Nucleation)
i = 1;
t = 10^-9;
while i<=l
   NucInvGamma = (B^a)*t^(-a-1)*exp(-B/t)/gamma(a); % (PDF) Probability distribution function of inverse gamma distribution
   NucRatePeak(i) = NucInvGamma; % sets values in an array for the nucleation rate peak
   t=t+(10^-9); % adds 1 nanosecond to the time
   i=i+1;
end
y = transpose(Pfraction); % transposed the Pfraction into columnar data which can be used later for exporting

%% Automatic determination of the fitting parameters a (alpha) and B (Beta)
```

```
% calculates the n value for the KAI model
KAIvar = log(log(1./(1-Pfraction([Begin:Last]))));
KAIn = polyfit(timevar,KAIvar,1);


TailLoc = find(expfraction>=TailMatch);
TailLoc = TailLoc(1);
exploc = find(expfraction>=ShapeMatch);

z=1;
while z < 30
   % Position finding with B (scale)
j=1;
while j<4
   if Pfraction(TailLoc)<expfraction(TailLoc)
      B = B + (B/30);
   elseif Pfraction(TailLoc)>expfraction(TailLoc)
      B = B - (B/30);
   elseif Pfraction(TailLoc)==expfraction(TailLoc)
      sprintf('Pfloc(1) = exploc(1)')
   end
   B
   % Cumulative Density Function
   t = 10^-9; % (beginning of) time in the upper integrand (s)
   i=1;
   ActualN = 0; % sets the initial value for ActualNuc, the nucleation rate
   while i<=l % this is the letter "l", not the numbner "1" !!!
      NucInvGamma = (B^a)*t^(-a-1)*exp(-B/t)/gamma(a); % (PDF) Probability distribution function of inverse gamma distribution
      NucRatePeak(i) = NucInvGamma; % sets values in an array for the nucleation rate peak
      ActualN(i+1) = ActualN(i) + NucInvGamma*10^-9; % stores the number of actual nuclei which have formed during the
polarization reversal process in the capacitor
      ActualNuc(i) = ActualN(i+1); % stores the number of actual nuclei which have formed during the polarization reversal process in
the capacitor - FOR PLOTTING
      t=t+(10^-9); % adds 1 nanosecond to the time
      i=i+1;
   end
   maxN = max(ActualNuc); % Holds the maximum value for nucleation
   NucPercent = ActualNuc./ActualNuc(timelimit); % Holds the normalized percentage of nucleation completed
   Pfraction = NucPercent;
   % This breaks the while loop when values begin to toggle around a minimum
   BStore(j) = B;
   if j>2
      if BStore(j)==BStore(j-2)
         break
      end
   end
   j=j+1;
end

%% Shape (body) matching with a (alpha)
exploc = find(expfraction>=ShapeMatch);
j=1;
while j<6
   Pfloc = find(Pfraction>=ShapeMatch); % holds the index values where the value of Pfraction, the calculated KAI curve, is greater
than 0.5, in order to calculate the n value there.
   if Pfloc(1)<exploc(1)
      a = a - (a/50);
   elseif Pfloc(1)>exploc(1)
      a = a + (a/50);
   elseif Pfloc(1)==exploc(1)
      sprintf('Pfloc(1) = exploc(1)')
   end
   a

   % setting up the integral
   t = 10^-9; % (beginning of) time in the upper integrand (s)
   i=1;
```

```
   ActualN = 0; % sets the initial value for ActualNuc, the nucleation rate
   while i<=l % this is the letter "l", not the numbner "1" !!!
      NucInvGamma = (B^a)*t^(-a-1)*exp(-B/t)/gamma(a); % (PDF) Probability distribution function of inverse gamma distribution
      NucRatePeak(i) = NucInvGamma; % sets values in an array for the nucleation rate peak
      ActualN(i+1) = ActualN(i) + NucInvGamma*10^-9; % stores the number of actual nuclei which have formed during the
polarization reversal process in the capacitor
      ActualNuc(i) = ActualN(i+1); % stores the number of actual nuclei which have formed during the polarization reversal process in
the capacitor - FOR PLOTTING
      t=t+(10^-9); % adds 1 nanosecond to the time
      i=i+1;
   end
   maxN = max(ActualNuc); % Holds the maximum value for nucleation
   NucPercent = ActualNuc./ActualNuc(timelimit); % Holds the normalized percentage of nucleation completed
   Pfraction = NucPercent;

   % This breaks the while loop when values begin to toggle around a minimum
   aStore(j) = a;
   if j>2
      if aStore(j)==aStore(j-2)
         break
      end
   end
   j=j+1;
   %clear Pfloc
end
z=z+1;
end

% Solving for the regression sum of squares (error)
ErStop = find(expfraction > ErrorStop); % Holds the positions of the polarization fractions over a certain fraction that was
transformed. The first value in this array is the position where to stop calcualting the fitting errors.
i=1;
while i <= ErStop(1)
   SSRcal = (Pfraction(i) - expfraction(i))^2; % Regression sum of squares
   SSRhold(i) = SSRcal; % holds the value in a array
   i=i+1;
end
SSR = sum(SSRhold)/ErStop(1); % Regression sum of squares

maxN = max(ActualNuc); % Holds the maximum value for nucleation
%NucPercent = ActualNuc./maxN; % Holds the percentage of nucleation completed
NucPercent = ActualNuc./ActualNuc(timelimit); % Holds the normalized percentage of nucleation completed

time = [0.001:0.001:0.001*(length(Pfraction))]; % sets the time in microseconds
time=transpose(time);
% Plot the Inverse Gamma NLS vs. Experimental data after automatic fitting
figure % creates a new figure
yyaxis left % sets up the left yaxis
p = plot(time,expfraction,time,Pfraction,'k'); % plotted data for the left y-axis
title('NLS (Inverse gamma dist.) comparison with experimental data') % plot title
xlabel('Time (microseconds)') % generates axis titles
ylabel('fraction of polarization reversal')
ylim([-0.01 1]) % sets bounds for the left y-axis
%xlim([0 (2-tcorrection)])
xlim([0 1])
p(1).LineWidth = 3; % sets the width of lines in the plot
p(2).LineWidth = 2;
caption = sprintf(' n = %1.2s \n a = %1.3s sec \n B = %1.3s sec \n t_0 voltage s.p. = %1.1s \n SSR =
%1.3s',Avramin,a,B,tzerosp,SSR); % text for the caption, limited to one decimal place by %1.1s
text(0.1,0.6,caption); % generates a text box at the coordinates (x,y,caption) according to the left y-axis
% setting up the right y-axis
yyaxis right % sets up the right y axis. syntax below will correspond to the right y-axis.
plot(time,NucRatePeak); % plotted data for the right y-axis
ylabel('Distribution Function')
legend('experimental','NLS model','Dist. Function') % creates a legend for both the left and right y-axes in one box

%InvGamNuc = transpose(NucRatePeak);
```

```
PfracInvGamma = transpose(Pfraction);
InvGammaStore = [PfracInvGamma,NucRatePeak];

%% Combination Algorithm
% Combines the Gaissuan and Inverse Gamma curves into one so the tail of
% the inverse gamma distribution will fit the switching curve

i=1;
j=1;
while i <= l
   if expfraction(i) <= GaussPre % Establishes where the Gaussian distribution closely fits the experimental data
      CombinedPfrac(i) = PfracGauss(i); % Establishes the vector for the combined cumulative distribution function with Gaussian for
the body and Inv. Gamma for teh tail
      CombinedNucDist(i) = NucGauss(i); % Establishes the vector for the combined distribution curve with Gaussian for the body
and Inv. Gamma for the tail
   elseif expfraction(i) > GaussPre
      GaussDifference = abs(expfraction(i) - PfracGauss(i));
      if GaussDifference <= DifferenceCondition
         CombinedPfrac(i) = PfracGauss(i);
         CombinedNucDist(i) = NucGauss(i);
      elseif GaussDifference > DifferenceCondition
         CombinedPfrac(i) = Pfraction(i);
         CombinedNucDist(i) = NucRatePeak(i);
         TransitionPfrac(j) = expfraction(i); % Tracks at chich polarization feaction the transition from Gaussian distribution to Inv.
Gamma distribution occurs
         j=j+1;
      end
   end
   i=i+1;
end
TransitionPfrac = TransitionPfrac(1)
i=1;
while i <= ErStop(1)
   SSRcal = (CombinedPfrac(i) - expfraction(i))^2; % Regression sum of squares
   SSRhold(i) = SSRcal; % holds the value in a array
   i=i+1;
end
SSR = sum(SSRhold)/ErStop(1); % Regression sum of squares

% Entropy
H = a + log(B*gamma(a)) - ((a+1)*psi(a))

% Plot the Combined NLS vs. Experimental data after automatic fitting
figure % creates a new figure
yyaxis left % sets up the left yaxis
p = plot(time,expfraction,time,CombinedPfrac,'k'); % plotted data for the left y-axis
title('Combined NLS comparison with experimental data') % plot title
xlabel('Time (microseconds)') % generates axis titles
ylabel('fraction of polarization reversal')
ylim([-0.01 1]) % sets bounds for the left y-axis
%xlim([0 (2-tcorrection)])
xlim([0 1.5])
p(1).LineWidth = 3; % sets the width of lines in the plot
p(2).LineWidth = 2;
caption = sprintf(' n = %1.2s \n Trans = %1.2s \n t_0 voltage s.p. = %1.1s \n SSR = %1.3s',Avramin,TransitionPfrac,tzerosp,SSR); %
text for the caption, limited to one decimal place by %1.1s
text(0.1,0.6,caption); % generates a text box at the coordinates (x,y,caption) according to the left y-axis
% setting up the right y-axis
yyaxis right % sets up the right y axis. syntax below will correspond to the right y-axis.
plot(time,CombinedNucDist); % plotted data for the right y-axis
ylabel('Distribution Function')
legend('experimental','NLS model','Dist. Function') % creates a legend for both the left and right y-axes in one box

CombinedPfrac = transpose(CombinedPfrac);
NucPercent=transpose(NucPercent);
PrOutput = [time,expfraction,-CombinedPfrac,NucRatePeak];
amp = abs(amp); % used to calcualte the amplitude of the applied field
```

```
AppliedField = (max(amp)/(10^6))/thickness; % The calculated applied field in MV/cm
Properties = [tzerosp,a,B,Avramin,SSR]; % a set of output properties
```

VITA

Leonard Jacques

Leonard Jacques attended the University of Maryland, Baltimore County (UMBC) for a B.S. in Mechanical Engineering as a member of the class of 2017 and the Meyerhoff Scholar's Program. During that time, he participated in materials research at NIST, The Pennsylvania State University (working for Dr. Susan Trolier-McKinstry), and the University of Florida. Leonard attended the Pennsylvania State University for his M.S. in Materials Science and Engineering, which he obtained in 2021. He continued his studies for a PhD in Engineering Science and Mechanics which he completed in the spring of 2025.